Doctoral theses at NTNU, 2023:332

Hursanay Fyhn

Dynamic Pore Network Study of Immiscible Two-Phase Flow in Porous Media

Doctoral thesis

NTNU
Norwegian University of Science and Technology
Thesis for the Degree of
Philosophiae Doctor
Faculty of Natural Sciences
Department of Physics

NTNU
Norwegian University of
Science and Technology

Hursanay Fyhn

Dynamic Pore Network Study of Immiscible Two-Phase Flow in Porous Media

Thesis for the Degree of Philosophiae Doctor

Trondheim, October 2023

Norwegian University of Science and Technology
Faculty of Natural Sciences
Department of Physics

NTNU
Norwegian University of
Science and Technology

NTNU
Norwegian University of Science and Technology

Thesis for the Degree of Philosophiae Doctor

Faculty of Natural Sciences
Department of Physics

ISBN 978-82-326-7364-3 (printed ver.)
ISBN 978-82-326-7363-6 (electronic ver.)
ISSN 1503-8181 (printed ver.)
ISSN 2703-8084 (online ver.)

Doctoral theses at NTNU, 2023:332

Printed by NTNU Grafisk senter

ئىز

ياش ئىدۇق ئۇزۇن سەپەرگە ئاتلىنىپ چىققاندا بىز،
ئەمدى ئاتقا مىنگۈدەك بولۇپ قالدى ئەنە نەۋرىمىز.
ئاز ئىدۇق مۈشكۈل سەپەرگە ئاتلىنىپ چىققاندا بىز،
ئەمدى چوڭ كارۋان ئاتالدۇق قالدۇرۇپ چۆللەردە ئىز.
قالدى ئىز چۆللەر ئارا، گاھى داۋانلاردا يەنە،
قالدى نى نى ئارسلانلار دەشتى-چۆلدە قەۋرىسىز.
قەۋرىسىز قالدى دېمەڭ، يۇلغۇن قىزارغان دالىدا،
گۈل-چېچەككە پۈركىنەر تاڭنا باھاردا قەۋرىمىز.
قالدى ئىز، قالدى مەنزىل، قالدى يىراقتا ھەممىسى،
چىقسا بوران، كۆچسە قۇملار، ھەم كۆمۈلمەس ئىزىمىز.
توختىماس كارۋان يولىدىن گەرچە ئاتلار بەك ئورۇق،
تاپقۇسى ھېچ بولمىسا بۇ ئىزنى نەۋرىمىز يا ئەۋرىمىز.

ئابدۇرېھىم ئۆتكۈر

This is a poem titled ”Trace” written by the Uyghur poet Abdurehim Otkur around the year 1985. It is about leaving traces while traversing the journey of life. I used to recite this poem all the time as a child, and now that I am older, I have finally started to grasp the meaning behind it. I have been a part of the research in academia which builds upon the traces left behind by the others, and albeit small, I have attempted to leave traces of my own with the works in this thesis.

Abstract

Porous media research has widespread applications in a variety of fields including biology, medicine, and geology. Notably, it can be used to mitigate the effects of climate change through methods of carbon capture and storage. Fundamental to all disciplines of porous media research is understanding how fluids move through pores under different conditions. In many cases, it involves the movement of multiple fluids rather than a single fluid. An example is the displacement of brine in aquifers with carbon dioxide during carbon sequestration processes. When fluids are immiscible, that is when they do not form a homogeneous mixture, various phenomena arise that can influence the flow. For example, the interfaces between the fluids create capillary pressure barriers that depend on the interfacial tensions, the radii of the pores, and the wetting angles. Due to these barriers, different amount of force is needed to push through different pores. A porous medium can have varying radii and wettability and hence varying capillary pressure barriers along its body. As a result, when being subjected to an externally applied pressure, depending on the magnitude of the pressure, certain regions of the porous medium might become active while others remain dormant. This effect can cause the volumetric flow rate as a function of the applied pressure to deviate from the linear Darcy's law in certain pressure regimes.

There are various ways to model immiscible fluid flow in porous media. The models can range from a simple capillary tube to a bundle of capillary tubes to a network of interconnected tubes. One way to model a dynamic pore network is through tracking and moving the interfaces. The procedure at every time step involves calculating the pressure field and thereafter the flow rates and moving the interfaces accordingly while abiding by a set of rules that makes that system more realistic.

The work in this thesis aims to contribute to a better understanding of immiscible two-phase flow in rigid porous media. The main body of work consists of 4 research papers that mostly use a numerical dynamic pore network model, and also capillary tube models. A focus was placed on steady-state non-linear dynamics in terms of the volumetric flow rate as a function of the global pressure difference. Other topics considered in this work include local statistics of porous media, critical phenomena in porous media, and the effects of compressibility.

Preface

This thesis is submitted to the Norwegian University of Science and Technology (NTNU) as a part of the requirements for the degree of philosophiae doctor (PhD). Of the last three years as a PhD candidate, approximately 1.5 years went into performing teaching duties and completing coursework corresponding to 30 ECTS. The remaining half of the time went into producing the research in this thesis. The main supervisor of this thesis is Alex Hansen and the co-supervisor is Knut Jørgen Måløy.

I am grateful to Alex Hansen for offering me a position as a PhD candidate and supervising me. I am also very thankful to Santanu Sinha for his guidance and support. I wish to express my gratitude towards my other colleagues as well, especially, Subhadeep Roy, Cheon HyeJeong, Sebastian Everard Nordby Price, Håkon Pedersen, Federico Lanza, Erika Eiser, Øivind Wilhelmsen, Signe Kjelstrup, Dick Bedeaux and Marie-Laure Olivier. I appreciate all the enjoyable conversations and collaborations I had with you during these past three years at PoreLab.

I wish to thank my husband Eirik from the bottom of my heart. You have celebrated with me through my successes and have given me the strength and encouragement I needed through my struggles. You are not only an amazing partner but also an astonishingly brilliant physicist. Your meticulous academic guidance and mental support can be found in every single part of this thesis. You have my deepest thanks.

Contents

Publications

I **Hursanay Fyhn, Santanu Sinha, Subhadeep Roy and Alex Hansen**, 95
Rheology of Immiscible Two-phase Flow in Mixed Wet Porous Media: Dynamic Pore Network Model and Capillary Fiber Bundle Model Results.
Transport in Porous Media **139**, 491–512 (2021)
DOI: 10.1007/s11242-021-01674-3

II **Hursanay Fyhn, Santanu Sinha and Alex Hansen**, 119
Effective Rheology of Immiscible Two-Phase Flow in Porous Media Consisting of Random Mixtures of Grains having Two Types of Wetting Properties.
Front. Phys. **11**:1175426 (2023)
DOI: 10.3389/fphy.2023.1175426

III **Hursanay Fyhn, Santanu Sinha and Alex Hansen**, 133
Local Statistics of Immiscible and Incompressible Two-Phase Flow in Porous Media.
Physica A: Statistical Mechanics and its Applications **616**, 128626 (2023)
DOI: 10.1016/j.physa.2023.128626

IV **Hyejeong L. Cheon, Hursanay Fyhn, Alex Hansen, Øivind Wilhelmsen and Santanu Sinha**, 151
Steady-State Two-Phase Flow of Compressible and Incompressible Fluids in a Capillary Tube of Varying Radius.
Transport in Porous Media **147**, 15–33 (2023)
DOI: 10.1007/s11242-022-01893-2

Introduction

1

1.1 Background motivation

Porous media are solids filled with holes, and they can be found everywhere. It might be easy to overlook the vastness of this category. Starting with ourselves, the human body is a trove of examples of porous media with different degrees of elasticity. To mention a few, arteries and veins are porous vessels that have the vital role of transporting blood [1]. Human skin transports fluids in and out through its pores, for example, by secreting sweat to regulate body temperature [2] and by absorbing topical medication or cosmetic products [3]. Bones are also porous materials that transport fluid and they make up the skeletal framework of the body [4, 5]. Looking outside of the human body and into the room you probably find yourself in, you might once again find several examples of porous materials. The porosity of papers determines their absorption ability [6]. The porous properties of ceramics influence their thermal and fracture properties [7, 8]. The strength of the cement in the walls is also a function of the pore structure [9, 10].

Porous media research can also be relevant at an even larger scale, namely the global scale. Arguably the biggest global challenge the world is facing right now is climate change. As described by the United Nations [11], climate change brings severe consequences to humankind and to all other life forms on earth. One example is an increase in heavy precipitation and rising sea levels which can cause flooding and landslides [12, 13]. The effects of such events have been deadly and economically costly [14]. Another example is the thawing of frozen soils i.e. permafrost [12]. There are large quantities of greenhouse gases, carbon dioxide (CO_2) and methane, trapped in the permafrost in regions around the Arctic [15, 16]. With thawing in these regions, these greenhouse gases get released and with that, a positive feedback loop is created that accelerates climate change. Yet another example is droughts that result from increases in temperature [12], which further increases the need for procuring clean drinkable water. One way to help mitigate the effects of drought is with desalination, i.e. removing salt from seawater and thereby making it drinkable. Desalination can be done through the method of reverse osmosis with the use of membranes [17, 18].

In all of these three examples, there is a need to understand the transport of fluids, liquids and also gases in the case of permafrost thawing, through various porous media such as soils and membranes. In other words, porous media research can be utilized to adapt to certain consequences of climate change. In addition to the aim of adaptation, porous media research can also be useful in preventing and reversing damages done to the environment and the atmosphere. Porous materials and transportation of fluids through porous media can be used in the processes of CO_2 sequestration. The idea is to separate and capture CO_2 from industrial sources instead of releasing it into the air, and thereafter store it in geological formations such as deep saline aquifers that are porous rock formations that are deep under the seabed [12, 19–25]. This task requires knowledge from porous media research regarding the transport of two fluid phases, water and gas, simultaneously through porous media.

The goal of the present thesis is to use theoretical and numerical methods to contribute to a better understanding of transport in porous media. Specifically, the work done in this thesis is focused on, but not limited to, steady-state non-linear dynamics of immiscible two-phase flow in rigid porous media. This is a central topic in papers I and II which examine disorder in wettability in porous media as a source of non-linearity. The non-linear dynamics refers to the non-linear relation between the global pressure difference and the total volumetric flow rate. Two fluids are immiscible if they do not mix into a homogeneous mixture. Unlike these papers where both fluids are incompressible and flow through porous media with connected pores, the model in paper IV is of a capillary tube with one of the fluids compressible. There, one can also see a weak non-linearity between the flow rate and the pressure drop. A different aspect of porous media is investigated in paper III, namely the local statistics and the reservoir independence of porous media. Some of the earlier works regarding non-linear dynamics are briefly summarised in section 1.2 and the outline of the thesis is given in section 1.3.

1.2 Earlier works on non-linearity

The relation between the externally applied global pressure ΔP and the total volumetric flow rate Q can be written as

$$Q \propto (|\Delta P| - P_t)^{\beta}, \tag{1.1}$$

where P_t is the minimum threshold pressure required to have a non-zero flow and β is an exponent. The widely used Darcy's law states that Q is related linearly to ΔP. Darcy's law is often valid for single-phase flow in porous media, but with multiple fluid phases present, the system could end up having $\beta > 1$ for certain pressure regimes. The explanation behind how and why different systems can produce different β is left for a later chapter. The short review here focuses on the earlier works regarding $\beta > 1$.

In 2009, Tallakstad et al. [26, 27] carried out an experimental study using a two-dimensional Hele-Shaw cell with glass beads, filled with air and a mixture of glycerin and water. They reported on a power-law of the form $|\Delta P| \propto Ca^{0.54\pm0.08}$ where Ca is the capillary number that is the ratio of viscous to capillary forces. The relation $Ca = \frac{\mu Q}{\sigma A}$, where σ is the interfacial tension and A is the area, and propagation of uncertainty means that the power law they discovered gives $\beta = 1.85 \pm 0.27$. Two years later, in 2011, Rassi et al. [28] used nuclear magnetic resonance to study bead packs filled with water and air and measured an exponent corresponding to β between 2.2 and 3.3. Using Hele-Shaw cell with a water-glycerol solution and a commercial food grade rapeseed oil, Aursjø et al. [29] in 2014 created a film flow dominated flow where they measured β that is 1.50 ± 0.11 or 1.35 ± 0.09 depending on the fractional flow rates. In more recent years, the group associated with Martin J. Blunt in Imperial College London has used methods such as X-ray microtomography to observe the non-linear behavior experimentally [30–32].

In paper I in this thesis, theoretical calculations were done to understand the non-linear behavior better. Dynamic network models were used in papers I and II and capillary tube models were used in papers I and IV to investigate the wide range of porous media and fluid combinations that can yield a $\beta > 1$. There have been several other theoretical and numerical works throughout the years that have also supported the existence of the non-linearity relating Q and ΔP

and reported on exponents β similar to the experimentally observed values [33–41]. The commonly used numerical models are network models [35–37], capillary tube or fiber models [38, 39, 41] and lattice Boltzmann models [40].

1.3 Outline of the thesis

The chapters of this thesis aim to provide derivations and explanations for the equations, methods, theories and models used in the papers. The thesis begins with a study of the forces at the scale of the interfaces in chapter 2. Various forms of the equation for the volumetric flow rate in a capillary tube are derived and explained in chapter 3. This includes a general form that holds for an arbitrary number of interfaces, number of fluid phases in the tube, interface curvatures, and types of fluids. The contents of chapters 2 and 3 are relevant for all of the papers I–IV. For porous media with many connected pores, the relation between the global pressure difference and the total volumetric flow rate at steady state is discussed in chapter 4, which is a central topic for papers I and II. Explanations concerning percolation and critical behavior in porous media that are relevant for paper II are covered in chapter 5. A short review regarding the statistical mechanical theory of porous media which is relevant for paper III is given in chapter 6. Most of the work in this thesis, papers I–III, was performed using a dynamic pore network model, and its workings are explained in detail in chapter 7. Selected highlights from papers I–IV are presented in chapter 8. Finally, the contents of the chapters of the thesis are summarized in chapter 9.

2

Interface properties

Imagine yourself walking outside with your friend who was clever enough to bring a raincoat. After a short while, it starts raining and you regret not listening to your friend's warning about the unpredictable Norwegian weather. All the while, you become increasingly aware of how the raindrops are promptly getting absorbed into your favorite cotton shirt while just gliding off of your friend's raincoat. The origin of these kinds of fascinating interactions can be understood by studying the variety of forces that act on the interface boundaries between different substances. This chapter examines situations involving two immiscible fluids and a solid.

2.1 Two immiscible fluids in contact with a solid

Consider a scenario where a drop of a fluid is submerged in another fluid and they are immiscible. The molecules of the droplet will experience a stronger pull by the molecules of the same phase than by the molecules from the other phase. This results in two types of forces acting on the interface. Firstly, there will be a net force pulling the surface molecules inwards toward the molecules of the same phase. This in turn creates a pressure build-up inside the droplet, balancing the forces in the orthogonal direction to the surface. Secondly, the attractive forces between the surface molecules of the same phase act tangentially to the surface, and this is termed interfacial tensions σ, which is in the units of force per unit length. The net effect of these two forces will cause the droplet to form a spherical shape, minimizing the surface area to volume ratio.

Naturally, the same physical principles apply when there are two immiscible fluids in contact with a solid as illustrated in figure 2.1. The fluid that wets the solid surface the most, and hence has the smallest wetting angle θ, can be referred to as the wetting (w) fluid. The other fluid that is resting on the solid as a droplet in figure 2.1 is more non-wetting and can therefore be referred to as the non-wetting (nw) fluid. The wetting angle θ through the nw fluid is larger than 90°. The same type of forces as in the previous example act across and along the interfaces. In figure 2.1, σ, σ_{w} and σ_{nw} are, respectively, the interfacial tension on the interfaces between the two fluids, between the w fluid and the solid, and between the nw fluid and the solid. A balance of the forces originating from these three interfaces determines the wettability and, with that, the angle θ. Horizontal force balance at the point where the three interfaces meet gives

$$\sigma \cos\theta = \sigma_{\mathrm{nw}} - \sigma_{\mathrm{w}}. \tag{2.1}$$

The vertical component of σ is equilibrated by the attractive forces the fluid molecules have with the solid.

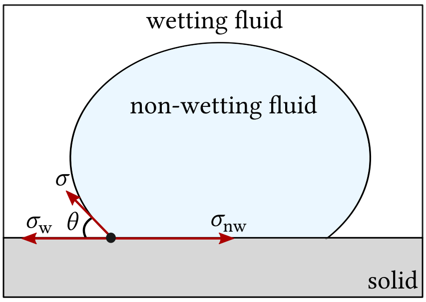

Figure 2.1: A sketch of two fluids on a solid surface. The interface between the two fluids makes a wetting angle θ with the solid. The symbols σ, σ_{w} and σ_{nw} are, respectively, the interfacial tension between the two fluids, between the wetting fluid and the solid and between the non-wetting fluid and the solid.

In the next step, let us look at a scenario where two immiscible fluids are flowing in a cylindrical solid tube with radius r, as illustrated in figure 2.2. Let the interface between the two fluids cover the entire cross-section of the tube. The w fluid has a pressure p_{w} and the nw fluid has a pressure p_{nw}. The capillary pressure p_c is conventionally defined as the difference between these as $p_c = p_{\mathrm{nw}} - p_{\mathrm{w}}$ and pushes from the nw fluid into the w fluid. Here, it is assumed that p_c is constant across the interface. In order to balance the forces on the interface between the fluids and understand the factors that determine the interface's shape, it is useful to examine different portions of figure 2.2(a) in figure 2.2(b–d).

Shown in figure 2.2(b) is a piece of the two-fluid interface that touches the solid wall, with dimensions $\mathrm{d}\tilde{r}$ in the radial direction and $r\,\mathrm{d}\alpha$ along the wall where $\mathrm{d}\alpha$ is a small angle. Figure 2.2(b.1) is the side

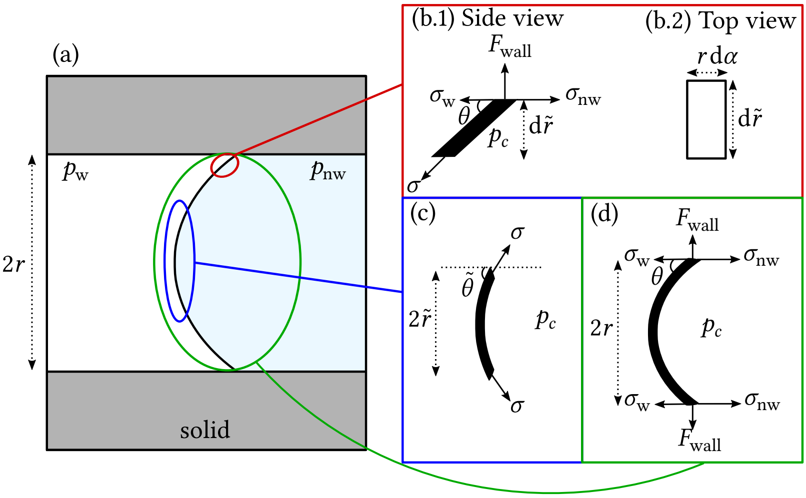

Figure 2.2: (a) A sketch of two immiscible fluids in a solid cylindrical tube with inner radius r. (b–d) show the forces acting on different portions of the interface between the two fluids. The capillary pressure p_c is the difference in pressure in the non-wetting fluid p_{nw} and the wetting fluid p_{w} and pushes into the wetting fluid. The symbols σ, σ_{w} and σ_{nw} are, respectively, the interfacial tension between the two fluids, between the wetting fluid and the solid, and between the non-wetting fluid and the solid. The two-fluid interface makes a wetting angle θ with the solid through the wetting fluid. The wall pulls on the interface with a force F_{wall}. (b) shows a piece of the interface that touches the solid wall, with dimensions $\mathrm{d}\tilde{r}$ in the radial direction and $r\,\mathrm{d}\alpha$ along the wall. (b.1) is the side view that is the same view as in (a) and (b.2) shows the view from the left in (a). (c) shows the central part of the interface between the two fluids that covers a radius $\tilde{r}$ of the pore space and makes an angle $\tilde{\theta}$ with the horizontal axis. (d) shows the entire interface.

view of the piece that is the same view as in (a) while figure 2.2(b.2) shows the view that is seen from the left in (a). The rest of the two-fluid interface pulls on this piece with σ and its vertical component $\sigma \sin\theta$ is balanced by the force from the wall F_{wall}. When it comes to the horizontal force balance, the contributions of all three interfacial tensions and the capillary pressure need to be considered. For small $\mathrm{d}\tilde{r}$, the cross-sectional area of the piece is approximately $r\,\mathrm{d}\alpha\,\mathrm{d}\tilde{r}$, meaning p_c is pushing from the right in figure 2.2(b.1) with a force $p_c r\,\mathrm{d}\alpha\,\mathrm{d}\tilde{r}$. The length on which the interfacial tensions are acting is $r\,\mathrm{d}\alpha$. Assuming that there is no acceleration, the horizontal force balance is then

$$p_c r\,\mathrm{d}\alpha\,\mathrm{d}\tilde{r} + \sigma_{\text{w}} r\,\mathrm{d}\alpha + \sigma\cos\theta\, r\,\mathrm{d}\alpha - \sigma_{\text{nw}} r\,\mathrm{d}\alpha = 0, \tag{2.2}$$

which when $\mathrm{d}\tilde{r} \longrightarrow 0$ becomes the same as equation (2.1), namely

$$\sigma\cos\theta = \sigma_{\text{nw}} - \sigma_{\text{w}}. \tag{2.3}$$

Figure 2.2(c) shows the central part of the interface between the two fluids that covers a radius $\tilde{r}$ of the pore space. At a radius $\tilde{r}$ from the center axis of the tube, the two-fluid interface makes an angle $\tilde{\theta}$ with the horizontal axis such that $\lim_{\tilde{r}\longrightarrow r} \tilde{\theta} = \theta$. The rest of the interface pulls on the portion in figure 2.2(c) with a force σ that acts on the circumference $2\pi\tilde{r}$. In addition, there will be a force from p_c pushing from the right in figure 2.2(c). Together, the horizontal force balance is

$$\pi\tilde{r}^2 p_c = 2\pi\tilde{r}\sigma\cos\tilde{\theta} \tag{2.4a}$$

$$\Longrightarrow \qquad p_c = \frac{2\sigma\cos\tilde{\theta}}{\tilde{r}}. \tag{2.4b}$$

From equation (2.4b), if p_c and σ are known, one can map out the entire shape of the interface between the two fluids by calculating $\tilde{\theta}$ at every $\tilde{r}$.

Figure 2.2(d) shows the entire two-fluid interface. The forces that are acting on the edge of this interface are no longer the pull from the rest of the interface as in figure 2.2(c) since there is none. Instead, the forces are from the wall F_{wall} and from the other two interface σ_{w} and σ_{nw}. The pressure difference between the fluids p_c is, as before, pushing from the right in the sketch. A horizontal force balance gives

$$\pi r^2 p_c = 2\pi r(\sigma_{\text{nw}} - \sigma_{\text{w}}). \tag{2.5}$$

Inserting equation (2.3) into equation (2.5) results in the Young-Laplace equation that is commonly seen in the literature [42]

$$p_c = \frac{2\sigma \cos \theta}{r}, \tag{2.6}$$

which is also what equation (2.4b) goes towards in the limit $\tilde{r} \longrightarrow r$.

It should be mentioned that instead of looking at the force balance as was done here, the fluid configurations and pressures in the pore space can equivalently be studied through the concept of conservation of energy, see for example the book by Blunt (2017) [42].

2.2 Simplifications

In the real world, the scenarios involving two fluids in a pore can have various other elements influencing the configuration and the flow than what is considered in the chapters of this thesis and in papers I–IV. For example, the wettability of a certain material can alter over time due to exposure to different substances [43, 44]. In this thesis, spatial variation in wettability is one of the main investigation points and the time frames of the studies are assumed to be short enough to not alter the local wettability.

Furthermore, real pores can have shapes that are highly irregular with, for instance, surface roughness that can influence the wetting angle [45]. At the molecular level, the intrinsic wetting angle should be the same as for a smooth surface, but depending on the local geometry it can be hard to discern which of the two fluids is wetting or non-wetting. Since roughness can make it hard for both fluids to pass through, the solid surface can appear to be non-wetting for both fluids during the initial exposure. The wetting fluid phase normally tends to reside in the corners and crevices. Therefore, during the initial encounter, the wetting fluid can fill up the irregularities, which can make the surface appear more wetting afterward. The wetting fluid on the edges can connect and carry flow through those layers and films while not having to displace the non-wetting fluid. Film flow has been a topic of interest in several studies [46, 47]. It is hard to quantify the exact effect of roughness, but an overall effective wetting angle can be defined, for example through the pressure needed for a non-zero displacement [42]. The roughness can also be directional, meaning the effect of roughness can vary depending on the flow direction.

The pores considered in the analytical calculations and the numerical simulations in this thesis are simplified structures as in figure 2.2 with cylindrical symmetry around a center axis and with an unchanging wetting angle. A certain degree of spatial disorder in shape is still included in the models by giving the pores a sinusoidal shape, meaning the radii of the pores vary with the position along the center axis. Furthermore, only a piston-like flow where the interfaces span the entire cross-section of the pore as in figure 2.2(a) is considered in this thesis, as that is often the way the fluids are transporten [42].

3 Flow through a capillary tube

This chapter concerns flow through a single capillary tube, which is a topic relevant for all of the papers I–IV. It starts with the case with one incompressible fluid in section 3.1 before moving on to how multiple incompressible fluids flow together in section 3.2. More specifically, the end goal is to derive the expression for the volumetric flow rate in a tube, q, for any number of different fluid phases with any number of interfaces between them. Thereafter, some smaller topics are addressed briefly, such as how to find time-averaged flow in section 3.3, the effects of compressibility in section 3.4, as well as, capillary bundle models in section 3.5.

3.1 Single-phase flow

Applying Newton's second law to an incompressible fluid results in the Navier-Stokes equation [48]

$$\mu\nabla^2\boldsymbol{v} = \rho\left(\frac{\partial\boldsymbol{v}}{\partial t} + \boldsymbol{v}\cdot\nabla\boldsymbol{v}\right) + \nabla p - \rho\boldsymbol{g}, \tag{3.1}$$

that describes the velocity $\boldsymbol{v}$ of the fluid. There are three different forces per unit volume in this equation that causes the fluid with density ρ to accelerate with a total acceleration $\mathrm{d}\boldsymbol{v}/\mathrm{d}t = \partial\boldsymbol{v}/\partial t + \boldsymbol{v}\cdot\nabla\boldsymbol{v}$ where t is the time. The fluid with viscosity μ resists flow with a force described by the first term, and the gradient in the pressure p and the gravitational acceleration $\boldsymbol{g}$ drives the flow as described by the third and the fourth terms.

Consider a thin capillary tube with small variations in the radius and with a center axis $\boldsymbol{x}$. Since the velocity $\boldsymbol{v}$ close to the tube wall will be in the x-direction and the tube is narrow, $\boldsymbol{v}$ in the entire tube will be

$$\boldsymbol{v} \approx v(\tilde{r})\,\hat{x} \tag{3.2}$$

where $\hat{x}$ is a unit vector along $\boldsymbol{x}$. The direction of $\boldsymbol{g}$ is the vertical direction $\boldsymbol{y}$ with unit vector $\hat{y}$. If the tube is placed horizontally, such that

$$\boldsymbol{g}\cdot\boldsymbol{v} = g\hat{y}\cdot v\hat{x} = 0, \tag{3.3}$$

the y component of equation (3.1) would mean that

$$\frac{\partial p}{\partial y}\hat{y} - \rho \boldsymbol{g} = \boldsymbol{0}. \tag{3.4}$$

Inserting equation (3.4) into equation (3.1) results in

$$\mu \nabla^2 \boldsymbol{v} = \rho\left(\frac{\partial \boldsymbol{v}}{\partial t} + \boldsymbol{v}\cdot\nabla\boldsymbol{v}\right) + \frac{\partial p}{\partial x}\hat{x}. \tag{3.5}$$

Another equation that is useful at this point is the conservation of mass [48]

$$\int \frac{\partial \rho}{\partial t}\,\mathrm{d}V = \int \rho \boldsymbol{v}\cdot\hat{n}\,\mathrm{d}S \tag{3.6}$$

which states that the total rate of change of mass with time inside a volume V must be equal to the rate at which mass crosses the surface S of that volume with normal vector $\hat{n}$. The right hand side of equation (3.6) can be rewritten using Gauss' theorem [49] to give

$$\int \frac{\partial \rho}{\partial t}\,\mathrm{d}V = \int \nabla\cdot(\rho\boldsymbol{v})\,\mathrm{d}V, \tag{3.7}$$

Since equation (3.7) should hold for any V, the integrands must be equal, meaning

$$\frac{\partial \rho}{\partial t} = \nabla\cdot(\rho\boldsymbol{v}). \tag{3.8}$$

For an incompressible fluid whose density is constant in time and space, equation (3.8) is reduced to

$$\nabla\cdot\boldsymbol{v} = 0. \tag{3.9}$$

With equation (3.2), equation (3.9) becomes

$$\frac{\partial v}{\partial x} \approx 0 \tag{3.10}$$

which further makes

$$\boldsymbol{v}\cdot\nabla\boldsymbol{v} = v\frac{\partial v}{\partial x}\hat{x} \approx \boldsymbol{0}. \tag{3.11}$$

Equation (3.2) can also be used to get

$$\nabla^2 \boldsymbol{v} \approx \frac{1}{\tilde{r}} \frac{\partial}{\partial \tilde{r}} \left(\tilde{r} \frac{\partial v}{\partial \tilde{r}} \right) \hat{x}. \tag{3.12}$$

Furthermore, assuming that the system is in a steady state where the velocity is unchanging with time makes

$$\frac{\partial \boldsymbol{v}}{\partial t} \approx \boldsymbol{0}. \tag{3.13}$$

Finally, inserting equations (3.11)–(3.13) into equation (3.5) gives

$$\frac{\mu}{\tilde{r}} \frac{\partial}{\partial \tilde{r}} \left(\tilde{r} \frac{\partial v}{\partial \tilde{r}} \right) = \frac{\partial p}{\partial x}. \tag{3.14}$$

The solution to this equation is

$$v = \frac{\tilde{r}^2}{4\mu} \frac{\partial p}{\partial x} + c_1 \ln \tilde{r} + c_2 \tag{3.15}$$

where c_1 and c_2 are integration constants. For v to be finite at $\tilde{r} = 0$, it must be that $c_1 = 0$. In addition, using a no-slip boundary condition, i.e. requiring v to be zero at $\tilde{r} = r$, gives the value for c_2, such that

$$v = \frac{\tilde{r}^2 - r^2}{4\mu} \frac{\partial p}{\partial x}. \tag{3.16}$$

Integrating this expression for v over a cross-section of the tube gives the total volumetric flow rate q through a single tube as

$$q = \int_0^r 2\pi \tilde{r} v \, \mathrm{d}\tilde{r} = -\frac{\pi r^4}{8\mu} \frac{\partial p}{\partial x}, \tag{3.17}$$

which is called Poiseuille flow [48].

3.2 Multi-phase flow

In this section, the results from section 3.1 regarding a single fluid are built upon to study multiple incompressible and immiscible fluid phases flowing in a cylindrical tube with approximately constant radius along its length. The derived equations hold for arbitrary curvature and direction of the curvature of the interfaces and arbitrary types of fluids. The studies begin in section 3.2.1 with a case with only one interface in a tube. Thereafter, in section 3.2.2, proof by induction is used to derive the general expression for the volumetric flow rate when having any number of interfaces between any number of fluid phases in a tube. In section 3.2.3, the role of the interface curvature is addressed by relating the results derived in section 3.2.2 to those from chapter 2.

3.2.1 One interface between two fluids

The sketch in figure 3.1 shows two fluids with an interface between them that covers the cross-section of the tube. Since the derivations of this section hold regardless of the wettability of the fluids with respect to the solid and the curvature of the interface, they are not specified here and the interface is represented by a dotted line in figure 3.1. The tube has a length l and the fluids are numbered 1 and 2. The pressure p at the inlet and the outlet of the tube are, respectively, p_{in} and p_{out}. Immediately to the left and to the right of the interface at x_k, p is respectively $p\left(x_k^-\right)$ and $p\left(x_k^+\right)$.

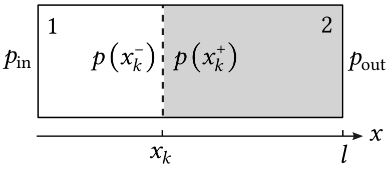

Figure 3.1: A sketch of two immiscible fluids in a cylindrical tube with an interface between them at position x_k along the center axis x of the tube. The tube has a length l and the fluids are numbered 1 and 2. The pressure at the inlet and the outlet are p_{in} and p_{out}, respectively. The pressure immediately to the right of the interface is $p(x_k^+)$ and immediately to the left is $p(x_k^-)$.

The derivations in section 3.1 hold true when considering either side of the interface in figure 3.1 separately. That is, both the Navier-Stokes equation in equation (3.1) and the mass balance in equation (3.6), hence also the expression for q in equation (3.17) that followed based on the assumptions should hold for either side of the interface.

Within each fluid phase, p varies linearly given that r is approximately constant. The reason for this is that q in equation (3.17) is constant along the tube due to the incompressibility of the fluids, which further makes the pressure gradient $\partial p/\partial x$ constant. At the interface positions x_k, p experiences a jump. To the left of the interface in figure 3.1

$$\left(\frac{\partial p}{\partial x}\right)_{\text{left}} = \frac{p\left(x_k^-\right) - p_{\text{in}}}{x_k}, \tag{3.18}$$

and to the right

$$\left(\frac{\partial p}{\partial x}\right)_{\text{right}} = \frac{p_{\text{out}} - p\left(x_k^+\right)}{l - x_k}. \tag{3.19}$$

Inserting equations (3.18) and (3.19) into equation (3.17) gives

$$(q)_{\text{left}} = -\frac{\pi r^4}{8\mu_1}\frac{p\left(x_k^-\right) - p_{\text{in}}}{x_k} \tag{3.20}$$

at the left side of the interface and

$$(q)_{\text{right}} = -\frac{\pi r^4}{8\mu_2}\frac{p_{\text{out}} - p\left(x_k^+\right)}{l - x_k} \tag{3.21}$$

at the right side of the interface, where μ_1 and μ_2 are the viscosities of the left fluid numbered 1 the right fluid numbered 2, respectively. Due to the conservation of volume, q must be the same over the entire tube, i.e. equation (3.20) and equation (3.21) must be equal

$$\frac{p\left(x_k^-\right) - p_{\text{in}}}{\mu_1 x_k} = \frac{p_{\text{out}} - p\left(x_k^+\right)}{\mu_2(l - x_k)}. \tag{3.22}$$

A useful quantity to introduce now is the difference in pressure across the interface

$$\delta_k p = p\left(x_k^+\right) - p\left(x_k^-\right). \tag{3.23}$$

The relation between $\delta_k p$ and the capillary pressure p_c introduced in chapter 2, as well as, the direction of the curvature of the interface are to be explained in section 3.2.3. Using equation (3.23) and doing some algebra on equation (3.22) results in

$$p\left(x_k^-\right) = \frac{\mu_1 x_k\left(p_{\text{out}} - \delta_k p\right) + \mu_2(l - x_k)p_{\text{in}}}{\mu_1 x_k + \mu_2(l - x_k)}. \tag{3.24}$$

This can be inserted into equation (3.20) to get

$$q = -\frac{\pi r^4}{8\mu_1 x_k}\left(\frac{\mu_1 x_k (p_{\text{out}} - \delta_k p) + \mu_2(l - x_k)p_{\text{in}}}{\mu_1 x_k + \mu_2(l - x_k)} - p_{\text{in}}\right) \tag{3.25a}$$

$$= -\frac{\pi r^4}{8\left(\mu_1 x_k + \mu_2(l - x_k)\right)}\left(p_{\text{out}} - p_{\text{in}} - \delta_k p\right). \tag{3.25b}$$

Let the pressure difference between the outlet and the inlet of the tube be denoted by

$$\Delta p = p_{\text{out}} - p_{\text{in}}, \tag{3.26}$$

and the effective viscosity be denoted by

$$\mu_{\text{eff}} = \sum_{i=1}^{n+1} \mu_i s_i. \tag{3.27}$$

In equation (3.27), the total number of fluids in the system is $n + 1$, and for fluid number i, μ_i is the viscosity and s_i is the saturation in that tube. The saturation is

$$s_i = \frac{V_i}{V} \tag{3.28}$$

where V_i is the total volume of fluid number i and V is the volume of the tube. Since the cross-sectional area along the tube is assumed to be approximately constant, the saturation can be written as

$$s_i = \frac{l_i}{l}, \tag{3.29}$$

where l_i is the total length of the tube covered by fluid number i. With equations (3.27) and (3.29), the case illustrated in figure 3.1 has

$$\mu_{\text{eff}} l = (\mu_1 s_1 + \mu_2 s_2) \cdot l = \mu_1 x_k + \mu_2(l - x_k). \tag{3.30}$$

Finally, inserting equations (3.26) and (3.30) into equation (3.25b) gives

$$q = -\frac{\pi r^4}{8\mu_{\text{eff}} l}\left(\Delta p - \delta_k p\right) \tag{3.31}$$

which is a variant of the Washburn equation [50].

3.2.2 Multiple interfaces between multiple fluids

The sketch in figure 3.2 shows n interfaces separating $n+1$ fluid portions. The fluids are incompressible. As in section 3.2.1, the derivations in this section are also independent of the type of the fluids, the number of different fluid types, and the curvature of the interfaces. Therefore, the interfaces in figure 3.2 are also represented by dotted lines to symbolize that they can bend in any direction with any wetting angle, and the compositions of the fluid portions are not specified. Note that there is no restriction saying that some or all of the $n + 1$ fluid portions cannot be of the same type of fluid.

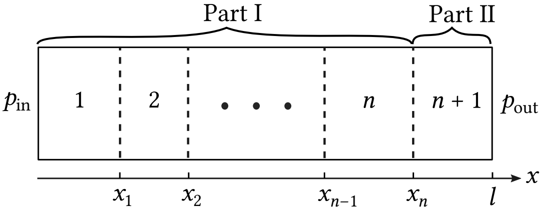

Figure 3.2: A sketch of a cylindrical tube containing shows n interfaces separating a total of $n + 1$ fluid portions. The interfaces are positioned at $x_k \in \{x_1, x_2, \ldots, x_n\}$ along the center axis x of the tube. The tube has a length l. The pressure at the inlet and the outlet are p_{in} and p_{out}, respectively.

I will now use the method of mathematical induction [49] to prove that the general expression for the volumetric flow rate in a tube with n interfaces separating $n + 1$ fluid portions is

$$q = -\frac{\pi r^4}{8\mu_{\text{eff}} l}\left(\Delta p - \sum_{k=1}^{n} \delta_k p\right). \tag{3.32}$$

If $n = 1$, equation (3.32) becomes equation (3.31) derived in section 3.2.1 for one interface. With this, the first step of the proof is completed. In the next step, it must be proven that if equation (3.32) is true when the total number of interfaces is $n - 1$ for any integer n, then it is also true when the total number of interfaces is n. Since the base case with $n = 1$ is already proven, completing the next step will prove the ultimate validity of equation (3.32).

Part I in figure 3.2 has $n - 1$ number of interfaces inside and has an outlet pressure of $p(x_n^-)$ which is the pressure at the immediate left side of the interface positioned at x_n. Based on the induction assumption that equation (3.32) is true for $n-1$ number of interfaces, the flow through part I can be written as

$$q = -\frac{\pi r^4}{8\mu_{\text{eff}}^n l}\left(p(x_n^-) - p_{\text{in}} - \sum_{k=1}^{n-1} \delta_k p\right), \tag{3.33}$$

where $\mu_{\text{eff}}^n = \sum_{i=1}^n \mu_i s_i$ from equation (3.27). Based on equation (3.17), part II in figure 3.2 consisting of only one type of fluid with viscosity μ_{n+1} has

$$q = -\frac{\pi r^4}{8\mu_{n+1}} \frac{p_{\text{out}} - p(x_n^+)}{l - x_n}. \tag{3.34}$$

Due to conservation of volume, q through part I in equation (3.33) and through part II in equation (3.34) must be equal, which means

$$\frac{1}{\mu_{\text{eff}}^n l}\left(p(x_n^-) - p_{\text{in}} - \sum_{k=1}^{n-1} \delta_k p\right) = \frac{1}{\mu_{n+1}} \frac{p_{\text{out}} - p(x_n^+)}{l - x_n}. \tag{3.35}$$

Rewriting this using equation (3.23) gives

$$p(x_n^-) = \frac{\mu_{\text{eff}}^n l(p_{\text{out}} - \delta_n p) + \mu_{n+1}(l - x_n)\left(p_{\text{in}} + \sum_{k=1}^{n-1} \delta_k p\right)}{\mu_{\text{eff}}^n l + \mu_{n+1}(l - x_n)}. \tag{3.36}$$

Inserting this into equation (3.33) and moving things around results in

$$q = -\frac{\pi r^4}{8\left(\mu_{\text{eff}}^n l + \mu_{n+1}(l - x_n)\right)}\left(p_{\text{out}} - \delta_n p - p_{\text{in}} - \sum_{k=1}^{n-1} \delta_k p\right). \tag{3.37}$$

From equation (3.27),

$$\mu_{\text{eff}} l = l \cdot \sum_{i=1}^{n+1} \mu_i s_i = \mu_{\text{eff}}^n l + \mu_{n+1}(l - x_n), \tag{3.38}$$

which inserted into equation (3.37) gives

$$q = -\frac{\pi r^4}{8\mu_{\text{eff}} l}\left((p_{\text{out}} - p_{\text{in}}) - \left(\delta_n p + \sum_{k=1}^{n-1} \delta_k p\right)\right). \tag{3.39}$$

Inserting the definition of Δp from equation (3.26) into this expression and using that $\sum_{k=1}^{n} \delta_k p = \delta_n p + \sum_{k=1}^{n-1} \delta_k p$, one ends up with the final expression that is equation (3.32). This completes the proof of equation (3.32).

3.2.3 Interface curvature between two fluids

The papers in this thesis consider flow of two immiscible fluids in porous media. Two of them, papers I and II, focus on the disorder in wettability and there arises the need to measure the wetting angle θ consistently though the same fluid. In this section, I address how equation (3.32) can be specialized when there are only two fluids in the system and the interfaces have an angle θ through one of the fluids.

Firstly, it should be mentioned that θ is conventionally measured through the wetting fluid which makes the capillary pressure $p_c = (2\sigma \cos\theta)/r$ (equation (2.6)) always positive. However, when working with a wide range of θ, both above and below 90°, the fluid through which it is measured will sometimes be the non-wetting fluid and sometimes be the wetting fluid, which means p_c can be positive or negative.

To understand the problem at hand, let us look at some examples shown in figure 3.3. The examples show two immiscible fluids numbered 1 and 2 in cylindrical tubes with an interface between them at position x_k along the center axis $\boldsymbol{x}$ of the tube with length l. The wetting angle θ is consistently measured through fluid 1. The bottom figures in (a)–(c) show the pressure p profile along those tubes in the examples. As before, p_{in} and p_{out} are the pressures at the inlet and the outlet, respectively, and the pressure immediately to the right of the interface is $p(x_k^+)$ and immediately to the left is $p(x_k^-)$.

In figure 3.3(a) and (b), θ which is measured through fluid 1 (the darker fluid) is the same and hence would give the same value of p_c when inserted into equation (2.6). This is true for θ both larger or smaller than 90°. Since p_c is completely the same for both cases, it alone does not contain information regarding the sign of the pressure gradient across the interface $\delta_k p = p\left(x_k^+\right) - p\left(x_k^-\right)$ (equation (3.23)). In figure 3.3(a), $\delta_k p < 0$, while in figure 3.3(b), $\delta_k p > 0$.

To solve this problem, I introduce a unit vector $\hat{J}$ that lies along $\boldsymbol{x}$ and always points from fluid 1 to 2, see figure 3.3. $\hat{J}$ is then a function of the interface positions x_k. The dot product between $\hat{J}$ and the unit vector $\hat{x}$ can be used to express $\delta_k p$ as a function of p_c as

$$\delta_k p = p_c\, \hat{J}(x_k) \cdot \hat{x} \tag{3.40a}$$

$$= \frac{2\sigma \cos\theta}{r} \hat{J}(x_k) \cdot \hat{x}. \tag{3.40b}$$

In figure 3.3(a), $\hat{J}(x_k) \cdot \hat{x} = 1$ and $\cos\theta < 0$ which from equation (3.40b) correctly gives $\delta_k p < 0$. In figure 3.3(b), $\hat{J}(x_k) \cdot \hat{x} = -1$ and $\cos\theta < 0$ which from equation (3.40b) correctly gives $\delta_k p > 0$. In figure 3.3(c), $\hat{J}(x_k) \cdot \hat{x} = 1$ and $\cos\theta > 0$ which from equation (3.40b) correctly gives $\delta_k p > 0$. With equation (3.40b), the correct pressure gradient will always be measured.

Finally, inserting equation (3.40) into equation (3.32) gives an expression for q of immiscible two-phase flow in a tube with wetting angle θ through one of the fluids,

$$q = -\frac{\pi r^4}{8\mu_{\text{eff}} l}\left(\Delta p - \sum_{k=1}^{n} p_c\, \hat{J}(x_k) \cdot \hat{x}\right) \tag{3.41a}$$

$$= -\frac{\pi r^4}{8\mu_{\text{eff}} l}\left(\Delta p - \sum_{k=1}^{n} \frac{2\sigma \cos\theta}{r} \hat{J}(x_k) \cdot \hat{x}\right). \tag{3.41b}$$

Note that if r and θ are constant, one would get pairwise canceling terms in the sum.

Having r or θ of the tube vary with position x, makes the capillary pressure position dependent. In paper I and paper IV, the capillary tubes were sinusoidal and hence had position-dependent r. As the position-dependent r of a tube is assumed to not deviate too much from its average value $\bar{r}$, the flow q through the tube can be approximated based on equation (3.41b) as

$$q = -\frac{\pi \bar{r}^4}{8\mu_{\text{eff}} l}\left(\Delta p - \sum_{k=1}^{n} \frac{2\sigma \cos\theta(x_k)}{r(x_k)} \hat{J}(x_k) \cdot \hat{x}\right). \tag{3.42}$$

3.3 Average flow

During numerical simulations of immiscible and incompressible fluids in capillary tubes, equations (3.32) and (3.41b) derived above can be used directly at each time step together with the information regarding the positions of the interfaces and how they move depending on the forces

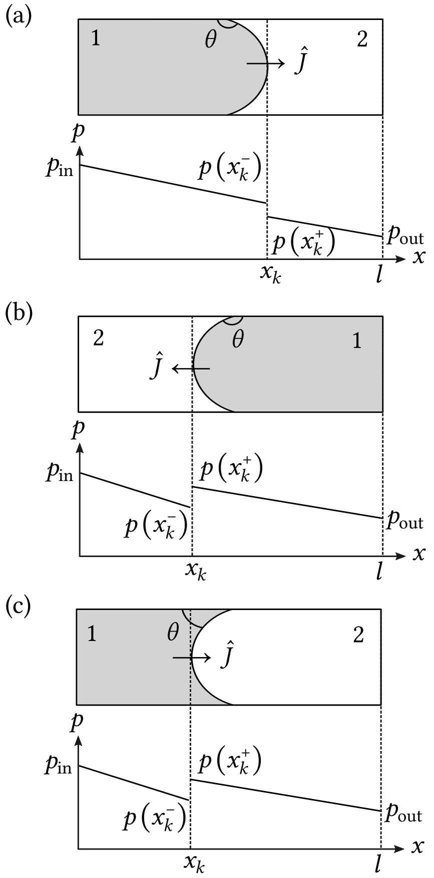

Figure 3.3: The top drawings in (a)–(c) depict two immiscible fluids numbered 1 and 2 in cylindrical tubes with an interface between them at position x_k along the center axis x of the tube. The tube has a length l. The wetting angle θ is consistently measured through fluid 1 and the unit vector $\hat{J}$ lies along $\boldsymbol{x}$ and points from fluid 1 to 2. The bottom figures in (a)–(c) show the pressure p profile along the tube where p_{in} and p_{out} are the pressure at the inlet and the outlet, respectively. The pressure immediately to the right of the interface is $p(x_k^+)$ and immediately to the left is $p(x_k^-)$.

in play. In certain cases, it can be of interest to have an expression for the time-averaged flow, for instance, for theoretical studies as in parts of paper I. This section will briefly sketch a possible way to find the average volumetric flow rate q of incompressible two-phase flow in a capillary tube with varying radius r and wetting angle θ along its center axis $\boldsymbol{x}$.

In the effective one-dimensional description in equation (3.42), the fluids move with a speed that is

$$\frac{\mathrm{d}x}{\mathrm{d}t} \approx \frac{q}{\pi \bar{r}^2}. \tag{3.43}$$

Due to the incompressibility of the fluids, $\frac{\mathrm{d}x}{\mathrm{d}t}$ is approximately constant in space along $\boldsymbol{x}$. However, it is not constant in time as the configuration of the interfaces in the tube changes with time. The time-averaged speed can be estimated as

$$\left\langle \frac{\mathrm{d}x}{\mathrm{d}t} \right\rangle = \frac{l}{\int_0^l \left(\frac{\mathrm{d}x}{\mathrm{d}t} \right)^{-1} \mathrm{d}x}, \tag{3.44}$$

where the numerator is the length of the tube and the denominator is the approximate time it takes to travel the entire length of the tube. Equation (3.44) can be computed using equations (3.42) and (3.43). Thereafter, the result can be used to find the expression for the time-averaged q, which based on equation (3.43) is

$$\langle q \rangle = \pi \bar{r}^2 \left\langle \frac{\mathrm{d}x}{\mathrm{d}t} \right\rangle. \tag{3.45}$$

3.4 Two-phase flow with compressibility

Different properties can be attributed to the fluids inside a capillary tube, and these can influence the overall flow in different ways. In paper IV, one of the two immiscible fluids in a tube is allowed to be compressible. A brief description of the consequences of this is given here.

Having one of the fluids compressible means some of the fluid portions in figure 3.2 are allowed to change volume depending on the pressure, for example, through the ideal gas law. In this scenario, the distance between the two adjacent interfaces, e.g. $x_{k+1} - x_k$, can change unlike in the case with two incompressible fluids traveling through a tube.

In the calculations in sections 3.2.1 and 3.2.2, the fact that q was constant through the entire tube was used several times. This is no longer true with a compressible fluid. Equation (3.17) can nonetheless be used with compressibility considered. The compressible fluid portions expand as they move from a higher pressure region at the inlet toward a lower pressure region at the outlet. Due to the incompressibility of the other fluid, its portions will retain the same volume. The combined effect will be increased volume transported per unit time, in other words, increased q towards the outlet.

3.5 Capillary bundle models

One of the simplest models of porous media must be those with one or many parallel capillary tubes [38, 51–53]. Due to their simplicity, theoretical calculations can be performed on these models, as in paper I, aiding the understanding of the origin of the observed phenomena. Furthermore, when entering uncharted territory in porous media research with properties that are not yet widely understood, these simple models can be a useful starting point.

Placing many capillary tubes in parallel creates a simple form of porous media. To have disorder, the radii r [52] or the wetting angle θ of the tubes in the bundle can be set to be different from each other. In paper I, where the disorder in θ was of interest, θ of the tubes were chosen randomly from various mathematical distributions. With disorder, the tubes will have varying resistances to flow in terms of the total capillary pressure barriers.

Flow through porous media

4

The content in this section moves up in scale to porous media with multiple connected pores, and the focus is placed on the relation between the global pressure difference across the porous media and the total volumetric flow rate in *steady state*. The commonly used Darcy's law connecting these two quantities, for both single and two-phase flow, is described in section 4.1. The situations where the flow behavior can deviate from the linear Darcy's law are described and explained in section 4.2, which is relevant for papers I and II.

4.1 Darcy's law

Based on the derived expression in equation (3.17), the total volumetric flow rate q through a tube depends linearly on the pressure gradient across the tube. This implies that q also depends linearly on the pressure difference across the tube Δp in equation (3.26), when the pressure gradient is uniform along the tube. When there is a collection of many equally contributing tubes that all behave linearly according to equation (3.17), it is a reasonable hypothesis that increasing the total pressure across the entire collection may cause the total volumetric flow rate of the collections to increase linearly as well. This is the essence of Darcy's law for single-phase flow in a porous medium, which is an empirical relationship introduced by Henry Darcy [54].

A collection of many individual pores that are interconnected constitutes a porous medium. Darcy's law, as formulated by e.g. Wyckoff et al. [55], can be written as

$$Q_i = -\frac{K_{ij}A_i}{\mu}\left(\frac{\partial P}{\partial x_j} - \rho g_j\right). \tag{4.1}$$

Here, Q_i is the total volumetric flow rate in the i direction over an area A_i with a normal vector also in the i direction. It relates linearly to $\partial P/\partial x_j$ which is the spatial derivative of the pressure P in the j direction. Furthermore, K_{ij} is the second-order permeability tensor, μ is the viscosity and ρ is the density of the fluid and g_j is the gravitational acceleration in the i direction.

In the papers presented in this thesis, the global pressure across a porous medium ΔP is in the same direction as the total volumetric flow rate Q. With L being the system length, the pressure gradient is then approximately $\Delta P/L$. In addition, the systems are considered to be unaffected by the gravitational acceleration, which can be the case if the system is for example placed on a flat surface orthogonal to the gravitational acceleration. With these considerations, equation (4.1) can be written as

$$Q = -\frac{KA}{\mu L}\Delta P. \tag{4.2}$$

In this expression, K is the permeability that quantifies the ability of a material to transport fluids, and it can be calculated by exposing the material containing a fluid with μ to a known ΔP and measuring Q [56].

When there are multiple immiscible fluid phases flowing simultaneously in a porous media, each fluid experiences resistance from the presence of the other fluids in addition to the porous material itself. This leads to a modification of the permeability in equation (4.2) from K to $k_{rf}K$. The relative permeability k_{rf} for fluid f here accounts for the amount by which the flow of that fluid is restricted by the other fluids. This is a quantity that is measured experimentally. Furthermore, instead of having a single μ as in equation (4.2), each fluid will have its own viscosity. Incorporating these ideas together with an assumption that the linear relationship between Q and ΔP still holds, the modified Darcy's law for each of these fluids, indexed $_f$, is written as [42, 57]

$$Q_f = -\frac{k_{rf}KA}{\mu_f L}\Delta P. \tag{4.3}$$

The total volumetric flow rate summed over all the fluids in the system, $Q = \sum_f Q_f$, is then

$$Q = -\frac{KA\Delta P}{L}\sum_f \frac{k_{rf}}{\mu_f}. \tag{4.4}$$

4.2 Non-linear behavior

Both the single-phase formulation of Darcy's law in equation (4.2) and the multi-phase formulation in equation (4.4) relate Q linearly to

ΔP. The linearity of the empirical Darcy's law has its origin in the assumption that all the pores that are capable of carrying flow are active and are contributing to the flow. While this is often true for single-phase flow, this is not always the case when there are multiple fluids present. The presence of the capillary pressure p_c barriers at the interfaces between the fluids, introduced in chapter 2, breaks down the linearity at certain pressure regimes. More generally, one can write Q as a function of the effective pressure difference $|\Delta P| - P_t$ as

$$Q \propto (|\Delta P| - P_t)^\beta. \tag{4.5}$$

Equation (4.5) can be Darcy-like with $\beta = 1$, but can also be non-linear with $\beta > 1$. The cases that can result in either of these will be explained in this section. Due to the complexity of a porous medium and the capillary barrier contributions from all of the pores, the porous medium itself can develop an overall threshold pressure P_t that resists ΔP. Note that the presence of P_t is relevant for the cases where the porous medium contains many fluid-fluid interfaces in its pores prior to being exposed to ΔP, since P_t originates in the p_c barriers created by such interfaces. P_t can be of a positive finite size or around zero, and the latter can happen even in the presence of the interfaces.

For immiscible two-phase flow in a porous medium, the linear Darcy-like behavior with $\beta = 1$ in equation (4.5) occurs if the flow carrying paths are unchanging with small changes in ΔP. As given in the arguments for Darcy's law at the beginning of section 4.1, linear flow rate contributions from all the individual pores (equation (3.41b)) combine to give a total flow Q which is also linear as a function of the effective pressure .[1] There are two ways in which the flow-carrying paths can be approximately unchanging. The most obvious way is if the entire porous medium is active. This happens when $|\Delta P|$ is large enough that essentially all the pores of the medium are actively transporting fluids. The second way is if the structure of the porous medium is such that it contains certain paths that provide significantly easier passage than everywhere else in the medium. The flow will then mainly be transported through those easy paths for a certain range of low $|\Delta P|$.

---

[1] Strictly speaking, the flow through an individual pore is an affine function of the pressure difference. If the capillary barriers of individual pores differ, it is not necessarily true that the total flow is exactly linear.

The non-linear and non-Darcy-like behavior with $\beta > 1$ in equation (4.5) can be expected when the pressure differences over the individual pores are comparable in size to the capilarry presure barriers. A porous medium is made up of many different pores, and with two immiscible fluids flowing, the pores will contain different numbers of interfaces at each instance in time. Based on equation (3.41b) for flow q in a pore, when the force from the pressure $|\Delta p|$ is pushing in a direction, it must overcome the total p_c due to all the interfaces in that pore in order to have a positive q in the same direction. A small increase in $|\Delta P|$ across a porous medium leads to small increases in $|\Delta p|$ across the pores of the medium. In certain situations, those increased $|\Delta p|$ manage to exceed the resistance of the capillary barriers in several more pores than the ones that were already active. This effect of increasing flow in the previously active pores in addition to opening new ones may be the reason Q is raised more than linearly with increased effective pressure.

When gradually increasing $|\Delta P|$ from zero across a porous medium, Q can alternate between being linear and non-linear in the effective pressure difference, with $\beta = 1$ and $\beta > 1$, respectively. This alternation can happen as many times as the porous structure dictates. For example, with the systems examined in paper I, as soon as $|\Delta P|$ exceeded P_t, it was observed that $\beta > 1$, and as the $|\Delta P|$ increased to a value large enough to activate the entire porous medium, the flow transitioned into a regime with $\beta = 1$. On the other hand, with the systems examined in paper II, several easy paths dominated the flow for the lowest possible $|\Delta P|$ and hence causing $\beta = 1$. Increasing $|\Delta P|$ further led to the opening of new paths after a while, giving $\beta > 1$. Then, similar to the other paper, when $|\Delta P|$ was large enough to activate the entire porous medium, the flow re-entered the linear regime.

5

Critical behavior in porous media

In paper II, a dynamic pore network model is used to simulate porous media made up of solid grains with certain wetting properties. This chapter focuses on one of the topics that are relevant for paper II, namely, critical behavior related to flow in porous media. The specific design of the model exhibits certain similarities with the Random Resistor Network (RRN) models that are widely used to study percolation problems. Due to their similarities, the critical phenomenon that is present in the RRN models was hypothesized to exist in the model used in paper II as well. RRN and its associated criticality are explained in brief terms in section 5.1. Thereafter, in section 5.2, the design of the porous network from paper II is explained. Note that this short explanation covers only the design of the network in paper II, the actual workings of the dynamic pore network model itself will be explained in a later chapter, chapter 7. Thereafter in section 5.3, the porous model's similarities and differences with RRN and how that may or may not result in any critical behavior are discussed.

5.1 RRN model

A random resistor network (RRN), as the name suggests, is a network of resistors that can have different resistances against the transport of the electric current. The resistors can, for instance, be chosen to have one of two resistances based on a probability and the most commonly studied case is with resistance being either infinite or zero [58, 59]. This is the case considered in this chapter and the probability with which one of these resistances is chosen will be called $\bar{p}_G$.

The quantity of interest in an RRN is the conductivity G that measures the material's ability to transport electric current. In the limit where RRN size is infinitely large, there exists a critical threshold probability $\bar{p}_{G,c}$ above which there are connected conducting paths of infinite extent [58, 59]. In this scenario, the overall conductivity of RRN goes as [59, 60]

$$G \propto (\bar{p}_G - \bar{p}_{G,c})^{t'} \tag{5.1}$$

as $\bar{p}_G$ approaches $\bar{p}_{G,c}$ from above. Since an infinite RRN starts conducting only for $\bar{p}_G \geq \bar{p}_{G,c}$ in an infinitely large system, G is zero for $\bar{p}_G \leq \bar{p}_{G,c}$. Equation (5.1) describes the critical behavior and the critical exponent t' have been found to be approximately 1.3 for two dimensional RRN [58, 59].

5.2 RRN inspired porous network model

The design of the porous network from paper II is such that it models porous media made up of two types of randomly distributed grains that have wettability that is either fully wetting (w) or fully non-wetting (nw). The grains are chosen to be nw based on an occupation probability $\bar{p}$, and the rest of the grains are set to be w. Wettabilities are consistently defined with respect to the same one of the two fluids. To the right of figure 5.1, the rules to assign wettability to the links of the network are illustrated. A pore space, or a link, lying between two w grains, is naturally also fully wetting and gets assigned 0° wetting angle in the network. Oppositely, a link between two nw grains is assigned nw property with 180° wetting angle. The capillary forces in the w and the nw links point in opposite directions. For a link placed between two opposite grain types, the capillary forces average to zero, hence a neutral wettability is assumed in those links in the network.

To the left in figure 5.1, two examples of networks are shown with nw grain occupation probabilities $\bar{p} = 0.25$ and 0.45. As expected, the neutrally wet (black) links lie on the borderlines between the regions saturated with w (blue) and nw (pink) links. The network with $\bar{p} = 0.45$ contains a more equal concentration of the w and nw grains. Therefore, in this network, there exist paths that are made up of only neutrally wet links that connect and loop over the entire system. Such paths can be called "connected paths". The network with $\bar{p} = 0.25$, on the other hand, does not have connected paths.

The connected paths with their complete neutral wettability do not have any capillary resistance. Therefore, when a very low $|\Delta P|$ is applied across the network, only such connected paths will be able to carry flow. The existence of connected paths together with their conductance at very low $|\Delta P|$ is a percolation problem. As seen in the examples in figure 5.1, not all $\bar{p}$ results in a network with connected paths. The investigations in paper II showed that there is a range

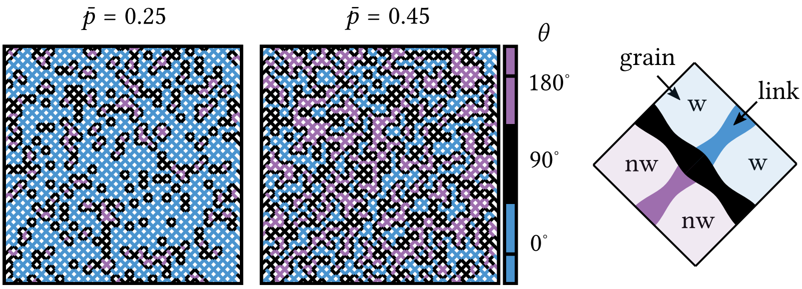

Figure 5.1: The maps of wetting angles θ of the links in pore network models with non-wetting grain occupation probabilities $\bar{p}$. To the right, one can see the rules for assigning θ to the links: θ is 180° (fully non-wetting (nw)), 0° (fully wetting (w)) or 90° (neutrally wetting), respectively, for links between two nw grains, between two w grains or between a nw and a w grain.

$1 - \bar{p}_c \leq \bar{p} \leq \bar{p}_c$ symmetric around $\bar{p} = 0.5$ that has close to one probability of having connected paths, and the same probability drops to zero outside of that range. This means, at very low $|\Delta P|$, the transport of fluids is close to zero outside of the critical range limited by the critical probability threshold $\bar{p}_c$, but gets larger than zero Q once $\bar{p}$ is inside the critical range. This transition from zero to non-zero flow is a step function for an infinitely large system.

From paper II, the value of $\bar{p}_c$ for this model seems to lie close to the site-percolation probability threshold for a two-dimensional square lattice which is 0.5927... [61, 62]. The reason for this can be understood by looking at the grains in the present model as the sites in a regular two-dimensional percolation model. Consider an infinitely large system. Below the critical range, as in the case with $\bar{p} = 0.25$ in figure 5.1, due to the high concentration of w grains, they are connected to each other and span the entire length of the network. In other words, the w grains percolate for $0 \leq \bar{p} \leq 1 - \bar{p}_c$ where $\bar{p}_c \approx 0.5927\ldots$. For all $1 - \bar{p}_c < \bar{p}$, the concentration of nw grains is large enough to break off the connected w grains into smaller clusters. See the example with $\bar{p} = 0.45$ in figure 5.1. On the opposite end of the spectrum of $\bar{p}$, the opposite is true where the nw and w grains exchange roles. That is, nw grains dominate and percolate for $\bar{p}_c \leq \bar{p} \leq 1$ and cease percolating if $\bar{p} < \bar{p}_c$. The percolation behavior should be independent of the direction. The connected paths require there to be different grain types on its two sides. Therefore, since any path of links will be cut off by a percolating cluster of grains outside of the critical range $1 - \bar{p}_c < \bar{p} < \bar{p}_c$, there cannot exist any connected path outside of this range in the limit of infinite system size.

In porous media, the concept analogous to the conductivity G in RRNs is the mobility M. The mobility M relates Q and $|\Delta P| - P_t$ and indicates how much the porous medium is conducting, and is the proportionality constant in equation (4.5),

$$Q = M(|\Delta P| - P_t)^{\beta}. \tag{5.2}$$

Due to the similarities between G and M, which will be further discussed in section 5.3, one can suspect the critical behavior associated with G (equation (5.1)) to also be present for M at very low $|\Delta P|$. The reason for considering the lowest possible $|\Delta P|$ here is because the dependence of M on the occupation probability $\bar{p}$ disappears with larger $|\Delta P|$. This is due to the pressures across the pores becoming much larger than the capillary barriers within. With this, one can hypothesize for the model in paper II at very low $|\Delta P|$ that

$$M \propto \begin{cases} (\bar{p} - (1 - \bar{p}_c))^{t'} & \text{for } \bar{p} \longrightarrow (1 - \bar{p}_c)^{+} \,, \\ (\bar{p}_c - \bar{p})^{t'} & \text{for } \bar{p} \longrightarrow (\bar{p}_c)^{-} \,, \end{cases} \tag{5.3}$$

where the symmetry of the system has been taken into consideration. Here, $\bar{p} \longrightarrow (1 - \bar{p}_c)^{+}$ means $\bar{p}$ approaches $1 - \bar{p}_c$ from above and $\bar{p} \longrightarrow (\bar{p}_c)^{-}$ means $\bar{p}$ approaches $\bar{p}_c$ from below. This can be rewritten in terms of the correlation length ξ. It is the distance over which the fluctuations are correlated in the thermodynamic limit with infinite system size and goes as

$$\xi \propto |\bar{p} - (\text{critical probability})|^{-\nu} \tag{5.4}$$

for $\bar{p}$ close to the critical point [60, 63]. The critical points are $1 - \bar{p}_c$ and $\bar{p}_c$ in this case. The correlation critical exponent is roughly $\nu = 4/3$ in two dimensions [64]. In finite-sized systems characterized by a size L, the biggest ξ can be is limited by L. Therefore at the critical points where ξ diverges, one can write the finite size scaling law [63]

$$L \propto |\bar{p} - (\text{critical probability})|^{-\nu}, \tag{5.5}$$

where the symmetry of the system has been taken into consideration. equation (5.5) can be inserted into equation (5.3) to get

$$M \propto L^{-t'/\nu} \tag{5.6}$$

close to the critical probabilities. To examine the possibility that M might exhibit critical behavior at low $|\Delta P|$, equation (5.6) was investigated in paper II and the results revealed an unexpectedly large value of t' that is around 5.7. This aroused the suspicion that the system might not be critical and that the criticality might have been smeared out. This is the topic of discussion in section 5.3.

5.3 The presence of criticality

The porous network model has both similarities and differences with the RRN model, and considering these can give hints as to whether the system is critical. Firstly, in both models, resistance properties are allocated based on an occupation probability. In RRN, the occupation probability $\bar{p}_G$ is applied directly to the links of the network, while in the porous model, the occupation probability $\bar{p}$ is applied to the grains and thereafter translated into the attributes of the links. This difference is merely a conversion of the probabilities and by itself should not alter the presence of criticality of the porous network. However, this difference could potentially give rise to a difference in the critical exponent.

The links in RRN have either zero or infinite resistance, resulting in a sharp transition from non-conducting to conducting when the critical threshold is reached. The links in the porous network have either zero resistance stemming from neutral wettability or a finite amount of resistance stemming from wetting or non-wetting conditions. The non-zero resistances are not large enough to resist flow completely regardless of the pressure. This is different from the infinite-resistance links in RRN which resist current completely. To have the same effect, the pressure experienced by the links in the porous network must be so small that only the zero-resistance links can be passed through. The smallest possible $|\Delta P|$ used in paper II were the ones that could be simulated within reasonable computational time. It could be that even those $|\Delta P|$ were not small enough for the finite resistance to have a significant impact. This could have partially contributed to smoothing out of the criticality.

In paper II, the biggest suspect for the obstruction of criticality is argued to be the links that do not contain any interfaces. The resistance of a certain link at a certain time stems from the capillary barriers from the fluid-fluid interfaces it contains at that time. The number of interfaces in a link can change in every time step and can at times be zero due to only having one type of fluid inside. When a link contains no interface within, it is indistinguishable from the neutrally wet links in the model and hence contributes to the flow in the same way. This is a special property of this porous model that does not have an equivalent in the design of RRN. This immediately blurs out the difference between the zero-resistance links and the non-zero-resistance links in the porous model and can possibly smear out the critical behavior.

Statistical mechanics of porous media

6

The flow of multiple immiscible fluids through macroscale porous media that is several orders of magnitude larger than the pore scale was the topic in chapter 4. For practical applications, when studying the general behavior of the flow in macroscale porous media, the interest lies in the overarching large-scale behaviors rather than the detailed description of every single pore. To this end, macroscale descriptions of the immiscible multiphase flow are in demand. As Dr. Blunt writes in his book [42], when taking a train from one station to another, it is much more useful with a simple map showing only the stations and the connections rather than a high-resolution seismic image of the ground. In section 4.1, the phenomenological approach to relate total volumetric flow rate Q to the global pressure drop ΔP through the experimentally measured relative permeabilities was mentioned. Although such phenomenological theories are often accurate in describing the physics, their domain of validity can be difficult to determine. This is in contrast to microscopic theories, where the underlying assumptions are typically easier to keep track of. It can be hard to pinpoint the physical origin of the observations at the macroscale that can stem from behaviors at the pore scale. In contrast, theories that utilize pore scale constituents provide the possibility to implement different interactions at the pore scale which may influence the final scaled-up description in various ways.

One way of developing macroscale descriptions is through a category of methods that have the commonality of deriving averaged models. Examples of such methods are the volume averaging method [65–69], the homogenization technique [70–72] and the thermodynamically constrained averaging theory [73–76]. The general idea is to average the local quantities describing the microscale behavior, such as mass and momentum balances or thermodynamic equations, over a suitable volume to obtain effective macroscale field descriptions [77]. The suitable volume is referred to as representative elementary volume (REV) and if the averaging region is an area rather than a volume, it is referred to as representative elementary area (REA) [78]. A REV characterizes and represents a physical point in the macroscopic field. It needs to be large enough to cover the rapid microscale fluctuations but be smaller than the characteristic length of the macroscale inhomogeneities [77, 78]. To quantitatively estimate the acceptable size of REV, statistical methods such as direct visual observation [79], standard deviation analysis [80], relative gradient error criterions [79, 81] and regression modelling [82] can be used.

A different kind of upscaling technique is statistical mechanics. Hansen et al. [83] developed statistical mechanics for immiscible two-phase flow in porous media. Their theory that led to a formalism resembling thermodynamics builds on the information theoretical statistical mechanics of Jaynes [84]. This was done for steady-state flow at the macroscopic level where macroscopic variables describing the flow remain constant or fluctuate around well-defined averages while the fluid configurations at the pore level are dynamic. One of the important assumptions used in that paper is investigated in paper III. The discussions here will start with a summary of the idea behind the Jaynes' theory before moving on to describing how it was used in the paper by Hansen et al. [83].

In his work [84], Jaynes started with the concept of Shannon entropy [85] as a measure of the amount of uncertainty, where the entropy is increased with uncertainty, reaching a maximum at the most uncertain state where all the outcomes are equally likely [86]. In a realistic situation, one often has some information about the outcomes. Jaynes incorporated this additional information as constraints into his theory and proposed to maximize entropy under these constraints through the use of Lagrange multipliers, thereby successfully incorporating into the theory what information is known. This provides an alternative way to derive for example probability distributions of a canonical or grand canonical ensemble compared to deriving them from a microcanonical ensemble.

Inspired by this, Hansen et al. [83] formulated the flow entropy associated with the macroscale movements of the fluid clusters as

$$\Sigma = -\int \mathrm{d}X\, \tilde{P}(X) \ln \tilde{P}(X). \tag{6.1}$$

The constituents of equation (6.1) can be explained using figure 6.1. Figure 6.1 is meant to represent flow through a porous medium where a mixture of two immiscible fluids is injected from the bottom with a total volumetric flow rate Q. The value of Q remains the same along the average flow direction z. Figure 6.1 also shows a cross-sectional plane orthogonal to z inside which there is a REA marked with hatching. In accordance with the definition of REA above, the REA here is large enough for the variables describing the properties of the medium itself and the fluids passing through it to have well-defined averages. The integral in equation (6.1) is over all the physically possible fluid configurations X in a plane as the one in figure 6.1, and $\tilde{P}(X)$ is the probability density for these configurations. The flow entropy, Σ, is the Shannon entropy and not a molecular entropy of regular thermodynamics. When the fluids are in motion through the porous medium, thermodynamical entropy is produced due to work done during irreversible processes such as viscous dissipation. The flow entropy Σ, on the other hand, describes what we know about the possible fluid structures and patterns during the steady state, and since this information does not change, Σ is constant in the steady state.

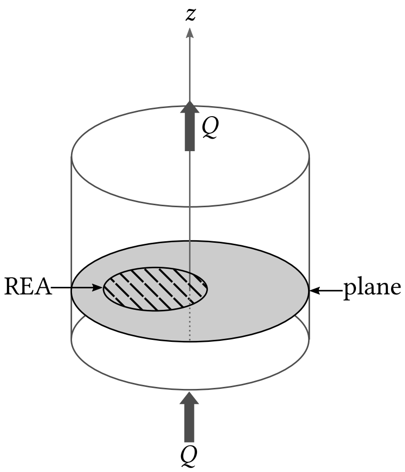

Figure 6.1: Sketch of a porous medium where fluids are injected from the bottom with a total volumetric flow rate Q which remains the same along the average flow direction z. The drawing shows a plane orthogonal to z within which a representative elementary area (REA), with hatched markings, is located. The part of the plane that is not REA is called the reservoir.

The flow configurations X in a plane in figure 6.1, is the union of the configurations inside the REA, X_p, and the configurations in the rest of the plane excluding the REA which can be called the reservoir, X_r,

$$X = X_p \cup X_r. \tag{6.2}$$

The *first* assumption Hansen et al. [83] employed is that X_p and X_r are independent such that $\tilde{P}(X)$ becomes the product of the configurational probability density for the REA $\tilde{P}_p(X_p)$ and the configurational probability density for the reservoir $\tilde{P}_r(X_r)$,

$$\tilde{P}(X) = \tilde{P}_p(X_p)\tilde{P}_r(X_r). \tag{6.3}$$

Inserting equation (6.3) into equation (6.1) and using the properties

$$\int \mathrm{d}X_p\, \tilde{P}_p(X_p) = 1 \tag{6.4}$$

and

$$\int \mathrm{d}X_r\, \tilde{P}_r(X_r) = 1, \tag{6.5}$$

one gets

$$\begin{aligned}
\Sigma &= -\int \mathrm{d}X_r \int \mathrm{d}X_p\, \tilde{P}_p(X_p)\tilde{P}_r(X_r) \ln\left(\tilde{P}_p(X_p)\tilde{P}_r(X_r)\right) && \text{(6.6a)}\\
&= -\int \mathrm{d}X_r \int \mathrm{d}X_p\, \tilde{P}_p(X_p)\tilde{P}_r(X_r) \left(\ln \tilde{P}_p(X_p) + \ln \tilde{P}_r(X_r)\right) && \text{(6.6b)}\\
&= -\int \mathrm{d}X_r\, \tilde{P}_r(X_r) \int \mathrm{d}X_p\, \tilde{P}_p(X_p) \ln \tilde{P}_p(X_p)\\
&\quad -\int \mathrm{d}X_p\, \tilde{P}_p(X_p) \int \mathrm{d}X_r\, \tilde{P}_r(X_r) \ln \tilde{P}_r(X_r) && \text{(6.6c)}\\
&= -\int \mathrm{d}X_p\, \tilde{P}_p(X_p) \ln \tilde{P}_p(X_p) - \int \mathrm{d}X_r\, \tilde{P}_r(X_r) \ln \tilde{P}_r(X_r) && \text{(6.6d)}\\
&= \Sigma_p + \Sigma_r. && \text{(6.6e)}
\end{aligned}$$

The last step, equation (6.6d) to equation (6.6e), defines the flow entropy in the REA

$$\Sigma_p = -\int \mathrm{d}X_p\, \tilde{P}_p(X_p) \ln \tilde{P}_p(X_p) \tag{6.7}$$

and the flow entropy in the reservoir Σ_r which is the rest of equation (6.6d).

The *second* assumption Hansen et al. [83] used, following Jaynes, is that $\tilde{P}_p(X_p)$ is such that Σ_p in equation (6.7) is maximized under the known constraints. REA can be characterized by three variables measured inside it, the volumetric flow rate Q_p, the pore area A_p, and the pore area that is covered by the wetting fluid $A_{w,p}$. These three variables depend on the configurations X_p inside REA and hence contain information regarding the characteristics of a porous medium and the fluids, such as the interfacial curvatures. The averages of these variables are then

$$Q_p = \int \mathrm{d}X_p\, \tilde{P}_p(X_p) Q_p(X_p), \tag{6.8a}$$

$$A_p = \int \mathrm{d}X_p\, \tilde{P}_p(X_p) A_p(X_p), \tag{6.8b}$$

$$A_{w,p} = \int \mathrm{d}X_p\, \tilde{P}_p(X_p) A_{w,p}(X_p). \tag{6.8c}$$

To find $\tilde{P}_p$ that maximizes equation (6.7) subject to the constraints in equations (6.4) and (6.8), one needs to maximized the Lagrangian

$$\begin{aligned} \mathscr{L} = &- \int \mathrm{d}X_p\, \tilde{P}_p(X_p) \ln \tilde{P}_p(X_p) \\ &+ \Lambda \left(1 - \int \mathrm{d}X_p\, \tilde{P}_p(X_p)\right) \\ &+ \lambda_{Q_p} \left(Q_p - \int \mathrm{d}X_p\, \tilde{P}_p(X_p) Q_p(X_p)\right) \\ &+ \lambda_{A_p} \left(A_p - \int \mathrm{d}X_p\, \tilde{P}_p(X_p) A_p(X_p)\right) \\ &+ \lambda_{A_{w,p}} \left(A_{w,p} - \int \mathrm{d}X_p\, \tilde{P}_p(X_p) A_{w,p}(X_p)\right). \end{aligned} \tag{6.9a}$$

$\mathscr{L}$ should be maximized with respect to $\tilde{P}_p$ as well as the Lagrange multipliers Λ, λ_{Q_p}, λ_{A_p} and $\lambda_{A_{w,p}}$. This means that,

$$\frac{\delta \mathscr{L}}{\delta \tilde{P}_p} = 0, \tag{6.10a}$$

$$\frac{\partial \mathscr{L}}{\partial \Lambda} = 0, \tag{6.10b}$$

$$\frac{\partial \mathscr{L}}{\partial \lambda_{Q_p}} = 0, \tag{6.10c}$$

$$\frac{\partial \mathscr{L}}{\partial \lambda_{A_p}} = 0, \tag{6.10d}$$

$$\frac{\partial \mathscr{L}}{\partial \lambda_{A_{w,p}}} = 0, \tag{6.10e}$$

where equation (6.10a) is a functional derivative while the rest are regular derivatives corresponding to the constraints in equations (6.4) and (6.8). Equation (6.10a) gives

$$-\ln \tilde{P}_p(X_p) - 1 - \Lambda - \lambda_{Q_p} Q_p(X_p) - \lambda_{A_p} A_p(X_p) - \lambda_{A_{w,p}} A_{w,p}(X_p) = 0. \tag{6.11}$$

Furthermore, Hansen et al. [83] defined three variables [1]

$$\theta = \frac{1}{\lambda_{Q_p}}, \tag{6.12a}$$

$$\pi = -\frac{\lambda_{A_p}}{\lambda_{Q_p}}, \tag{6.12b}$$

$$\mu = -\frac{\lambda_{A_{w,p}}}{\lambda_{Q_p}}. \tag{6.12c}$$

These variables, together with equation (6.11), gives

$$\tilde{P}_p(X_p) = \frac{1}{Z} \exp\left(-\frac{Q_p(X_p)}{\theta} + \frac{\pi A_p(X_p)}{\theta} + \frac{\mu A_{w,p}(X_p)}{\theta}\right), \tag{6.13}$$

with the partition function

$$Z = \mathrm{e}^{1+\Lambda} = \int \mathrm{d}X_p \exp\left(-\frac{Q_p(X_p)}{\theta} + \frac{\pi A_p(X_p)}{\theta} + \frac{\mu A_{w,p}(X_p)}{\theta}\right),$$

---

[1] These letters have different meanings outside of this chapter.

$$\tag{6.14}$$

so that equation (6.10b) is satisfied.

Inserting equation (6.13) into equation (6.7), and using equations (6.10c)–(6.10e), leads to the expression for the flow entropy

$$\Sigma_p = -\int \mathrm{d}X_p\, \tilde{P}_p(X_p) \ln\left(\frac{\exp\left(-\frac{Q_p(X_p)}{\theta} + \frac{\pi A_p(X_p)}{\theta} + \frac{\mu A_{w,p}(X_p)}{\theta}\right)}{Z}\right) \tag{6.15a}$$

$$= -\ln\left(\frac{1}{Z}\right) - \int \mathrm{d}X_p\, \tilde{P}_p(X_p)\left(-\frac{Q_p(X_p)}{\theta} + \frac{\pi A_p(X_p)}{\theta} + \frac{\mu A_{w,p}(X_p)}{\theta}\right), \tag{6.15b}$$

which after the integration becomes

$$\Sigma_p = \ln Z + \frac{Q_p}{\theta} - \frac{\pi A_p}{\theta} - \frac{\mu A_{w,p}}{\theta}. \tag{6.16}$$

The quantity θ resembles temperature in ordinary thermodynamics if it is an intensive quantity in area. This is the case when the constraints are given in terms of extensive quantities, given that the Shannon entropy and Λ are extensive. Next, Hansen et al. [83] define a new variable Q_G that correspond to a free energy in ordinary thermodynamics,

$$Z = \mathrm{e}^{\frac{-Q_G}{\theta}}. \tag{6.17}$$

From equation (6.16), Q_G is then

$$Q_G = Q_p - \Sigma_p\theta - \pi A_p - \mu A_{w,p}. \tag{6.18}$$

Starting with equation (6.13) for the REA configurational probability density $\tilde{P}_p$, which led to for example the expression for Q_G in equation (6.18), one can derive many useful relations describing the flow. For example, relations between various effective fluid velocities and saturation [83]. In paper III, a fundamental assumption used in the process of finding $\tilde{P}_p$ is tested, namely equation (6.3) claiming independence between $\tilde{P}_p$ for the REA and $\tilde{P}_r$ for the reservoir. Under the validity of this assumption, the distributions of Q_p and saturation $S_{w,p} = A_{w,p}/A_p$ in REA, averaged over the motion of the fluids and the disorder of the porous medium itself, should be independent of the size of the reservoir. On the other hand, if equation (6.3) is not true, then one should not expect the distributions of Q_p and $S_{w,p}$ to be independent of the reservoir size. The results in paper III show that the distributions are indeed independent of the reservoir size, for sufficiently large reservoirs, indicating the validity of equation (6.3).

Dynamic pore network model

7

There are many ways to model porous media numerically and a representative simplified model can often be more useful than an overly explicit model. Network modeling of porous media embraces this idea by attempting to partition the space in a way that approximately emulates the connectivity and other useful geometric features of real porous media [87, 88]. This is done by representing larger pore bodies as nodes and connecting them using narrower links acting as pore throats. The nodes and links in a network model often take on simplified forms, e.g. spheres for nodes and cylinders for links. By compromising on the details, one can be able to simulate larger systems using these network models and hence be able to predict macroscale transport properties and flow behavior. As with the capillary bundle models in section 3.5, the constituents of the network models can be assigned properties as needed for the investigation. Examples of such properties are the distribution of the radii and the wetting angles of the network itself and the viscosity and compressibility of the fluids within.

Two-phase flow in a porous medium under very slow flow conditions can be approximated as being quasi-static with intermittent motions that fill a whole pore at the time [89]. These kinds of models are called quasi-static models where, in every time step, one fluid displaces the other fluid completely in the pores that are subjected to the largest displacing forces. Due to very slow flow rates, the capillary forces dominate while the viscous forces can be neglected. During imbibition, where the wetting fluid displaces the non-wetting fluid, the smallest pores are invaded first due to their high capillary pressures. For the same reason, during drainage, where the non-wetting fluid displaces the wetting fluid, the largest pores are invaded first. Quasi-static models are used to study equilibrium behaviors where incremental global pressure changes can be applied to go from one equilibrium to another [87].

At higher flow rates, one needs to consider dynamic flow where both the viscous and the capillary forces are relevant. Dynamic network models are a group of models that are applicable under these conditions. In these models, invasion of a pore is determined by the total capillary pressure, and the flow rate is proportional to the difference between the total pressure difference over the pore and the total capillary pressure. The basis of the algorithms used in the dynamic pore network models in papers I–III is based on the work by Sinha et al. [90] where an interface-tracking approach is used. There have been several predecessors to these interface-tracking algorithms [35, 91–95]. In comparison to those, the model by Sinha et al. [90] is more general in several aspects. The model can be used to simulate both transient and steady-state flow conditions. The driving force can be set to be a constant global pressure drop or a constant total volumetric flow rate. Different network geometries with different boundary conditions can be modeled. Furthermore, one of the most important features of this model is the clever collection and distribution of the fluids at the nodes while conserving the volumes of each fluid.

The dynamic pore network models used in papers I–III have a common basic structure and flow-transportation rules. In the following, the mutual initialization steps of these networks are described in section 7.1. After the initialization, the fluids get propagated through the network based on a certain set of rules and methods. The process at each time step can be divided into three parts. First, the pressure field is calculated using the conjugate gradient method, which is explained in detail in section 7.2. Second, the flow rates in the links are calculated, and are then used to propagate the fluids forward based on a set of rules. This is explained in section 7.3. At the end of each time step, one can measure and save the relevant quantities and move on to the next time step.

7.1 Initialization

The dynamic pore networks used in papers I–III are shaped similarly to the example in figure 7.1. The example has 4 × 4 nodes marked with black circles that are connected by 8 × 4 links marked with blue lines. In general, the networks can have any size. The networks are considered to model horizontal two-dimensional flow where the gravity effects are neglected. The nodes do not retain any fluid during the simulation but are there to mediate the collection and distribution of the fluids from and to the links. The desired disorder can be assigned to the links at the initialization stage as well. In papers I–III, the length of the links was kept the same while their radii and wetting angles could vary.

The pressure difference between the first (bottom) and the last (top) rows of the nodes defines the global pressure drop ΔP which is the driving force. The total volumetric flow rate Q is defined over a cross-section orthogonal to the average flow. If a network has a periodic boundary condition (PBC) in the flow direction, the links connecting the first and the last rows, i.e. the bottom row of links in figure 7.1, will have pressure difference ΔP with magnitude equal to the global pressure difference, as will be explained below.

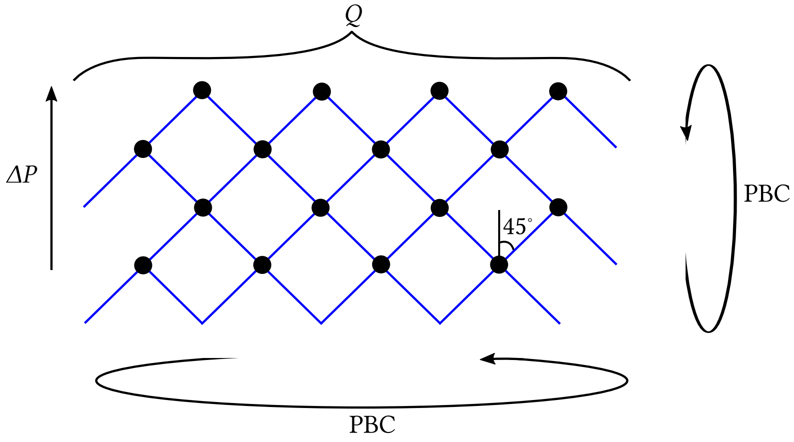

Figure 7.1: An example of the dynamic pore network model with 4 × 4 nodes marked with black circles that are connected by 8 × 4 links marked with blue lines. The links are oriented 45° from the average flow direction. The global pressure drop ΔP is the driving force giving a total volumetric flow rate Q. The network can have periodic boundary conditions (PBCs) in both directions.

In figure 7.1, each node in the network connects to four links where the links are positioned 45° from the average flow direction. This is the connectivity used in papers I–III, but can be altered if needed. At the initialization step, the information regarding all the connections between the nodes and the links should be stored in arrays so that they can be easily accessed during the distribution and transportation of the fluids.

In papers I–III, the steady-state behavior of the flow was of interest. There are two ways boundary conditions can be adjusted to accommodate for this. The first way, which is the way that can be done in the experiments, is to inject two fluids simultaneously through alternate inlets. The downside of this approach is that it creates boundary effects, resulting in a small region with homogeneous steady-state properties. To avoid this, one can instead use periodic boundary conditions as in figure 7.1, which is the approach used in the networks in papers I–III. This can be achieved by prefilling the links in the network with two fluids and then connecting the inlet and the outlet links of the network so the network becomes a closed system. After many rounds of circulation, the entire system can approach steady state with no boundary effects, in contrast to the first method. With this, one can use smaller systems compared to the first method, decreasing the computational cost. The downside of the second method is that it can generally not be done in experiments. It may, nonetheless, be the preferred numerical method due to it being more computationally efficient and being able to give similar steady-state statistics as the first method.

For a network that is twice periodic and thus closed, the saturation of the fluids inside the network is conserved in time. Therefore, the saturation of the network is an initialization parameter. There are several ways a certain saturation can be achieved. One can, for example, start by filling a fraction of the network in the flow direction completely with one of the two fluids and the rest with the other fluid depending on the chosen saturation. One can also fill entire links at a time with one of the fluids until the desired saturation is reached and fill the rest of the links with the other fluid. The way it was done in papers I–III was that each link in the network got filled with the desired saturation amount at the beginning of the simulation. This method facilitates a better mixture of the two fluids from the start and with it a shorter time to approach steady state.

7.2 Calculating the pressure field

7.2.1 Building the equations

At each time step, the pressure field, i.e. the local pressures at the nodes of the network, needs to be calculated. The equations that need to be solved for this purpose come from Kirchhoff's junction rule, stating that the algebraic sum of the currents into any junction is zero [96].

In the network, the sum of the volumetric flow rates q that come into a node must be equal to those that go out from the same node during the same time step. In other words, at each node i, the net volumetric flow rate at each time step is zero,

$$\sum_h q_h C_{i,h} = 0 \tag{7.1}$$

where the sum is over all the links h that connect directly to node i. In equation (7.1), since q_h is in the direction of the total flow Q which can be called the upward direction, then $C_{i,h}$ is

$$C_{i,h} = \begin{cases} 1 & \text{if link } h \text{ is below node } i, \\ -1 & \text{if link } h \text{ is above node } i. \end{cases} \tag{7.2}$$

In the networks used in papers I–III, h in equation (7.1) goes from 1 to 4.

Inserting the expression for q from equation (3.42) into equation (7.1) gives

$$\sum_h -\frac{\pi \bar{r}_h^4}{8\mu_{\text{eff},h} l}\left(\Delta p_h - \sum_{k=1}^{n} \frac{2\sigma \cos\theta_h(x_k)}{r_h(x_k)} \hat{J}(x_k) \cdot \hat{x}\right) C_{i,h} = 0. \tag{7.3}$$

Here, the second sum over interfaces k that are within link h is the total capillary pressure in that link,

$$p_{c,h}^{\text{tot}} = -\sum_{k=1}^{n} \frac{2\sigma \cos\theta_h(x_k)}{r_h(x_k)} \hat{J}(x_k) \cdot \hat{x}. \tag{7.4}$$

The link mobility can be defined as

$$m_h = \frac{\pi \bar{r}_h^4}{8\mu_{\text{eff},h} l}. \tag{7.5}$$

With equations (7.4) and (7.5), one can write equation (7.3) more compactly as

$$\sum_h m_h \Delta p_h C_{i,h} = \sum_h m_h p_{c,h}^{\text{tot}} C_{i,h}. \tag{7.6}$$

Everywhere except at the inlet and the outlet, the pressure difference Δp in equation (7.6) is the difference between the pressure at the node that lies above the link across which it is defined in the direction of the flow Q, denoted as p_{up}, and the node that lies in the opposite direction, denoted as p_{down}. As described in section 7.1, the networks used in papers I–III have periodic boundary conditions. The driving force comes from enforcing a jump in the pressure $|\Delta P|$ across the links that connect the inlet and the outlet nodes. What this means is that always when calculating q over these links, $|\Delta P|$ must be added to the node pressures in a way such that when looking down from the bottom inlet nodes, one should see a pressure that is $|\Delta P|$ more than the pressure at the outlet nodes. Similarly, when looking up from the top outlet nodes, one should see a pressure that is $|\Delta P|$ less than the pressure at the inlet nodes. With these factors combined, one can write Δp_h across the links as

$$\Delta p_h = \begin{cases} p_{\mathrm{up},h} - \left(p_{\mathrm{down},h} + |\Delta P|\right) & \text{below the bottom nodes,} \\ \left(p_{\mathrm{up},h} - |\Delta P|\right) - p_{\mathrm{down},h} & \text{above the top nodes,} \\ p_{\mathrm{up},h} - p_{\mathrm{down},h} & \text{across others.} \end{cases} \tag{7.7}$$

Combining equation (7.6) for all the nodes gives a system of linear equation

$$A\boldsymbol{p} = \boldsymbol{b} \tag{7.8}$$

for the pressure vector

$$\boldsymbol{p} = \begin{pmatrix} p_1 \\ p_2 \\ \vdots \\ p_N \end{pmatrix} \tag{7.9}$$

with components corresponding to the pressures at the nodes and N being the total number of nodes. The matrix A in equation (7.8) has dimensions $N \times N$ and is symmetric. The left-hand side of equation (7.8), $A\boldsymbol{p}$, contains all the terms that are linearly dependent on the node pressures in equation (7.6) for all the nodes, while the rest is in $\boldsymbol{b}$. The N dimensional vector $\boldsymbol{b}$ is made up of the right-hand side of equation (7.6) with the capillary pressures, as well as, the boundary terms with ΔP from equation (7.7), for all the nodes.

Properties of the matrix A

The goal is to solve equation (7.8) to find $\boldsymbol{p}$. One way to solve it is by using the conjugate gradient method, which requires that A is symmetric and positive definite [97–100]. The matrix A is positive definite if

$$\langle \boldsymbol{p}, \boldsymbol{p} \rangle_A = \boldsymbol{p}^\mathsf{T} A \boldsymbol{p} > 0 \quad \text{for all} \quad \boldsymbol{p} \in \mathbb{R}^N \setminus \{\boldsymbol{0}\}, \tag{7.10}$$

where $^\mathsf{T}$ is the transpose, $\mathbb{R}^N$ is N dimensional real space, and "$\setminus\{\boldsymbol{0}\}$" means that the zero vector is excluded. A symmetric matrix is positive definite if and only if it only has positive eigenvalues. The matrix A is symmetric by definition, but not positive definite as one of its eigenvalues is zero. This stems from the fact that equation (7.8) does not specify $\boldsymbol{p}$ uniquely. Specifically, adding a constant pressure c_p at all the nodes,

$$\boldsymbol{p} \longrightarrow \boldsymbol{p} + \begin{pmatrix} c_p \\ c_p \\ \vdots \\ c_p \end{pmatrix}, \tag{7.11}$$

leaves all the volumetric flow rates through the links invariant. With $\boldsymbol{u}_0 = \left(c_p, c_p, \dots, c_p\right)^\mathsf{T}$, this implies that

$$A\boldsymbol{p} - \boldsymbol{b} = A(\boldsymbol{p} + \boldsymbol{u}_0) - \boldsymbol{b} \implies A\boldsymbol{u}_0 = 0, \tag{7.12}$$

meaning that A has an eigenvector $\boldsymbol{u}_0$ with eigenvalue 0 which further indicates that A can at best be positive semidefinite.

The problem can be solved by removing one degree of freedom that corresponds to the eigenvalue $\lambda = 0$. First, it needs to be shown that all other eigenvalues of A are positive and that the geometric multiplicity of $\lambda = 0$ is 1, meaning that all the other eigenvectors of A that are not parallel to $\boldsymbol{u}_0$ have $\lambda > 0$. This can be done by using a method inspired by the proof of the Gershgorin circle theorem [101, 102].

All eigenvectors of A can be made orthogonal since A is symmetric. Let $\boldsymbol{u}$ be an eigenvector orthogonal to $\boldsymbol{u}_0$, which means that the elements of $\boldsymbol{u}$ are not all the same. As a result, there must exist at least one node where the magnitude of $\boldsymbol{u}$ is larger than or equal to all of its neighbors and strictly larger than at least one. Let the value at this node be u_1, and let the values at the four connected nodes be u_2, u_3, u_4 and u_5. Let the mobilities of the corresponding links be m_2, m_3, m_4 and m_5. Because $\boldsymbol{u}$ is an eigenvector, it satisfies

$$A\boldsymbol{u} = \lambda \boldsymbol{u} \tag{7.13}$$

for some eigenvalue λ. The row of this equation corresponding to four connected nodes with u_1 at its center is

$$(m_2 + m_3 + m_4 + m_5)u_1 - m_2 u_2 - m_3 u_3 - m_4 u_4 - m_5 u_5 = \lambda u_1. \tag{7.14}$$

Rewriting this equation while dividing by u_1 gives

$$\sum_{i=2}^{5} m_i - \lambda = \sum_{i=2}^{5} m_i \frac{u_i}{u_1}. \tag{7.15}$$

The conditions $|u_i/u_1| \leq 1$ for all $i \in \{2,3,4,5\}$ and $|u_i/u_1| < 1$ for at least one $i \in \{2,3,4,5\}$ mean that $\sum_{i=2}^{5} |m_i| \left|\frac{u_i}{u_1}\right| < \sum_{i=2}^{5} |m_i|$. Using this on equation (7.15), one can see that

$$\left|\sum_{i=2}^{5} m_i - \lambda\right| < \sum_{i=2}^{5} |m_i|. \tag{7.16}$$

Hence, $\lambda > 0$ and $\lambda < 2\sum_{i=2}^{5} |m_i|$. This shows that all the eigenvalues corresponding to eigenvectors that are orthogonal to $\boldsymbol{u}_1$ are positive.

To use the conjugate gradient method that requires a positive definite symmetric matrix, one can reduce the dimensionality of A and $\boldsymbol{p}$ and consider only $\boldsymbol{p}$ in the subspace orthogonal to $\boldsymbol{u}_0$. This means to consider only the pressure fields with zero average since

$$\boldsymbol{p} \cdot \boldsymbol{u}_0 = \sum_{i=1}^{N} p_i u_{0,i} = c_p^N \sum_{i=1}^{N} p_i = 0. \tag{7.17}$$

In practice, it does not matter what the average is, and a more practical approach can be to simply fix one component of $\boldsymbol{p}$, such as $p_N = 0$. This gives a physically equivalent system while fixing the average value of the pressure field. Hence, a well-defined problem can be obtained by defining $\boldsymbol{p}_r = (p_1, p_2, \dots, p_{N-1})^\mathsf{T}$, $\boldsymbol{b}_r = (b_1, b_2, \dots, b_{N-1})^\mathsf{T}$ and

$$A_r = \begin{pmatrix} A_{11} & \cdots & A_{1(N-1)} \\ \vdots & \ddots & \vdots \\ A_{(N-1)1} & \cdots & A_{(N-1)(N-1)} \end{pmatrix}, \tag{7.18}$$

as can be seen in the following. The task is then to solve

$$A_r \boldsymbol{p}_r = \boldsymbol{b}_r. \tag{7.19}$$

The positive definitiveness of A_r follows from the positive semidefiniteness of A. Let $\{\boldsymbol{u}_1, \dots, \boldsymbol{u}_{N-1}\}$ be the orthogonal eigenvectors of A with positive eigenvalues $\{\lambda_1, \dots, \lambda_{N-1}\}$. For any $\boldsymbol{p}_r \neq \boldsymbol{0}$, one can write

$$\boldsymbol{p} = \begin{pmatrix} \boldsymbol{p}_r \\ 0 \end{pmatrix} = a_0 \boldsymbol{u}_0 + \sum_{i=1}^{N-1} a_i \boldsymbol{u}_i, \tag{7.20}$$

with $a_i \neq 0$ for at least one $i \in \{1, \dots, N-1\}$ due to the requirement that $\boldsymbol{p}_r \neq \boldsymbol{0}$. Therefore,

$$\begin{aligned} \boldsymbol{p}_r^{\mathsf{T}} A_r \boldsymbol{p}_r &= \begin{pmatrix} \boldsymbol{p}_r^{\mathsf{T}} & 0 \end{pmatrix} A \begin{pmatrix} \boldsymbol{p}_r \\ 0 \end{pmatrix} && \text{(7.21a)} \\ &= \left(a_0 \boldsymbol{u}_0^{\mathsf{T}} + \sum_{j=1}^{N-1} a_j \boldsymbol{u}_j^{\mathsf{T}} \right) A \left(a_0 \boldsymbol{u}_0 + \sum_{i=1}^{N-1} a_i \boldsymbol{u}_i \right) && \text{(7.21b)} \\ &= \sum_{j=1}^{N-1} \sum_{i=1}^{N-1} a_j a_i \lambda_i \delta_{i,j} && \text{(7.21c)} \\ &= \sum_{i=1}^{N-1} a_i^2 \lambda_i \; > \; 0 && \text{(7.21d)} \end{aligned}$$

for all $\boldsymbol{p}_r \neq \boldsymbol{0}$, where $\delta_{i,j}$ is the Kronecker-delta

$$\delta_{i,j} = \begin{cases} 1 & \text{if } i = j, \\ 0 & \text{if } i \neq j. \end{cases} \tag{7.22}$$

Therefore, A_r is positive definite.

The subscript r in A, $\boldsymbol{p}$ and $\boldsymbol{b}$ is dropped below.

7.2.2 Conjugate gradient method

The minimizing function and the other definitions

Solving equation (7.19) is be equivalent to extremizing a function $f(\boldsymbol{p})$ that has the gradient

$$\nabla f(\boldsymbol{p}) = A\boldsymbol{p} - \boldsymbol{b}. \tag{7.23}$$

A function f that satisfies this is

$$f(\boldsymbol{p}) = \frac{1}{2}\boldsymbol{p}^{\mathsf{T}} A \boldsymbol{p} - \boldsymbol{p}^{\mathsf{T}} \boldsymbol{b}. \tag{7.24}$$

The solution $\boldsymbol{p}$ of equation (7.19) minimizes $f(\boldsymbol{p})$ and makes $\nabla f(\boldsymbol{p}) = 0$. To see that the gradient of equation (7.24) is equation (7.23), start by writing $f(\boldsymbol{p})$ in the component form

$$f(\boldsymbol{p}) = \frac{1}{2} \sum_{ij} p_i A_{ij} p_j - \sum_i p_i b_i. \tag{7.25}$$

Differentiating this with respect to p_η gives the component η of $\nabla f(\boldsymbol{p})$,

$$\frac{\partial f}{\partial p_\eta} = \frac{1}{2} \sum_{ij} \left(\delta_{i\eta} A_{ij} p_j + p_i A_{ij} \delta_{j\eta} \right) - \sum_i \delta_{i\eta} b_i. \tag{7.26}$$

Using equation (7.22) and that the matrix A is symmetric, i.e. $A_{\eta i} = A_{i\eta}$, equation (7.26) can be written as

$$\frac{\partial f}{\partial p_\eta} = \frac{1}{2} \sum_i \left(A_{\eta i} + A_{i\eta} \right) p_i - b_\eta \tag{7.27a}$$

$$= \sum_i A_{\eta i} p_i - b_\eta \tag{7.27b}$$

$$= (A\boldsymbol{p} - \boldsymbol{b})_\eta. \tag{7.27c}$$

This shows that equation (7.23) is indeed the gradient of equation (7.24).

One way to find the minimum of $f(\boldsymbol{p})$ is through the method of steepest descent. At each step in this method, one moves in the direction in which $f(\boldsymbol{p})$ decreases most rapidly, which is the direction of the negative gradient $-\nabla f(\boldsymbol{p})$. The process is repeated until the minimum is reached. The gradients that arise during the iterations can sometimes be similar, making the rate of convergence slow. This problem is overcome with the method of conjugate gradient where the directions $\boldsymbol{u}$ along which $\boldsymbol{p}$ is propagated are orthogonal to each other in the inner-product space defined by A.

Two vectors $\boldsymbol{u}_i$ and $\boldsymbol{u}_j$ are **conjugate** with respect to A if

$$\left\langle \boldsymbol{u}_i, \boldsymbol{u}_j \right\rangle_A = \boldsymbol{u}_i^{\mathsf{T}} A \boldsymbol{u}_j = 0 \quad \text{for all } i \neq j, \tag{7.28}$$

where $\langle \boldsymbol{u}_i, \boldsymbol{u}_j \rangle_A = \boldsymbol{u}_i^\top A \boldsymbol{u}_j$ denotes the inner product defined by A. A positive definite A is needed for this inner product and the inner product space $(\mathbb{R}^N, \langle \cdot, \cdot \rangle_A)$ to be well defined. This can be seen in the following. Another equivalent definition of a positive definite A than what is mentioned before is that there exists an invertible matrix B such that

$$A = B^\top B. \tag{7.29}$$

Inserting equation (7.29) into the inner product given in equation (7.28) and defining a vector $\tilde{\boldsymbol{u}} = B\boldsymbol{u}$, one gets

$$\langle \boldsymbol{u}_i, \boldsymbol{u}_j \rangle_A = \boldsymbol{u}_i^\top B^\top B \boldsymbol{u}_j = \tilde{\boldsymbol{u}}_i^\top \tilde{\boldsymbol{u}}_j = \langle \tilde{\boldsymbol{u}}_i, \tilde{\boldsymbol{u}}_j \rangle . \tag{7.30}$$

This shows that an inner product in A, that is $\langle \cdot, \cdot \rangle_A$, can be mapped onto a regular inner product $\langle \cdot, \cdot \rangle$ and hence be well-defined given that A is positive definite.

A set of N mutually conjugate vectors with respect to A, $\{\boldsymbol{u}_0, \boldsymbol{u}_1, \dots, \boldsymbol{u}_{N-1}\}$, mutually fulfill equation (7.28). This set then forms a basis in $\mathbb{R}^N$, i.e. $\operatorname{span}\{\boldsymbol{u}_0, \boldsymbol{u}_1, \dots, \boldsymbol{u}_{N-1}\} = \mathbb{R}^N$. The linear span, $\operatorname{span}\{\dots\}$, of a set of vectors is the set of all linear combinations of those vectors. The **solution** to equation (7.19) can be expressed in this basis as

$$\boldsymbol{p} = \sum_{i=0}^{N-1} \alpha_i \boldsymbol{u}_i. \tag{7.31}$$

To determine the expression for the coefficients α, one can multiply equation (7.19) with $\boldsymbol{u}_t^\top$,

$$\boldsymbol{u}_t^\top A \boldsymbol{p} = \boldsymbol{u}_t^\top \boldsymbol{b}. \tag{7.32}$$

Using equation (7.31) and equation (7.28), the left hand side of equation (7.32) becomes

$$
\begin{aligned}
\boldsymbol{u}_t^\top A\boldsymbol{p} &= \boldsymbol{u}_t^\top A \sum_{i=0}^{N-1} \alpha_i \boldsymbol{u}_i && \text{(7.33a)}\\
&= \sum_{i=0}^{N-1} \alpha_i \boldsymbol{u}_t^\top A \boldsymbol{u}_i && \text{(7.33b)}\\
&= \sum_{i=0}^{N-1} \alpha_i \langle \boldsymbol{u}_t, \boldsymbol{u}_i \rangle_A && \text{(7.33c)}\\
&= \langle \boldsymbol{u}_t, \boldsymbol{u}_t \rangle_A \sum_{i=0}^{N-1} \alpha_i \delta_{it} && \text{(7.33d)}\\
&= \alpha_t \langle \boldsymbol{u}_t, \boldsymbol{u}_t \rangle_A . && \text{(7.33e)}
\end{aligned}
$$

This equates to the right-hand side of equation (7.32) that is

$$\boldsymbol{u}_t^\top \boldsymbol{b} = \langle \boldsymbol{u}_t, \boldsymbol{b} \rangle , \tag{7.34}$$

and give

$$\alpha_t = \frac{\langle \boldsymbol{u}_t, \boldsymbol{b} \rangle}{\langle \boldsymbol{u}_t, \boldsymbol{u}_t \rangle_A}. \tag{7.35}$$

As a **direct method**, one can start with a full set of conjugate directions $\{\boldsymbol{u}_0, \boldsymbol{u}_1, \dots, \boldsymbol{u}_{N-1}\}$, and then compute the coefficients α using equation (7.35) and get the solution $\boldsymbol{p}$ to equation (7.19) by inserting them into equation (7.31).

An iterative approach

With an **iterative approach** where the directions $\boldsymbol{u}$ are cleverly chosen, it is possible to approximate the solution within a set tolerance without having to use all N vectors in the basis set. In this method, $\boldsymbol{u}_t$ at each step t is chosen such that it follows along the direction of $-\nabla f(\boldsymbol{p}_t)$ (equation (7.23)) as close as possible while being conjugate with respect to A to all the previous directions $\boldsymbol{u}_{\{i<t\}}$. This is achieved by subtracting from $-\nabla f(\boldsymbol{p}_t)$ the projections of $-\nabla f(\boldsymbol{p}_t)$ on all $\boldsymbol{u}_{\{i<t\}}$ in the inner-product space defined by A i.e. $\left(\mathbb{R}^N, \langle \cdot, \cdot \rangle_A\right)$. The expression this gives is

$$\boldsymbol{u}_t = -\nabla f(\boldsymbol{p}_t) - \sum_{i=0}^{t-1} \frac{\langle \boldsymbol{u}_i, -\nabla f(\boldsymbol{p}_t) \rangle_A}{\langle \boldsymbol{u}_i, \boldsymbol{u}_i \rangle_A} \boldsymbol{u}_i. \tag{7.36}$$

This is a Gram-Schmidt orthonormalization that produces vectors that are mutually orthogonal in $\left(\mathbb{R}^N, \langle\cdot,\cdot\rangle_A\right)$.

The idea behind the conjugate gradient algorithm is to gradually build up the basis set $\{\boldsymbol{u}_0, \boldsymbol{u}_1, \dots, \boldsymbol{u}_{N-1}\}$ using equation (7.36) and check at every step t if the residual

$$\boldsymbol{r}_t = \boldsymbol{b} - A\boldsymbol{p}_t \tag{7.37}$$

is sufficiently small, and return $\boldsymbol{p}_t$ as the approximated solution if it is. The convergence to the solution happens in at most N steps, see equation (7.31). Comparing equation (7.37) with equation (7.23), it is apparent that

$$\boldsymbol{r}_t = -\nabla f(\boldsymbol{p}_t). \tag{7.38}$$

Inserting this into equation (7.36) gives a cleaner expression that is

$$\boldsymbol{u}_t = \boldsymbol{r}_t - \sum_{i=0}^{t-1} \frac{\langle \boldsymbol{u}_i, \boldsymbol{r}_t\rangle_A}{\langle \boldsymbol{u}_i, \boldsymbol{u}_i\rangle_A} \boldsymbol{u}_i. \tag{7.39}$$

Before presenting the algorithm in its entirety, each of its components needs to be derived and explained. Starting with the **initial guess**, following the idea of choosing the directions as close as possible to the steepest descent direction, the first direction should naturally be

$$\boldsymbol{u}_0 = -\nabla f(\boldsymbol{p}_0) = \boldsymbol{b} - A\boldsymbol{p}_0. \tag{7.40}$$

The initial guess $\boldsymbol{p}_0$ has to be $\boldsymbol{0}$ in order to determine the coefficients α through equation (7.35). Alternatively, if one wishes to choose $\boldsymbol{p}_0 \neq \boldsymbol{0}$ as the initial guess, one can redefine the equations. Instead of solving for $\boldsymbol{p}$ in $A\boldsymbol{p} = \boldsymbol{b}$ (equation (7.19)), solve for $\boldsymbol{p}_*$ in

$$A\boldsymbol{p}_* = \boldsymbol{b} - A\boldsymbol{p}_0 \tag{7.41}$$

with initial guess $\boldsymbol{p}_{*,0} = \boldsymbol{0}$, where $\boldsymbol{p}_*$ is defined through

$$\boldsymbol{p} = \boldsymbol{p}_0 + \boldsymbol{p}_* \tag{7.42a}$$

$$= \boldsymbol{p}_0 + \sum_{i=0}^{N-1} \alpha_i \boldsymbol{u}_i. \tag{7.42b}$$

Note that if $\boldsymbol{p}_0 = \boldsymbol{0}$, the expressions return to their original forms.

The updated expression of the coefficients α that accommodates for both $\boldsymbol{p}_0 = \boldsymbol{0}$ and $\boldsymbol{p}_0 \neq \boldsymbol{0}$ can be derived in the same way as was done for equation (7.35), and the end result is

$$\alpha_t = \frac{\langle \boldsymbol{u}_t, \boldsymbol{b} - A\boldsymbol{p}_0 \rangle}{\langle \boldsymbol{u}_t, \boldsymbol{u}_t \rangle_A}. \tag{7.43}$$

This expression can be used in the final algorithm in its current form. However, an alternative form can make the algorithm more computationally efficient. The rewriting-technique is one that reappears in the derivations of the other components of the algorithm further on. From equation (7.42b), the approximate solution at step t is

$$\boldsymbol{p}_t = \boldsymbol{p}_0 + \sum_{i=0}^{t-1} \alpha_i \boldsymbol{u}_i \tag{7.44}$$

which makes

$$\begin{aligned} \langle \boldsymbol{u}_t, A\boldsymbol{p}_t \rangle &= \langle \boldsymbol{u}_t, A\boldsymbol{p}_0 \rangle + \sum_{i=0}^{t-1} \alpha_i \langle \boldsymbol{u}_t, A\boldsymbol{u}_i \rangle && \text{(7.45a)} \\ &= \langle \boldsymbol{u}_t, A\boldsymbol{p}_0 \rangle, && \text{(7.45b)} \end{aligned}$$

where the summation term disappears in the last line due to equation (7.28). Using this and equation (7.37), equation (7.43) can be rewritten as

$$\begin{aligned} \alpha_t &= \frac{\langle \boldsymbol{u}_t, \boldsymbol{b} - A\boldsymbol{p}_t \rangle}{\langle \boldsymbol{u}_t, \boldsymbol{u}_t \rangle_A} && \text{(7.46a)} \\ &= \frac{\langle \boldsymbol{u}_t, \boldsymbol{r}_t \rangle}{\langle \boldsymbol{u}_t, \boldsymbol{u}_t \rangle_A}. && \text{(7.46b)} \end{aligned}$$

From equation (7.44),

$$\boldsymbol{p}_{t+1} = \boldsymbol{p}_t + \alpha_t \boldsymbol{u}_t. \tag{7.47}$$

Inserting this into equation (7.37) gives

$$\begin{aligned} \boldsymbol{r}_{t+1} &= \boldsymbol{b} - A(\boldsymbol{p}_t + \alpha_t \boldsymbol{u}_t) && \text{(7.48a)} \\ &= \boldsymbol{r}_t - \alpha_t A\boldsymbol{u}_t. && \text{(7.48b)} \end{aligned}$$

Further modifications

One last step remains before the algorithm can be presented in its simplest and most efficient form. This is to modify the expressions in equations (7.39) and (7.46b) further. To do this, two statements need to first be proven by the **method of induction** [49], a method that was also used in section 3.2.2. These two statements can then be combined to produce a third useful statement at the end.

The first statement that needs to be proven is

$$\langle \boldsymbol{r}_{t+1}, \boldsymbol{u}_i \rangle = 0 \quad \text{for } i \le t. \tag{7.49}$$

That is, the residual obtained in the conjugate gradient method is orthogonal to all previous step directions. With equations (7.46b) and (7.48b), this equation can be written into an alternative form that can aid in the upcoming proof,

$$\langle \boldsymbol{r}_{t+1}, \boldsymbol{u}_i \rangle = \langle \boldsymbol{r}_t, \boldsymbol{u}_i \rangle - \alpha_t \langle A\boldsymbol{u}_t, \boldsymbol{u}_i \rangle \tag{7.50a}$$

$$= \langle \boldsymbol{r}_t, \boldsymbol{u}_i \rangle - \frac{\langle \boldsymbol{r}_t, \boldsymbol{u}_t \rangle}{\langle \boldsymbol{u}_t, \boldsymbol{u}_t \rangle_A} \langle \boldsymbol{u}_t, \boldsymbol{u}_i \rangle_A \,. \tag{7.50b}$$

In the first step of the proof, look at the case $t = 0$. This is satisfied because

$$\langle \boldsymbol{r}_1, \boldsymbol{u}_0 \rangle = \langle \boldsymbol{r}_0, \boldsymbol{u}_0 \rangle - \frac{\langle \boldsymbol{r}_0, \boldsymbol{u}_0 \rangle}{\langle \boldsymbol{u}_0, \boldsymbol{u}_0 \rangle_A} \langle \boldsymbol{u}_0, \boldsymbol{u}_0 \rangle_A = 0. \tag{7.51}$$

In the second step of the proof, given the assumption that

$$\langle \boldsymbol{r}_t, \boldsymbol{u}_i \rangle = 0 \quad \text{for } i \le t - 1 \tag{7.52}$$

is true, one must check that equation (7.49) holds. The condition for equation (7.49), $i \le t$, can be split into $i = t$ and $i < t$. When $i = t$, equation (7.50b) gives

$$\langle \boldsymbol{r}_{t+1}, \boldsymbol{u}_t \rangle = \langle \boldsymbol{r}_t, \boldsymbol{u}_t \rangle - \frac{\langle \boldsymbol{r}_t, \boldsymbol{u}_t \rangle}{\langle \boldsymbol{u}_t, \boldsymbol{u}_t \rangle_A} \langle \boldsymbol{u}_t, \boldsymbol{u}_t \rangle_A = 0. \tag{7.53}$$

When $i < t$, the first term of equation (7.50b), $\langle \boldsymbol{r}_t, \boldsymbol{u}_i \rangle$ is zero due to the assumption in equation (7.52). The second term of equation (7.50b) contains $\langle \boldsymbol{u}_t, \boldsymbol{u}_i \rangle_A$ which is zero for $i < t$ due to equation (7.28). This concludes the proof of equation (7.49).

Equation (7.49) can now be used to rewrite equation (7.46b). Inserting equation (7.39) into equation (7.46b),

$$\alpha_t = \frac{\langle \boldsymbol{u}_t, \boldsymbol{r}_t \rangle}{\langle \boldsymbol{u}_t, \boldsymbol{u}_t \rangle_A} \tag{7.54a}$$

$$= \frac{\left\langle \boldsymbol{r}_t - \sum_{i=0}^{t-1} \frac{\langle \boldsymbol{u}_i, \boldsymbol{r}_t \rangle_A}{\langle \boldsymbol{u}_i, \boldsymbol{u}_i \rangle_A} \boldsymbol{u}_i, \boldsymbol{r}_t \right\rangle}{\langle \boldsymbol{u}_t, \boldsymbol{u}_t \rangle_A} \tag{7.54b}$$

$$= \frac{\langle \boldsymbol{r}_t, \boldsymbol{r}_t \rangle}{\langle \boldsymbol{u}_t, \boldsymbol{u}_t \rangle_A} - \frac{\sum_{i=0}^{t-1} \frac{\langle \boldsymbol{u}_i, \boldsymbol{r}_t \rangle_A}{\langle \boldsymbol{u}_i, \boldsymbol{u}_i \rangle_A} \langle \boldsymbol{u}_i, \boldsymbol{r}_t \rangle}{\langle \boldsymbol{u}_t, \boldsymbol{u}_t \rangle_A}. \tag{7.54c}$$

The last term here is zero due to equation (7.49), which leaves

$$\alpha_t = \frac{\langle \boldsymbol{r}_t, \boldsymbol{r}_t \rangle}{\langle \boldsymbol{u}_t, \boldsymbol{u}_t \rangle_A}. \tag{7.55}$$

This is the form that will be used in the final algorithm.

In the next step, the method of proof by induction will be used once more to prove another statement that is

$$\operatorname{span}\{\boldsymbol{r}_0, \boldsymbol{r}_1, \dots, \boldsymbol{r}_t\} = \operatorname{span}\{\boldsymbol{u}_0, \boldsymbol{u}_1, \dots, \boldsymbol{u}_t\}. \tag{7.56}$$

The first step in proving that the linear spans of these two sets are the same is to start with the sets containing only the first vectors $\{\boldsymbol{r}_0\}$ and $\{\boldsymbol{u}_0\}$. From equation (7.37) and equation (7.40) one can see that $\boldsymbol{r}_0 = \boldsymbol{u}_0$, which completes step one of the proof. In step two, equation (7.56) where the index of the vectors in the sets goes up to t must be shown to hold given the assumption that it holds when the index goes up to $t-1$, i.e. given that

$$\operatorname{span}\{\boldsymbol{r}_0, \boldsymbol{r}_1, \dots, \boldsymbol{r}_{t-1}\} = \operatorname{span}\{\boldsymbol{u}_0, \boldsymbol{u}_1, \dots, \boldsymbol{u}_{t-1}\}. \tag{7.57}$$

Due to equation (7.39) relating $\boldsymbol{u}$ to $\boldsymbol{r}$, the right-hand side of equation (7.56) is

$$\operatorname{span}\{\boldsymbol{u}_0, \boldsymbol{u}_1, \dots, \boldsymbol{u}_{t-1}, \boldsymbol{u}_t\} = \operatorname{span}\{\boldsymbol{u}_0, \boldsymbol{u}_1, \dots, \boldsymbol{u}_{t-1}, \boldsymbol{r}_t\}. \tag{7.58}$$

Inserting equation (7.57) into the right-hand side of this returns equation (7.56), thus completing step two. The two steps combined prove the validity of equation (7.56) by induction.

To summarize, two statements have been proven using the method of induction. The first statement in equation (7.49) means $\boldsymbol{r}_{t+1}$ is orthogonal to all $\boldsymbol{u}_i$ for $i \le t$. The second statement in equation (7.56) means all vectors that are orthogonal to all $\boldsymbol{u}_i$ for $i \le t$, also have to be orthogonal to all $\boldsymbol{r}_i$ for $i \le t$. The combination of these two statements means that $\boldsymbol{r}_{t+1}$ is orthogonal to all $\boldsymbol{r}_i$ for $i \le t$. This results in a third statement

$$\left\langle \boldsymbol{r}_i, \boldsymbol{r}_j \right\rangle = 0 \quad \text{for all } i \neq j, \tag{7.59}$$

namely that the $\boldsymbol{r}$ vectors in the conjugate gradient method are mutually orthogonal. Equation (7.59) can be used to rewrite equation (7.39).

Due to the symmetry of A, equation (7.39) can also be written as

$$\boldsymbol{u}_{t+1} = \boldsymbol{r}_{t+1} - \sum_{i=0}^{t} \frac{\langle A\boldsymbol{u}_i, \boldsymbol{r}_{t+1} \rangle}{\langle \boldsymbol{u}_i, A\boldsymbol{u}_i \rangle} \boldsymbol{u}_i. \tag{7.60}$$

From equation (7.48b),

$$\langle A\boldsymbol{u}_i, \boldsymbol{r}_{t+1} \rangle = \left\langle \frac{\boldsymbol{r}_i - \boldsymbol{r}_{i+1}}{\alpha_i}, \boldsymbol{r}_{t+1} \right\rangle \tag{7.61}$$

which from equation (7.59) is zero for all $i \le t-1$. With this, only the last term in the sum in equation (7.60) remains, leaving

$$\boldsymbol{u}_{t+1} = \boldsymbol{r}_{t+1} - \frac{\langle A\boldsymbol{u}_t, \boldsymbol{r}_{t+1} \rangle}{\langle \boldsymbol{u}_t, A\boldsymbol{u}_t \rangle} \boldsymbol{u}_t. \tag{7.62}$$

The numerator in the second term of equation (7.62) can be rewritten as

$$\begin{aligned}
\langle A\boldsymbol{u}_t, \boldsymbol{r}_{t+1} \rangle &= \langle \boldsymbol{r}_{t+1}, A\boldsymbol{u}_t \rangle && \text{(7.63a)} \\
&= \boldsymbol{r}_{t+1}^{\top} A\boldsymbol{u}_t && \text{(7.63b)} \\
&= \boldsymbol{r}_{t+1}^{\top} \frac{\boldsymbol{r}_t - \boldsymbol{r}_{t+1}}{\alpha_t} && \text{(7.63c)} \\
&= -\frac{\boldsymbol{r}_{t+1}^{\top} \boldsymbol{r}_{t+1}}{\alpha_t}, && \text{(7.63d)}
\end{aligned}$$

where the symmetry of A was used in equation (7.63a), equation (7.48b) was used in equation (7.63c) and equation (7.59) was used in equation (7.63d). The denominator in the second term of equation (7.62) can be rewritten as

$$
\begin{aligned}
\langle \boldsymbol{u}_t, A\boldsymbol{u}_t \rangle &= \left(\boldsymbol{r}_t - \frac{\langle A\boldsymbol{u}_{t-1}, \boldsymbol{r}_t \rangle}{\langle \boldsymbol{u}_{t-1}, A\boldsymbol{u}_{t-1} \rangle} \boldsymbol{u}_{t-1} \right)^{\mathsf{T}} A\boldsymbol{u}_t && \text{(7.64a)} \\
&= \frac{\boldsymbol{r}_t^{\mathsf{T}} \left(\boldsymbol{r}_t - \boldsymbol{r}_{t+1} \right)}{\alpha_t} - \frac{\langle A\boldsymbol{u}_{t-1}, \boldsymbol{r}_t \rangle}{\langle \boldsymbol{u}_{t-1}, A\boldsymbol{u}_{t-1} \rangle} \boldsymbol{u}_{t-1}^{\mathsf{T}} A\boldsymbol{u}_t && \text{(7.64b)} \\
&= \frac{\boldsymbol{r}_t^{\mathsf{T}} \boldsymbol{r}_t}{\alpha_t}, && \text{(7.64c)}
\end{aligned}
$$

where equation (7.62) was used in equation (7.64a), equation (7.48b) was used in the first term in equation (7.64b). The second term of equation (7.64b) is zero due to equation (7.28) and the first term reduces to equation (7.64c) with equation (7.59). Finally, inserting equations (7.63d) and (7.64c) into equation (7.62) gives

$$
\boldsymbol{u}_{t+1} = \boldsymbol{r}_{t+1} + \frac{\boldsymbol{r}_{t+1}^{\mathsf{T}} \boldsymbol{r}_{t+1}}{\boldsymbol{r}_t^{\mathsf{T}} \boldsymbol{r}_t} \boldsymbol{u}_t. \tag{7.65}
$$

The advantage of equation (7.65) is that it only has dot-products between vectors, an $\mathcal{O}(N)$ operation, which is considerably faster than matrix multiplications, an $\mathcal{O}\left(N^2\right)$ operation.

The algorithm

Putting together all of the derived equations, equations (7.38), (7.40), (7.47), (7.48b), (7.55) and (7.65), an iterative algorithm for the conjugate gradient method can be constructed as in algorithm 1.

Algorithm 1 An algorithm for the conjugate gradient method

```
Input $\boldsymbol{p}_0$, $\boldsymbol{b}$, $A$ and tolerance
$\boldsymbol{u}_0 = \boldsymbol{b} - A\boldsymbol{p}_0$
$\boldsymbol{r}_0 = \boldsymbol{u}_0$
$t = 0$
while ($|\boldsymbol{r}_t| >$ tolerance) do
    $\alpha_t = \frac{\boldsymbol{r}_t^\mathrm{T}\boldsymbol{r}_t}{\boldsymbol{u}_t^\mathrm{T}A\boldsymbol{u}_t}$
    $\boldsymbol{p}_{t+1} = \boldsymbol{p}_t + \alpha_t\boldsymbol{u}_t$
    $\boldsymbol{r}_{t+1} = \boldsymbol{r}_t - \alpha_t A\boldsymbol{u}_t$
    $\boldsymbol{u}_{t+1} = \boldsymbol{r}_{t+1} + \frac{\boldsymbol{r}_{t+1}^\mathrm{T}\boldsymbol{r}_{t+1}}{\boldsymbol{r}_t^\mathrm{T}\boldsymbol{r}_t}\boldsymbol{u}_t$
    $t = t + 1$
end while
return $\boldsymbol{p}_{t+1}$
```

7.3 Propagating forward in time

The local pressures at the nodes of the network found using the procedure described in section 7.2 are in the next step used to find the local volumetric flow rate q through the links. Additionally, the global pressure $|\Delta P|$ must be added to the node pressures according to equation (7.7). The expression for q in equation (3.42) is then

$$q = \begin{cases} -m\left(p_\mathrm{up} - p_\mathrm{down} - |\Delta P| + p_c^\mathrm{tot}\right) & |\Delta P|\text{-links,} \\ -m\left(p_\mathrm{up} - p_\mathrm{down} + p_c^\mathrm{tot}\right) & \text{others.} \end{cases} \tag{7.66}$$

where the $|\Delta P|$-links refer to those links that are below the bottom nodes or equivalently above the top nodes. Furthermore, m is the link mobility in equation (7.5) and p_c^tot is the total capillary pressure in equation (7.4). As in section 7.2.1, the expression for q is in the direction of the total flow Q which is referred to as the upward direction. For each link, the pressure at the node that lies above the link in the direction of the total flow Q is p_up, and the node that lies in the opposite direction is p_down.

For the time evolution of the system from the current time step to the next that is Δt seconds away, a suitable time interval Δt must be identified. The time interval Δt can be chosen based on the q calculated from equation (7.66), such that even the fastest movements are accounted for. In the network algorithm, small amounts of fluids from the injecting links are collected into the nodes at every time step and are distributed further into the links with outgoing flow. For this purpose, it is essential that the total length traveled by the fluids is well below the length of a single link. In the networks in papers I–III, Δt at each time step is chosen such that any meniscus or interface inside any link does not move more than 10% of the link length l. The average speed in each link is the quotient of q in that link and the average cross-sectional area a of that link. The minimum time it takes to move a distance $0.1l$ in any link is then chosen as the universal Δt for that time step, i.e.

$$\Delta t = \left(\frac{0.1l}{q/a}\right)_{\min} . \tag{7.67}$$

The essence of the algorithm is to record the position of all the interfaces in the network and move them according to q and Δt at each time step following a set of rules. Every link injects into and receives from its neighboring nodes depending on the sign of q in that link. The nodes only act as a collecting and distributing medium rather than a physical pore space. If $q > 0$ the flow is upwards and the link injects into the node that is above it in the direction of the total Q and receives from the node that is in the opposite direction. If $q < 0$ the flow is downwards and the link injects downwards and receives from above. The algorithm is such that the links first inject and then receive fluids, in that order.

In the beginning, the interfaces in every link are moved by a length $q\Delta t/a$, which means the positions x of the interfaces are updated to

$$x + \frac{q\Delta t}{a}. \tag{7.68}$$

When interface positions exceed the length of the link in either direction, $> l$ or < 0, the volume (length times the average area a) of fluids that have moved outside of the link is stored in the receiving nodes. The excess volume of the wetting (w) fluid V_{w} and the non-wetting (nw) fluid V_{nw} are calculated separately and stored in the receiving nodes. The positions of the interfaces that end up outside the link are deleted.

After calculating V_w and V_nw for every node, these volumes get distributed further into the links during the same time step. When injecting, one option is to alternate between whether the w or nw fluid is injected first at consecutive time steps. The injected amount should naturally depend on the receiving rate, in other words, q of the receiving link. From the total amount $q_j \Delta t$ that is injected into a receiving link j from an injecting node i, the amount of the w and the nw fluids should respectively be

$$\left(q_j \Delta t\right) \frac{V_{\mathrm{w},i}}{V_{\mathrm{w},i} + V_{\mathrm{nw},i}} \quad \text{and} \quad \left(q_j \Delta t\right) \frac{V_{\mathrm{nw},i}}{V_{\mathrm{w},i} + V_{\mathrm{nw},i}}. \tag{7.69}$$

Volume is conserved with this method of distribution since the volume that comes into a node at a time step equals the volume that goes out from that node in the same time step per equation (7.1).

One last task remains before moving on to the next time step. To create a more realistic scenario, the interfaces that lie closer to each other than a preset tolerance are merged. Thereafter, if there is a maximum limit for the number of interfaces in each link, the closest lying interfaces are merged until the desired maximum number is achieved. In the models in papers I–III, the merging algorithm aims to preserve the center of mass except when handling interfaces at the two ends of the link. The idea is illustrated in figure 7.2. The dashed lines are the original position of the interfaces while the solid lines are after the merging algorithms have been performed. In both cases, the darker-colored fluid, which can be either nw or w, is in two pieces with widths Δx_1 and Δx_2. The separation of these two fluid pieces, measured by the distance $\mathrm{d}l$ between the interfaces numbered 2 and 3, is shorter than a tolerance thus they need to be merged. In case 2, one of the darker fluid pieces is too close to the end of the link, while this is not the case in case 1, which is the reason they are processed differently. When merging in case 1, interfaces 2 and 3 are deleted. Thereafter, preserving the center of mass, interfaces 1 and 4 are moved distances

$$\frac{\Delta x_1 \, \mathrm{d}l}{\Delta x_1 + \Delta x_2} \quad \text{and} \quad \frac{\Delta x_2 \, \mathrm{d}l}{\Delta x_1 + \Delta x_2} \tag{7.70}$$

respectively, ending up at positions 5 and 6 in figure 7.2. In case 2, interfaces 2 and 3 are deleted and interface 4 is moved a distance $\mathrm{d}l$ to position 5.

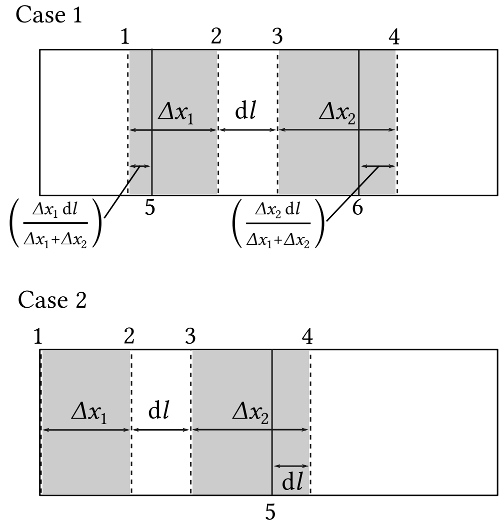

Figure 7.2: The rules for merging of the interfaces are illustrated through two examples. The dashed lines are the original position of the interfaces while the solid lines are after the merging. Interfaces are numbered. The darker-colored fluid is in two pieces with widths Δx_1 and Δx_2 that are separated a distance $\mathrm{d}l$. In case 1, the merging preserves the center of mass. In case 2, due to one of the fluid pieces being close to the end of the link, the merging is done by moving the other fluid piece only.

This concludes the procedures performed at every time step. After measuring and saving the quantities of interest, one can move on to the next time step by repeating the calculation of the pressure field (section 7.2) and propagate forward in time (section 7.3).

8

Research highlights

Most of the work I have done for my doctoral degree during the past few years is contained in the publications. In this chapter, I will present selected highlights from these papers without going into detail. This is because the papers are included in their entirety at the end of this thesis and the relevant explanations have also been given in the earlier chapters of this thesis.

A central topic in several of the papers is the expression relating the global applied pressure $\mathit{\Delta P}$ to the total volumetric flow rate,

$$Q \propto (|\mathit{\Delta P}| - P_t)^{\beta} \tag{8.1}$$

where β may vary depending on the situation as discussed in chapter 4. The factors that can contribute to this expression becoming non-linear with $\beta > 1$ include having multiple immiscible fluids and having disorders in the porous media. In papers I and II, the varying wettability of the pores was investigated as a source of disorder that causes non-linearity.

Porous media in nature can have wettability that alters along its body. Furthermore, the range of variation in wettability can be of different magnitude. The wetting condition of a porous medium has a major influence on the location, the flow, and the distribution of fluids [103]. Towards the goal of studying non-uniform wettability's influence on the rheology of two-phase immiscible flow, the work in paper I isolates the effect in terms of the mean wetting angle and the spread of the wetting angles of the pore spaces. The effect of varying the saturation of the fluids is also considered. An example of the results of paper I is shown in figure 8.1 where the wetting angle distribution's mean is $\bar{\theta} = 60^{\circ}$ and the standard deviation is $\delta\theta = 30^{\circ}$, and saturation of one of the two fluids is $S_A = 0.5$. At high $|\mathit{\Delta P}|$, figure 8.1 shows a linear dependence of Q on $(|\mathit{\Delta P}| - P_t)$ with $\beta = 1$. Out of this high-pressure limit, non-linearity occurs with $\beta > 1$. With variation in the parameters $\bar{\theta}$, $\delta\theta$ and S_A, β at the high-pressure regime stayed around 1 while out of this limit, the results demonstrate a more complicated behavior. The values of β at the lower pressure limit at different combinations of $\bar{\theta}$, $\delta\theta$ and S_A are shown in figure 8.2. It can be seen here that β is a quantity that depends on the wettability distribution condition and the saturation and can take on values anywhere in the interval $[1.0, 1.8]$. The values of β in figure 8.2 are highest for saturations approaching 0.5. Plotting β at $S_A = 0.5$ against $\bar{\theta}$ and $\delta\theta$ in figure 8.3, one can see that β is generally higher when the difference in wettability of the two fluids are larger and when this difference is present for a larger fraction of the porous network. The findings from paper I all together show that the immiscible two-phase flow in porous media is affected not only by the mean wetting angle but also by the spread of the wetting angles.

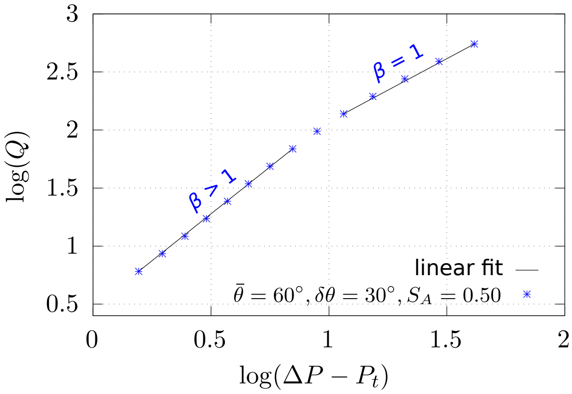

Figure 8.1: Taken from paper I. An example of the results that relate the total volumetric flow rate Q to the difference between the global pressure difference ΔP and the threshold pressure P_t. The wetting angle distribution's mean is $\bar{\theta} = 60^\circ$, and standard deviation is $\delta\theta = 30^\circ$. The saturation of one of the two fluids is $S_A = 0.5$. Here, $\Delta P = |\Delta P|$. β is the slope.

The effect of wettability is studied in a different way in paper II than in paper I where the wetting angles were assigned directly to the pores. A large class of porous media consists of solid grains, and the work in paper II investigates immiscible two-phase flow in porous media consisting of random mixtures of grains. These grains are assigned one of the two types of wettability based on a probability p^+. The wetting angle in a pore between two grains of the same type is the opposite of that between two grains of the other type, and between two opposite types of grains the wettability averages to neutral. With this design, some of the systems developed a non-zero P_t as in paper I, and the results from these systems are shown in figure 8.4a. As in figure 8.1 from paper I, there are two regimes in figure 8.4a. There is a linear regime with $\beta = 1$ at high pressures and a non-linear regime at lower pressures where β is around 2.2-2.3 for the cases tested. For a range of p^{+}, the system had $P_t = 0$ and the results from these systems are shown in figure 8.4b. Unlike before, the results here show three regimes instead of two. With decreasing $|\Delta P|$, β goes from being 1 to a value around 2.56 then to 1 again. The lower linear regime is due to the unique zero-resistance paths in this model.

The studies in papers I and II combined show that the wettability distribution of the porous media is an important factor that has a significant influence on immiscible two-phase flow in porous media. In order to fully characterize the flow it is in general insufficient to assume a uniform wettability. Future work may study spatial correlation in the wettability distributions, for instance with certain regions with uniform wettability surrounded by the rest with non-uniform wettability.

Paper III addresses a different topic with regards to immiscible two-phase flow in porous media, namely the local statistics. Specifically, the main goal of this paper is to test the condition stating that the configurational probability densities for the system and the reservoir are independent. This condition is needed in creating a statistical mechanical description of porous media that can further be used to derive equations reminiscent of thermodynamics, see chapter 6. If the said condition is met, the distributions of the averaged local quantities in the system should be independent of the reservoir size L_x. The local quantities classifying the system are the system saturation $S_{w,p}$, whose distributions are shown in figure 8.5, and the system volumetric flow rate per unit system length Q_p/l_p, whose distributions are shown in figure 8.6. The results combine to show that the independence condition seems to be valid for large enough reservoir sizes L_x.

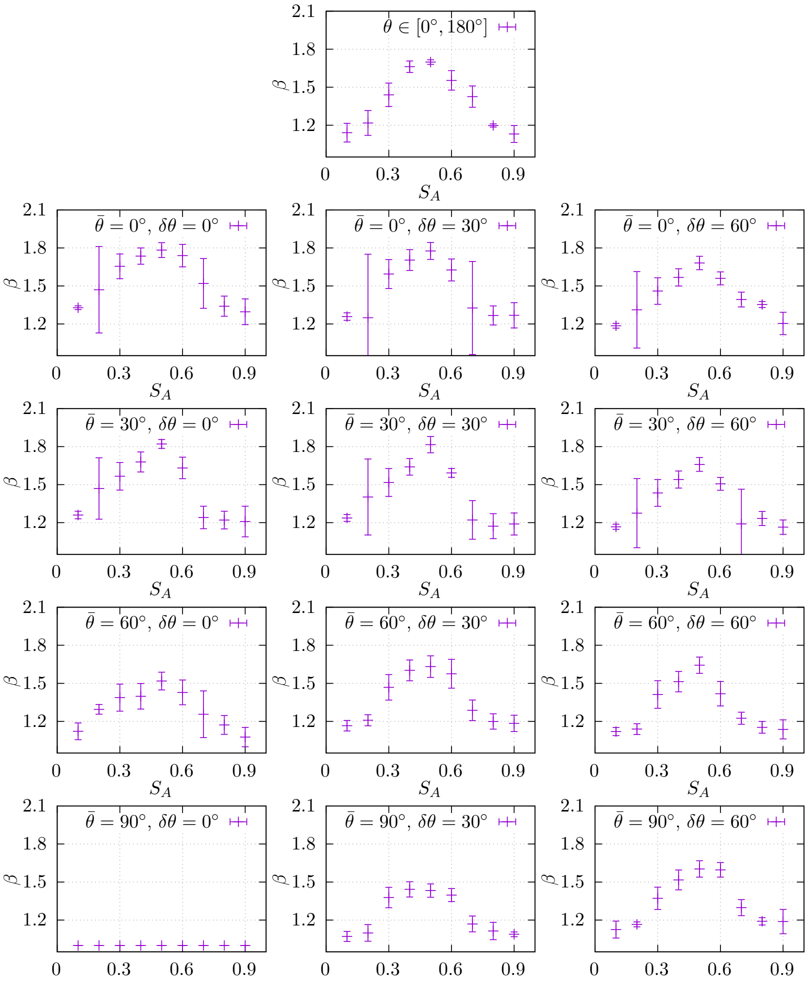

Figure 8.2: Taken from paper I. Figures showing the dependence of β in the low-pressure limit on the saturation of one of the fluids S_A when the distributions of the wetting angles $\rho(\theta)$ is a uniform distribution with $\theta \in [0^\circ, 180^\circ]$ (uppermost) and normal distributions with means $\bar{\theta} \in \{0^\circ, 30^\circ, 60^\circ, 90^\circ\}$ and standard deviations $\delta\theta \in \{0^\circ, 30^\circ, 60^\circ\}$.

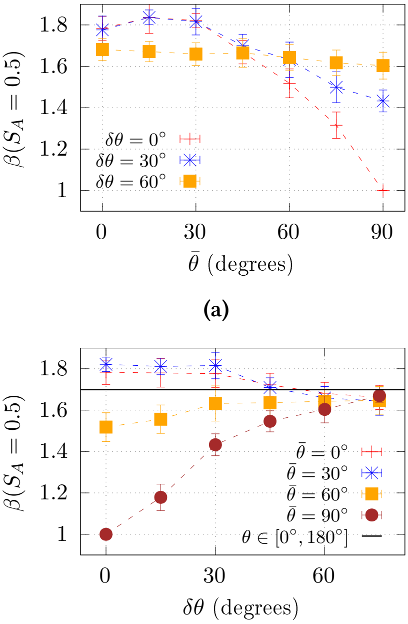

(a)

(b)

Figure 8.3: Taken from paper I. The values of the exponent β at saturation $S_A = 0.5$ as functions of (a) the mean $\bar{\theta}$ and (b) the standard deviation $\delta\theta$ of the wetting angle distribution. $\theta \in [0^\circ, 180^\circ]$ mean uniformly distributed wetting angles.

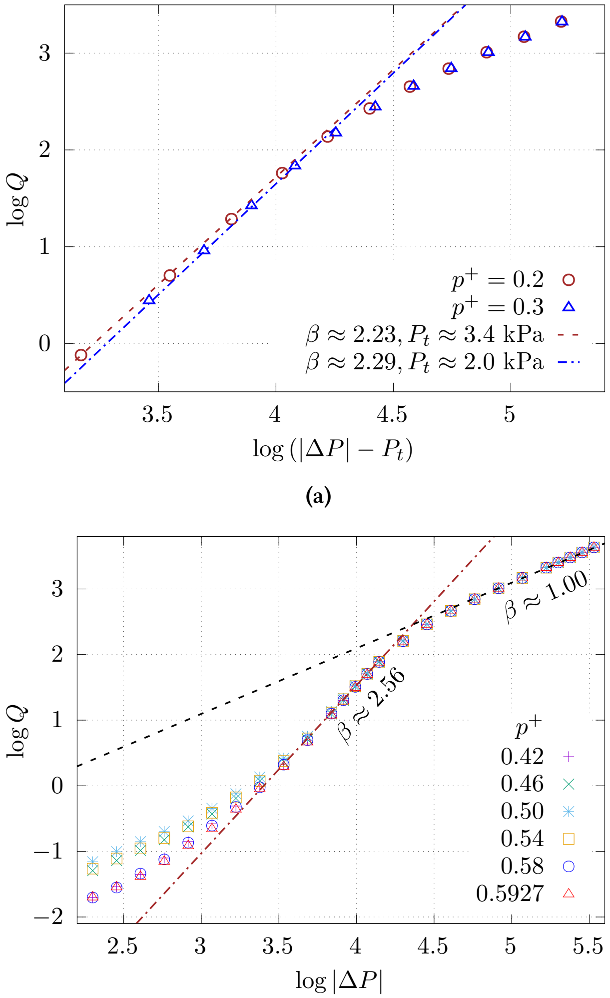

(a)

(b)

Figure 8.4: Taken from paper II. Total volumetric flow rate Q as a function of the difference between the global pressure difference $|\Delta P|$ and the threshold pressure P_t. The results in (a) have $P_t \neq 0$ and in (b) have $P_t = 0$. p^+ is the non-wetting grain occupation probability. β is the slope.

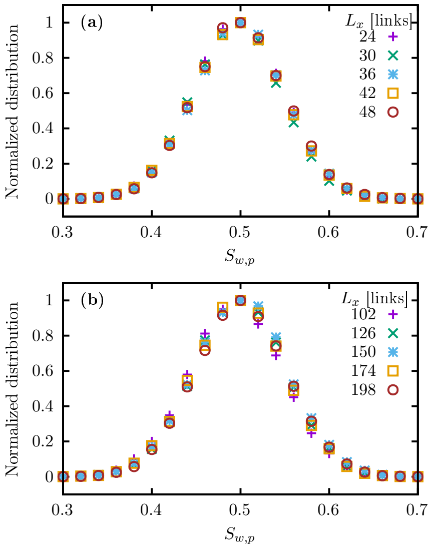

Figure 8.5: Taken from paper III. Normalized histograms of the system wetting fluid saturation $S_{w,p}$. The reservoir size L_x is close to the system size in (a) and is much larger in (b).

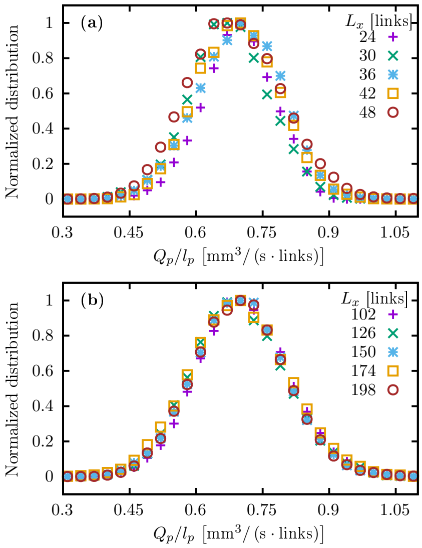

Figure 8.6: Taken from paper III. Normalized histograms of the system volumetric flow rate per link Q_p/l_p. The reservoir size L_x is close to the system size in (a) and is much larger in (b).

9

Conclusions

The main goal of this work has been to contribute to the understanding of immiscible two-phase flow in rigid porous media. An emphasis has been placed on steady-state non-linear dynamics in terms of the volumetric flow rate as a function of the global pressure difference. Additionally, local statistics of porous media were studied. There are many equations, theories and models that were used in the papers without having the luxury of space to explain their origin. The contents in the chapters of this thesis rectify this by providing more thorough derivations and explanations where suitable.

The scale of the interfaces was addressed in chapter 2. There, the equation for the capillary pressure was derived by balancing the forces that act on different interfaces as well as on different portions of the interfaces. The resulting equations are relevant for all of the papers I–IV.

Various forms of the equation for volumetric flow rate in a capillary tube were used in papers I–IV. They have been derived and explained in chapter 3. Firstly, Poiseuille flow equation for the volumetric flow rate of single-phase flow was derived through manipulations of the Navier-Stokes equation together with the mass conservation equation. Building on this knowledge, the study was extended to the case with multiple incompressible and immiscible fluid phases flowing in a cylindrical tube. The method of proof by induction was used to derive an expression for the volumetric flow rate that holds for an arbitrary number of interfaces, number of fluid phases in the tube, interface curvatures, and types of fluids. Several smaller topics were subsequently addressed, and they were the role of interface curvature in the form of capillary pressure, ideas behind finding time-averaged volumetric flow rate, effects of compressibility, as well as, some ideas for capillary bundle models.

The content in chapter 4 moved up in scale to larger porous media made up of many connected pore spaces. The focus of this chapter was the relation between the global pressure difference across the porous medium and the total volumetric flow rate at steady state, a topic relevant for papers I and II. A description of the commonly used Darcy's law was given for both single and two-phase flows. This was followed by the explanations of the cases where the flow deviates from Darcy's law.

The model in paper II had a percolation-type design that has the potential to exhibit critical behavior related to the flow in porous media. The inspiration behind the model and the design of the model was described in chapter 5. This was followed by the explanation of the hypothesized criticality in the model, as well as, the arguments for and against the existence of the criticality.

Paper III was about testing the porous systems' reservoir independence, a condition that is needed in creating a statistical mechanical description of porous media. Explanation regarding the concerning statistical mechanical theory and the role of the tested condition in that theory were reviewed briefly in chapter 6.

Most of the work in this thesis was done using a dynamic pore network model. In papers I–III, different properties that were suitable for and demanded by each study were implemented into the model. The models in these papers all had a common basic structure and flow-transportation rules. These were covered in detail in chapter 7. The algorithm was explained chronologically, starting with the initialization step followed by the procedures performed at every time step: calculating the pressure field with the conjugate gradient method and using it to find the flow rates, and then transporting the fluids through the network with the calculated flow rates based on a certain set of rules. Both the derivation and the algorithm of the conjugate gradient method as well as the transportation rules were explained thoroughly in this chapter.

The flow patterns in the dynamic pore network model are potentially influenced by how the fluids are distributed from the nodes. In this thesis, the wetting and the non-wetting fluids are distributed approximately the same from the nodes into the links. This can be reasonable for porous media with rigorous mixing in the nodes. However, this is not necessarily always the case. In future works, it could be of interest to study other rules for fluid distribution from nodes. For example, the distribution process could take into consideration which links would prefer which type of fluid. The pore sizes and the wettabilities are among the factors that would influence this. Another possibility is to take into consideration the momentum directions when distributing from the nodes.

All in all, the chapters in this thesis were aimed to complement the contents of papers I–IV. In addition to presenting a wider background and motivation for the research field in chapter 1, chapters 2–7 provide derivations and explanations for the equations, methods, theories and models used in the papers. Furthermore, some highlights from the papers are summarized in chapter 8.

Bibliography

1. **C. Gopalan, E. Kirk.**
   Biology of Cardiovascular and Metabolic Diseases (Academic Press, 2022).
   DOI: https://doi.org/10.1016/b978-0-12-823421-1.00004-4
2. **G.E. Folk, A Semken.**
   The evolution of sweat glands.
   International Journal of Biometeorology **35**, 180–186 (1991).
   DOI: https://doi.org/10.1007/bf01049065
3. **F. Rodrigues, M.B.P. Oliveira.**
   Cell-based in vitro models for dermal permeability studies in *Concepts and Models for Drug Permeability Studies*
   155–167
   (Elsevier, 2016).
   DOI: https://doi.org/10.1016/b978-0-08-100094-6.00010-9
4. **J.D. Currey.**
   Bones: structure and mechanics (Princeton university press, 2006).
   ISBN: 978-0-691-12804-7
5. **S.P. Fritton, S. Weinbaum.**
   Fluid and solute transport in bone: flow-induced mechanotransduction.
   Annual review of fluid mechanics **41**, 347–374 (2009).
   DOI: https://doi.org/10.1146/annurev.fluid.010908.165136
6. **N. Astuti, N. Wibowo, M. Ayub.**
   The porosity calculation of various types of paper using image analysis.
   Jurnal Pendidikan Fisika Indonesia **14**, 46–51 (2018).
   DOI: https://doi.org/10.15294/jpfi.v14i1.9878
7. **A. Wagh, J. Singh, R. Poeppel.**
   Dependence of ceramic fracture properties on porosity.
   Journal of materials science **28**, 3589–3593 (1993).
   DOI: https://doi.org/10.1007/bf01159841

8. **P. Colombo, C. Vakifahmetoglu, S. Costacurta.**
Fabrication of ceramic components with hierarchical porosity.
Journal of materials science **45**, 5425–5455 (2010).
DOI: https://doi.org/10.1007/s10853-010-4708-9

9. **X. Chen, S. Wu, J. Zhou.**
Influence of porosity on compressive and tensile strength of cement mortar.
Construction and Building Materials **40**, 869–874 (2013).
DOI: https://doi.org/10.1016/j.conbuildmat.2012.11.072

10. **H. Zhao, Q. Xiao, D. Huang, S. Zhang, *et al.***
Influence of pore structure on compressive strength of cement mortar.
The Scientific World Journal **2014** (2014).
DOI: https://doi.org/10.1155/2014/247058

11. **United Nations.**
What is Climate Change?
URL: https://www.un.org/en/climatechange/what-is-climate-change.
Accessed: 2023-08-01.

12. **H. Lee, J. Romero.**
Summary for Policymakers. In: Climate Change 2023: Synthesis Report. Contribution of Working Groups I, II and III to the Sixth Assessment Report of the Intergovernmental Panel on Climate Change,
1–34 (2023).
DOI: https://doi.org/10.59327/ipcc/ar6-9789291691647.001

13. **S.L. Gariano, F. Guzzetti.**
Landslides in a changing climate.
Earth-Science Reviews **162**, 227–252 (2016).
DOI: https://doi.org/10.1016/j.earscirev.2016.08.011

14. **U. Ozturk *et al.***
How climate change and unplanned urban sprawl bring more landslides.
Nature **608**, 262–265 (2022).
DOI: https://doi.org/10.1038/d41586-022-02141-9

15. **E.A. Schuur *et al.***
Climate change and the permafrost carbon feedback.
Nature **520**, 171–179 (2015).
DOI: https://doi.org/10.1038/nature14338

16. **S.A. Zimov, E.A. Schuur, F.S. Chapin III.**
Permafrost and the global carbon budget.
Science **312**, 1612–1613 (2006).
DOI: https://doi.org/10.1126/science.1128908

17. **M. Qasim, M. Badrelzaman, N.N. Darwish, N.A. Darwish, N. Hilal.**
Reverse osmosis desalination: A state-of-the-art review.
Desalination **459**, 59–104 (2019).
DOI: https://doi.org/10.1016/j.desal.2019.02.008

18. **K.P. Lee, T.C. Arnot, D. Mattia.**
A review of reverse osmosis membrane materials for desalination—Development to date and future potential.
Journal of Membrane Science **370**, 1–22 (2011).
DOI: https://doi.org/10.1016/j.memsci.2010.12.036

19. **C.M. White, B.R. Strazisar, E.J. Granite, J.S. Hoffman, H.W. Pennline.**
Separation and capture of CO2 from large stationary sources and sequestration in geological formations—coalbeds and deep saline aquifers.
Journal of the Air & Waste Management Association **53**, 645–715 (2003).
DOI: https://doi.org/10.1080/10473289.2003.10466206

20. **X. Ji, C. Zhu.**
CO2 storage in deep saline aquifers in *Novel materials for carbon dioxide mitigation technology*
299–332
(Elsevier, 2015).
DOI: https://doi.org/10.1016/b978-0-444-63259-3.00010-0

21. **B. Li, Y. Duan, D. Luebke, B. Morreale.**
Advances in CO2 capture technology: A patent review.
Applied Energy **102**, 1439–1447 (2013).
DOI: https://doi.org/10.1016/j.apenergy.2012.09.009

22. **I. Zacharoudiou, E.S. Boek, J. Crawshaw.**
The impact of drainage displacement patterns and Haines jumps on CO2 storage efficiency.
Scientific reports **8**, 15561 (2018).
DOI: https://doi.org/10.1038/s41598-018-33502-y

23. **M. Oschatz, M. Antonietti.**
A search for selectivity to enable CO 2 capture with porous adsorbents.
Energy & Environmental Science **11**, 57–70 (2018).
DOI: https://doi.org/10.1039/c7ee02110k

24. **M.E. Boot-Handford *et al.***
Carbon capture and storage update.
Energy & Environmental Science 7, 130–189 (2014).
DOI: https://doi.org/10.1039/c3ee42350f

25. **M. Bui *et al.***
Carbon capture and storage (CCS): the way forward.
Energy & Environmental Science **11**, 1062–1176 (2018).
DOI: https://doi.org/10.1039/c7ee02342a

26. **K.T. Tallakstad *et al.***
Steady-state two-phase flow in porous media: statistics and transport properties.
Physical review letters **102**, 074502 (2009).
DOI: https://doi.org/10.1103/physrevlett.102.074502

27. **K.T. Tallakstad *et al.***
Steady-state, simultaneous two-phase flow in porous media: An experimental study.
Physical Review E **80**, 036308 (2009).
DOI: https://doi.org/10.1103/physreve.80.036308

28. **E.M. Rassi, S.L. Codd, J.D. Seymour.**
Nuclear magnetic resonance characterization of the stationary dynamics of partially saturated media during steady-state infiltration flow.
New Journal of Physics **13**, 015007 (2011).
DOI: https://doi.org/10.1088/1367-2630/13/1/015007

29. **O. Aursjø *et al.***
Film flow dominated simultaneous flow of two viscous incompressible fluids through a porous medium.
Frontiers in physics **2**, 63 (2014).
DOI: https://doi.org/10.3389/fphy.2014.00063

30. **Y. Gao, Q. Lin, B. Bijeljic, M.J. Blunt.**
Pore-scale dynamics and the multiphase Darcy law.
Physical Review Fluids **5**, 013801 (2020).
DOI: https://doi.org/10.1103/physrevfluids.5.013801

31. **Y. Zhang, B. Bijeljic, Y. Gao, Q. Lin, M.J. Blunt.**
Quantification of Nonlinear Multiphase Flow in Porous Media.
Geophysical Research Letters **48**, e2020GL090477 (2021).
DOI: https://doi.org/10.1029/2020gl090477

32. **Y. Zhang, B. Bijeljic, M.J. Blunt.**
Nonlinear multiphase flow in hydrophobic porous media.
Journal of Fluid Mechanics **934**, R3 (2022).
DOI: https://doi.org/10.1017/jfm.2021.1148

33. **X. Xu, X. Wang.**
Non-Darcy behavior of two-phase channel flow.
Physical Review E **90**, 023010 (2014).
DOI: https://doi.org/10.1103/physreve.90.023010

34. **J. Sales, H.J. Seybold, C.L. Oliveira, J.S. Andrade.**
Bubble dynamics in stationary two-phase flow through disordered porous media.
Frontiers in Physics, 170 (2022).
DOI: https://doi.org/10.3389/fphy.2022.860190

35. **S. Sinha *et al.***
Effective rheology of two-phase flow in three-dimensional porous media: experiment and simulation.
Transport in porous media **119**, 77–94 (2017).
DOI: https://doi.org/10.1007/s11242-017-0874-4

36. **M. Grøva, A. Hansen.**
Two-phase flow in porous media: power-law scaling of effective permeability.
in *Journal of Physics: Conference Series*
319
(2011),
012009.
DOI: https://doi.org/10.1088/1742-6596/319/1/012009

37. **S. Sinha, A. Hansen.**
Effective rheology of immiscible two-phase flow in porous media.
Europhysics Letters **99**, 44004 (2012).
DOI: https://doi.org/10.1209/0295-5075/99/44004

38. **S. Roy, A. Hansen, S. Sinha.**
Effective rheology of two-phase flow in a capillary fiber bundle model.
Frontiers in Physics **7**, 92 (2019).
DOI: https://doi.org/10.3389/fphy.2019.00092

39. **S. Sinha, A. Hansen, D. Bedeaux, S. Kjelstrup.**
Effective rheology of bubbles moving in a capillary tube.
Physical Review E **87**, 025001 (2013).
DOI: https://doi.org/10.1103/physreve.87.025001

40. **A. Yiotis, A Dollari, M. Kainourgiakis, D. Salin, L. Talon.**
Nonlinear Darcy flow dynamics during ganglia stranding and mobilization in heterogeneous porous domains.
Physical Review Fluids **4**, 114302 (2019).
DOI: https://doi.org/10.1103/physrevfluids.4.114302

41. **F. Lanza, A. Rosso, L. Talon, A. Hansen.**
Non-Newtonian rheology in a capillary tube with varying radius.
Transport in Porous Media **145**, 245–269 (2022).
DOI: https://doi.org/10.1007/s11242-022-01848-7

42. **M.J. Blunt.**
Multiphase flow in permeable media: A pore-scale perspective
(Cambridge University Press, 2017).
DOI: https://doi.org/10.1017/9781316145098

43. **M. Trojer, M.L. Szulczewski, R. Juanes.**
Stabilizing Fluid-Fluid Displacements in Porous Media Through Wettability Alteration.
Phys. Rev. Appl. **3**, 054008 (5 2015).
DOI: https://doi.org/10.1103/physrevapplied.3.054008

44. **K. Li, A. Firoozabadi.**
Experimental study of wettability alteration to preferential gas-wetting in porous media and its effects.
SPE Reservoir Evaluation & Engineering **3**, 139–149 (2000).
DOI: https://doi.org/10.2118/62515-pa

45. **N.R. Morrow.**
The effects of surface roughness on contact: angle with special reference to petroleum recovery.
Journal of Canadian Petroleum Technology **14** (1975).
DOI: https://doi.org/10.2118/75-04-04

46. **M. Moura, E.G. Flekkøy, K.J. Måløy, G. Schäfer, R. Toussaint.**
Connectivity enhancement due to film flow in porous media.
Physical Review Fluids **4**, 094102 (2019).
DOI: https://doi.org/10.1103/physrevfluids.4.094102

47. **M. Tuller, D. Or.**
Hydraulic conductivity of variably saturated porous media: Film and corner flow in angular pore space.
Water resources research **37**, 1257–1276 (2001).
DOI: https://doi.org/10.1029/2000wr900328

48. **F.M. White.**
Fluid mechanics 7th ed. (McGraw-Hill Education, 2011).
ISBN: 978-007-131121-2

49. **R.A. Adams, C. Essex.**
Calculus: A Complete Course 8th ed. (Pearson, 2013).
ISBN: 978-0321781079

50. **E.W. Washburn.**
The dynamics of capillary flow.
Physical review **17**, 273 (1921).
DOI: https://doi.org/10.1103/physrev.17.273

51. **S. Sinha, A. Hansen, D. Bedeaux, S. Kjelstrup.**
Effective rheology of bubbles moving in a capillary tube.
Phys. Rev. E **87**, 025001 (2 2013).
DOI: https://doi.org/10.1103/physreve.87.025001

52. **S. Roy, S. Sinha, A. Hansen.**
Role of pore-size distribution on effective rheology of two-phase flow in porous media.
Frontiers in Water **3**, 709833 (2021).
DOI: https://doi.org/10.3389/frwa.2021.709833

53. **F. Lanza, A. Rosso, L. Talon, A. Hansen.**
Non-Newtonian rheology in a capillary tube with varying radius.
Transport in Porous Media **145**, 245–269 (2022).
DOI: https://doi.org/10.1007/s11242-022-01848-7

54. **H. Darcy.**
Les fontaines publiques de la ville de Dijon (Victor Dalmont, éditeur, 1856).

55. **R. Wyckoff, H. Botset, M. Muskat, D. Reed.**
The measurement of the permeability of porous media for homogeneous fluids.
Review of Scientific Instruments **4**, 394–405 (1933).
DOI: https://doi.org/10.1063/1.1749155

56. **P.G. Nutting.**
Physical analysis of oil sands.
AAPG Bulletin **14**, 1337–1349 (1930).
DOI: https://doi.org/10.1306/3d932938-16b1-11d7-8645000102c1865d

57. **R.D. Wyckoff, H.G. Botset.**
The flow of gas-liquid mixtures through unconsolidated sands.
Physics **7**, 325–345 (1936).
DOI: https://doi.org/10.1063/1.1745402

58. **J.P. Straley.**
Critical exponents for the conductivity of random resistor lattices.
Physical Review B **15**, 5733 (1977).
DOI: https://doi.org/10.1103/physrevb.15.5733

59. **B. Derrida, J. Vannimenus.**
A transfer-matrix approach to random resistor networks.
Journal of Physics A: Mathematical and General **15**, L557 (1982).
DOI: https://doi.org/10.1088/0305-4470/15/10/007

60. **D. Stauffer.**
Scaling theory of percolation clusters.
Physics reports **54**, 1–74 (1979).
DOI: https://doi.org/10.1016/0370-1573(79)90060-7

61. **R.M. Ziff.**
Spanning probability in 2D percolation.
Physical review letters **69**, 2670 (1992).
DOI: https://doi.org/10.1103/physrevlett.69.2670

62. **M. Newman, R.M. Ziff.**
Efficient Monte Carlo algorithm and high-precision results for percolation.
Physical Review Letters **85**, 4104 (2000).
DOI: https://doi.org/10.1103/physrevlett.85.4104

63. **J. Cardy.**
Finite-Size Scaling in Current Physics-Sources and Comments (Elsevier Science, 1988).

64. **M.I. Levinshtein, B.I. Shklovskii, M.S. Shur, A.L. Efros.**
The relation between the critical exponents of percolation theory.
Soviet Journal of Experimental and Theoretical Physics **42**, 197 (1975).

65. **S. Whitaker.**
Flow in porous media II: The governing equations for immiscible, two-phase flow.
Transport in porous media **1**, 105–125 (1986).
DOI: https://doi.org/10.1007/bf00714688

66. **S. Whitaker.**
The method of volume averaging (Springer Science & Business Media, 1999).
DOI: https://doi.org/10.1007/978-94-017-3389-2

67. **D. Lasseux, F.J. Valdés-Parada.**
A macroscopic model for immiscible two-phase flow in porous media.
Journal of Fluid Mechanics **944**, A43 (2022).
DOI: https://doi.org/10.1017/jfm.2022.487

68. **S. Whitaker.**
The closure problem for two-phase flow in homogeneous porous media.
Chemical Engineering Science **49**, 765–780 (1994).
DOI: https://doi.org/10.1016/0009-2509(94)85021-6

69. **J. Chen, S. Sun, X. Wang.**
Homogenization of two-phase fluid flow in porous media via volume averaging.
Journal of Computational and Applied Mathematics **353**, 265–282 (2019).
DOI: https://doi.org/10.1016/j.cam.2018.12.023

70. **J.-L. Auriault, O Lebaigue, G Bonnet.**
Dynamics of two immiscible fluids flowing through deformable porous media.
Transport in Porous Media **4**, 105–128 (1989).
DOI: https://doi.org/10.1007/bf00134993

71. **J.-L. Auriault.**
Nonsaturated deformable porous media: Quasistatics.
Transport in Porous media **2**, 45–64 (1987).
DOI: https://doi.org/10.1007/bf00208536

72. **D Picchi, I Battiato.**
The impact of pore-scale flow regimes on upscaling of immiscible two-phase flow in porous media.
Water resources research **54**, 6683–6707 (2018).
DOI: https://doi.org/10.1029/2018wr023172

73. **W.G. Gray, C.T. Miller.**
Introduction to the thermodynamically constrained averaging theory for porous medium systems (Springer, 2014).
DOI: https://doi.org/10.1007/978-3-319-04010-3

74. **C.T. Miller, W.G. Gray, C.E. Kees.**
Thermodynamically constrained averaging theory: principles, model hierarchies, and deviation kinetic energy extensions.
Entropy **20**, 253 (2018).
DOI: https://doi.org/10.3390/e20040253

75. **I. Rybak, W. Gray, C. Miller.**
Modeling two-fluid-phase flow and species transport in porous media.
Journal of Hydrology **521**, 565–581 (2015).
DOI: https://doi.org/10.1016/j.jhydrol.2014.11.051

76. **A.S. Jackson, C.T. Miller, W.G. Gray.**
Thermodynamically constrained averaging theory approach for modeling flow and transport phenomena in porous medium systems: 6. Two-fluid-phase flow.
Advances in Water Resources **32**, 779–795 (2009).
DOI: https://doi.org/10.1016/j.advwatres.2008.11.010

77. **I. Battiato *et al.***
Theory and applications of macroscale models in porous media.
Transport in Porous Media **130**, 5–76 (2019).
DOI: https://doi.org/10.1007/s11242-019-01282-2

78. **M. Hassanizadeh, W.G. Gray.**
General conservation equations for multi-phase systems: 1. Averaging procedure.
Advances in water resources **2**, 131–144 (1979).
DOI: https://doi.org/10.1016/0309-1708(79)90025-3

79. **M.S. Costanza-Robinson, B.D. Estabrook, D.F. Fouhey.**
Representative elementary volume estimation for porosity, moisture saturation, and air-water interfacial areas in unsaturated porous media: Data quality implications.
Water Resources Research **47** (2011).
DOI: https://doi.org/10.1029/2010wr009655

80. **M Stroeven, H Askes, L. Sluys.**
Numerical determination of representative volumes for granular materials.
Computer methods in applied mechanics and engineering **193**, 3221–3238 (2004).
DOI: https://doi.org/10.1016/j.cma.2003.09.023

81. **J. Li, L. Zhang, Y Wang, D. Fredlund.**
Permeability tensor and representative elementary volume of saturated cracked soil.
Canadian Geotechnical Journal **46**, 928–942 (2009).
DOI: https://doi.org/10.1139/t09-037

82. **T. Rahman, H.L. Ramandi, H. Roshan, S. Iglauer.**
Representative elementary volume of rock using X-ray micro-computed tomography: a new statistical approach.
Geofluids **2020**, 1–13 (2020).
DOI: https://doi.org/10.1155/2020/8866486

83. **A. Hansen, E.G. Flekkøy, S. Sinha, P.A. Slotte.**
A statistical mechanics framework for immiscible and incompressible two-phase flow in porous media.
Advances in Water Resources **171**, 104336 (2023).
DOI: https://doi.org/10.1016/j.advwatres.2022.104336

84. **E.T. Jaynes.**
Information theory and statistical mechanics.
Physical review **106**, 620 (1957).
DOI: https://doi.org/10.1103/physrev.106.620

85. **C.E. Shannon.**
A mathematical theory of communication.
The Bell system technical journal **27**, 379–423 (1948).
DOI: https://doi.org/10.1002/j.1538-7305.1948.tb01338.x

86. **P.-S. Laplace.**
A philosophical essay on probabilities (Dover publications, 1951).

87. **V Joekar-Niasar, S. Hassanizadeh.**
Analysis of fundamentals of two-phase flow in porous media using dynamic pore-network models: A review.
Critical reviews in environmental science and technology **42**, 1895–1976 (2012).
DOI: https://doi.org/10.1080/10643389.2011.574101

88. **M.J. Blunt.**
Flow in porous media—pore-network models and multiphase flow.
Current opinion in colloid & interface science **6**, 197–207 (2001).
DOI: https://doi.org/10.1016/s1359-0294(01)00084-x

89. **R. Chandler, J. Koplik, K. Lerman, J.F. Willemsen.**
Capillary displacement and percolation in porous media.
Journal of Fluid Mechanics **119**, 249–267 (1982).
DOI: https://doi.org/10.1017/s0022112082001335

90. **S. Sinha, M.A. Gjennestad, M. Vassvik, A. Hansen.**
Fluid meniscus algorithms for dynamic pore-network modeling of immiscible two-phase flow in porous media.
Frontiers in Physics **8**, 548497 (2021).
DOI: https://doi.org/10.3389/fphy.2020.548497

91. **E. Aker, K. JØrgen MÅlØy, A. Hansen, G.G. Batrouni.**
A two-dimensional network simulator for two-phase flow in porous media.
Transport in porous media **32**, 163–186 (1998).
DOI: https://doi.org/10.1023/a:1006510106194

92. **E. Aker, K.J. Måløy, A. Hansen.**
Simulating temporal evolution of pressure in two-phase flow in porous media.
Physical Review E **58**, 2217 (1998).
DOI: https://doi.org/10.1103/physreve.58.2217

93. **H.A. Knudsen, E. Aker, A. Hansen.**
Bulk flow regimes and fractional flow in 2D porous media by numerical simulations.
Transport in Porous Media **47**, 99–121 (2002).
DOI: https://doi.org/10.1023/a:1015039503551

94. **M. Erpelding *et al.***
History independence of steady state in simultaneous two-phase flow through two-dimensional porous media.
Physical Review E **88**, 053004 (2013).
DOI: https://doi.org/10.1103/physreve.88.053004

95. **T. Ramstad, A. Hansen, P.-E. Øren.**
Flux-dependent percolation transition in immiscible two-phase flows in porous media.
Physical Review E **79**, 036310 (2009).
DOI: https://doi.org/10.1103/physreve.79.036310

96. **H.D. Young, R.A. Freedman, A.L. Ford.**
University physics with modern physics 13th ed. (Pearson Education Limited, 2011).
ISBN: 978-0-321-69686-1

97. **G. George Batrouni, A. Hansen.**
Fourier acceleration of iterative processes in disordered systems.
Journal of statistical physics **52**, 747–773 (1988).
DOI: https://doi.org/10.1007/bf01019728

98. **M.R. Hestenes, E. Stiefel.**
Methods of Conjugate Gradients for Solving Linear Systems.
Journal of research of the national bureau of standards **49** (1952).

99. **G.H. Golub, C.F.V. Loan.**
Matrix computation 3rd ed. (The Johns Hopkins University Press, 1996).
ISBN: 0-8018-5414-8

100. **J. Stoer, R. Bulirsch, R Bartels, W. Gautschi, C. Witzgall.**
Introduction to numerical analysis (Springer, 1980).
DOI: https://doi.org/10.1007/978-0-387-21738-3

101. **R.S. Varga.**
Geršgorin and his circles (Springer Science & Business Media, 2010).
ISBN: 3540211004

102. **H.E. Bell.**
Gershgorin's theorem and the zeros of polynomials.
The American Mathematical Monthly **72**, 292–295 (1965).
DOI: https://doi.org/10.2307/2313703

103. **W.G. Anderson.**
Wettability literature survey-part 1: rock/oil/brine interactions and the effects of core handling on wettability.
Journal of petroleum technology **38**, 1125–1144 (1986).
DOI: https://doi.org/10.2118/13932-pa

PAPER I

Reference

Hursanay Fyhn, **Santanu Sinha**, **Subhadeep Roy** and **Alex Hansen**,
Rheology of Immiscible Two-phase Flow in Mixed Wet Porous Media: Dynamic Pore Network Model and Capillary Fiber Bundle Model Results.
Transport in Porous Media **139**, 491–512 (2021)
DOI: 10.1007/s11242-021-01674-3

CONTRIBUTIONS

HF developed the theory, performed the analytical and numerical calculations of the CFB model, contributed to editing of the code of the DPN model, ran the simulations and analyzed the data of the DPN model and wrote the first draft. SS suggested the idea of the problem and developed the code for the DPN model. SR sketched the initial calculation related to the CFB model and helped in data analysis. All the authors contributed in developing the theory and writing the manuscript to its final form.

Transport in Porous Media (2021) 139:491–512
https://doi.org/10.1007/s11242-021-01674-3

Rheology of Immiscible Two-phase Flow in Mixed Wet Porous Media: Dynamic Pore Network Model and Capillary Fiber Bundle Model Results

Hursanay Fyhn[1] · **Santanu Sinha**[1,2] · **Subhadeep Roy**[1] · **Alex Hansen**[1]

Received: 16 May 2021 / Accepted: 17 August 2021 / Published online: 28 August 2021

Abstract

Immiscible two-phase flow in porous media with mixed wet conditions was examined using a capillary fiber bundle model, which is analytically solvable, and a dynamic pore network model. The mixed wettability was implemented in the models by allowing each tube or link to have a different wetting angle chosen randomly from a given distribution. Both models showed that mixed wettability can have significant influence on the rheology in terms of the dependence of the global volumetric flow rate on the global pressure drop. In the capillary fiber bundle model, for small pressure drops when only a small fraction of the tubes were open, it was found that the volumetric flow rate depended on the excess pressure drop as a power law with an exponent equal to 3/2 or 2 depending on the minimum pressure drop necessary for flow. When all the tubes were open due to a high pressure drop, the volumetric flow rate depended linearly on the pressure drop, independent of the wettability. In the transition region in between where most of the tubes opened, the volumetric flow depended more sensitively on the wetting angle distribution function and was in general not a simple power law. The dynamic pore network model results also showed a linear dependence of the flow rate on the pressure drop when the pressure drop is large. However, out of this limit the dynamic pore network model demonstrated a more complicated behavior that depended on the mixed wettability condition and the saturation. In particular, the exponent relating volumetric flow rate to the excess pressure drop could take on values anywhere between 1.0 and 1.8. The values of the exponent were highest for saturations approaching 0.5, also, the exponent generally increased when the difference in wettability of the two fluids were larger and when this difference was present for a larger fraction of the porous network.

Keywords Mixed wet · Porous media · Two-phase flow · Rheology · Darcy equation · Wetting angle

---

✉ Hursanay Fyhn
hursanay.fyhn@ntnu.com

[1] PoreLab, Department of Physics, Norwegian University of Science and Technology (NTNU), NO-7491 Trondheim, Norway

[2] Beijing Computational Science Research Center, 10 East Xibeiwang Road, Haidian District, Beijing 100193, China

1 Introduction

The study of rheology of two-phase flow in porous media is pivotal for many disciplines, and the wettability conditions of the system is an important factor that directly affects the rheology. Examples for relevant disciplines include drug delivery in biology (Vafai 2010), studies of human skin behavior relevant for cosmetic and medical sectors (Elkhyat et al. 2001), creation of self-cleaning and fluid repelling materials relevant for textile industry (Li et al. 2017) and oil recovery (Kovscek et al. 1993) and carbon dioxide sequestration (Krevor et al. 2015) in geophysics (Blunt 2017; Marle 1981). All of these examples, dealing with different kinds of porous media, will benefit from a better understanding of two-phase flow under different wetting conditions. Two-phase flow means simultaneous flow of two fluids in the same space. When an immiscible fluid is injected into a porous medium filled with another fluid, different transient flow mechanisms occur depending on the flow conditions, such as capillary fingering (Lenormand and Zarcone 1989), viscous fingering (Toussaint et al. 2005; Måløy et al. 1985; Løvoll et al. 2004) and stable displacement (Frette et al. 1997; Méheust et al. 2002). After the transient flow mechanisms have surpassed, steady state sets in, which is the regime in which the rheology of two-phase flow under different wetting conditions is examined in this work.

Darcy's law is widely used to describe the flow of fluids through a porous medium which states that the volume of fluid flowing per unit area per unit time depends linearly on the applied pressure drop across a representative elementary volume in that porous medium (Blunt 2017). That is indeed the case for large applied pressures; however, the linearity gets modified into a power law at the low pressure limit. For the flow to start, the applied pressure has to overcome the disordered capillary barriers (Sinha and Hansen 2012). When the applied pressure is so small that it exceeds the capillary barriers in only parts of the porous medium, the capillary forces will be comparable to the viscous forces. In this case, the volumetric flow rate scales nonlinearly with the pressure drop due to the fact that increasing the pressure drop by a small amount creates new connecting paths in addition to increase the flow in the previously connected paths. Earlier works (Roy et al. 2019; Sinha et al. 2021; Tallakstad et al. 2009a; Rassi et al. 2011; Tallakstad et al. 2009b; Aursjø et al. 2014; Gao et al. 2020a; Zhang et al. 2021) have provided experimental, theoretical and numerical evidences for this phenomena in porous media under uniform wetting conditions. Instead of assuming uniform wetting conditions, we here investigate the same phenomena using non-uniform wetting conditions, theoretically and numerically.

The wetting condition of a porous medium is a major factor controlling the location, flow and distribution of fluids (Anderson 1986), and is a result of the interplay between the attractive forces on the surface of the adjoining materials. When two immiscible fluids flow in a porous medium, the relative values of the surface tensions between each pair of the three phases, namely the fluids and the solid, determine the wetting angle and hence the equilibrium configuration of the fluids. In nature, the wettability of a porous medium tends to alter along the system and results in a range of different wetting angles. For instance, the internal surface of reservoir rocks is composed of many minerals with different surface chemistry and absorption properties, which can cause wettability variations (Anderson 1986). There are different types of non-uniform wetting conditions depending on the degree of non-uniformity as well as the geometrical and topological distribution of regions with different wettability. The examples include fractional wettability where grains with same type of wettability are packed together in different proportions or mixed wettability where there are continuous paths with one type of wettability (Anderson 1986; Salathiel 1973). It is often useful to make these distinctions because the physical processes which create non-uniform wetting conditions can result in different forms of connectedness. In this work, we want to study how the deviation from uniform wetting conditions affect the rheology. Hence, it is desirable to isolate the effect of non-uniform wettability in terms of the mean wetting angle and the spread of the wetting angles. To this end, we use mathematical models with wetting angles determined from various distributions. We use the term *mixed wet* to denote the resulting non-uniform wetting conditions, but note that this term can also imply geometrical effects mentioned above which are not considered here. We leave for future work the problem of how other types of non-uniform wetting conditions can affect the rheology further. A mechanism for a correlated wettability distribution for pore-network modeling, where the wettability depends on the connected oil paths, was demonstrated previously by some of the authors of this manuscript (Flovik et al. 2015) and may be adopted in future.

Several works in the past have investigated multiphase flow in mixed wet porous media, and discovered clear discrepancies in the fluid behavior in uniform wet systems and in mixed wet systems. Experimental studies have found that the main determinant of the filling sequence in a porous medium is the wettability rather than the pore size (Scanziani et al. 2020; Gao et al. 2020b). There were also findings from experimental studies indicating that the processes where it is necessary to allow the flow of both fluids favor mixed wetting conditions (AlRatrout et al. 2018; Alhammadi et al. 2017), such as oil recovery or fluid transport through membranes or in biological tissue. These experimental findings show the importance of understanding the effect of wettability even further, which is easier to do through analytical and numerical studies where large range of wetting conditions can be examined in short time. In the papers by Sinha et al. (2011) and Flovik et al. (2015), pore network models similar to the one used in the present article were used to investigate the effect of wettability alteration due to changes in salinity in oil-brine mixtures. The wettability alterations were done by changing between either complete wetting and complete non-wetting conditions in the first article (Sinha et al. 2011), and by changing the wetting angles continuously between two limits depending on the cumulative flow of the wetting phase in the second article (Flovik et al. 2015). The results from both show that local alterations of the wettability introduce qualitative changes in the flow patterns by destabilizing the trapped clusters. While such past numerical studies provide important insight into the behaviors of mixed wet porous media and support the usefulness of mixed wettability, they consider limited cases of the wetting angle conditions and do not consider the effect of the applied pressure on the flow. In the present work, we conduct a systematic analysis of the effect of mixed wetting conditions, both in terms of a wide range of different mean wetting angles as well as different spread of the wetting angles. In doing so we manage to perform a direct study of the relation between the total volumetric flow rate and the pressure drop across the system as influenced by the mixed wettability.

Stated more in detail, the investigations in this work have been carried out by, firstly, calculating the total volumetric flow rate in a model consisting of a bundle of capillary tubes with mixed wet properties (Roy et al. 2019; Sinha et al. 2013). Thereafter, case studies with various specific wetting angle distribution have been performed through numerical calculations which confirmed the analytical results in addition to providing a holistic picture. Secondly, mixed wetting conditions have been implemented into a dynamic network model (Sinha et al. 2021) where the motion of the fluid interfaces are followed through the porous medium. The results confirm that the volumetric flow rate Q indeed depends on the applied pressure drop ΔP as

$$Q \propto \left(|\Delta P| - |P_t|\right)^{\beta} , \tag{1}$$

where P_t is the minimum pressure drop necessary for flow. The exponent $\beta > 1$ in the low pressure limit and $\beta = 1$ in the high pressure limit. More specifically in the low pressure limit, the capillary fiber bundle model considering a simple system gives $\beta = 2$ and $\beta = 3/2$, while the dynamic pore network model considering a more sophisticated system gives values varying anywhere between $\beta \in [1.0, 1.8]$ depending on the system wettability configuration.

The models and the wetting condition implementing methods, as well as previously existing relevant theories, are explained in Sect. 2. The theoretical and numerical results are presented and discussed in Sect. 3, and a conclusion summarizing the findings is given in Sect. 4.

2 Methodology

2.1 The Capillary Fiber Bundle Model Description

The first model that is used to investigate immiscible two phase flow in mixed wet porous media is a capillary fiber bundle (CFB) model (Roy et al. 2019; Sinha et al. 2013). This model consists of a bundle of parallel capillary tubes, disconnected from each other, each carrying the two immiscible fluids. A typical porous medium normally has a varying radius for the links in the system, which is a factor that contributes to the capillary pressure being position dependent. To emulate this effect, sinusoidal shaped tubes have been used in this model. A sketch of the model is shown in Fig. 1.

As the main goal of this work is to examine the effect of mixed wettability, each one of the tubes in the CFB model has been given a wetting angle θ chosen randomly from a certain predefined distribution $\rho(\theta)$. This means that each tube has the same assigned wetting angle over its entire length. The flow is driven by applying a global pressure drop ΔP over the system. The total global volumetric flow rate Q of the bundle of tubes is then calculated

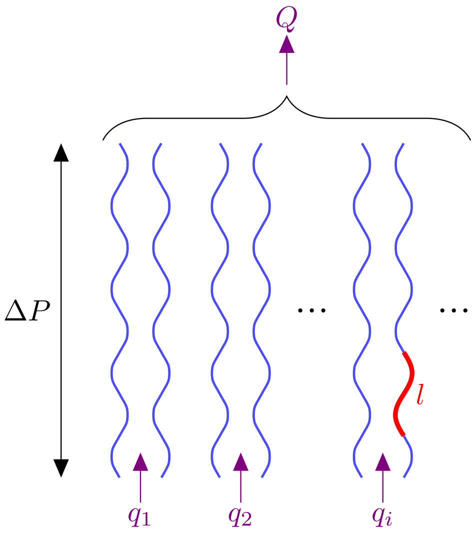

Fig. 1 Capillary fiber bundle (CFB) model consists of a bundle of parallel sinusoidally shaped capillary tubes with period l. A global pressure drop ΔP drives the flow with volumetric flow rate q_i in each tube i which combine to produces a total volumetric flow rate Q

by considering the contributions to the flow given by each tube. This calculation has been carried out both analytically and numerically.

2.2 The Dynamic Pore Network Model Description

The second model that is used for the investigations in this work is a dynamic pore network (DPN) model, a complex numerical model which is not analytically solvable (Sinha et al. 2021; Aker et al. 1998; Knudsen et al. 2002; Tørå et al. 2012; Gjennestad et al. 2018). A sketch of the network used in the model is given in Fig. 2 and a short description will be given here. In this two-dimensional (2D) simulation, a porous network is modeled through a combination of links oriented with the same angle (45°) from the flow direction and nodes connecting those links. The movement of the two immiscible fluids are modeled through tracking of their interfaces at each instant in time. The fluids get distributed to the neighboring links when they reach a node at the end of the link in which they have been traveling. The nodes themselves retain no volume. Embracing the concept of varying radius of the typical porous media, similar to what has been done in the CFB model, the links in this model is made to be hourglass shaped as shown with a zoomed in sketch in Fig. 2.

The mixed wettability has been implemented into the DPN model by randomly choosing a wetting angle θ for each one of the links in the network from a certain predefined wetting angle distribution $\rho(\theta)$. As in the case with the first model, the flow in the DPN model is driven by a pressure drop ΔP over the system. When using periodic boundary conditions, ΔP is defined across a period of the system. The total volumetric flow rate Q is constant over all the cross sections normal to the direction of the overall flow, as the one illustrated with a horizontal line in Fig. 2.

2.3 Commonalities

There are several commonalities in the two models. The smallest computational unit, which will be denoted SCU for ease of reference, in the CFB model is a single tube and that in the DPN model is a single link. Even though each SCU in the two models has uniform wettability, the entire system consisting of various such entities together describes a mixed wet porous media. In both models, the radius of each SCU i, with cylindrical symmetry around the center axis $\mathbf{x}$ has the form

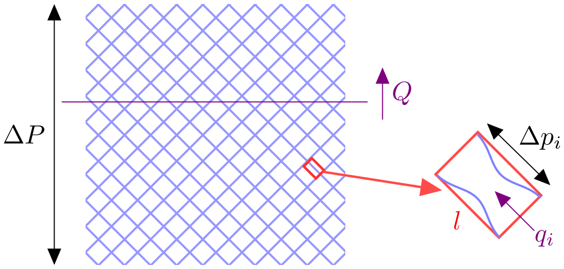

Fig. 2 Two-dimensional dynamic pore network (DPN) model consists of hourglass-shaped links with same length l oriented with the same angle (45°) from the flow direction. A global pressure drop ΔP drives the flow. The total volumetric flow rate Q is constant over all the cross sections normal to the direction of the overall flow. Each link i has a local flow rate q_i, length l and a pressure drop Δp_i over it

$$r_i(x) = \frac{r_{0,i}}{1 - a\cos\left(\frac{2\pi x}{l}\right)}, \tag{2}$$

where $r_{0,i}$ is a constant and a is the amplitude of the periodic variation. In the DPN model, l in Eq. (2) is the length of the links, since the shape of the links covers only one period of oscillation, giving an hourglass form as shown in Fig. 2. In the CFB model, l in Eq. (2) is the wavelength of the shape of the tubes, as shown in Fig. 1.

The flow within SCUs are governed by the following equations. In SCU i, the capillary pressure $p_{c,i}(x)$ across an interface between the two immiscible fluids with wetting angle θ_i can be derived from the Young–Laplace equation to be (Blunt 2017)

$$p_{c,i}(x) = \frac{2\sigma\cos\theta_i}{r_i(x)}, \tag{3}$$

where σ is the surface tension. For each SCU with length l' experiencing a pressure drop Δp across its body, the fluid within it is forced to move due to the force exerted by the total effective pressure. Total effective pressure is the difference between Δp and the total capillary pressure $\sum_k p_c(x_k)$ due to all the interfaces with positions $x_k \in [0, l']$. Assuming that the radius does not deviate too much from its average value $\bar{r}_i$, the volumetric flow rate q_i in SCU i is given by (Sinha et al. 2021; Washburn 1921)

$$q_i = -\frac{\pi\bar{r}_i^4}{8\mu_i l'}\left(\Delta p_i - \sum_k p_{c,i}(x_k)\right) \tag{4}$$

where μ_i is the saturation weighted viscosity of the fluids given by

$$\mu_i = s_{A,i}\mu_A + s_{B,i}\mu_B. \tag{5}$$

Here, $s_{A,i} = l'_{A,i}/l'$ and $s_{B,i} = l'_{B,i}/l'$ are saturations of the two fluids A and B with viscosities μ_A and μ_B and lengths $l'_{A,i}$ and $l'_{B,i}$. In the DPN model, l' is the same as l from Eq. (2). In the CFB model, l' is the length of the whole tube. The capillary number Ca, which is the ratio of viscous to capillary forces, is related to q_i through $Ca = \mu Q/(\sigma\alpha)$ where Q is the sum of all q_i through a cross sectional area α (Sinha et al. 2021).

Note that due to the incompressible nature of the fluids examined in this work, q given by Eq. (4) is the same for any position along a single SCU. Also note that all θ in this work are defined through fluid A, as shown in Fig. 3, which means the wetting angles of fluid B are $180° - \theta$. The fluid that makes the smallest angle with the solid wall is the wetting fluid in that region of the pore space and the other fluid is the non-wetting fluid.

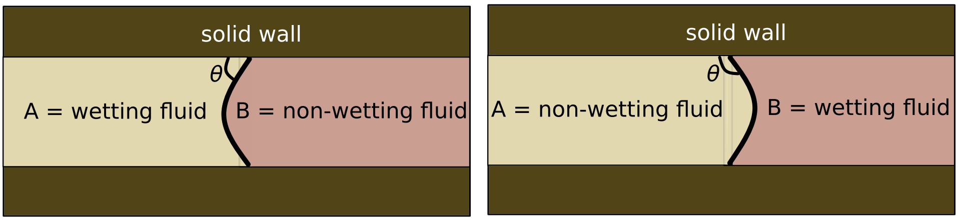

Fig. 3 Wetting angles θ in this work are defined through fluid A. The fluid that makes the smallest angle with the solid wall is the wetting fluid while the other one is the non-wetting fluid

3 Results

3.1 The Capillary Fiber Bundle Model Results

The analysis of flow in a single tube is presented in Subsect. 3.1.1. The theory is extended to a bundle of tubes with non-uniform wettability in Subsect. 3.1.2. The results from numerically solving the equations derived in Subsect. 3.1.2 give a holistic picture of the system. They are presented in Subsect. 3.1.3 and agree with the theoretical calculations from Subsect. 3.1.2. A further explanation of the results is given in Subsect. 3.1.4.

3.1.1 A Single Tube

In the paper by Sinha et al. (2013), they calculate the flow properties in a capillary tube with $\cos(\theta) = 1$. Here, for a single tube, we will follow their calculations while keeping θ as a variable as it is needed for the rest of the work. The parameters r_0, μ, l, σ, a, l' and Δp, as given in Eqs. (2) to (5), are kept constant for all the tubes. All the tubes have the same length $l' = L$ and global applied pressure $\Delta p = \Delta P$.

We start by considering a capillary tube with N bubbles. A "bubble" is one type of fluid restricted on two sides by the other fluid. Each bubble j has the center of mass position x_j and a width Δx_j. From Eqs. (2) to (5), we find that the volumetric flow rate through one tube is

$$q = -\frac{\pi \bar{r}^4}{8\mu L}\left[\Delta P + \sum_{j=0}^{N-1} \cos\theta \frac{4a\sigma}{r_0} \sin\left(\frac{\pi \Delta x_j}{l}\right) \sin\left(\frac{2\pi}{l}(x_0 + \delta x_j)\right)\right], \tag{6}$$

where $\delta x_j = x_j - x_0$. Due to the incompressible nature of the fluids, the velocity of the bubbles is approximately constant along the axis of flow and equal to $\mathrm{d}x_0/\mathrm{d}t \approx \mathrm{d}x_j/\mathrm{d}t \approx q/(\pi \bar{r}^2)$. In addition, the effect of the variation in Δx_j and δx_j can be assumed to be small. With this, Eq. (6) can be rewritten as

$$\frac{\mathrm{d}x_0}{\mathrm{d}t} = -\frac{\bar{r}^2}{8\mu L}\left[\Delta P + \cos\theta\left(\Gamma_s \sin\left(\frac{2\pi x_0}{l}\right) + \Gamma_c \cos\left(\frac{2\pi x_0}{l}\right)\right)\right], \tag{7}$$

where

$$\Gamma_s = \sum_{j=0}^{N-1} \frac{4a\sigma}{r_0} \sin\left(\frac{\pi \Delta x_j}{l}\right) \cos\left(\frac{2\pi \delta x_j}{l}\right) \tag{8}$$

and

$$\Gamma_c = \sum_{j=0}^{N-1} \frac{4a\sigma}{r_0} \sin\left(\frac{\pi \Delta x_j}{l}\right) \sin\left(\frac{2\pi \delta x_j}{l}\right). \tag{9}$$

With algebraic manipulations, Eq. (7) can be rewritten as

$$\frac{\mathrm{d}x}{\mathrm{d}t} = -\frac{\bar{r}^2}{8\mu L}\left[\Delta P - \cos\theta\sqrt{\Gamma_s^2 + \Gamma_c^2}\, \sin\left(\frac{2\pi x}{l}\right)\right], \tag{10}$$

where $x = x_0 + [\arctan(\Gamma_c/\Gamma_s) + \pi]l/2\pi$. Defining

$$\gamma = k_\gamma \cos\theta \tag{11}$$

with

$$k_\gamma = \sqrt{\Gamma_s^2 + \Gamma_c^2}, \tag{12}$$

write Eq. (10) as

$$\frac{\mathrm{d}x}{\mathrm{d}t} = -\frac{\bar{r}^2}{8\mu L}\left[\Delta P - \gamma \sin\left(\frac{2\pi x}{l}\right)\right]. \tag{13}$$

We wish to calculate the average velocity of the bubbles as they travel from one end to the other end of a tube segment with length l using a time T,

$$\left\langle \frac{\mathrm{d}x}{\mathrm{d}t} \right\rangle = \frac{l}{T}. \tag{14}$$

T can be calculated by using the equation of motion in Eq. (13),

$$\begin{aligned} T &= \int_0^l \left(\frac{\mathrm{d}x}{\mathrm{d}t}\right)^{-1} \mathrm{d}x \\ &= -\frac{8\mu L}{\gamma \bar{r}^2} \int_0^l \frac{1}{\frac{\Delta P}{\gamma} - \sin\left(\frac{2\pi x}{l}\right)} \mathrm{d}x \\ &= -\frac{8\mu L l}{\bar{r}^2} \frac{\operatorname{sgn}(\Delta P)}{\sqrt{\Delta P^2 - \gamma^2}}. \end{aligned} \tag{15}$$

Inserting the result in Eq. (15) into Eq. (14) and using the relation $\mathrm{d}x/\,\mathrm{d}t \approx q/(\pi \bar{r}^2)$ gives the average volumetric flux equation

$$\langle q \rangle = -\frac{\pi \bar{r}^4}{8\mu L} \operatorname{sgn}(\Delta P)\Theta(|\Delta P| - |\gamma|)\sqrt{\Delta P^2 - \gamma^2}, \tag{16}$$

where Θ is the Heaviside step function. From Eq. (16), we see that on average, the direction of flow is opposite to the pressure drop, as expected. Additionally, we see that for a nonzero flow, ΔP needs to exceed a certain threshold γ that is specific for the tube.

3.1.2 A Bundle of Tubes

In the CFB model, the global volumetric flow rate Q of a bundle of tubes is the sum of the time-averaged individual volumetric flow rates $\langle q \rangle$ of all the tubes that carry flow. As remarked at the end of Subsect. 3.1.1, the tubes that carry flow are those that have a threshold γ that satisfies the requirement $|\Delta P| > |\gamma|$. We will define a quantity P_t which is the minimum possible γ a tube can have. This means that the first active path across the entire system occurs once ΔP exceeds P_t. Let us also define $\gamma_{\max}$ as the maximum possible γ a tube can have, for later use. The factors that determine γ can be seen from Eq. (11). Among those, θ is the only variable that varies from tube to tube, while the other quantities are set to be universal. Under a constant ΔP, what determines which tubes in the bundle will conduct flow, while others do not is therefore their θ. Using Eq. (11) and that $\theta \in [0°, 180°]$, the requirement for flow to happen in a tube can be rewritten as

$$\theta_a < \theta < \theta^+_{P_t} \quad \text{and} \quad \theta^-_{P_t} < \theta < \theta_b, \tag{17}$$

with

$$\theta_a = \arccos\left(\min\left(1, \frac{|\Delta P|}{k_\gamma}\right)\right), \tag{18}$$

$$\theta_b = \arccos\left(\max\left(-1, -\frac{|\Delta P|}{k_\gamma}\right)\right) = 180^\circ - \theta_a, \tag{19}$$

$$\theta^\pm_{P_t} = \arccos\left(\pm\frac{|P_t|}{k_\gamma}\right). \tag{20}$$

Note that $\theta^+_{P_t} = \theta^-_{P_t}$ when $|P_t| = 0$.

Since the flow requirement in Eq. (17) indicates the range of θ that give the system a nonzero flow, Q can be expressed as a function of the probability distribution $\rho(\theta)$ of the wetting angles through

$$Q = \int_{\theta_a}^{\theta^+_{P_t}} \langle q \rangle \rho(\theta)\,\mathrm{d}\theta + \int_{\theta^-_{P_t}}^{\theta_b} \langle q \rangle \rho(\theta)\,\mathrm{d}\theta. \tag{21}$$

Inserting Eq. (16) into Eq. (21) gives

$$Q = -\frac{\pi \bar{r}^4 \operatorname{sgn}(\Delta P)}{8\mu L}\left[\int_{\theta_a}^{\theta^+_{P_t}} \sqrt{\Delta P^2 - \gamma^2}\rho(\theta)\,\mathrm{d}\theta + \int_{\theta^-_{P_t}}^{\theta_b} \sqrt{\Delta P^2 - \gamma^2}\rho(\theta)\,\mathrm{d}\theta\right]. \tag{22}$$

Case studies with several different forms of $\rho(\theta)$ will be done numerically in Subsect. 3.1.3. Here, we will solve Eq. (22) for a general $\rho(\theta)$ and show that the exponent β in

$$Q \propto (|\Delta P| - |P_t|)^\beta \tag{23}$$

is

$$\beta = \begin{cases} 1, & \text{for } |\Delta P| - |P_t| \gg |\gamma_{\max}| \quad \text{(case 1)}, \\ 2, & \text{for } |P_t| \ll |\Delta P| - |P_t| \ll |\gamma_{\max}| \quad \text{(case 2)}, \\ 1.5, & \text{for } |\Delta P| - |P_t| \ll |P_t| \quad \text{(case 3)}. \end{cases} \tag{24}$$

Here, $|\gamma_{\max}|$ is the maximum possible threshold pressure a tube can have.

Case 1: $|\Delta P| - |P_t| \gg |\gamma_{\max}|$

Using that $|\Delta P|$ is large in this case, we can write

$$\sqrt{\Delta P^2 - \gamma^2} \approx |\Delta P|. \tag{25}$$

Inserting Eq. (25) into Eq. (22) and using that the distribution $\rho(\theta)$ is normalized to 1, gives

$$Q \approx -\frac{\pi \bar{r}^4 \operatorname{sgn}(\Delta P)}{8\mu L}|\Delta P| \approx -\frac{\pi \bar{r}^4 \operatorname{sgn}(\Delta P)}{8\mu L}\left(|\Delta P| - |P_t|\right). \tag{26}$$

In the last step, we have used that $|P_t|$ which is the minimum $|\Delta P|$ needed to achieve $Q > 0$, is a much smaller number than $|\Delta P|$. For the equations derived for all three cases in Eq. (24), we wish to express Q in terms of $|\Delta P| - |P_t|$ for ease of comparison with Eq. (23). Comparing Eq. (26) with Eq. (23), one gets $\beta = 1$ for case 1.

Common for Case 2 and Case 3:

Equation (24) states that the effective pressure obeys $|\Delta P| - |P_t| \ll |\gamma_{\max}|$ in case 2, while it obeys $|\Delta P| - |P_t| \ll |P_t|$ in case 3. From Eq. (11), the threshold pressure γ is so that $|\gamma| \leq k_\gamma$. This criterion should also be followed by the maximum possible $|\gamma|$ which is $|\gamma_{\max}|$ and the minimum possible $|\gamma|$ which is $|P_t|$. Combining these information, a common requirement for cases 2 and 3 should be

$$|\Delta P| - |P_t| \ll k_\gamma. \tag{27}$$

Equation (18) then becomes

$$\begin{aligned} \theta_a &= \arccos\left(\frac{|\Delta P|}{k_\gamma}\right), \\ &= \arccos\left(\frac{|\Delta P| - |P_t| + |P_t|}{k_\gamma}\right), \\ &\approx \arccos\left(\frac{|P_t|}{k_\gamma}\right) - \frac{|\Delta P| - |P_t|}{\sqrt{k_\gamma^2 - P_t^2}}. \end{aligned} \tag{28}$$

where Eq. (27) was used in the last step.

Next, based on Eq. (27), Taylor expanding the integrands of Eq. (22) with respect to θ around $\theta_{P_t}^{\pm}$ gives

$$\begin{aligned} Q \approx &- \frac{\pi \bar{r}^4 \mathrm{sgn}(\Delta P)}{8\mu L}\left[\int_{\theta_a}^{\theta_{P_t}^+} \sqrt{\Delta P^2 - P_t^2}\, \rho\left(\theta_{P_t}^+\right) \mathrm{d}\theta\right] \\ &- \frac{\pi \bar{r}^4 \mathrm{sgn}(\Delta P)}{8\mu L}\left[\int_{\theta_{P_t}^-}^{\theta_b} \sqrt{\Delta P^2 - P_t^2}\, \rho\left(\theta_{P_t}^-\right) \mathrm{d}\theta\right]. \end{aligned} \tag{29}$$

Performing this integrations using the integration limits given in Eqs. (20) and (28) and that $\theta_b = 180° - \theta_a$ (Eq. (19)) gives

$$\begin{aligned} Q \approx &-\left[\frac{\pi \bar{r}^4 \mathrm{sgn}(\Delta P)}{8\mu L} \frac{\rho\left(\theta_{P_t}^+\right) + \rho\left(\theta_{P_t}^-\right)}{\sqrt{k_\gamma^2 - P_t^2}}\right] \\ &\times \left(|\Delta P| - |P_t|\right)^{3/2}\left(\left(|\Delta P| - |P_t|\right) + 2|P_t|\right)^{1/2}. \end{aligned} \tag{30}$$

Equation (30) holds true for both cases 2 and 3.

Case 2: $|P_t| \ll |\Delta P| - |P_t| \ll |\gamma_{\max}|$

The part of the criterion for this case that says $|P_t| \ll |\Delta P| - |P_t|$ makes it so that $\left(\left(|\Delta P| - |P_t|\right) + 2|P_t|\right)^{1/2} \approx \left(|\Delta P| - |P_t|\right)^{1/2}$ which can be used to write Eq. (30) as

$$Q \approx -\left[\frac{\pi \bar{r}^4 \operatorname{sgn}(\Delta P)}{8\mu L} \frac{\rho\left(\theta^+_{P_t}\right) + \rho\left(\theta^-_{P_t}\right)}{\sqrt{k_\gamma^2 - P_t^2}}\right]\left(|\Delta P| - \left|P_t\right|\right)^2. \tag{31}$$

Comparing Eq. (31) to Eq. (23) gives $\beta = 2$ for case 2.

Case 3: $|\Delta P| - \left|P_t\right| \ll \left|P_t\right|$

The criterion for this case makes it so that $\left(\left(|\Delta P| - \left|P_t\right|\right) + 2\left|P_t\right|\right)^{1/2} \approx \sqrt{2\left|P_t\right|}$ which can be used to write Eq. (30) as

$$Q \approx -\left[\frac{\pi \bar{r}^4 \operatorname{sgn}(\Delta P)}{8\mu L} \frac{\rho\left(\theta^+_{P_t}\right) + \rho\left(\theta^-_{P_t}\right)}{\sqrt{k_\gamma^2 - P_t^2}} \sqrt{2\left|P_t\right|}\right]\left(|\Delta P| - \left|P_t\right|\right)^{3/2}. \tag{32}$$

Comparing Eq. (32) to Eq. (23) gives $\beta = 3/2$ for case 3.

In the transition region between case 1 and cases 2 and 3, where $|\Delta P| - \left|P_t\right| \approx k_\gamma$, the volumetric flow depends more sensitively on the wetting angle distribution function $\rho(\theta)$, and is in general not a simple power law. Nevertheless, we can use the analysis presented here to compute the height of that transition region. Taking the logarithm of Q, we find that

$$\log(Q) = \begin{cases} \eta + \log\left(\frac{|\Delta P|}{k_\gamma} - \frac{|\gamma|}{k_\gamma}\right) & \text{for case 1,} \\ \eta + 2\log\left(\frac{|\Delta P|}{k_\gamma} - \frac{|\gamma|}{k_\gamma}\right) + \log\left(\frac{\rho\left(\theta^+_{P_t}\right) + \rho\left(\theta^-_{P_t}\right)}{\sqrt{1 - (P_t/k_\gamma)^2}}\right) & \text{for case 2,} \\ \eta + 1.5\log\left(\frac{|\Delta P|}{k_\gamma} - \frac{|\gamma|}{k_\gamma}\right) + \log\left(\frac{\rho\left(\theta^+_{P_t}\right) + \rho\left(\theta^-_{P_t}\right)}{\sqrt{1 - (P_t/k_\gamma)^2}}\right) & \\ \qquad + \log\left(\sqrt{\frac{2\left|P_t\right|}{k_\gamma}}\right) & \text{for case 3,} \end{cases} \tag{33}$$

where η is a constant that is the same for all the three cases. Evaluating this at $|\Delta P| - \left|P_t\right| = k_\gamma$ we see that the height difference between case 2 and case 1 in a logarithmically scaled plot is

$$h = \log\left(\frac{\rho\left(\theta^+_{P_t}\right) + \rho\left(\theta^-_{P_t}\right)}{\sqrt{1 - (P_t/k_\gamma)^2}}\right), \tag{34}$$

and the height difference between case 3 and case 1 is

$$h = \log\left(\frac{\rho\left(\theta^+_{P_t}\right) + \rho\left(\theta^-_{P_t}\right)}{\sqrt{1 - (P_t/k_\gamma)^2}}\right) + \log\left(\sqrt{\frac{2\left|P_t\right|}{k_\gamma}}\right). \tag{35}$$

This is shown in Fig. 4. It is assumed in the above analysis that $\rho\left(\theta^+_{P_t}\right)+\rho\left(\theta^-_{P_t}\right) < \sqrt{1-(P_t/k_\gamma)^2}$, since $\rho(\theta)$ is a normalized probability distribution. Hence, $h < 0$, which means that the β in the transition region must be larger than outside the transition region.

3.1.3 Numerical Results

Here, we study numerically the volumetric flow rate Q's response to a wide range of an applied pressures ΔP. In addition to verify the analytical results from Subsect. 3.1.2, this numerical study allows us to probe the transition region where ΔP is the same order of magnitude as $\gamma_{\max}$. We present results with three different normal and uniform distributions of θ, and note that we find similar results also for many other distributions.

First, consider $\rho(\theta)$ to be a uniform distribution,

$$\rho(\theta) = \begin{cases} \frac{1}{\theta_b-\theta_a}, & \text{for } \theta \in [\theta_a, \theta_b] \text{ with } 0^\circ < (\theta_a, \theta_b) < 180^\circ, \\ 0, & \text{otherwise .} \end{cases} \tag{36}$$

The results from when θ is uniformly distributed between $[\theta_a = 0^\circ, \theta_b = 90^\circ]$, $[\theta_a = 0^\circ, \theta_b = 89^\circ]$ and $[\theta_a = 0^\circ, \theta_b = 60^\circ]$ are shown in Fig. 5a. These results confirm the analytical calculations performed in Subsect. 3.1.2. When $|\Delta P| - |P_t| \gg |\gamma_{\max}|$, case 1, all three examples do indeed satisfy $\beta = 1$, reflecting linear Darcy flow. The region where $|P_t| \ll |\Delta P| - |P_t| \ll |\gamma_{\max}|$ resulting in $\beta = 2$, case 2, covers the rest of the plot for $\rho(\theta)$ with $\theta \in [0^\circ, 90^\circ]$, since in this case $P_t = 0$. For $\rho(\theta)$ with $\theta \in [0^\circ, 89^\circ]$ however, that same region is approximately only the center part of the plot $(-1 < \log((\Delta P - P_t)/k_\gamma) < 0)$ while the rest belongs to the regime where $\beta = 1.5$. The region $|\Delta P| - |P_t| \ll |P_t|$, case 3, that gives $\beta = 1.5$ is dominating in the case with $\theta \in [0^\circ, 60^\circ]$. For this distribution, the transition from $\beta = 1$ to $\beta = 1.5$ happens quickly due to $|P_t| = k_\gamma \cos(60^\circ)$ being a larger number than in the other two cases, rendering the region where the applied pressure can satisfy the requirement for $\beta = 2$, namely $|P_t| \ll |\Delta P| - |P_t| \ll |\gamma_{\max}|$, very small.

The CFB model has also been numerically tested with $\rho(\theta)$ being normal distribution with mean $\bar{\theta}$ and standard deviation $\delta\theta$ given by

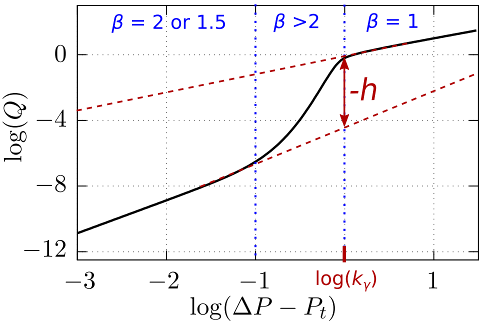

Fig. 4 Height h of the transition region is defined as the distance between the two lines that are extrapolations of the linear parts of the curve at $\Delta P - P_t = k_\gamma$. Here, Q is the volumetric flow rate and $\Delta P - P_t$ is the excess pressure

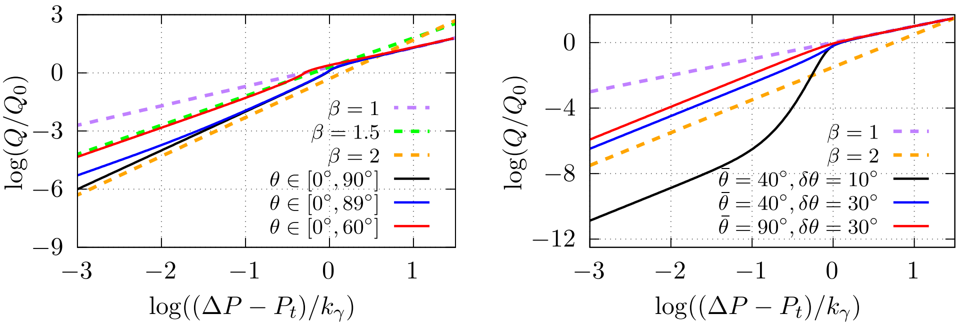

(a) **(b)**

Fig. 5 Relation between the total volumetric flow rate Q and the excess pressure $\Delta P - P_t$ for wetting angles θ (**a**) uniformly distributed between $[0°, 90°]$, $[0°, 89°]$ and $[0°, 60°]$, and (**b**) normally distributed with $(\bar{\theta} = 40°, \delta\theta = 40°)$, $(\bar{\theta} = 40°, \delta\theta = 40°)$ and $(\bar{\theta} = 40°, \delta\theta = 40°)$ where $\bar{\theta}$ is the mean and $\delta\theta$ is the standard deviation. Here, ΔP is the applied pressure and P_t is the minimum threshold pressure. The flow rates have been normalized with $Q_0 = -(\pi\bar{r}^4 \mathrm{sgn}(\Delta P) k_\gamma)/(8\mu L)$ and the pressures have been normalized with k_γ. Straight lines with gradients β has been added

$$\rho(\theta) = \frac{\exp\left\{-\frac{1}{2}\left(\frac{\theta-\bar{\theta}}{\delta\theta}\right)^2\right\}}{\int_{0°}^{180°} \exp\left\{-\frac{1}{2}\left(\frac{\theta-\bar{\theta}}{\delta\theta}\right)^2\right\} \mathrm{d}\theta} \qquad \text{for } \theta \in [0°, 180°]. \tag{37}$$

The results from when θ is normally distributed with $(\bar{\theta} = 40°, \delta\theta = 10°)$, $(\bar{\theta} = 40°, \delta\theta = 30°)$ and $(\bar{\theta} = 90°, \delta\theta = 30°)$ are shown in Fig. 5b. These results once again confirm the analytical calculations performed in Subsect. 3.1.2. Toward the right in Fig. 5b where $|\Delta P| - |P_t| \gg |\gamma_{\max}|$, case 1, all three examples follow $\beta = 1$. Toward the left in Fig. 5b where $|P_t| \ll |\Delta P| - |P_t| \ll |\gamma_{\max}|$, the results follow $\beta = 2$, case 2. Notice that $P_t = 0$ for all these three cases. Since a nonzero Q occurs only when $|\Delta P| > |P_t|$, the requirement for $\beta = 1.5$, namely $|\Delta P| - |P_t| \ll |P_t|$, case 3, is not satisfied here. In Fig. 5b, the transition region between when $\beta = 1$ and when $\beta = 2$ exhibits a gradient $\beta > 2$, in accordance with the analysis above. The same effect can also slightly be seen in Fig. 5a, but is much more apparent in Fig. 5b. One can also see from Fig. 5b that β is larger for smaller $\delta\theta$ and means $\bar{\theta}$ further away from 90°. This can be understood from Eq. (34), since smaller $\delta\theta$ and larger $|\bar{\theta} - 90°|$ implies smaller $\rho(90°)$. From Eq. (34), we see that smaller $\rho(90°)$ implies a larger height difference h. Physically, this can be understood from the fact that a smaller $\rho(90°)$ means that a smaller fraction of the total number of tubes are active in the low pressure regime.

3.1.4 The Origin of β

We can write volumetric flow rate as $Q = N\bar{q}$, where N is the number of open tubes and $\bar{q}$ is the average flow per open tube. Put differently, $\bar{q}$ is the average of $\langle q \rangle$ for all the open tubes. We propose that β can be understood from how each of these factors change with applied pressure ΔP. Suppose that increasing the pressure difference from $|\Delta P_0| - |P_t|$ to $|\Delta P| - |P_t| = \bar{x}\left(|\Delta P_0| - |P_t|\right)$ transforms the number of open tubes and the flow per tube according to $N_0 \to \bar{x}^{\bar{a}} N_0$ and $\bar{q}_0 \to \bar{x}^{\bar{b}} \bar{q}_0$, respectively. In this case, we see that the volumetric flow change from $Q_0 = N_0 \bar{q}_0$ to

$$Q = \left(\frac{|\Delta P| - |P_t|}{|\Delta P_0| - |P_t|} \right)^{\bar{a}+\bar{b}} Q_0, \tag{38}$$

so $\beta = \bar{a} + \bar{b}$.

Consider first $\bar{q}$. From Eq. (16), we know that the volumetric flow for a tube with threshold pressure γ is $\langle q \rangle \propto \sqrt{\Delta P^2 - \gamma^2} = \sqrt{(\Delta P - \gamma)(\Delta P - \gamma + 2\gamma)}$. Thus, we see that $\langle q \rangle \propto (\Delta P - \gamma)^{1/2}$ if $(\Delta P - \gamma) \ll \gamma$ and $\langle q \rangle \propto (\Delta P - \gamma)^1$ if $(\Delta P - \gamma) \gg \gamma$. Hence, if most of the active tubes have threshold pressure just below the applied pressure (case 3), then $\bar{a} = 1/2$. On the other hand, if most of the active tubes have threshold pressure well-below the applied pressure (cases 1 and 2), then $\bar{a} = 1$.

Next, consider the number of active tubes transporting fluid, N. This is given by

$$N = N_{\max} \left[\int_{\theta_a}^{\theta^+_{P_t}} \rho(\theta)\, \mathrm{d}\theta + \int_{\theta^-_{P_t}}^{\theta_b} \rho(\theta)\, \mathrm{d}\theta \right], \tag{39}$$

where $N_{\max}$ is the total number of tubes in the system. When the applied pressure is larger than the maximal threshold pressure $\gamma_{\max}$, then all the tubes are active and $N = N_{\max}$. Thus, for case 1, we have $\bar{b} = 0$ and consequently $\beta = \bar{a} + \bar{b} = 1$. On the other hand, when $|\Delta P| - |P_t| \ll |\gamma_{\max}|$, then $\theta^+_{P_t} - \theta_a = \theta_b - \theta^-_{P_t} = \left(|\Delta P| - |P_t|\right) / \sqrt{k_\gamma^2 - P_t^2} \ll 1$, as seen from Eq. (28). Thus,

$$N = \frac{N_{\max}(\rho(\theta_a) + \rho(\theta_b))}{\sqrt{k_\gamma^2 - P_t^2}} \left(|\Delta P| - |P_t|\right), \tag{40}$$

so $\bar{b} = 1$. Combining this with the result for $\bar{a}$ we see that in case 2, we get $\beta = \bar{a} + \bar{b} = 2$, and in case 3, we get $\beta = \bar{a} + \bar{b} = 1.5$. This explains why $\beta \in \{1, 1.5, 2\}$ when either all tubes are active (case 1) or only a small fraction is active (cases 2 and 3).

3.2 The Dynamic Pore Network Model Results

3.2.1 Data Collecting and Processing Procedures

Using the method described in Subsect. 2.2, numerical simulations of the DPN model have been performed. The following factors and parameters have been kept constant during all simulations. The 2D network used was made of 64×64 links and had periodic boundary conditions in all directions. All the links had length $l = 1$ mm, average radii $\bar{r} \in [0.1l, 0.4l]$ and amplitude of the periodic variation $a = 1$ mm, see Eq. (2). The viscosities of the fluids A and B were $\mu_A = \mu_B = 0.01$ Pa·s, see Eq. (5). The surface tension between the fluids were 0.03 N/m, see Eq. (3). In this closed network system, the control parameter was the saturation of one of the fluids in the whole system, which was tested for values $S_A \in \{0.1, 0.2, 0.3, 0.4, 0.5, 0.6, 0.7, 0.8, 0.9\}$.

The distributions of the wetting angles, $\rho(\theta)$, have firstly been tested for a uniform distribution with $\theta \in [0°, 180°]$. Secondly, normal distributions with means

$\bar{\theta} \in \{0°, 30°, 60°, 90°\}$ and, with each mean, standard deviations $\delta\theta \in \{0°, 30°, 60°\}$ were also tested. The $\rho(\theta)$ mentioned until now were implemented into the network with all of the above-mentioned values of S_A. In addition to this, at $S_A = 0.5$, several more normally distributed θ were examined. They were with means $\bar{\theta} \in \{0°, 30°, 60°, 90°\}$ and, with each mean, standard deviations $\delta\theta \in \{15°, 45°, 75°\}$, as well as, with means $\bar{\theta} \in \{15°, 45°, 75°\}$ and, with each mean, standard deviations $\delta\theta \in \{0°, 30°, 60°\}$. Note that the normally distributed θ could go outside the interval $[0°, 180°]$, which is equivalent to a slightly increased weight around 0° or 180° because the angle only comes in through $\cos\theta$, as seen in Eq. (3). Another thing to note is that only distributions with $\bar{\theta} \leq 90°$ have been considered. This is because since the fluids have the same viscosity, a symmetry is in place where the case with mean $\bar{\theta}$ and saturation S_A is the same as the case with mean $180° - \bar{\theta}$ and saturation $1 - S_A$.

For each S_A, the system was driven by various different Q, and for each Q, 20 different realizations of the network were performed and averaged over. The global applied pressure ΔP in the direction of the flow was measured, and was calculated by averaging over the fluctuations after the system had reached a steady state. After obtaining a set of Q and ΔP for every $\rho(\theta)$ at every S_A, data analysis had to be performed to determine the global threshold pressure P_t below which there is no flow through the whole system, as well as the exponent β in $Q \propto \left(|\Delta P| - |P_t|\right)^{\beta}$. Note that similar to the CFB model, the first active path across the entire system in DPN occurs once ΔP exceeds P_t.

The process of determining P_t and β started with deciding the indices of the data points that belonged to the linear and power law regimes through visual examination. As shown with an example in Fig. 6, this meant deciding the indices of the datapoints that lied between $n^{\text{start}}_{\beta\approx 1}$ to $n^{\text{end}}_{\beta\approx 1}$ and belonged to the region with $\beta \approx 1$, as well as the indices between $n^{\text{start}}_{\beta>1}$ to $n^{\text{end}}_{\beta>1}$ that belonged to the region with $\beta > 1$. The error bars were calculated as the absolute values of the difference between the results and the results that would have been if the range of data points included from each region were reduced. The next step was to perform linear fitting of $Q^{1/\beta}$ against ΔP on the data points from $n^{\text{start}}_{\beta>1}$ to $n^{\text{end}}_{\beta>1}$. The linear fitting was of the form $c_1 Q^{1/\beta} + c_2$ with c_1 and c_2 real numbers. Due to the definition that $P_t = \Delta P$ exactly when $Q^{1/\beta}$ becomes nonzero, $P_t = c_2$. This procedure was repeated for a range of different βs, and the P_t that gave the least root-mean-square error was chosen as the final candidate. Thereafter, linear fitting $\log(Q)$ versus $\log(\Delta P - P_t)$ separately for the data points from index $n^{\text{start}}_{\beta\approx 1}$ to $n^{\text{end}}_{\beta\approx 1}$ and data points from index $n^{\text{start}}_{\beta>1}$ to $n^{\text{end}}_{\beta>1}$ gave the values of β in those regions.

Fig. 6 Linear fitting the data points from index $n^{\text{start}}_{\beta\approx 1}$ to $n^{\text{end}}_{\beta\approx 1}$ and data points from index $n^{\text{start}}_{\beta>1}$ to $n^{\text{end}}_{\beta>1}$ separately gives β in those regions

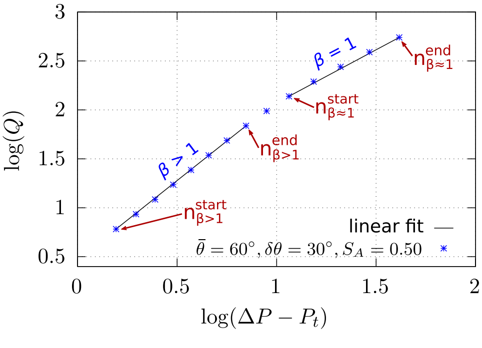

3.2.2 Simulation Results

All of the simulations performed, using the parameters and the different wetting angle distributions $\rho(\theta)$ described in Subsect. 3.2.1, resulted in a Darcy-like flow with $\beta \approx 1$ in the high pressure limit where most of the links were active. The transition region with $\beta > 2$ flow, as in the case with the CFB model, was not observed with the DPN model. Note that the DPN model, compared to the CFB model, simulates a porous medium that has a more complex interplay of the fluids in the links which separate and rejoin. It could be speculated that this advanced behavior of the network eliminates the transition region originally observed in the CFB model, in other words, the transition region may be an artifact of the CFB model. In the low pressure limit result of the DPN model, the exponent β shows dependence on the saturation and the wettability properties of the network. This is also the case with the threshold pressure of the network P_t. A closer exploration of the latter two factors will now be presented.

The results for β in the *low pressure limit* are shown in Fig. 7 and takes on various values in the range $\beta \in [1.00 \pm 0.05, 1.82 \pm 0.05]$. The phenomenon with $\beta > 1$ originates from that many links in the network are not yet opened in the low pressure regime, which means increasing ΔP increases the number of active links in addition to increasing the flow within each active link. The overall combined effect of these allows the volume of fluid transported to rise much more than if all the links were already open. This is the same as in the capillary fiber bundle model, but here β takes on a larger range of values depending on the saturation and the wetting conditions.

The results for P_t are shown in Fig. 8. The exponents β in Fig. 7, as well as, the minimum threshold pressures P_t in Fig. 8 have a tendency to be largest for saturations around 0.5 and decrease steadily with increasing saturation of either one of the fluids. The reason is that when one of the fluids dominates the system, $S_A \rightarrow 0.1$ or 0.9, it is easy for that dominating fluid to create an active flow-path through the system. This is because those connected links that contain the same fluid will not experience a interfacial capillary pressure barrier. This decreases the overall threshold P_t of the system, which is the cumulative effect of the interfacial capillary barriers in the network. There will be few new links to become active as ΔP increases under these circumstances which will further make Q less reactive toward changes in ΔP, meaning a decreased β. In contrast, when there are comparable amounts of the fluids A and B in the system, $S_A \rightarrow 0.5$, ΔP has to overcome the cumulative capillary pressure barrier created by the large number of interfaces between A and B. This naturally has an increasing effect on P_t. When ΔP is increased under such conditions, the requirement for non-zero flow for many links are satisfied at once, causing a drastic increase in Q as a response, which increases β. Lastly regarding the effect of saturation, in the three middle rows in Fig. 8, the maxima of the P_t plots are skewed to the left of $S_A = 0.5$. In those cases, θ is concentrated around a $\bar{\theta} < 90°$, which makes fluid A is the most wetting fluid while B is the most non-wetting fluid. It is easier for the wetting fluid to get transported in a porous medium, meaning when the saturation of the wetting fluid is lower, $S_A < 0.5$, the system will require a higher applied pressure to achieve a nonzero flow making the system's P_t higher.

The variations in β for different $\rho(\theta)$ are more subtle than in the case with P_t. To get a clear overview of the differences, the maximum values, $\beta(S_A = 0.5)$, have been plotted as functions of $\bar{\theta}$ and $\delta\theta$ in Fig. 9a and 9b, respectively. Both the exponents β in Fig. 9a and 9b and the minimum threshold pressure P_t in Fig. 8 vary with $\bar{\theta}$ and $\delta\theta$ of the normal distributions. The interfacial capillary pressures, given by Eq. (3), increase with the

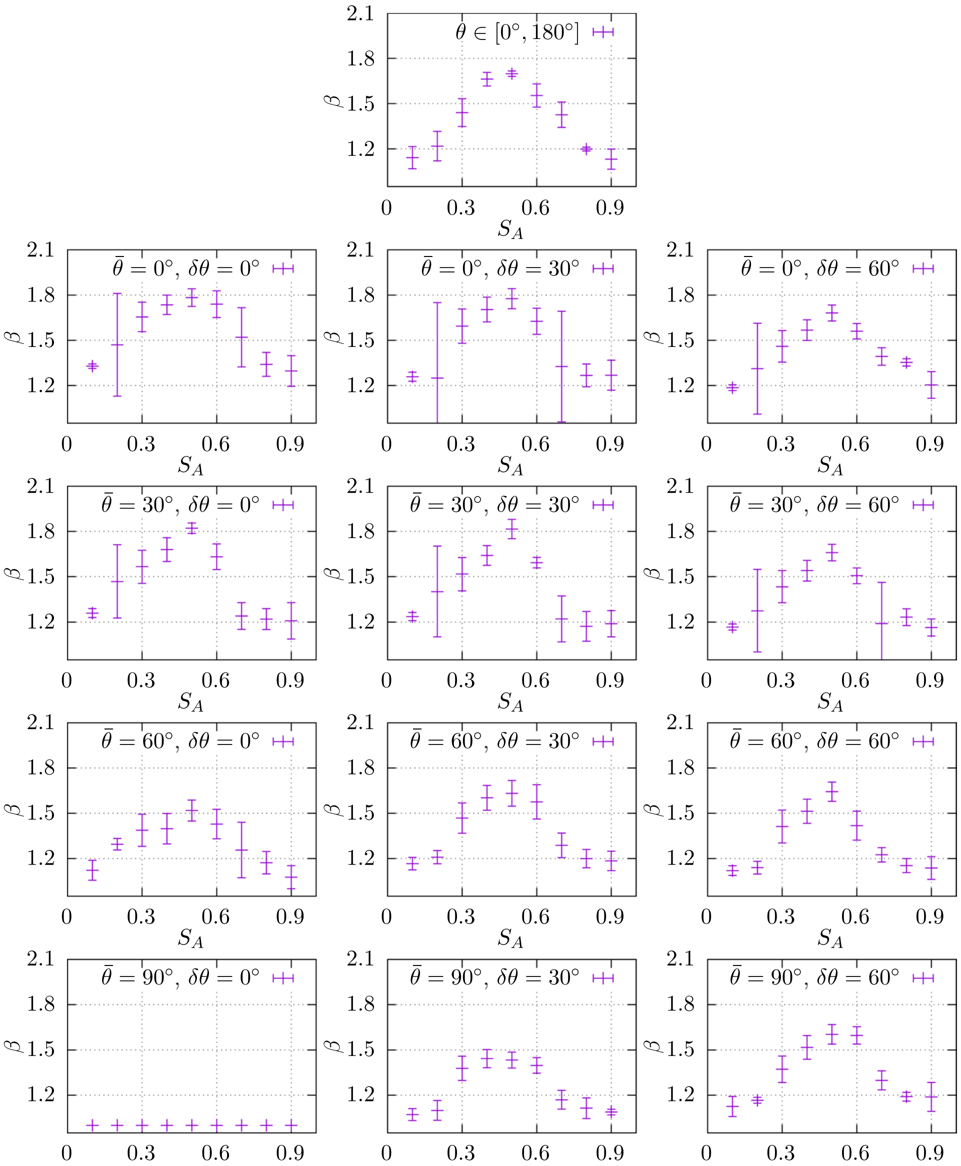

Fig. 7 Dependence of β in the low pressure limit on the saturation of one of the fluids S_A when the distributions of the wetting angles $\rho(\theta)$ is uniform distribution with $\theta \in [0°, 180°]$ (uppermost) and normal distributions with means $\bar{\theta} \in \{0°, 30°, 60°, 90°\}$ and standard deviations $\delta\theta \in \{0°, 30°, 60°\}$

distance between the wetting angles and 90°. This happens with increasing $\delta\theta$ for wetting angles with mean around $\bar{\theta} \approx 90°$, or with decreasing $\delta\theta$ for $\bar{\theta}$ deviating from 90°. Note that a larger $\delta\theta$ means that the wettability is allowed to deviate more from $\bar{\theta}$. This reflects in the values of P_t in Fig. 8 where the peaks of the plots in row 2 and 3 decrease from left to right, while the peaks in row 5 increase from left to right, and the peaks decrease from top to bottom. The same effect also creates the trend of decreasing β as $\bar{\theta} \to 90°$ in Fig. 9a. When links have a wetting angle θ close to 90°, many links will open

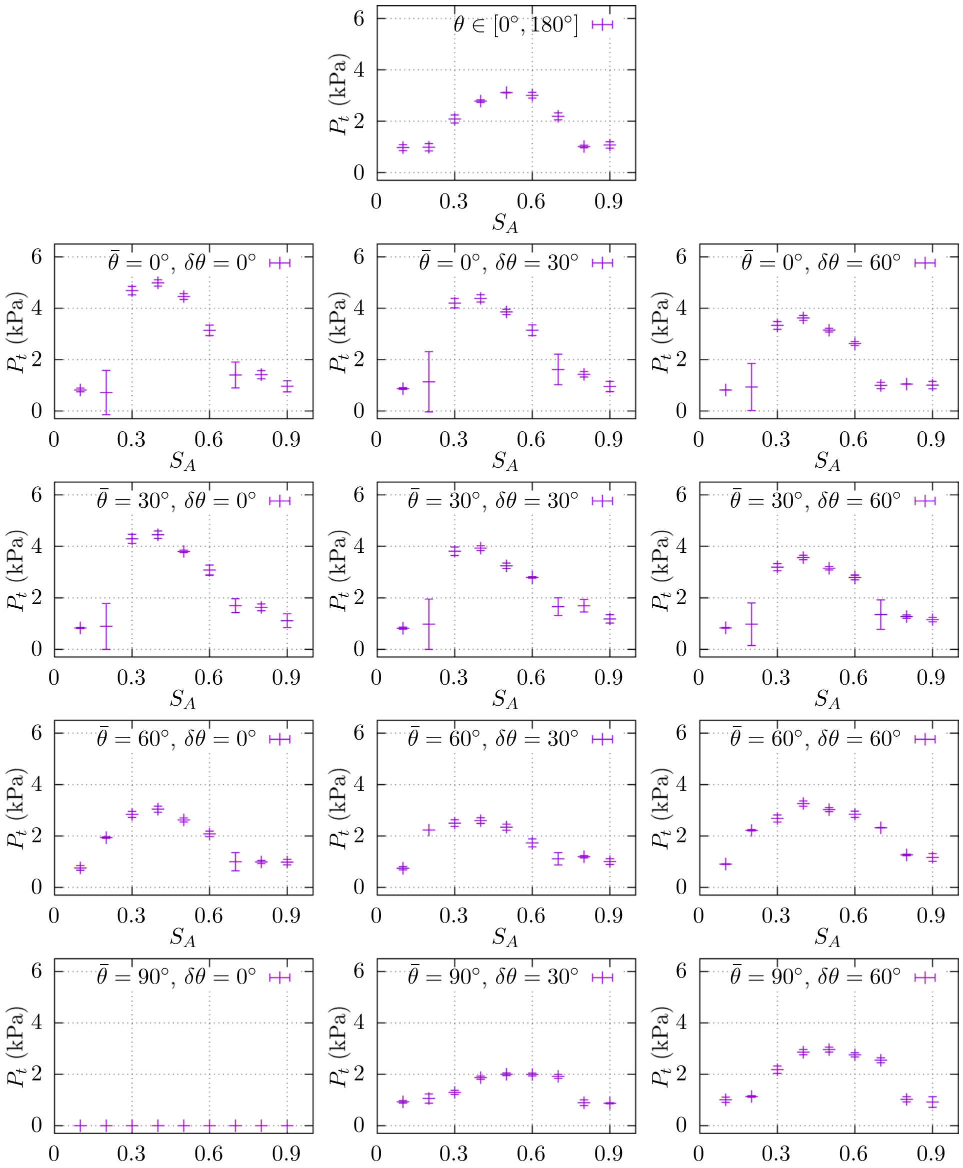

Fig. 8 Dependence of the threshold pressures P_t on the saturation of one of the fluids S_A when the distributions of the wetting angles $\rho(\theta)$ is uniform distribution with $\theta \in [0°, 180°]$ (uppermost) and normal distributions with means $\bar{\theta} \in \{0°, 30°, 60°, 90°\}$ and standard deviations $\delta\theta \in \{0°, 30°, 60°\}$

at very small pressure ΔP, which means increasing ΔP in the typical low pressure limit does not open many new links, hence raises Q with a small β. Figure 9b also supports this phenomena. Figure 9b, in addition, shows the expected result that as $\delta\theta$ increases, β for the various normal distributions approach a value close to that of the uniform distribution with $\theta \in [0°, 180°]$. Instead of having a small range of wetting angles around a $\bar{\theta}$, uniform distribution provides wetting angles anywhere between 0° to 180° with equal probability. Therefore, it makes sense that uniform distribution results in β and P_t values

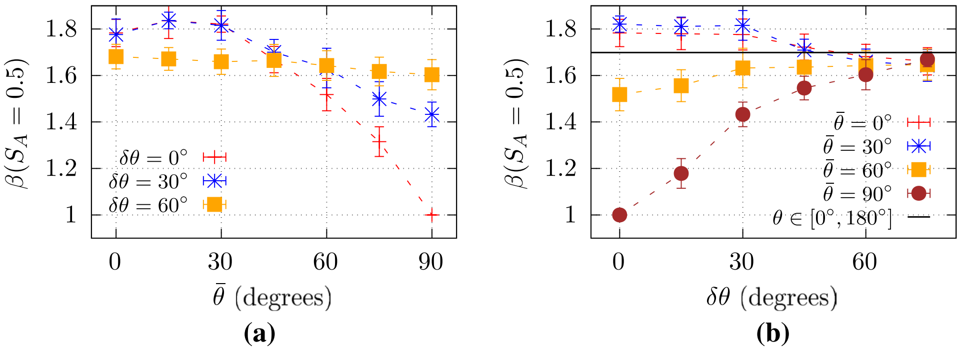

Fig. 9 Values of β at $S_A = 0.5$ as functions of (**a**) the mean $\bar{\theta}$ and (**b**) the standard deviation $\delta\theta$ of the wetting angle distribution. $\theta \in [0°, 180°]$ in (**b**) indicates uniformly distributed wetting angles

most similar to those of normal distributions with largest $\delta\theta$ which have the most variation in the wetting angles.

From the results presented here we see that both P_t and β depend on the wetting angle distribution $\rho(\theta)$. In particular, they are affected not only by the mean wetting angle, but also by the spread of wetting angles. Thus, in order to fully characterize the flow through a porous media, it is in general insufficient to assume a uniform wettability.

4 Conclusion

We studied systematically the effect of mixed wetting conditions on the effective rheology of two-phase flow in porous media by using the capillary fiber bundle (CFB) model and the dynamic pore network (DPN) model. Although the two models are not quantitatively comparable, they are qualitatively similar. Both models show that mixed wettability conditions can have significant influence on the rheology in terms of the dependence of the global volumetric flow rate Q on the global pressure drop ΔP. In the CFB model, the effect of mixed wettability, in other words the shape of the wetting angle distribution, plays the most significant role in the transition regime between low and high ΔP limit where most of the tubes open. In the DPN model, the whole process leading up to opening of all the possible links produces a Q that depends on the wettability of the system. Hence, the studies carried out in this work show that the behavior of immiscible two-phase flow in porous media changes when we move from uniform to mixed wet conditions. The wettability distribution of the porous media is therefore an important factor that should be taken into account when studying the rheology in porous media. Future works may study spatial correlation in the wettability distributions, as well as, the effect of varying viscosities of the fluids, which have not been done in this study.

From the CFB model, we found that the exponent β in $Q \propto \left(|\Delta P| - |P_t|\right)^{\beta}$ is 1, 2 and 3/2 in the high, low and very low effective pressure limits, respectively. The numerical solutions in addition revealed the $\beta > 2$ behavior in the transition region between these extreme limits, which was due to the rapid opening of tubes in that pressure range. In this model, the functional form of the wetting angle distribution $\rho(\theta)$ has the largest effect in the transition region, since this is the region where most tubes become active.

In the DPN model, on the other hand, we found that $\rho(\theta)$ is influential for the behavior at all pressure drops below the Darcy regime. The transition region with $\beta > 2$ flow could not be observed with the DPN model, leading to the speculation that the transition region could have been an artifact of the CFB model. In the low pressure limit, β had values varying anywhere between $\beta \in [1.00 \pm 0.05, 1.82 \pm 0.05]$. Both β in this pressure limit and the threshold pressure P_t showed the tendency to be largest for saturations around 0.5 and decrease steadily with increasing saturation of either one of the fluids. The reason is that when there is comparable amount of both fluids in the system, there will be large number of interfaces in the system giving large interfacial capillary pressure for the link. This works to increase P_t as well as making Q more reactive toward changes in ΔP, which increases β. Finally, we found that β generally increases when the difference in wettability of the two fluids is larger, and when this difference is present for a larger fraction of the porous network. This is because a larger difference in wettability, meaning that the wetting angle is further away from 90°, gives rise to a larger interfacial capillary pressure and the overall threshold pressure. This in turn makes the effect of opening new pathways more prominent.

Author Contributions HF developed the theory, performed the analytical and numerical calculations of the CFB model, contributed to editing of the code of the DPN model, ran the simulations and analyzed the data of the DPN model and wrote the first draft. SS suggested the idea of the problem and developed the code for the DPN model. SR sketched the initial calculation related to the CFB model and helped in data analysis. All the authors contributed in developing the theory and writing the manuscript to its final form.

Funding Open access funding provided by NTNU Norwegian University of Science and Technology (incl St. Olavs Hospital - Trondheim University Hospital). This work was partly supported by the Research Council of Norway through its Center of Excellence funding scheme, project number 262644. SS was partially supported by the National Natural Science Foundation of China under grant number 11750110430.

Declaration

Conflicts of interest The authors declare no conflict of interest.

References

Aker, E., Måløy, K.J., Hansen, A., Batrouni, G.G.: A two-dimensional network simulator for two-phase flow in porous media. Transp. Porous Med. **32**(2), 163–186 (1998). https://doi.org/10.1023/A:1006510106194

Alhammadi, A.M., AlRatrout, A., Singh, K., Bijeljic, B., Blunt, M.J.: In situ characterization of mixed-wettability in a reservoir rock at subsurface conditions. Sci. Rep. **7**(1), 1–9 (2017). https://doi.org/10.1038/s41598-017-10992-w

AlRatrout, A., Blunt, M.J., Bijeljic, B.: Wettability in complex porous materials, the mixed-wet state, and its relationship to surface roughness. Proceedings of the National Academy of Sciences **115**(36), 8901–8906 (2018). https://doi.org/10.1073/pnas.1803734115

Anderson, W.G.: Wettability literature survey-part 1: rock/oil/brine interactions and the effects of core handling on wettability. J. Petrol. Technol. **38**(10), 1125–1144 (1986). https://doi.org/10.2118/13932-PA

Aursjø, O., Erpelding, M., Tallakstad, K.T., Flekkøy, E.G., Hansen, A., Måløy, K.J.: Film flow dominated simultaneous flow of two viscous incompressible fluids through a porous medium. Front. Phys. **2**, 63 (2014). https://doi.org/10.3389/fphy.2014.00063

Blunt, M.J.: Multiphase flow in permeable media: A pore-scale perspective. Cambridge University Press, Cambridge (2017). https://doi.org/10.1017/9781316145098

Elkhyat, A., Agache, P., Zahouani, H., Humbert, P.: A new method to measure in vivo human skin hydrophobia. Int. J. Cosmetic Sci. **23**(6), 347–352 (2001). https://doi.org/10.1046/j.0412-5463.2001.00108.x

Flovik, V., Sinha, S., Hansen, A.: Dynamic wettability alteration in immiscible two-phase flow in porous media: effect on transport properties and critical slowing down. Front. Phys. **3**, 86 (2015). https://doi.org/10.3389/fphy.2015.00086

Frette, O.I., Måløy, K.J., Schmittbuhl, J., Hansen, A.: Immiscible displacement of viscosity-matched fluids in two-dimensional porous media. Phys. Rev. E **55**(3), 2969 (1997). https://doi.org/10.1103/PhysRevE.55.2969

Gao, Y., Lin, Q., Bijeljic, B., Blunt, M.J.: Pore-scale dynamics and the multiphase darcy law. Phys. Rev. Fluids **5**(1), 013801 (2020a). https://doi.org/10.1103/PhysRevFluids.5.013801

Gao, Y., Raeini, A.Q., Selem, A.M., Bondino, I., Blunt, M.J., Bijeljic, B.: Pore-scale imaging with measurement of relative permeability and capillary pressure on the same reservoir sandstone sample under water-wet and mixed-wet conditions. Adv. Water Resour. **146**, 103786 (2020b). https://doi.org/10.1016/j.advwatres.2020.103786

Gjennestad, M.A., Vassvik, M., Kjelstrup, S., Hansen, A.: Stable and efficient time integration of a dynamic pore network model for two-phase flow in porous media. Front. Phys. **6**, 56 (2018). https://doi.org/10.3389/fphy.2018.0005

Knudsen, H.A., Aker, E., Hansen, A.: Bulk flow regimes and fractional flow in 2d porous media by numerical simulations. Transp. Porous Media **47**, 99–121 (2002). https://doi.org/10.1023/A:1015039503551

Kovscek, A., Wong, H., Radke, C.: A pore-level scenario for the development of mixed wettability in oil reservoirs. AIChE J **39**(6), 1072–1085 (1993). https://doi.org/10.1002/aic.690390616

Krevor, S., Blunt, M.J., Benson, S.M., Pentland, C.H., Reynolds, C., Al-Menhali, A., Niu, B.: Capillary trapping for geologic carbon dioxide storage - from pore scale physics to field scale implications. Int. J. Greenhouse Gas Control **40**, 221–237 (2015). https://doi.org/10.1016/j.ijggc.2015.04.006

Lenormand, R., Zarcone, C.: Capillary fingering: percolation and fractal dimension. Transp. Porous Media **4**(6), 599–612 (1989). https://doi.org/10.1007/BF00223630

Li, S., Huang, J., Chen, Z., Chen, G., Lai, Y.: A review on special wettability textiles: theoretical models, fabrication technologies and multifunctional applications. J. Mater. Chem. A **5**(1), 31–55 (2017). https://doi.org/10.1039/c6ta07984a

Løvoll, G., Méheust, Y., Toussaint, R., Schmittbuhl, J., Måløy, K.J.: Growth activity during fingering in a porous hele-shaw cell. Phys. Rev. E **70**(2), 026301 (2004). https://doi.org/10.1103/PhysRevE.70.026301

Måløy, K.J., Feder, J., Jøssang, T.: Viscous fingering fractals in porous media. Phys. Rev. Lett. **55**(24), 2688 (1985). https://doi.org/10.1103/PhysRevLett.55.2688

Marle, C.: Multiphase flow in porous media. Éditions technip (1981)

Méheust, Y., Løvoll, G., Måløy, K.J., Schmittbuhl, J.: Interface scaling in a two-dimensional porous medium under combined viscous, gravity, and capillary effects. Phys. Rev. E **66**(5), 051603 (2002). https://doi.org/10.1103/PhysRevE.66.051603

Rassi, E.M., Codd, S.L., Seymour, J.D.: Nuclear magnetic resonance characterization of the stationary dynamics of partially saturated media during steady-state infiltration flow. New J. Phys. **13**(1), 015007 (2011). https://doi.org/10.1088/1367-2630/13/1/015007

Roy, S., Hansen, A., Sinha, S.: Effective rheology of two-phase flow in a capillary fiber bundle model. Front. Phys. (2019). https://doi.org/10.3389/fphy.2019.00092

Salathiel, R.: Oil recovery by surface film drainage in mixed-wettability rocks. J. Petrol. Technol. **25**(10), 1216–1224 (1973). https://doi.org/10.2118/4104-PA

Scanziani, A., Lin, Q., Alhosani, A., Blunt, M.J., Bijeljic, B.: Dynamics of fluid displacement in mixed-wet porous media. Proceedings of the Royal Society A **476**(2240), 20200040 (2020). https://doi.org/10.1098/rspa.2020.0040

Sinha, S., Hansen, A.: Effective rheology of immiscible two-phase flow in porous media. EPL (Europhys. Lett.) **99**(4), 44004 (2012). https://doi.org/10.1209/0295-5075/99/44004

Sinha, S., Grøva, M., Ødegården, T.B., Skjetne, E., Hansen, A.: Local wettability reversal during steady-state two-phase flow in porous media. Phys. Rev. E **84**(3), 037303 (2011). https://doi.org/10.1103/PhysRevE.84.037303

Sinha, S., Hansen, A., Bedeaux, D., Kjelstrup, S.: Effective rheology of bubbles moving in a capillary tube. Phys. Rev. E **87**(2), 025001 (2013). https://doi.org/10.1103/PhysRevE.87.025001

Sinha, S., Gjennestad, M.A., Vassvik, M., Hansen, A.: Fluid meniscus algorithms for dynamic pore-network modeling of immiscible two-phase flow in porous media. Front. Phys. **8**, 567 (2021). https://doi.org/10.3389/fphy.2020.548497. (**ISSN 2296-424X**)

Tallakstad, K.T., Knudsen, H.A., Ramstad, T., Løvoll, G., Måløy, K.J., Toussaint, R., Flekkøy, E.G.: Steady-state two-phase flow in porous media: statistics and transport properties. Phys. Rev. Lett. **102**(7), 074502 (2009a). https://doi.org/10.1103/PhysRevLett.102.074502

Tallakstad, K.T., Løvoll, G., Knudsen, H.A., Ramstad, T., Flekkøy, E.G., Måløy, K.J.: Steady-state, simultaneous two-phase flow in porous media: an experimental study. Phys. Rev. E **80**(3), 036308 (2009b). https://doi.org/10.1103/PhysRevE.80.036308

Tørå, G., Øren, P.-E., Hansen, A.: A dynamic network model for two-phase flow in porous media. Transp. Porous Media **92**(1), 145–164 (2012). https://doi.org/10.1007/s11242-011-9895-6

Toussaint, R., Løvoll, G., Méheust, Y., Måløy, K.J., Schmittbuhl, J.: Influence of pore-scale disorder on viscous fingering during drainage. EPL (Europhys. Lett.) **71**(4), 583 (2005). https://doi.org/10.1209/epl/i2005-10136-9

Vafai, K.: Porous media: applications in biological systems and biotechnology. CRC Press, USA (2010). https://doi.org/10.1201/9781420065428

Washburn, E.W.: The dynamics of capillary flow. Phys. Rev. **17**(3), 273 (1921). https://doi.org/10.1103/PhysRev.17.273

Zhang, Y., Bijeljic, B., Gao, Y., Lin, Q., Blunt, M.J.: Quantification of nonlinear multiphase flow in porous media. Geophys. Res. Lett. **48**(5), e2020GL090477 (2021). https://doi.org/10.1029/2020GL090477

PAPER II

Reference

Hursanay Fyhn, Santanu Sinha and Alex Hansen,
Effective Rheology of Immiscible Two-Phase Flow in Porous Media Consisting of Random Mixtures of Grains having Two Types of Wetting Properties.
Front. Phys. **11**:1175426 (2023)
DOI: 10.3389/fphy.2023.1175426

CONTRIBUTIONS

HF performed the numerical simulations and the data analysis, and wrote the first draft of the manuscript. HF wrote the code specific for this project based on algorithms written by SS. AH and SS suggested the idea of the problem. AH worked out the relation to percolation theory. All authors contributed to the article and approved the submitted version.

frontiers | Frontiers in Physics

TYPE Original Research
PUBLISHED 27 June 2023
DOI 10.3389/fphy.2023.1175426

OPEN ACCESS

EDITED BY
Matteo Icardi,
University of Nottingham,
United Kingdom

REVIEWED BY
Nuno A. M. Araújo,
University of Lisbon, Portugal
Muhammad Sahimi,
University of Southern California,
United States

*CORRESPONDENCE
Hursanay Fyhn,
✉ hursanay.fyhn@ntnu.no

RECEIVED 27 February 2023
ACCEPTED 13 June 2023
PUBLISHED 27 June 2023

CITATION
Fyhn H, Sinha S and Hansen A (2023), Effective rheology of immiscible two-phase flow in porous media consisting of random mixtures of grains having two types of wetting properties.
Front. Phys. 11:1175426.
doi: 10.3389/fphy.2023.1175426

Effective rheology of immiscible two-phase flow in porous media consisting of random mixtures of grains having two types of wetting properties

Hursanay Fyhn[1]*, Santanu Sinha[2] and Alex Hansen[1]

[1]PoreLab, Department of Physics, Norwegian University of Science and Technology, Trondheim, Norway,
[2]PoreLab, Department of Physics, University of Oslo, Oslo, Norway

We consider the effective rheology of immiscible two-phase flow in porous media consisting of random mixtures of two types of grains having different wetting properties using a dynamic pore network model under steady-state flow conditions. Two immiscible fluids, denoted by "A" and "B", flow through the pores between these two types of grains denoted by "+" and "–". Fluid "A" is fully wetting, and "B" is fully non-wetting with respect to "+" grains, whereas it is the opposite with "–" grains. The direction of the capillary forces in the links between two "+" grains is, therefore, opposite compared to the direction in the links between two "–" grains, whereas the capillary forces in the links between two opposite types of grains average to zero. For a window of grain occupation probability values, a percolating regime appears where there is a high probability of having connected paths with zero capillary forces. Due to these paths, no minimum threshold pressure is required to start a flow in this regime. When varying the pressure drop across the porous medium from low to high in this regime, the relation between the volumetric flow rate in the steady state and the pressure drop goes from being linear to a power law with exponent 2.56, and then to linear again. Outside the percolation regime, there is a threshold pressure necessary to start the flow and no linear regime is observed for low pressure drops. When the pressure drop is high enough for there to be a flow, we find that the flow rate depends on the excess pressure drop to a power law with exponents around 2.2–2.3. At even higher excess pressure drops, the relation becomes linear. We see no change in the exponent for the intermediate regime at the percolation critical points where the zero-capillary force paths disappear. We measure the mobility at the percolation threshold at low pressure drops so that the flow rate *versus* pressure drop is linear. Assuming a power law, the mobility is proportional to the difference between the occupation probability and the critical occupation probability to a power of around 5.7.

KEYWORDS
porous media, rheology, mixed wettability, two-phase flow, percolation

1 Introduction

It was in 1827 that Ohm published his law stating that electrical current is proportional to the voltage drop across a conductor [1], meeting fierce resistance from the physics community in the beginning. Darcy arrived in 1856 at a similar law for single-phase flow in porous media, i.e., the volumetric flow rate is proportional to the pressure drop across the porous medium [2]. Both of these fundamental laws are examples of there being a linear relationship between current and driving force. In the case of the Darcy law, the derivation based on pore scale physics has been a challenge, see e.g., Whitaker's derivation based on momentum transfer [3].

The Darcy law for single-phase flow through a porous sample is given as follows:

$$Q = -\frac{AK}{\mu L}\ \Delta P, \tag{1}$$

where Q is the volumetric flow rate along the axis of the cylindrical sample, ΔP is the pressure drop along it in the flow direction, A is the area of the sample orthogonal to the flow direction, K is the permeability of the sample, μ is the viscosity of the liquid, and L is the system length.

In 1936, the Darcy law (1) was generalized to the simultaneous flow of two immiscible liquids by Wyckoff and Botset by essentially splitting it into two [4].

$$Q_w = -\frac{AKk_{rw}}{\mu_w L}\ \Delta P, \tag{2}$$

$$Q_n = -\frac{AKk_{rn}}{\mu_n L}\ \Delta P, \tag{3}$$

where the subscripts w and n refer to the wetting properties of the two fluids with respect to the matrix; w refers to the more wetting fluid and n to the less wetting fluid. The idea behind this split is simple. The wetting fluid will see a pore space reduced by the presence of the other fluid, leading to a reduction in effective permeability for the wetting fluid. The reduction parameter is the wetting relative permeability k_{rw}. Completely analogously, the non-wetting fluid sees an effective reduction of the permeability by a factor k_{rn}, the non-wetting relative permeability. The split was given physical contents when Wyckoff and Botset assumed that the two relative permeabilities were functions of the wetting saturation S_w alone, the wetting saturation being the pore volume occupied by the wetting fluid divided by the total pore volume and assuming the fluids are incompressible. Barenblatt et al. [5] have later shown that this assumption is valid if there exists a local phase equilibrium between the fluids, a condition that is fulfilled only for slow flows. A further assumption built into Eqs 2, 3 is that there are no macroscopic saturation gradients present.

The total volumetric flow rate is given by the sum of the volumetric flow rates of each fluid as follows

$$Q = Q_w + Q_n, \tag{4}$$

and as a consequence, the generalized Darcy Eqs 2, 3 predict the following expression:

$$Q = -\frac{AK}{L}\left[\frac{k_{rw}}{\mu_w} + \frac{k_{rn}}{\mu_n}\right]\ \Delta P, \tag{5}$$

that is, a total volumetric flow rate being proportional to the pressure drop.

Eqs 2, 3 assume that there are no macroscopic saturation gradients. If this is not the case, the pressure is split into one associated with the non-wetting fluid, P_n, and one associated with the wetting fluid, P_w. Their difference is equal to the capillary pressure function, $P_n - P_w = P_c(S_w)$, which is also assumed to depend only on the S_w. Eqs 2, 3 will then contain terms of the type $\nabla P_c = (dP_c/dS_w)\nabla S_w$, thus setting up the pressure gradient and the saturation gradient as driving forces. When these equations are combined with mass conservation, the result is a closed set of equations that determine how the saturation develops within the porous medium.

When the saturation changes inhomogeneously in the porous medium with time, one implicitly assumes that fluid interfaces move within the porous medium. It was then a surprise when Tallakstad et al. [6, 7] reported a flow rate Q depending on ΔP as follows:

$$Q \propto |\Delta P|^{\beta}, \tag{6}$$

with $\beta \approx 1.85$ for a two-dimensional glass-bead-filled Hele–Shaw cell filled with a water–glycerol mixture and air in the flow regime where the generalized Darcy Eqs 2, 3 are supposed to be valid. This study was followed up by an NMR study of the three-dimensional glass bead packings by Rassi et al. [8] finding an exponent β varying between 2.2 and 3.3. Aursjø et al. [9] using the same model porous medium as Tallakstad et al. [6, 7], but with two incompressible fluids, found $\beta \approx 1.5$ or 1.35, depending on the fractional flow rates. Similar results, in the sense that β is considerably larger than one, have since been observed by a number of groups; see [10–13]. There has also been a considerable effort to understand these results theoretically and reproduce them numerically [6, 7, 14–25].

It should be pointed out that the power law behavior seen in Eq. 6 is different from that described by Wilkinson in 1986 [26]. In his work, Wilkinson used the invasion percolation model to work out the dependence of the relative permeabilities on the capillary pressure, which could be linked to the saturation. He found that the non-wetting relative permeability k_{rn} would depend on the difference between the capillary pressure P_c and a critical capillary pressure P_c^c related to the percolation critical point, which is shown as follows:

$$k_{rn} \sim \left(P_c - P_c^c\right)^t, \tag{7}$$

where t is the percolation conduction exponent [27]. This is, however, a very different problem from that giving rise to Eq. 6. The power law in (7) is a direct reflection of the geometry of the clusters of the non-wetting fluid in the system *after* the invasion process. Hence, it is a *static* problem. The power law in (6) is, as we shall see, the result of a *dynamic* process caused by the motion of the fluid interfaces.

The power law behavior in Eq. 6 is due to a competition between the capillary and the viscous forces. It is straightforward to understand why the flow rate should increase faster than linear when these forces are in competition. When the pressure difference across the porous medium is increased, more interfaces begin to move, leading to a higher effective permeability [28]. The reason why it should be a power law is less obvious. The best argument was perhaps already given by Tallakstad et al. [6, 7] through comparing the pressure drop across fluid clusters with the capillary pressures holding them in place. Capillary fiber bundle models [29, 30] are porous media in the form of bundles of capillary fibers, and they are typically simple enough to be mathematically solvable [16, 19–21, 24, 25]. When the fibers have undulating radii along the long axis, they show non-linear volumetric flow rate vs. pressure drop; they are not quite of the form (6) but rather

$$Q = \begin{cases} 0 & \text{if } |\Delta P| \le P_t, \\ M\,(|\Delta P| - P_t)^{\beta} & \text{if } P_t < |\Delta P| < P_{\max}, \\ M_D\,(|\Delta P| - P_t) & \text{if } P_{\max} \ll |\Delta P|, \end{cases} \tag{8}$$

where P_t is a threshold pressure necessary for the flow to occur, $P_{\max}$ is the maximum threshold pressure found in any capillary fiber, and M and M_D are mobilities. A non-zero threshold pressure is in general necessary in porous media when neither of the two immiscible fluids percolates when dealing with porous media and not just the capillary fiber bundle model [10, 15, 21]. The existence of a non-zero threshold pressure makes the measurement of β much harder than when it is zero as this implies determining two parameters simultaneously, (P_t, β), rather than just one, β.

A central unanswered question is whether the exponent β is universal in the sense that there are classes of systems that all have the same value, i.e., can one define universality classes? Intuitively, this is a very appealing idea as one has a diverging length scale, as in equilibrium critical phenomena as $|\Delta P| \to P_t$ mentioned previously [6, 7]. The experimental measurements of β have so far neither given any indication of the existence of universality classes nor have the computational efforts due to the difficulties in dealing with two unknown parameters, P_t and β. Roy et al. [19] found using a capillary fiber bundle model that $\beta = 2$ if the fiber-to-fiber probability distribution of thresholds includes $P_t = 0$ with a finite probability; otherwise, $\beta = 3/2$. The fibers here had smoothly undulating radii along the flow direction. Lanza et al. [24] who studied a non-Newtonian mixture of immiscible Newtonian and non-Newtonian fluids in a capillary fiber bundle model found a different value of β when the radius distribution is jagged from when it is smooth.

Eq. 8, which was derived for the capillary fiber bundle model, predicts there being a pressure drop $|\Delta P| = P_t$ below which the flow rate Q is zero. This threshold may be zero. Within the capillary fiber bundle model, this means that some capillary tubes belonging to the bundle have interfaces that move as soon as there is a pressure difference across them. There is, however, one important mechanism missing in the capillary fiber bundle models: in the porous medium, the immiscible fluids may be percolating. In other words, there are pathways through the porous medium along which there are no interfaces. In this case, there will be a *linear* regime when the pressure drop is low enough so that the interfaces surrounding the percolating paths do not move. When the pressure drop is increased sufficiently for them to do so, the non-linear power law regime sets in.

Recently, Fyhn et al. [21] studied the exponent β and the threshold pressure P_t in a capillary fiber bundle model and a dynamic pore network model under mixed wet conditions. In the dynamic pore network model, each link was given a wetting angle—in the sense that if there is an interface in the link, this is the angle it will make with the walls of the tube—drawn from a given probability distribution. In the capillary fiber bundle model, each undulating tube is given a wetting angle from a given probability distribution. In both models, a constitutive law of the form (8) was found. The capillary fiber bundle model could be solved analytically, giving the following equation:

$$\beta = \begin{cases} 1 & \text{if } |\Delta P| - P_t \gg P_{\max}, \\ 2 & \text{if } P_t \ll |\Delta P| - P_t \ll P_{\max}, \\ 3/2 & \text{if } 0 < |\Delta P| - P_t \ll P_t. \end{cases} \tag{9}$$

The network model studies showed a less clear picture, with β varying between 1 and 1.8, depending on the saturation and the wetting angle distribution. It was not possible to resolve whether there were regions of fixed β or whether it varied continuously with the parameters of the model. This was due to the non-zero threshold pressure P_t, which needed to be determined together with β.

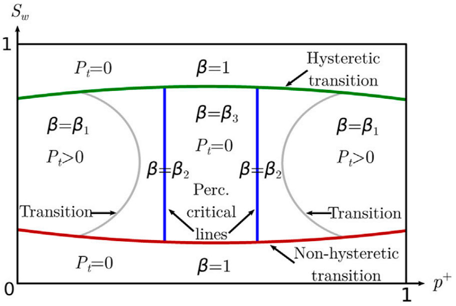

FIGURE 1
Phase diagram showing the exponent β and the threshold pressure P_t plotted against the occupation probability p^+ and the saturation S_w. The diagram is symmetric about the $p^+ = 1/2$ line. The two vertical blue lines are critical lines associated with the two percolation transitions. The lower red line is separating the two-phase flow from the single-phase flow. There is no hysteresis associated with this line. The upper green line also distinguishes between two-phase and single-phase flows. However, in this case, there is hysteresis. The two gray lines represent the transition lines from threshold pressure $P_t = 0$ to a non-zero value. The nature of these lines is unknown.

We study here a model for immiscible two-phase flow in a porous medium made from two types of grains that have different wetting properties with respect to the fluids. The model treats the interfacial tension between the two fluids similarly to a model introduced by Irannezhad et al. [31, 32]. We imagine a packing of two types of grains, say type "+" and type "−." Two immiscible fluids, denoted by "A" and "B," flow through the pores between the grains denoted by "+" or "−". Fluid "A" is fully wetting, and "B" is fully non-wetting with respect to "+" grains, whereas it is the opposite with respect to "−" grains. The direction of the capillary forces in the links between two "+" grains is, therefore, opposite compared to the direction in the links between two "−" grains, whereas *the capillary forces in the links between two opposite types of grains are zero.*

The probability that a grain is of "+" type is p^+. A second parameter is the wetting saturation S_w. There is a rich phase diagram when plotting the threshold pressure P_t as a function of the two control variables p^+ and S_w, which is illustrated in Figure 1. It should be noted, in particular, in this phase diagram that there is a region in the middle where the threshold pressure $P_t = 0$. This region is limited by two p^+ = constant critical lines. Each line signifies a percolation transition [27]. The two curved gray lines signify a possible shift of the two blue transition lines due to the dynamics of the model. There are also two other lines: one green line marked "hysteretic transition" and one red line marked "non-hysteretic" transition. Crossing such a line, one of the two fluids stops moving and we are essentially dealing with a single-phase flow problem. When the wetting fluid stops moving, there is no hysteresis. On the other hand, when the non-wetting fluid stops, there is hysteresis in the sense that

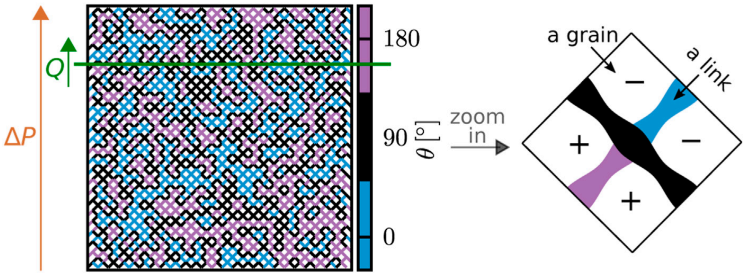

FIGURE 2
Dynamic pore network model implemented on a square lattice consists of links oriented 45° from the overall flow direction. The flow is driven by a global applied pressure ΔP, and the total volumetric flow rate Q is measured over a cross section normal to the direction of the overall flow. The wetting angle θ of each link is based on its adjacent grains. The grains are assigned "+" with an occupation probability p^+, and the rest of the grains are assigned "−". If both of the adjacent grains are assigned "+", $\theta = 180^\circ$ (marked pink). If both of the adjacent grains are assigned "−", $\theta = 0^\circ$ (marked blue). Lastly, if one of the adjacent grains is "+" and the other one is "−", then $\theta = 90^\circ$ (marked black), and hence, there are no capillary forces associated with interfaces in the link.

wetting saturation has to be lowered more to get the non-wetting fluids moving again [33].

In the region where $P_t = 0$, while still having two-phase flow, we observe an exponent $\beta = \beta_3 = 2.56 \pm 0.05$ for saturation $S_w = 0.5$. This value is also seen when setting $p^+ = p_c$ or $p^+ = 1 - p_c$, where $p_c \approx 0.5927$ is the site percolation threshold for square lattices, i.e., $\beta = \beta_2 = \beta_3$. For p^+ much lower than $1 - p_c$ or p^+ much higher than p_c, still for saturation $S_w = 0.5$, we see $\beta = \beta_1 = 2.25 \pm 0.1$. The large uncertainty in β seen here stems from $P_t > 0$.

It is surprising that $\beta_2 = \beta_3$ within the precision we are able to obtain. The exponent β_2 is obtained at the percolation threshold where the paths where fluid surfaces meet no resistance are fractal with fractal dimension 4/3 as they are the external perimeters of percolation clusters [34]. The reason for not seeing the critical behavior reflected in β comes from there also being other links that have no interfacial tension in them as they contain no interfaces, thus driving the system away from criticality. In order to investigate whether there are any traces at all in the transport properties of the percolation critical point, we have studied the mobility M at low pressure drops as p^+ approaches a critical value, where we expect it to vanish with an exponent t' of the same type as the conductivity exponent t in ordinary percolation in the vicinity of the critical p^+ [27, 35]. We find that $t' \approx 5.7$, indicating that the system is *not* critical and M falls off faster than algebraic. We, therefore, expect there to be two extra transition lines (marked in gray in Figure 1) that distinguish between $P_t = 0$ and $P_t > 0$. The nature of these lines is unknown.

We use a dynamic pore network model [36–40] for this study. It has been used earlier in the context of modeling-mixed wetting porous media; see [21, 41, 42]. We describe the model in Section 2 including our use of the wetting model similar to that introduced by Irannezhad et al. [31, 32]. Section 3 explains how we identify the paths through the network that have no capillary forces associated with them and relate them to a site percolation problem. Section 4 presents the analysis of the low pressure drop mobility at the percolation critical points. Section 5 constitutes our investigation of the volumetric flow rate Q vs. pressure drop ΔP. We fix the saturation $S_w = 0.5$ and scan through this line in the phase diagram in Figure 1 for different values of p^+. We also tested whether there would be hysteresis with respect to increasing or decreasing the pressure drop, finding none. Section 6 contains a summary and our conclusions.

2 Dynamic pore network model

A sketch of the dynamic pore network (DPN) model used in this work is given in Figure 2, showing a square two-dimensional network with links with the same length tilted 45° from the flow direction. ΔP across the network drives the flow leading to Q, which is measured over a cross section of the system normal to the direction of the overall flow. The zoomed-in sketch to the right in Figure 2 illustrates the rules for using the wetting properties of the grains to assign wetting angles θ to the links, where θ is consistently defined through one of the fluids. In contrast to earlier models [21, 41, 42] that assign the wetting angles to the pores or links directly, the physical basis for this model is a mixture of grains and the wettability of the pore space in-between depends on the wettability of the surrounding grains, similar to the system introduced by Irannezhad et al. [31, 32]. We assume two types of grains, they being either fully non-wetting with $\theta = 180^\circ$ or fully wetting with $\theta = 0^\circ$. Having fully non-wetting or fully wetting grains maximizes the difference between the two types of grains in terms of their wettability and, hence, maximizes any impact on the rheology that comes as a result of this difference. The grains are denoted fully non-wetting and assigned a notation "+" with an occupation probability p^+, and the rest of the grains are then fully wetting with a notation "−". For each link, θ is determined based on the link's adjacent grains. Each grain in the network is connected to four links, which means each link has two adjacent grains, as shown in Figure 2. If both of the adjacent grains are assigned "+", the link will have $\theta = 180^\circ$. If both of the adjacent grains are assigned "−", then $\theta = 0^\circ$. Lastly, if one of the adjacent grains is "+" and the other one is "−", the link in the middle should be easy to pass through for both fluids, and the wettability should be neutral with $\theta = 90^\circ$.

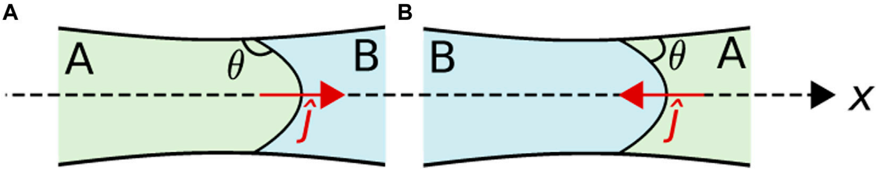

FIGURE 3
Wetting angle θ is consistently measured through fluid A in both examples **(A,B)**, regardless of the wettability situation. The unit vector $\hat{J}$ lies along the center axis $\boldsymbol{x}$ and points in the direction out of the fluid within which θ is measured, which, in this case, is from fluid A to fluid B.

The networks have periodic boundary conditions in both directions. Two fluids that flow through the network are immiscible, and their movement is traced through the position of their interfaces at each instant in time. Whenever the fluids flowing in a link reach the crossing point with the three other links, namely, a node, the fluids get distributed into the neighboring links in the same time step instead of being retained in the node itself [36].

The volumetric flow in each link with length l, pointing along the link's center axis $\boldsymbol{x}$, is given by the following equation:

$$q = -\frac{\pi \bar{r}^4}{8\mu l}\left(\Delta p - \hat{x}\cdot\left(\sum_k p_t(x_k)\hat{J}_k\right)\right), \qquad (10)$$

where it has been assumed that the radius does not deviate too much from its average value $\bar{r}$ [36]. Here, $\mu = s_A\mu_A + s_B\mu_B$ is the saturation weighted viscosity of the fluids, where s_A and s_B are saturations of the two fluids A and B, respectively, with viscosities μ_A and μ_B in the links (in contrast to S_w, which is the average saturation over the whole network). Figure 3 can be used to further explain the variables in Eq. 10. The unit vector $\hat{J}$ lies along the $\boldsymbol{x}$-axis and points in the direction *out of* the fluid within which θ is defined. In Figure 3, θ is consistently measured through fluid A in both examples (a) and (b), regardless of if fluid A is more or less wetting with respect to the solid. Hence, $\hat{J}$ also consistently points across the interface starting from fluid A toward fluid B. The sum in Eq. 10 is taken over the interfaces numbered k with varying $\hat{J}_k$ with positions $x_k \in [0, l]$ along $\boldsymbol{x}$. The dot product of this sum with the unit vector $\hat{x}$ in the positive $\boldsymbol{x}$ direction is taken afterward to obtain the total capillary pressure. The capillary pressure across one interface at position x which has an angle θ with the solid through fluid A is modeled by using the Young–Laplace equation [43],

$$p_t(x) = \frac{2\sigma\cos\theta}{r(x)}, \qquad (11)$$

where σ is the surface tension and

$$r(x) = \frac{r_0}{1 - a\cos\left(\frac{2\pi x}{l}\right)} \qquad (12)$$

is the radius where a is the amplitude of the periodic variation, and r_0/a is randomly chosen from the interval $[0.1l, 0.4l]$. This way, p_t varies with both the position along a link and from link to link.

For all simulations in the following, the two immiscible fluids have been given surface tension $3.0 \cdot 10^{-5}$ N/mm and viscosity 0.1 Pa·s for both. The overall network saturation is kept constant at 0.5, meaning there are equal amounts of the two fluids. The links in the network have length $l = 1$ mm. In all the figures, the logarithms are in base 10.

3 Easy links and connected paths

There are three types of links in the model: those that are of the "++" type, those that are of the "−−" type, and the "+−" = "− +" type. We will, in the following, refer to the latter type as "easy links" since they offer no capillary resistance to interfaces that happen to be in them. Paths of connected easy links may percolate, i.e., stretch across the network forming loops as we are implementing bi-periodic boundary conditions. We will refer to such percolating paths of easy links as "connected paths"; see Figure 4.

The geometry of the easy links and connected paths may be mapped onto an ordinary site percolation problem [27]. The links altogether form a square lattice. The nodes of the *dual* lattice form another square lattice [44] and are assigned "+" or "−". These values are placed at random. The distribution of neighboring "+" sites in this dual lattice forms an ordinary site percolation problem. In an infinitely large lattice, there will be a percolating "+" cluster when $p^+ \geq p_c$, where p_c is the site percolation threshold 0.5927. . .. If we, on the other hand, focus on the "−" sites, there will be a cluster of such sites that percolate if $p^- = 1 - p^+ \geq p_c$ or $p^+ \leq 1 - p_c \approx 0.4073\ldots$ [45]. Hence, if $0 \leq p^+ \leq 1 - p_c$, the "−" clusters percolate, if $1 - p_c \leq p^+ \leq p_c$, neither the "−" sites nor the "+" sites percolate, and if $p_c \leq p^+$, the "+" sites percolate. We show in Figure 5 a map of the wetting angles associated with different values of p^+. The easy links are shown in black.

We note that if neither the "+" sites nor the "−" sites percolate ($1 - p_c \leq p^+ \leq p_c$), there must be connected paths. We, furthermore, note that if either of the two site types percolates, there cannot be any connected paths. At the two thresholds, $p^+ = 1 - p_c$ and $p^+ = p_c$, the connected paths appear together with the appearance of a percolating cluster of either "−" or "+" type as the perimeter of the incipient percolating cluster is a connected path. At the percolation thresholds, we know that the fractal dimension of the perimeter, and hence the corresponding connected path, is 4/3 [34]. For values away from the critical points, the connected paths are not fractal. Hence, the structure of the easy link clusters and the connected path is very different away from the critical points while still being in the interval $1 - p_c \leq p^+ \leq p_c$.

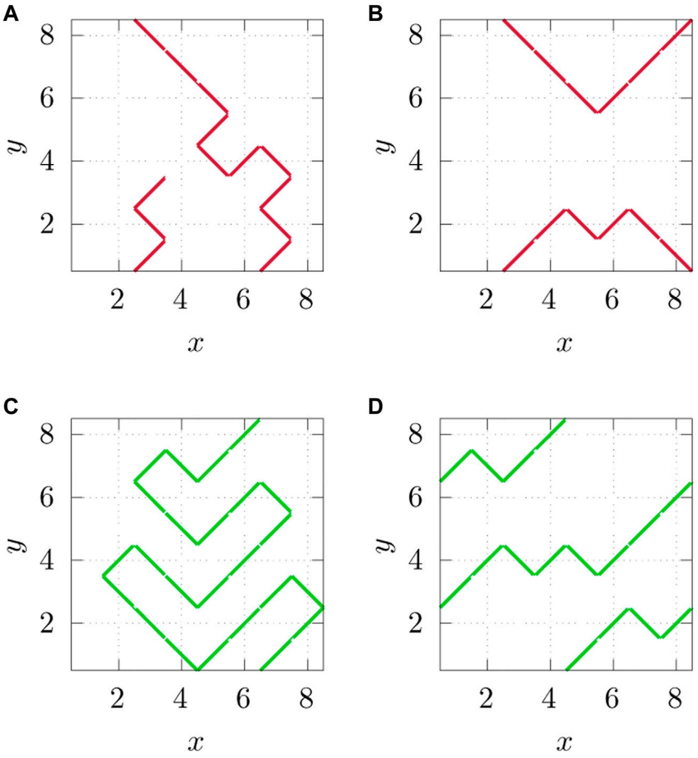

FIGURE 4
Due to periodic boundary conditions in both directions parallel and orthogonal to Q, it is not enough for a path to connect the bottom to the top of the network in the direction of Q to qualify as a connected path; it also has to loop back to itself. We show here four examples of clusters of easy links in an 8 × 8 lattice. Figures **(A,B)** do not qualify as connected paths, as defined for the networks in this work, while **(C,D)** do. The cluster of easy links in **(A)** connects the top and the bottom of the network but needs one additional link centered at $(x, y) = (4, 4)$ to form a connected path. The cluster of easy links in **(B)** forms a closed loop but does not cross the network fully in the flow direction, which is along the y-axis. In **(C)**, the link centered at position $(x, y) = (1, 7)$ meets the link centered at $(x, y) = (6, 8)$ due to the periodic boundary condition in the y-direction and completes the loop, hence making the path a connected path. The effect of having a periodic boundary condition in the x-direction is apparent in **(D)**, where the link centered at $(x, y) = (8, 2)$ connects to the link at $(x, y) = (1, 3)$, and similarly, $(x, y) = (8, 6)$ connects to $(x, y) = (1, 7)$ and $(x, y) = (4, 8)$ connects to $(x, y) = (5, 1)$, thus completing the loop.

The probability of finding a connected path as a function of p^+ is investigated by testing 1,000 randomly generated networks with size $L \times L$ for each $p^+ \in \{0.3000, 0.3001, 0.3002, \ldots, 0.7000\}$. The results are shown in Figure 6 for $L = 50$ links and $L = 100$ links. We see that the two curves cross very close to $1 - p_c$ and p_c.

4 Mobility

As we will show with the results presented in the following section, the constitutive law between the volumetric flow rate Q and the pressure drop $|\Delta P|$ can be written as follows:

$$Q = \begin{cases} M|\Delta P| & \text{if } |\Delta P| < P_l, \\ M_m|\Delta P|^{\beta_3} & \text{if } P_l < |\Delta P| < P_u, \\ M_D|\Delta P| & \text{if } P_u < |\Delta P|, \end{cases} \tag{13}$$

in the region $1 - p_c \le p^+ \le p_c$. Here, P_l and P_u are two crossover pressures. There are three regimes: 1) a linear regime for low pressure drops, 2) a non-linear regime for intermediate pressure drops, and 3) a linear regime for high pressure drops. Each regime is characterized by a mobility, $M(p^+, S_w)$, $M_m(p^+, S_w)$, and $M_D(p^+, S_w)$, respectively.

If we move to values of p^+ where $P_t > 0$, regime (1) disappears. Hence, we have that $M(p^+, S_w)$ tends to zero as p^+ reaches the boundary between the $P_t = 0$ region and the $P_t > 0$ region. We hypothesize, in the following, that the boundaries of this region are given by the percolation thresholds $1 - p_c$ and p_c.

Expecting that $M(p^+, S_w)$ shows similar behavior to the conductivity in percolation [35], we make the assumption that the mobility vanishes as

$$M \sim \begin{cases} (p^+ - (1 - p_c))^{t'} & \text{for } p^+ \to (1 - p_c)^+, \\ (p_c - p^+)^{t'} & \text{for } p^+ \to (p_c)^-, \end{cases} \tag{14}$$

where t' is a transport exponent of the same type as the conductivity exponent t in ordinary percolation, which is 1.303(8) according to [46]. In Eq. 14, $p^+ \to (1 - p_c)^+$ means p^+ approaches $1 - p_c$ from

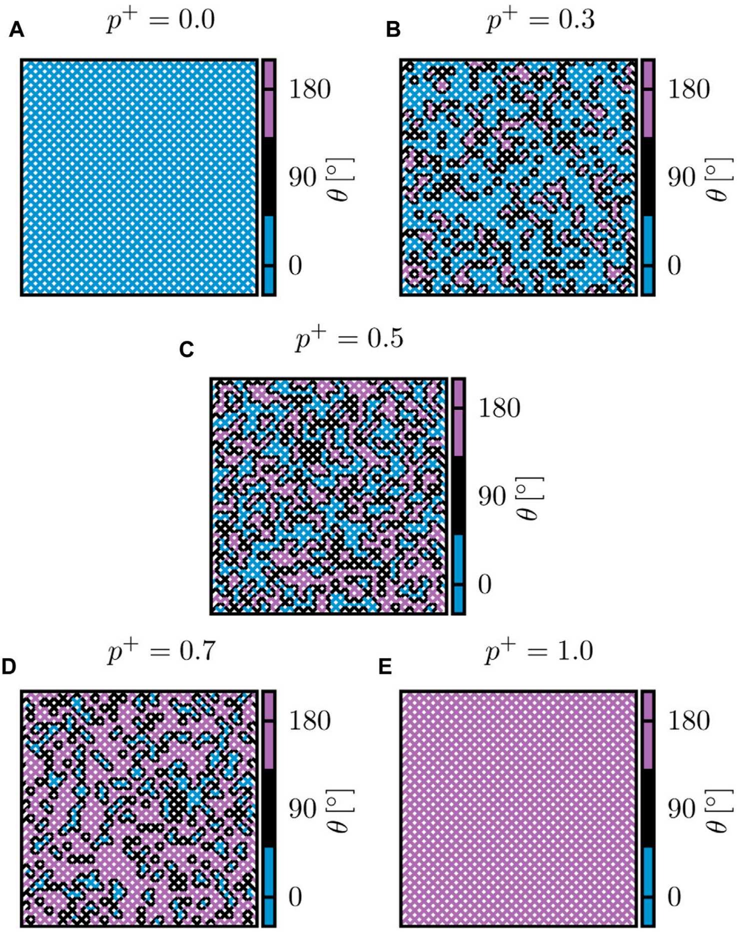

FIGURE 5
At $p^+ = 0$, shown in **(A)**, all the grains are fully wetting grains that are noted as "−" in Figure 2. This means that the pore space between these grains, namely, the links in DPN, all have $\theta = 0^\circ$. Oppositely at $p^+ = 1.0$, shown in **(E)**, there are only links that have $\theta = 180^\circ$. In these two extreme cases, there is no easy link in the network with neutral wettability $\theta = 90^\circ$. Moving away from these extremes, when $p^+ = 0.3$ in **(B)** or when $p^+ = 0.7$ in **(D)**, links with $\theta = 90^\circ$ are present but not enough to create a connected path that crosses the entire system. At the middle point of $p^+ = 0.5$ **(C)**, DPN has half of each type of grain, creating the highest possible probability for having connected paths with only $\theta = 90^\circ$ links. In these examples, $p^+ = 0.5$ **(C)** is the only one that lies within the limit $1 - p_c < p^+ < p_c$, and it is only here we find connected paths.

above and $p^+ \to (p_c)^-$ means p^+ approaches p_c from below. By using finite size scaling analysis, we obtain the following equation:

$$M \sim L^{-t'/\nu}, \tag{15}$$

where ν is the correlation length exponent in percolation, which is known to be 4/3 [47].

To investigate the relation given in Eq. 15, we set $p^+ = 0.5927 \approx p_c$ and network-dimensions $L \times L$ for L between 50 and 90 links. The lowest numerically feasible $|\Delta P|$ is used in order to stay in the lower linear regime in Eq. 13, specifically 2.8 Pa/link $\lessapprox |\Delta P|/L \lessapprox$ 5.8 Pa/link. When operating at low $|\Delta P|$, the flow, which is mainly through the connected paths, stabilizes quickly and retains approximately a constant value compared to the fluctuating flow at higher $|\Delta P|$. For these simulations, the flow is driven for approximately 40 pore volumes of fluid through the network, where one pore volume is equal to the total volume of the pore space in the network. The values of Q are calculated by averaging over the last 20 pore volumes simulated. Variation in the connected paths a network can have is covered by averaging the results over 50 network realizations. The results are shown in Figure 7, where we get $t'/\nu = 4.3 \pm 1.0$, giving the following equation:

$$t' = 5.7 \pm 1.3. \tag{16}$$

This is a huge value. A possible explanation for the observed value is that the system is *not* at a critical point in spite of the

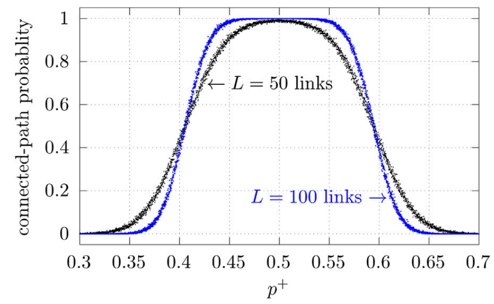

FIGURE 6
Probability for having connected paths in systems with non-wetting grain probability p^+ and size $L \times L$, where L is either 50 or 100 links.

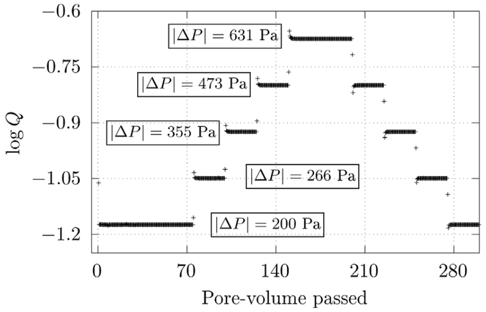

FIGURE 8
Increasing global pressure difference $|\Delta P|$ with the injected pore volumes raises the volumetric flow rate Q, and subsequently decreasing $|\Delta P|$ returns Q to the original value. Q was measured in units mm^3/s.

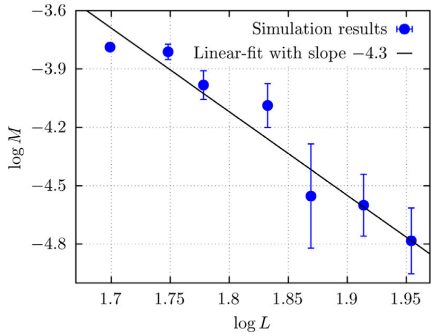

FIGURE 7
Mobility M in networks with size $L \times L$. The slope of the linear fit is $-t'/\nu = -4.3 \pm 1.0$. The saturation was set to $S_w = 0.5$ in this calculation.

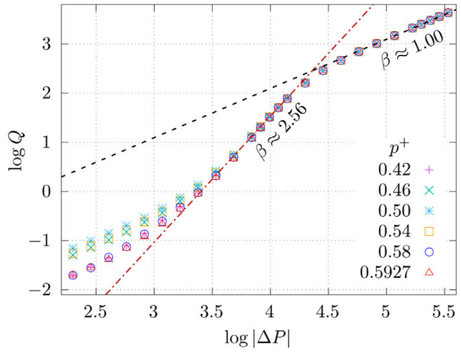

FIGURE 9
Total volumetric flow rate Q as a function of global pressure difference $|\Delta P|$ in systems with different non-wetting grain occupation probabilities p^+. The results of linear fit with slopes β are included in the plot, where β is the exponent in $Q \propto |\Delta P|^\beta$. Q was measured in units mm^3/s, and $|\Delta P|$ was measured in units Pa. This figure is the basis for Eq. 13.

geometry of the easy links and the connected paths indicating this. In our argumentation, we have not taken into account the *empty* links, i.e., those links that do not contain any interfaces. They will be indistinguishable from the easy links with respect to the dynamics. These empty links drive the system away from the percolation critical point, and Figure 7 is in reality, indicative of non-algebraic behavior. We have indicated this possible shift in transition in the phase diagram shown in Figure 1.

5 Non-Darcy behavior

In the simulations performed for this section, networks have dimensions 100 × 100 links^2. For each $|\Delta P|$, the flow is driven for approximately 100 pore volumes of fluid through the network. This ensures the steady-state flow, and the value of Q in the steady state is calculated by averaging over the total flow rate during approximately the last 25 pore volumes simulated.

5.1 Hysteresis

We pose, here, the question of whether there are any hysteretic effects from raising and lowering the pressure drop $|\Delta P|$ on the volumetric flow rate Q. The result is shown in Figure 8. With the passing of time, measuring in terms of injected pore volumes, $|\Delta P|$ applied across a network is raised and then lowered in steps. The $|\Delta P|$ values used, 200 Pa, 266 Pa, 355 Pa, 473 Pa, and 631 Pa, are from the lowest numerically feasible range. It can be observed from Figure 8 that whenever

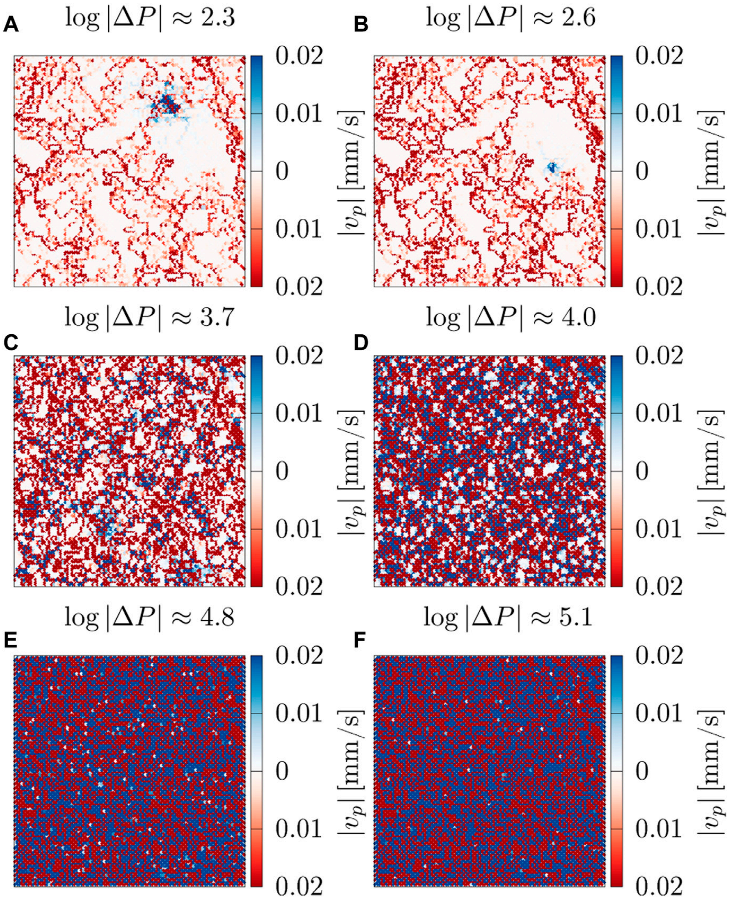

FIGURE 10
Maps of steady-state averaged absolute velocities $|v_p|$ at different global pressure differences $|\Delta P|$, where velocities through links with the wetting angle $\theta = 90^\circ$ have shades of red and those through links with $\theta \in \{0^\circ, 180^\circ\}$ have shades of blue. The network had non-wetting grain occupation probability $p^+ = 0.5$. $|\Delta P|$ was measured in units Pa.

$|\Delta P|$ is returned to the same value, Q also quickly stabilizes back to the previous value it had with the same $|\Delta P|$. This shows that the steady-state results generated using the DPN model do not depend on long-term memory [48].

5.2 Volumetric flow rate dependence on pressure drop

The results relating Q and $|\Delta P|$ in systems with zero P_t and different values of p^+ are shown in Figure 9. We used $p^+ \in \{0.42, 0.46, 0.50, 0.54, 0.58, \text{and } 0.5927\}$ for the simulations. For each of these p^+ values, the results were averaged over 10 randomly chosen networks that have connected paths, meaning 10 networks were randomly chosen from a subset of networks with zero threshold pressure P_t. To assist the understanding of Figure 9, velocity maps of a network with $p^+ = 0.5$ at various $|\Delta P|$ have been plotted in Figure 10. The velocity maps show the steady-state averaged absolute velocities; in other words, they show the average speed of the fluid. The velocities are color coded so that those through neutral links with $\theta = 90^\circ$ are in shades of red, and the rest that are through links with $\theta \in \{0^\circ, 180^\circ\}$ are in shades of blue. The results in Figures 9, 10 show three regimes in terms of β, as indicated in Eq. 13.

The lowest regime in Eq. 13 seems to correspond to $\log|\Delta P| \lessapprox 2.8$ in Figure 9; in other words, $|\Delta P|/L \lessapprox 6.3$ Pa/link. The transition from this regime to the next is more gradual for p^+ away from 0.5 in Figure 9. In this regime with very low $|\Delta P|$, we find $\beta = 1.00 \pm 0.01$. The velocity maps of a network with $p^+ = 0.5$ at two different $|\Delta P|$ in this regime are shown in Figures 10A,B, and they indicate that the flow is mainly through the neutrally wet (red) links. When increasing $\log|\Delta P|$ from Figure 10A to Figure 10B, the impact mainly manifests in the increase of the speed of the

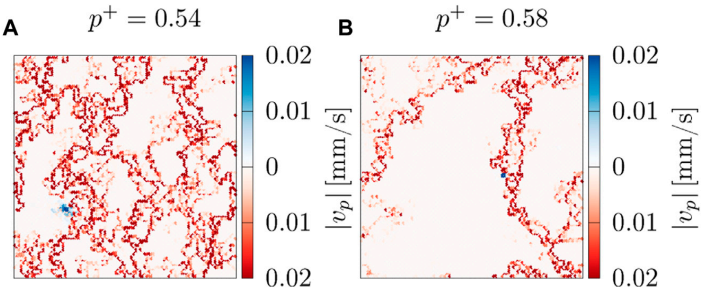

FIGURE 11
Maps of steady-state averaged absolute velocities $|v_p|$ at log $|\Delta P| \approx 2.3$, where $|\Delta P|$ is the global pressure difference. The velocities through links with the wetting angle $\theta = 90^\circ$ have shades of red, and those through links with $\theta \in \{0^\circ, 180^\circ\}$ have shades of blue. p^+ is the non-wetting grain occupation probability.

fluids rather than the creation of new paths. Therefore, it makes sense that the flow remains Darcy-like with β approximately equal to 1. In the lowest regime in Figure 9, it is apparent that the mobility M in Eq. 13 decreases when p^+ moves away from 0.5 toward $p_c \approx 0.5927$ and $1 - p_c \approx 0.4073$. In this regime, the flow is mainly through the connected paths. The network has more connected-path links and transports more fluid for the same $|\Delta P|$ value, hence resulting in a larger Q value, meaning a larger M value when p^+ moves toward 0.5. For instance, at log $|\Delta P| \approx 2.3$, the number of active connected-path links is high at $p^+ = 0.5$, as can be seen in Figure 10A, slightly lower at $p^+ = 0.54$, as can be seen in Figure 11A, and significantly lower at $p^+ = 0.58$, as can be seen in Figure 11B, making Q at $p^+ = 0.58$ significantly less than in the other two cases.

The middle regime in Eq. 13 seems to correspond to $3.3 \lessapprox$ log $|\Delta P| \lessapprox 4.1$ in Figure 9; in other words, 20.0 Pa/Link $\lessapprox |\Delta P|/L \lessapprox 125.9$ Pa/link. Here, the exponent in Eq. 13 is $\beta = \beta_3 = 2.56 \pm 0.05$, and M_m is the same for all p^+ values examined. When log $|\Delta P|$ increases from Figure 10C to Figure 10D in this regime, the velocity maps show that there is a significant increase in the number of flow carrying links, meaning Q also increases significantly. The opening of new paths in addition to the increased flow in the already active paths explains β being large. At this level of $|\Delta P|$, M_m and β being the same for all p^+ examined makes sense as the connected paths that differentiate networks with different p^+ no longer are the main contributors to the flow.

The highest regime in Eq. 13 seems to correspond to log $|\Delta P| \gtrapprox 4.5$ in Figure 9; in other words, $|\Delta P|/L \gtrapprox 316.2$ Pa/link. Here, the exponent in Eq. 13 is $\beta = 1.00 \pm 0.01$, and M_D is the same for all p^+ examined. The velocity maps taken from two different points in this regime are shown in Figures 10E,F. In both cases, almost all the links in the network are carrying flow, regardless of their wettability; hence, increasing $|\Delta P|$ does not create new paths. The effect of capillary barriers in the links becomes insignificant in comparison to the enormous pressure drop across the links, making all p^+ produce the same Q at the same $|\Delta P|$. Increasing $|\Delta P|$ in this regime increases Q linearly, which is indicative of Darcy flow.

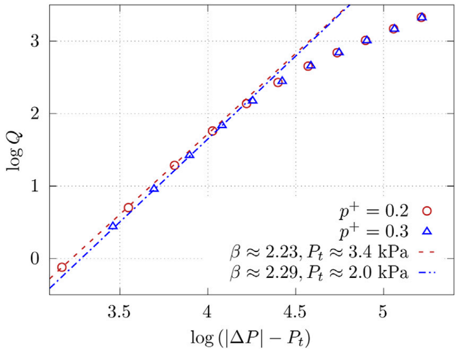

FIGURE 12
Total volumetric flow rate Q as a function of effective pressure in systems with different non-wetting grain occupation probabilities p^+. The effective pressure is the difference between the global pressure difference $|\Delta P|$ and the threshold pressure P_t. The results of linear fit with slopes β are included in the plot, where β is the exponent in $Q \propto (|\Delta P| - P_t)^\beta$. Q and $|\Delta P|$ were measured in the units of mm^3/s and Pa, respectively.

As the results in Section 3 show, there are very few to zero connected paths outside of the range $1 - p_c \leq p^+ \leq p_c$ examined in Figure 9. If p^+ was very close to the range examined in Figure 9, the behavior of β and M would have been expected to be the same as in Figure 9 since the flow will similarly be carried by the connected paths. To test p^+ further away, simulations have been performed with $p^+ = 0.2$ and 0.3, and the results are shown in Figure 12. Here, P_t is not zero, unlike the systems used for Figure 9 and corresponding constitutive Eq. 13. In this case, we find a constitutive equation

$$Q = \begin{cases} 0 & \text{if } |\Delta P| \leq P_t, \\ M_m(|\Delta P| - P_t)^\beta & \text{if } P_t < |\Delta P| < P_u, \\ M_D(|\Delta P| - P_t) & \text{if } |\Delta P| < P_u, \end{cases} \tag{17}$$

where P_u is the crossover pressure between non-linear and Darcy behavior. By varying P_t from 0.00 Pa to the lowest $|\Delta P|$ in the datasets with an increment of 0.01 Pa, mathematical linear fits with slopes β were calculated at the lowest pressures to find the candidate that gave the least root-mean-square error. This gave $\beta = 2.23 \pm 0.05$ and $P_t = (3.4 \pm 0.5)$ kPa for $p^+ = 0.2$, and $\beta =$

2.29 ± 0.05 and $P_t = (2.0 \pm 0.5)$ kPa for $p^+ = 0.3$. The regime these β correspond to is the middle regime discussed in Figure 9, where the behavior was also non-linear due to the capillary barriers created by the interfaces between the two fluids. Fyhn *et al.* [21] have observed $\beta > 1$ behavior even in networks with the same wetting angle everywhere, which would be the same as having $p^+ \to 0.0$ or 1.0 here. Due to the lack of connected paths in systems with $p^+ = 0.2$ and 0.3, the lowest regime in Figure 9 does not appear for the results in Figure 12. Lastly, the highest regime where $\beta \approx 1$ should occur for all where the flow pushes through almost the entire network and there is almost no influence of p^+. This is indeed what we see in Figure 12 as well.

6 Conclusion

We studied the effect of having porous media consisting of randomly mixed dual-wettability grains on the immiscible two-phase flow using a dynamic pore network model. The model treats the interfacial tension between the two fluids similarly to a model introduced by Irannezhad et al. [31, 32]. The model has two parameters, the saturation S_w and the probability p^+ to have a grain of "+" type. The model, which is explained in Figure 2, contains links (pores) of three types when filled with two immiscible fluids A and B: links that are wetting with respect to fluid type A, links that are wetting with respect to fluid type B, and *easy links* where there are no capillary forces associated with interfaces. The parameter p^+ controls the number of links generating capillary forces and easy links. The model has a rich phase diagram, sketched in Figure 1. There is a region $1 - p_c \le p^+ \le p_c$, where p_c is the site percolation threshold, where the easy links form connected paths across the network. Outside this region, i.e., for $p^+ \ll 1 - p_c$ or $p^+ \gg p_c$, easy links do not percolate. We find two classes of constitutive equations for the volumetric flow rate Q vs. pressure drop $|\Delta P|$. For $1 - p_c \le p^+ \le p_c$, we observed the constitutive Eq. 13—see Figure 9—whereas for $p^+ \ll 1 - p_c$ or $p^+ \gg p_c$, we observed a constitutive Equation 17; see Figure 12. The crucial point that distinguishes these is whether there is a non-zero threshold pressure P_t.

When $1 - p_c \le p^+ \le p_c$, we observed the following: at the regimes with the lowest and highest $|\Delta P|$, it seems that $\beta = 1.00 \pm 0.01$ because there is no significant change in the paths fluids are flowing through, and increasing $|\Delta P|$ only increases the flow in the already active paths. At the lowest $|\Delta P|$, the flow is mainly through connected paths with zero resistance. When $p^+ \to 0.5$ in this regime, there are more connected paths, which means more fluid gets transported, making Q hence M higher. At the highest $|\Delta P|$, almost the entire network is always active. On the other hand, $\beta > 1$ in the middle regime where an increase in $|\Delta P|$ increases the flow in the active paths and, in addition, opens new conducting paths. In the middle and the highest regimes, the flow is no longer mainly through the connected paths, and the differences between the pressures across the links and the capillary barriers in the links are large. With the diminished role of the connected paths and capillary barriers at higher pressure drops, M_m and M_D do not depend strongly on p^+. The exponent in the middle regime was found to be $\beta = \beta_3 = 2.56 \pm 0.05$. We saw no systematic dependence of β on p^+.

For $p^+ = 0.2$, however, $\beta = 2.23 \pm 0.05$ and $P_t = (3.4 \pm 0.5)$ kPa, and for $p^+ = 0.3$, $\beta = 2.29 \pm 0.05$ and $P_t = (2.0 \pm 0.5)$ kPa. Due to the necessity of determining P_t and β simultaneously at these p^+ values, there is more uncertainty associated with the measurements of β. It is not possible to verify or falsify whether there is a fixed $\beta = \beta_2$, or whether it depends on p^+ and S_w.

The existence of connecting paths is a percolation problem. They disappear when $p^+ \to (1 - p_c)^+$ or $p^+ \to (p_c)^-$. It would, therefore, be expected that the mobility M defined in Eq. 13 would exhibit a critical behavior similar to the conductance near a critical point. By making the hypothesis that M behaves as in Eq. 14 and using finite size scaling, we determined $t' \approx 5.7$; see Figure 7. This is a huge value and raises the suspicion that the system is *not* critical where percolation theory dictates that it should be. Possible suspects for causing this push away from criticality are the links that do not contain interfaces. They are not easy links, but they have precisely the same effect on the dynamics of the flow as the easy links. If this is so, the transition lines would then be shifted, as shown in Figure 1.

We have only explored a small part of the phase diagram of this rich model in this first study. The phase diagram should be investigated in more detail and over a wider range of parameters. The nature of the transition lines is as of now unknown and should also be further investigated. There are percolation transitions in the model. The question as to where they are and what their properties are as the transport is not through percolation clusters remains unclear.

Data availability statement

The original contributions presented in the study are included in the article/Supplementary Material; further inquiries can be directed to the corresponding author.

Author contributions

HF performed the numerical simulations and the data analysis, and wrote the first draft of the manuscript. HF wrote the code specific for this project based on algorithms written by SS. AH and SS suggested the idea of the problem. AH worked out the relation to percolation theory. All authors contributed to the article and approved the submitted version.

Funding

This work was supported by the Research Council of Norway through its Center of Excellence funding scheme, project number 262644.

Acknowledgments

The authors would like to thank S. B. Santra and D. Jnana for discussions on the percolation problem that this system poses.

Conflict of interest

The authors declare that the research was conducted in the absence of any commercial or financial relationships that could be construed as a potential conflict of interest.

Publisher's note

References

1 Ohm GS. *Die galvanische kette, matematisch bearbeitet*. Berlin: T. H. Riemann (1827).

2 Darcy H. *Les fontaines publiques de la ville de Dijon*. Paris: Dalmont (1856).

3 Whitaker S. Flow in porous media I: A theoretical derivation of Darcy's law. *Transport in porous media* (1986) 1:3–25. doi:10.1007/bf01036523

4 Wyckoff R, Botset H. The flow of gas-liquid mixtures through unconsolidated sands. *Physics* (1936) 7:325–45. doi:10.1063/1.1745402

5 Barenblatt G, Patzek T, Silin D. The mathematical model of non-equilibrium effects in water-oil displacement. In: *Spe/doe improved oil recovery symposium*. Richardson, TX: OnePetro (2002).

6 Tallakstad KT, Knudsen HA, Ramstad T, Løvoll G, Måløy KJ, Toussaint R, et al. Steady-state two-phase flow in porous media: Statistics and transport properties. *Phys Rev Lett* (2009) 102:074502. doi:10.1103/physrevlett.102.074502

7 Tallakstad KT, Løvoll G, Knudsen HA, Ramstad T, Flekkøy EG, Måløy KJ. Steady-state, simultaneous two-phase flow in porous media: An experimental study. *Phys Rev E* (2009) 80:036308. doi:10.1103/physreve.80.036308

8 Rassi EM, Codd SL, Seymour JD. Nuclear magnetic resonance characterization of the stationary dynamics of partially saturated media during steady-state infiltration flow. *New J Phys* (2011) 13:015007. doi:10.1088/1367-2630/13/1/015007

9 Aursjø O, Erpelding M, Tallakstad KT, Flekkøy EG, Hansen A, Måløy KJ. Film flow dominated simultaneous flow of two viscous incompressible fluids through a porous medium. *Front Phys* (2014) 2:63. doi:10.3389/fphy.2014.00063

10 Sinha S, Bender AT, Danczyk M, Keepseagle K, Prather CA, Bray JM, et al. Effective rheology of two-phase flow in three-dimensional porous media: Experiment and simulation. *Transport in porous media* (2017) 119:77–94. doi:10.1007/s11242-017-0874-4

11 Gao Y, Lin Q, Bijeljic B, Blunt MJ. Pore-scale dynamics and the multiphase Darcy law. *Phys Rev Fluids* (2020) 5(1):013801. doi:10.1103/physrevfluids.5.013801

12 Zhang Y, Bijeljic B, Gao Y, Lin Q, Blunt MJ. Quantification of nonlinear multiphase flow in porous media. *Geophys Res Lett* (2021) 48(5). doi:10.1029/2020gl090477

13 Zhang Y, Bijeljic B, Blunt MJ. Nonlinear multiphase flow in hydrophobic porous media. *J Fluid Mech* (2022) 934:R3. doi:10.1017/jfm.2021.1148

14 Grøva M, Hansen A. Two-phase flow in porous media: Power-law scaling of effective permeability. *J Phys Conf Ser* (2011) 319:012009. doi:10.1088/1742-6596/319/1/012009

15 Sinha S, Hansen A. Effective rheology of immiscible two-phase flow in porous media. *Europhysics Lett* (2012) 99:44004. doi:10.1209/0295-5075/99/44004

16 Sinha S, Hansen A, Bedeaux D, Kjelstrup S. Effective rheology of bubbles moving in a capillary tube. *Phys Rev E* (2013) 87(2):025001. doi:10.1103/physreve.87.025001

17 Xu X, Wang X. Non-Darcy behavior of two-phase channel flow. *Phys Rev E* (2014) 90(2):023010. doi:10.1103/physreve.90.023010

18 Yiotis A, Dollari A, Kainourgiakis M, Salin D, Talon L. Nonlinear Darcy flow dynamics during ganglia stranding and mobilization in heterogeneous porous domains. *Phys Rev Fluids* (2019) 4(11):114302. doi:10.1103/physrevfluids.4.114302

19 Roy S, Hansen A, Sinha S. Effective rheology of two-phase flow in a capillary fiber bundle model. *Front Phys* (2019) 7:92. doi:10.3389/fphy.2019.00092

20 Roy S, Sinha S, Hansen A. Immiscible two-phase flow in porous media: Effective rheology in the continuum limit (2019). Available at: https://arxiv.org/abs/1912.05248 (Accessed December 11, 2019).

21 Fyhn H, Sinha S, Roy S, Hansen A. Rheology of immiscible two-phase flow in mixed wet porous media: Dynamic pore network model and capillary fiber bundle model results. *Transport in Porous Media* (2021) 139:491–512. doi:10.1007/s11242-021-01674-3

22 Sales J, Seybold HJ, Oliveira CL, Andrade JS. Bubble dynamics in stationary two-phase flow through disordered porous media. *Front Phys* (2022) 170. doi:10.3389/fphy.2022.860190

23 Feder J, Flekkøy EG, Hansen A. *Physics of flow in porous media*. Cambridge: Cambridge University Press (2022).

24 Lanza F, Rosso A, Talon L, Hansen A. Non-Newtonian rheology in a capillary tube with varying radius. *Transport in Porous Media* (2022) 145(1):245–69. doi:10.1007/s11242-022-01848-7

25 Cheon HL, Fyhn H, Hansen A, Wilhelmsen Ø, Sinha S. Steady-state two-phase flow of compressible and incompressible fluids in a capillary tube of varying radius. *Transport in Porous Media* (2023) 147:15–33. doi:10.1007/s11242-022-01893-2

26 Wilkinson D. Percolation effects in immiscible displacement. *Phys Rev A* (1986) 34:1380–91. doi:10.1103/physreva.34.1380

27 Stauffer D, Aharony A. *Introduction to percolation theory*. Abingdon, UK: Taylor & Francis (2018).

28 Roux S, Herrmann H. Disorder-induced nonlinear conductivity. *Europhys Lett* (1987) 4(11):1227–31. doi:10.1209/0295-5075/4/11/003

29 Scheidegger AE. Theoretical models of porous matter. *Prod Monthly* (1953) 17:17.

30 Scheidegger AE. *The physics of flow through porous media*. 3rd. Toronto: University of Toronto press (2020).

31 Irannezhad A, Primkulov BK, Juanes R, Zhao B. Fluid-fluid displacement in mixed-wet porous media. *Phys Rev Fluids* (2023) 8:L012301. doi:10.1103/PhysRevFluids.8.L012301

32 Irannezhad A, Primkulov BK, Juanes R, Zhao B. Characteristics of fluid-fluid displacement in model mixed-wet porous media: patterns, pressures, and scalings (2006). Available at: https://arxiv.org/abs/2302.03072 (Accessed February 6, 2023).

33 Knudsen HA, Hansen A. Two-phase flow in porous media: Dynamical phase transition. *Eur Phys J B-Condensed Matter Complex Syst* (2006) 49:109–18. doi:10.1140/epjb/e2006-00019-y

34 Grossman T, Aharony A. Structure and perimeters of percolation clusters. *J Phys A: Math Gen* (1986) 19:L745–51. doi:10.1088/0305-4470/19/12/009

35 Redner S. Fractal and multifractal scaling of electrical conduction in random resistor networks (2007). Available at: https://arxiv.org/abs/0710.1105 (Accessed October 4, 2007).

36 Sinha S, Gjennestad MA, Vassvik M, Hansen A. Fluid meniscus algorithms for dynamic pore-network modeling of immiscible two-phase flow in porous media. *Front Phys* (2021) 8:567. doi:10.3389/fphy.2020.548497

37 Aker E, Måløy KJ, Hansen A, Batrouni GG. A two-dimensional network simulator for two-phase flow in porous media. *Transport in porous media* (1998) 32(2):163–86. doi:10.1023/a:1006510106194

38 Knudsen HA, Aker E, Hansen A. Bulk flow regimes and fractional flow in 2D porous media by numerical simulations. *Transport in Porous Media* (2002) 47:99–121. doi:10.1023/a:1015039503551

39 Tørå G, Øren P-E, Hansen A. A dynamic network model for two-phase flow in porous media. *Transport in Porous Media* (2012) 92(1):145–64. doi:10.1007/s11242-011-9895-6

40 Gjennestad MA, Vassvik M, Kjelstrup S, Hansen A. Stable and efficient time integration of a dynamic pore network model for two-phase flow in porous media. *Front Phys* (2018) 6:56. doi:10.3389/fphy.2018.00056

41 Sinha S, Grøva M, Ødegården TB, Skjetne E, Hansen A. Local wettability reversal during steady-state two-phase flow in porous media. *Phys Rev E* (2011) 84(3):037303. doi:10.1103/physreve.84.037303

42 Flovik V, Sinha S, Hansen A. Dynamic wettability alteration in immiscible two-phase flow in porous media: Effect on transport properties and critical slowing down. *Front Phys* (2015) 3:86. doi:10.3389/fphy.2015.00086

43 Blunt MJ. *Multiphase flow in permeable media: A pore-scale perspective*. Cambridge: Cambridge University Press (2017).

44 Straley JP. Critical exponents for the conductivity of random resistor lattices. *Phys Rev B* (1977) 15(12):5733–7. doi:10.1103/physrevb.15.5733

45 Xun Z, Hao D, Ziff RM. Site percolation on square and simple cubic lattices with extended neighborhoods and their continuum limit. *Phys Rev E* (2021) 103:022126. doi:10.1103/physreve.103.022126

46 Cen W, Liu D, Mao B. Molecular trajectory algorithm for random walks on percolation systems at criticality in two and three dimensions. *Physica A: Stat Mech its Appl* (2012) 391(4):925–9. doi:10.1016/j.physa.2011.01.003

47 Den Nijs M. A relation between the temperature exponents of the eight-vertex and q-state Potts model. *J Phys A: Math Gen* (1979) 12(10):1857–68. doi:10.1088/0305-4470/12/10/030

48 Erpelding M, Sinha S, Tallakstad KT, Hansen A, Flekkøy EG, Måløy KJ. History independence of steady state in simultaneous two-phase flow through two-dimensional porous media. *Phys Rev E* (2013) 88(5):053004. doi:10.1103/physreve.88.053004

PAPER III

Reference

Hursanay Fyhn, **Santanu Sinha and Alex Hansen**,
Local Statistics of Immiscible and Incompressible Two-Phase Flow in Porous Media.
Physica A: Statistical Mechanics and its Applications **616**, 128626 (2023)
DOI: 10.1016/j.physa.2023.128626

CONTRIBUTIONS

HF: Numerical simulations, Data analysis, Wrote the code for the model, Developing the theory, Methodology, Writing the manuscript. SS: Wrote the code for the model, Developing the theory, Methodology, Writing the manuscript. AH: Developing the theory, Methodology, Writing the manuscript

Physica A 616 (2023) 128626

Contents lists available at ScienceDirect

Physica A

journal homepage: www.elsevier.com/locate/physa

Local statistics of immiscible and incompressible two-phase flow in porous media

Hursanay Fyhn [a],[*], Santanu Sinha [b], Alex Hansen [a]

[a] *PoreLab, Department of Physics, Norwegian University of Science and Technology, NTNU, N-7491 Trondheim, Norway*
[b] *PoreLab, Department of Physics, University of Oslo, N-0316 Oslo, Norway*

ARTICLE INFO

Article history:
Received 31 August 2022
Received in revised form 9 January 2023
Available online 27 February 2023

Keywords:
Porous media
Statistical mechanics
Network model

ABSTRACT

We consider immiscible and incompressible two-phase flow in porous media under steady-state conditions using a dynamic pore network model. We focus on the fluctuations in a Representative Elementary Area (REA), with the aim to demonstrate that the statistical distributions of the volumetric flow rate and the saturation within the REA become independent of the size of the entire model when the model is large enough. This independence is a necessary condition for developing a local statistical theory for the flow, which in turn opens for the possibility to formulate a description at scales large enough for the typical pore size to be negligible using differential equations.

1. Introduction

When two or more immiscible fluids compete for space while flowing in a porous medium, we are dealing with multiphase flow [1–4]. Finding a proper description of multiphase flow at the Darcy scale, which may be orders of magnitude larger than the pore scale, is a central problem in porous media research. On the Darcy scale, the only practical approach to the multiphase flow problem is to replace the original porous medium with a continuous medium and then describe the flow through a set of differential equations relating the fluid velocities to the driving forces, e.g. pressure gradients, saturation gradients and gravity. The approach dominating any practical applications of immiscible two-phase flow that today requires calculations is based on relative permeability theory [5]. This is a purely phenomenological theory essentially stating that the two immiscible fluids get into each other way and therefore reduce the effective permeability each fluid experiences. Add a capillary pressure function to take into account the capillary forces between the two fluids, and the theory is complete [6]. This phenomenological approach has the flaw that it provides no path to implement into it our increasing understanding of the interactions and flow of the fluids at both the pore scale and the molecular scale.

Solving the *scale-up problem* in immiscible two-phase flow in porous media consists of expressing the flow at the pore scale in terms of the flow at the molecular scale and then expressing the flow at the Darcy scale in terms of the flow at the pore scale. The favored approach to the scale-up problem is that of homogenization. That is, start with a description of the problem on small scale using variables appropriate for that scale. Then average these variables over the large scale, followed by closure assumptions.

One example of the homogenization approach of scaling up immiscible two-phase flow in porous media starts from mechanical principles such as momentum conservation to arrive at an effective description of the flow through homogenization [7–12]. Thermodynamically Constrained Averaging Theory (TCAT) [13–18] is a very different approach

---

[*] Corresponding author.
E-mail addresses: hursanay.fyhn@ntnu.no (H. Fyhn), santanu.sinha@ntnu.no (S. Sinha), alex.hansen@ntnu.no (A. Hansen).

https://doi.org/10.1016/j.physa.2023.128626

to the scale-up problem. It is based on volume averages of thermodynamic quantities defined at the sub-pore and pore scale, together with closure relations at the homogeneous scale as formulated by Whittaker [7]. Another homogenization approach is that of Kjelstrup et al. [19–21], who use Euler scaling to work out the averages of intensive variables such as pressure. This approach manages to keep the number of variables down in contrast to other approaches. We also point to the homogenization approach based on expressing the central thermodynamic potentials in terms of geometric variables that characterize the porous medium, the fluid interfaces and the contact lines and the Minkowski functionals combined with powerful theorems from differential geometry [22–25].

These homogenization approaches succeed in taking the description of the flow from the sub-pore scale to scales just above the pore scale. They do not, however, take into account the fluid structures that appear at even larger scales. These structures result from the way the fluids arrange themselves within the porous medium, i.e., their cluster structure. They profoundly affect the flow on the intermediate scales below the Darcy scale — and this must be reflected in the flow at the Darcy scale. Energetically, these structures are not dominating, and therefore easy to discard in the different homogenization approaches. However, any scale-up attempt taking the problem from the pore scale to the Darcy scale needs to take these structures into account. As the structures appear over many length scales, a different approach from those based on homogenization techniques is needed.

Looking back in history, there is an upscaling technique that is capable of dealing with structures and correlations that stretch across scales: statistical mechanics [26]. The early developers of thermodynamics constructed their approach in order to understand heat and its relation to work in parallel to the development of the steam engine. It is based on conservation laws and symmetries, especially dilation symmetry. It treats the medium as a continuum and provides the necessary differential equations. Statistical mechanics was developed to understand how the motion of atoms and molecules leads to the thermodynamic relations, i.e., it provides the scaling up from the molecular scale to the continuum scale, thus circumventing the necessity to solve the equations of motion for every molecule.

One may therefore get the impression that thermodynamics and statistical mechanics are inextricably linked to atomic and molecular systems. This is, however, not correct. Jaynes [27] developed a generalized statistical mechanics in the fifties based on the statistical approach to information developed by Shannon a few years earlier [28]. This approach, in turn, originates in the *principle of sufficient reason* formulated by Laplace [29]: If we know nothing about a process with two outcomes, the optimal choice of probabilities for the two outcomes is 50 % for each. Shannon constructed a *function of ignorance* measuring quantitatively what we do *not* know about a given process having a number of different outcomes. One of his criteria for this function, called the Shannon entropy, was that it would have its maximum value when the probabilities for all outcomes would be equal, which is a generalization of the Laplace principle of sufficient reason. Jaynes took this approach further by adding the criterion that the Shannon entropy is maximum given what is known about the process. This leads to a set of equations that determine the probabilities for the different outcomes. This is Jaynes' generalization of statistical mechanics.

An important caveat in applying the Jaynes maximum entropy approach is that it does not work for driven systems [30]. Immiscible two-phase flow in porous media does represent a driven system where there is production of entropy due to viscous dissipation and irreversible motion of fluid interfaces and contact lines. Nevertheless, in a recent paper, Hansen et al. [31] developed a statistical mechanics for immiscible and incompressible two-phase flow in porous media based on the Jaynes principle of maximum entropy, leading to a formalism resembling thermodynamics that describes the flow at the continuum level. The trick to make it work was not to consider the molecular entropy which is being produced when the fluids move, but rather the entropy associated with the flow patterns of the fluids. This entropy is *not* being produced under steady-state flow conditions. Furthermore, it is this entropy that properly describes the fluid structures on scales above the pore scale, whereas the molecular entropy associated with dissipation dominate at scales up to the pore scale.

The Jaynes approach solves the scale-up problem in the same way as it was solved through ordinary statistical mechanics for atomistic systems. It is the aim of the present paper to investigate numerically a necessary criterion which was only assumed to be true in [31] for the Jaynes approach to be applicable to immiscible two-phase flow in porous media: can we partition the porous medium into a "system" in contact with a "reservoir" as in ordinary thermodynamics? The term "reservoir" has very different meanings in thermodynamics and in porous media research. In this work, the term is used in a thermodynamical sense, which is that a reservoir is a system large enough so that the variables describing it do not change when brought into contact with a system small enough for its variables to be affected. The way we answer the question just posed is this: Based on a numerical model, we record the statistics of key parameters in the system for different sizes of the reservoir, finding that the statistics is independent of the reservoir size when it is large enough.

We note that there have been earlier attempts at capturing the evolution of retention in unsaturated porous media subject to quasi-static changes in imposed pressure. Xu and Louge [32] formulate drainage or imbibition through porous media using an Ising model that predicts the retention curve of saturation vs capillary pressure. This is a very different approach with different aims from that of Hansen et al. [31] who focus on steady-state flow.

We will in the following relate the concept of a "system" to that of a *Representative Elementary Area* (REA) [33]. At each point in the pore space of the porous medium, we may place an area that is orthogonal to the streamline passing through it. The area qualifies as an REA if it is large enough for the variables describing the properties of the medium itself and the fluids passing through it to have well-defined averages. To obtain meaningful averages, the length scale of REA must be larger than the microscopic characteristic length of the porous medium to avoid rapid small-scale fluctuations, and must also be smaller than the characteristic length of the large-scale inhomogeneities [13,34].

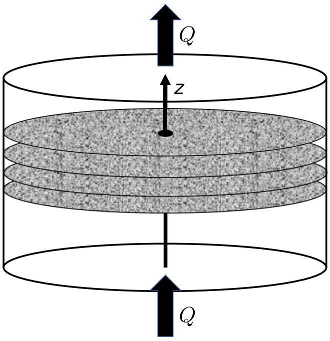

Fig. 1. A porous medium in the shape of a cylinder. There is a flow of volumetric flow rate Q passing through it. Four planes cutting through the cylinder orthogonally to the average flow direction, i.e., the z-axis, are shown. The volumetric flow rate Q is the same through each plane. However, the volumetric flow rate of each fluid, Q_w and Q_n vary from plane to plane.

The statistical mechanics developed by Hansen et al. for immiscible and incompressible two-phase flow in porous media [31], leading to a thermodynamics-like formalism for the macroscopic variables describing the flow [35–38], is reviewed in Section 2. We go into some detail here in order to place the present work in a proper context.

The dynamic pore network model [39,40] used in this work is introduced in Section 3. The model is implemented as a two-dimensional lattice where the REA is defined as a one-dimensional sub-lattice placed orthogonally to the average flow direction.

The aim of this paper is to demonstrate that Eq. (4) is valid for our dynamic pore network model. This equation states that the statistics of the variables characterizing the REA do not depend on the statistics of the reservoir apart from local interactions. We report on our findings in Section 4. We first investigate how the statistics of the variables we focus on, the wetting saturation and the Darcy velocity, vary with the size of the sub-lattice we consider, see Section 4.1. This allows us to determine when the sub-lattice is large enough to act as an REA. We then proceed to study the dependence of the variable fluctuations on the size of the REA in Section 4.2. Surprisingly, whereas the fluctuations of the wetting saturation, scale as the inverse of the square root of the size of the REA, the average Darcy flow velocity fluctuations scale as the inverse of the size of the REA to the power 0.83. Lastly, in Section 4.3 we test whether the statistics measured in the REA are independent of the size of the reservoir. We do indeed find that this is, thus verifying the validity of Eq. (4) for our dynamical pore network model.

A pertinent question is, what would happen if the verification of Eq. (4) would have failed? It would invalidate the statistical mechanics of Ref. [31], but it would also have a negative impact on any attempt at constructing a local theory for immiscible two-phase flow at the Darcy scale in that all quantities are local. Rather than having the theory represented in the form of differential equations, they would contain integrals over space. We summarize and discuss this in Section 5 in addition to the other results.

2. Statistical mechanics

We review in the following the statistical mechanics approach to immiscible and incompressible two-phase flow in porous media of Hansen et al. [31]. Envision a homogeneous cylindrical block of porous medium as shown in Fig. 1, with a volumetric flow rate Q flowing through it. This flow consists of two immiscible and incompressible fluids which are well mixed before entering the porous medium. Keeping the flow entering into the porous media constant creates a steady-state flow within the porous medium. By steady-state flow we mean that the macroscopic variables describing the flow remain constant or fluctuate around well-defined averages. It is important to note that this does not imply that the pore scale interfaces between the fluids remain static. Rather, at the scale of the fluid clusters, there may be strong activity where clusters form and break up. Steady-state flow is a concept that is defined at the macroscopic Darcy level, not at the pore level. We may split Q into the volumetric flow rate of the more wetting fluid, Q_w, and the volumetric flow rate of the less wetting fluid, Q_n, so that

$$Q = Q_w + Q_n \; . \tag{1}$$

The flow is dissipative and hence molecular entropy is produced. There is viscous dissipation and the motion of fluid interfaces and contact lines contains a dissipative element [41]. This means that there is a production of entropy as hydrodynamic motion is converted into thermal motion. The Jaynes maximum entropy principle should therefore not be applicable [30]. We now explain how we get around this hurdle.

There are three scales that stand out in porous media: the molecular scale, the pore scale and the Darcy scale. At the sub-pore scale, the dissipation dominates the flow and methods from non-equilibrium thermodynamics are

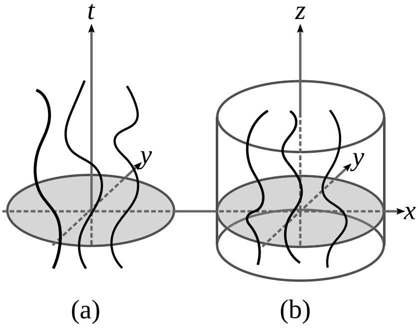

Fig. 2. We are illustrating to the left (a) the world lines of molecules in a two-dimensional gas in a space–time diagram. To the right (b), we show some streamlines of a fluid mixture flowing in a porous medium.

appropriate [19–21]. However, on scales above the pore scale, it is the fluid clusters and how they move that dominate. One may associate an entropy with these fluid structures.

In order to construct this *flow entropy,* we imagine a cylindrical porous plug as shown in Fig. 1. There is immiscible two-phase flow in the direction of the cylinder axis. We now focus on a set of imaginary planes that cut through the porous plug orthogonal to the cylinder axis as shown in Fig. 1. Imagine each plane is divided into voxels with sufficient resolution. Each voxel is associated with a number of variables describing the flow through it. To be concrete, suppose we model the porous medium using the Lattice Boltzmann method (LBM) [42]. The voxels would then be the nodes of the lattice along the plane used in LBM and the variables would be the LBM variables associated with these nodes. The configuration in the plane, X, would be the values the voxel variables have at that particular instance in each voxel. Measuring over many configurations we may define a *configurational probability density* $P(X)$. This, in turn, defines our entropy,

$$\Sigma = -\int dX\ P(X)\ \ln P(X)\ , \tag{2}$$

where the integral is over all *physically feasible configurations* in the plane. Note the important fact that since the structure of the porous matrix varies from plane to plane, this quenched disorder must be taken into account.

Before taking the next step, it is useful to think of the following system: We imagine a two-dimensional gas confined inside a box. The molecules of the gas move around incessantly. At a given moment, the position and velocity of each molecule will define an instantaneous gas configuration. The aim of statistical mechanics in this context is to provide the configurational probability density for these instantaneous configurations. There is no production of entropy in this system from the motion of the molecules. It is in equilibrium. However, we may represent the gas in a three-dimensional *space–time plot,* see Fig. 2(a). Then, each molecule is represented by its world line and the configurations represent the world lines cutting through planes orthogonal to the time axis.

Fig. 2(b) shows the streamlines of a fluid flowing through a porous medium. There is a striking analogy between these streamlines and the world lines of the molecules in the space–time plot of molecules of the two-dimensional gas, when we interpret the z-axis in Fig. 2(b) as a "time" axis. Figure 7 in Ref. [43] illustrates this point in more detail. Cuts through the porous medium as shown in Fig. 1 are then analogous to the snapshots of configurations of the gas molecules taken at different times. The flow entropy defined in Eq. (2) then corresponds to the entropy of the gas molecules, and as in the gas, there is no production of this flow entropy along the z-axis.

The volumetric flow rate Q has the same value for all planes orthogonal to the flow axis. Hence, with the flow axis acting as a "time" axis, Q is a conserved quantity along this axis. We may therefore interpret Q as being analogous to the internal energy of the two-dimensional gas. Note that neither Q_w nor Q_n are conserved, only their sum Q (Eq. (1)) is. However, both have well-defined averages. The porous medium block of Fig. 1 may be seen as an analog of a two-dimensional gas that does not exchange heat with its surroundings. In other words, it is the analog of a *microcanonical system.*

Fig. 3 shows one of the planes cutting through the porous medium orthogonally to the flow direction, i.e., the z-axis. A sub-area of this plane that is large enough to reflect the behavior of the entire plane is chosen. Hence, this area acts as an REA [33]. We characterize this REA by three variables in addition to its total area A: Q_p the volumetric flow rate through it, A_p which is the area inside the REA covered by pores, and $A_{w,p}$ which is the part of the pore area that is covered by the wetting fluid. The configurations within the REA we refer to as X_p. These configurations are a subset of the configurations X in the entire plane. Denoting X_r as the part of X which excludes the REA gives

$$X = X_r \cup X_p\ . \tag{3}$$

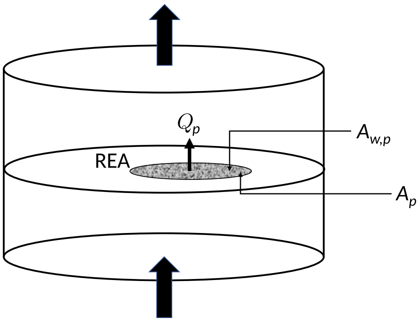

Fig. 3. Shows one of the planes cutting through the porous media block orthogonal to the flow direction which is upwards as marked with the arrows. In the plane, a sub-area that is large enough to reflect the behavior of the entire plane so that it acts as a Representative Elementary Area (REA) is selected. The REA is characterized by three variables besides its area A: The volumetric flow rate through it, Q_p, the area covered by the pores, A_p, and the area filled with the wetting fluid $A_{w,p}$.

We now refer to the discussion in the Introduction (Section 1) and interpret the REA as the *system* and the plane excluding the REA as the *reservoir*. For the Jaynes maximum entropy approach to be applicable, we must have that

$$P(X) = p_r(X_r)p(X_p) \; , \tag{4}$$

where $p_r(X_r)$ is the configurational probability for the reservoir and $p(X_p)$ is the configurational probability for the REA. The significance of this equation is that it ensures that it is possible to consider the REA as an autonomous system that interacts with the reservoir. Without this property, a local description of the flow at the Darcy scale would then not be possible.

It is the aim of this paper to verify the validity of Eq. (4). This equation allows us to define a flow entropy for the REA,

$$\Sigma_p = -\int dX_p \; p(X_p) \; \ln p(X_p) \; , \tag{5}$$

where the integral runs over all physically feasible configurations.

We maximize the entropy with the constraints that the averages of Q_p, A_p and $A_{w,p}$ are known. This gives [31]

$$p(X_p) = \frac{1}{Z} \; \exp\left[-\frac{Q_p(X_p)}{\theta} + \frac{\pi A_p(X_p)}{\theta} + \frac{\mu A_{w,p}(X_p)}{\theta}\right] \; , \tag{6}$$

where the partition function Z is given by

$$Z(\theta, \pi, \mu) = \int dX_p \; e^{-Q_p(X_p)/\theta + \pi A_p(X_p)/\theta + \mu A_{w,p}(X_p)/\theta} \; . \tag{7}$$

Here $Q_p(X_p)$, $A_p(X_p)$ and $A_{w,p}(X_p)$ are the variable values for the REA configuration X_p. It is through these three variables that contact is made with the pore-scale physics since this is where the configuration X_p enters. Three parameters appear in this equation: 1. the *agiture* θ which plays a role similar to that of temperature (and we note that the name, which is a contraction of the words "agitation" and "temperature" has been chosen to emphasize that this is *not* a temperature), 2. the *flow pressure* π which is conjugate of the pore area A_p — and hence the porosity, and 3. the *flow derivative* μ which plays the role similar to the chemical potential and which is the conjugate to the wetting area $A_{w,p}$ and hence the wetting saturation $S_{w,p} = A_{w,p}/A_p$.

Eq. (7) constitutes the scaling up from the microscopic level, in other words the pore level, to the Darcy level, since we may from it determine the values of the macroscopic variables. We have thus succeeded in turning the scale-up problem from being a physical one to the mathematical problem of integration in Eq. (7). The macroscopic variables that ensue from this approach are related through a thermodynamics-like formalism with all its richness [31,35].

In ordinary thermodynamics, one finds a set of *general* relations between the macroscopic variables. They stem either from the Euler theorem for homogeneous functions or from the Gibbs relation [44,45]. The same applies to the present formulation of the two-phase flow problem. We sketch the approach in the following.

We define an average pore velocity $v_p = Q_p/A_p$ and an entropy density $\sigma_p = \Sigma_p/A_p$. The average pore velocity v_p depends on the flow entropy density σ_p and the wetting saturation $S_{w,p}$: $v_p = v_p(\sigma_p, S_{w,p})$. With these variables, we may construct an equivalent to the *Gibbs relation,*

$$dv_p = \theta \; d\sigma_p - \mu \; dS_{w,p} \; . \tag{8}$$

We do a Legendre transform of the average flow velocity v_p from $(\sigma_p, S_{w,p})$ to (σ_p, μ) as control variables, finding

$$\hat{v}_n(\sigma_p, \mu) = v_p(\sigma_p, \mu) - S_{w,p}(\sigma_p, \mu)\mu \; , \tag{9}$$

where we have defined the *thermodynamic non-wetting velocity* [35]

$$\hat{v}_n = \left(\frac{\partial Q_p}{\partial A_{n,p}}\right)_{A_{w,p},\sigma} . \tag{10}$$

There is also the *thermodynamic wetting velocity*

$$\hat{v}_w = \left(\frac{\partial Q_p}{\partial A_{w,p}}\right)_{A_{n,p},\sigma} . \tag{11}$$

The non-wetting area $A_{n,p}$ is the area of the REA that is covered by the non-wetting fluid. We furthermore have that

$$S_{w,p} = -\left(\frac{\partial \hat{v}_n}{\partial \mu}\right)_{\sigma} , \tag{12}$$

and

$$\mu = -\left(\frac{\partial v_p}{\partial S_{w,p}}\right)_{\sigma} . \tag{13}$$

Eqs. (9) through (13) demonstrate the power of this approach. These relations are far from obvious.

There is one more central aspect that needs to be brought to light. The thermodynamic velocities defined in Eqs. (10) and (11) are *not* the pore velocities of the fluids

$$v_w = \frac{Q_{w,p}}{A_{w,p}} , \tag{14}$$

and

$$v_n = \frac{Q_{n,p}}{A_{n,p}} , \tag{15}$$

where $Q_p = Q_{w,p} + Q_{n,p}$ in analogy with Eq. (1). Rather, they are related through the two equations [35–37]

$$v_w = \hat{v}_w - S_{w,p} v_m , \tag{16}$$

$$v_n = \hat{v}_n + S_{n,p} v_m , \tag{17}$$

where $S_{n,p} = A_{n,p}/A_p = 1 - S_{w,p}$ and v_m is the *co-moving velocity*. It turns out from experimental and numerical data that the co-moving velocity is extraordinarily simple [37],

$$v_m = a(\sigma) + b(\sigma)\mu , \tag{18}$$

where $a(\sigma)$ and $b(\sigma)$ are functions of the flow entropy density. There is no equivalent to the co-moving velocity in ordinary thermodynamics [38].

Calculating the partition function $Z(\theta, \pi, \mu)$ defined in Eq. (7) requires a knowledge of the pore-scale configurations X_p through the three variables $Q_p(X_p)$, $A_p(X_p)$ and $A_{w,p}(X_p)$. Furthermore, the integral runs only over physically feasible configurations. As already mentioned, this is where the characteristics of a given porous medium and the fluids enter. It is here details of the pore scale physics enters, such as interfacial tension gradients and interface curvature at the fluid–fluid interfaces. This is where contact is made between this theory and the ongoing research on the pore-scale physics of immiscible two-phase flow.

3. Dynamic pore network model

In order to explore the validity of Eq. (4), we use a dynamic pore network model [40,46] originally developed by Aker et al. [39] and then further developed in e.g., [47–53], including direct comparison with experimental systems, [54,55]. In the latter of these two references, the performance of the model is also compared to other models.

We illustrate the model as it is implemented in the context of the present paper in Fig. 4. We use a square lattice where the links represent single pores, all having the same length l, but with a distribution in their radii. The lattice has dimensions $L_x \times L_y$ measured in units of l, and we implement periodic boundary conditions in both the flow direction and the transversal direction. The square lattice is oriented at 45° angle with respect to the average flow direction.

The links connecting neighboring nodes contain the pore throats. The nodes have no volume associated with them. The variation in the cross-sectional area of the pore throat and pore bodies are modeled by an hourglass shape so that a fluid meniscus in link i will generate a capillary pressure according to the Young–Laplace Equation [3]

$$p_{c,i}(x) = \frac{2\gamma \cos\theta}{r_i(x)} , \tag{19}$$

where $x \in [0, l]$ is the position of the interface along the center axis of the link, having a length l. Here γ is the surface tension and θ is the wetting angle measured through the wetting fluid which is the fluid that has the smallest angle

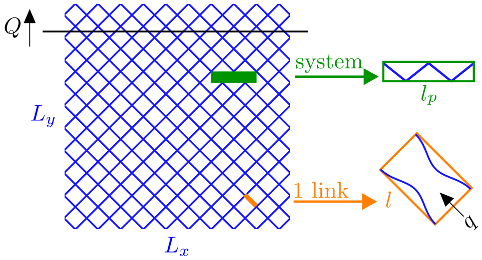

Fig. 4. Two dimensional dynamic pore network model with dimensions $L_x \times L_y$ links consists of hourglass shaped links with length l and volumetric flow rate q passing through them, oriented 45° from the average flow direction. The total volumetric flow rate Q is constant over all the cross sections normal to the average flow direction. An example of a "system" with length $l_p = 4$ links is marked, and the rest of the network surrounding the system is the "reservoir".

with the solid wall. We note that this expression is only valid under hydrostatic conditions. Hence, using it in a dynamic setting implies the assumption that the motion of the interfaces is slow. This assumption is difficult to justify during Haines jumps. We still use it as an approximation that enters together with all the other approximations that the model requires. We furthermore ignore hysteretic effects associated with the wetting angle with the same justification as for using the Young–Laplace equation. The variable indicating the shape of the link in Eq. (19) is the radius of the link at position x, which is given by

$$r_i(x) = \frac{r_{0,i}}{1 - c \cdot \cos\left(\frac{2\pi x}{l}\right)} , \tag{20}$$

where c is the amplitude of the variation and r_0/c is randomly chosen from the interval $[0.1l, 0.4l]$, thus creating a disorder in the properties of the network.

The fluids within a given link are pushed with a force caused by the total effective pressure across it which is the difference between the pressure drop between the two nodes it is attached to, Δp, and the total capillary pressure $\sum_k p_c(x_k)$ due to all the interfaces with positions $x_k \in [0, l]$. The model has been set to allow up to four interfaces in each link, and this necessitates merging of the interfaces as described in [40].

The constitutive relation between the volumetric flow rate q_i through link i and pressure drop Δp_i across the same link is [40,56]

$$q_i = -\frac{\pi \bar{r}_i^4}{8\mu_i l}\left(\Delta p_i - \sum_k p_{c,i}(x_k)\right) , \tag{21}$$

where $\bar{r}_i$ is the average hydraulic radius along the link. Furthermore, we have that $\mu_i = s_{w,i}\mu_{w,i} + s_{n,i}\mu_{n,i}$ is the saturation-weighted viscosity of the fluids in link i where $s_{w,i} = V_{w,i}/V_i$ and $s_{n,i} = V_{n,i}/V_i$ are the saturations of the wetting fluid and the non-wetting fluid respectively with viscosities $\mu_{w,i}$ and $\mu_{n,i}$, and volumes $V_{w,i}$, $V_{n,i}$, and $V_i = \pi \bar{r}_i^2 l$.

In order to calculate the flow through the links and move the interfaces correspondingly, we solve the Kirchhoff for the network using a conjugate gradient algorithm [57]. Our numerical precision in determining the flow rates is 10^{-6}.

Using the terminology introduced in the Introduction, we divide the network into a "system", corresponding to the REA, and a "reservoir" which is the rest of the network. The systems are chosen as illustrated with an example in Fig. 4 where the system is placed orthogonally to the flow direction, i.e., in the same way as in Fig. 3. Systems are made up of l_p number of links, for instance, the system in Fig. 4 has $l_p = 4$ links. The pore area A_p of a system is the sum of the transverse area, the area orthogonal to the total flow direction, of each link belonging to that system,

$$A_p = \sum_{i=1}^{l_p} \sqrt{2}\pi(\bar{r}_i)^2 , \tag{22}$$

where $\sqrt{2} = 1/\cos(45°)$ comes from the fact that links in the model are oriented in 45° angle from the flow direction. Similarly, the total wetting fluid pore area of the system $A_{w,p}$ is the sum of the product of the transverse area and the wetting fluid saturation in each link,

$$A_{w,p} = \sum_{i=1}^{l_p} \sqrt{2}\pi(\bar{r}_i)^2 s_{w,i} . \tag{23}$$

The volumetric flow rate through a system with l_p links is

$$Q_p = \sum_{i=1}^{l_p} q_i , \tag{24}$$

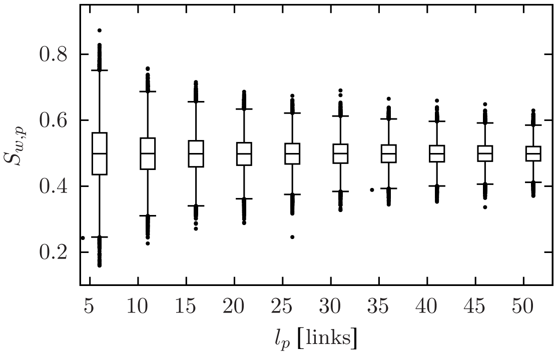

Fig. 5. Box plots showing the wetting fluid saturation $S_{w,p}$ in systems with width l_p. The model has dimensions 120 × 60 links^2.

and its wetting saturation is

$$S_{w,p} = \frac{A_{w,p}}{A_p} \ . \tag{25}$$

4. Numerical investigations

The simulations start from a random distribution of fluids within the network. The model is then integrated forwards in time while monitoring the pressure drop across it. When the pressure drop settles to a well-defined and stable average value, the model has reached steady-state flow. At this point, 20 system locations are chosen randomly at every 100th time-iteration, to get measurements that are mostly uncorrelated in time and space. Within each of these systems, the values of Q_p/l_p and $S_{w,p}$ are measured. This procedure ensures averaging not only over the motion of the fluids but also over the disorder of the porous medium itself. This process is repeated for a time corresponding to the passing of approximately 25 pore volumes of fluid through the model, where pore volume is the total volume of the links in the model. We do this for different widths l_p for the systems. In addition, the changes in the model size are studied by testing various model widths L_x while keeping the total length of the model fixed at $L_y = 60$ links. The links in the model are all $l = 1$ mm long. The two immiscible fluids have $\gamma = 3.0 \cdot 10^{-5}$ N/ mm, $\mu_w = \mu_{nw} = 0.1$ Pa s and $\theta = 70°$. The overall wetting saturation for the network is fixed at $S_w = 0.5$. Due to the periodic boundary conditions, the volume of the fluids is conserved and the total saturation is constant. The total volumetric flow rate per unit width of the network is fixed at $Q/L_x = 0.7$ mm^3/(s link). The capillary number can be calculated from $Ca = \mu Q/(\gamma A_{\text{tot}})$ where A_{tot} is the total cross sectional area [40], giving $Ca \approx 0.012$.

4.1. System variable statistics

Figs. 5 and 6 show box plots of $S_{w,p}$ and Q_p/l_p as functions of l_p, for a network with dimensions 120 × 60 links^2. In each box plot, the lower edge of the box which we can denote b_1, the center line (median) b_2 and the upper edge b_3 correspond to the 25th, 50th and 75th percentiles of the data, respectively. The lower and upper limits that exclude the outliers are $b_1 - 1.5(b_3 - b_1)$ and $b_3 + 1.5(b_3 - b_1)$, respectively.

Since the control parameters for the entire network are fixed at $S_w = 0.5$ and $Q/L_x = 0.7$ mm^3/(s link), the average values $\langle S_{w,p}\rangle$ and $\langle Q_p/l_p\rangle$ in the systems will be the same as these values if measured with large enough statistics while the fluctuations around them will depend on l_p. In Figs. 5 and 6, the medians for all system sizes, l_p, agree well with these expected average values. This factor indicates the existence of REAs since the intensive quantities inside REA must have well-defined averages that are independent of the size of the REA. This agreement is even true for systems as small as $l_p = 6$ links.

Furthermore, both Figs. 5 and 6 show a steady decrease in the variations in the distributions with increasing l_p as the edges of the boxes approach the medians. This is more prominent for Q_p/l_p in Fig. 6 than for $S_{w,p}$ in Fig. 5. This is a reflection of Q/L_x being constant for any cut through the model orthogonally to the average flow direction, since $Q_p/l_p \to Q/L_x$ as $l_p \to L_x$. On the other hand, $S_{w,p}$ has no such restrictions and is therefore allowed to fluctuate, even when $l_p = L_x$. The fact that there is a smaller spread in both distributions with increased l_p is another factor that signals possible REAs.

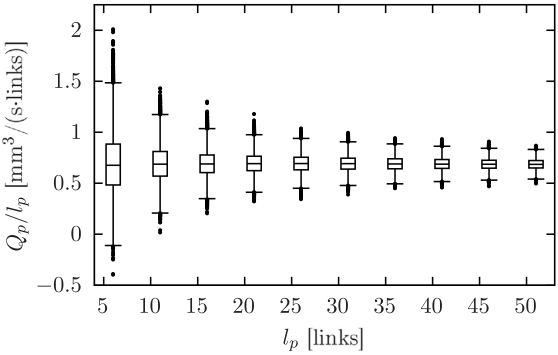

Fig. 6. Box plots showing the volumetric flow rate per unit system-width Q_p/l_p in systems with width l_p. The model has dimensions 120 × 60 links^2.

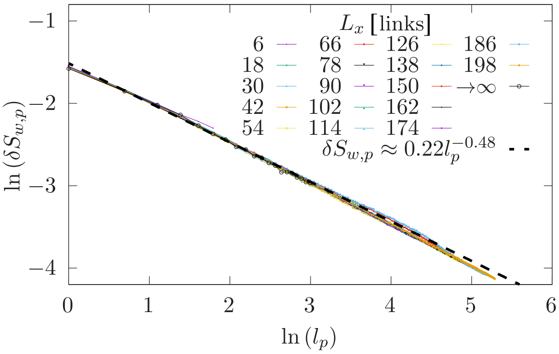

Fig. 7. Standard deviation of the wetting fluid saturation $S_{w,p}$ in systems with widths l_p residing in models having widths L_x and length 60 links.

4.2. Size dependence of fluctuations

One way to quantitatively study the fluctuations in $\xi \in \left\{S_{w,p}, Q_p/l_p\right\}$ is through their corrected standard deviations given by [58]

$$\delta\xi = \sqrt{\frac{\sum_i^N (\xi_i - \langle\xi\rangle)^2}{N-1}} \tag{26}$$

where N is the number of measurements and $\langle\xi\rangle = \left(\sum_i^N \xi_i\right)/N$ is the mean. The standard deviations of $S_{w,p}$ and $\delta Q_p/l_p$ as a function of the system width l_p are shown in Figs. 7 and 8, respectively.

We note the difference in behavior in Figs. 7 and 8 in that $\delta Q_p/l_p$ drops off dramatically when l_p approaches L_x whereas no such effect is seen for $\delta S_{w,p}$. This is caused by the fact that Q is not fluctuating in the planes orthogonal to the average flow direction, whereas there is no such constraint for S_w, which is a factor also mentioned earlier. To avoid the measurements taken inside the systems being affected by the boundary effects, REA needs to be adequately smaller than the total model.

We also show in Figs. 7 and 8 the results of extrapolation to infinitely large model $L_x \to \infty$. To understand how this was calculated, start by looking at Fig. 9 where the results from Figs. 7 and 8 have been plotted in a different way. In order to extrapolate to $L_x \to \infty$, the simulation results used must be from cases where the systems are much smaller than the model. To comply with this, the extrapolation process was performed for $l_p \in [1, 20]$ links and $L_x \in [150, 198]$ links. For these values of l_p and L_x, Fig. 9 shows that there is a linear relationship between $\delta\xi \in \left\{\delta S_{w,p}, \delta Q_p/l_p\right\}$ and $1/L_x$. Therefore, linear regression fit of the form

$$\delta\xi = \frac{c_1}{L_x} + \delta\xi_\infty \ , \tag{27}$$

can be performed for each l_p, where c_1 and $\delta\xi_\infty$ are constants. It can be observed from Eq. (27) that $\delta\xi \to \delta\xi_\infty$ when $L_x \to \infty$, hence $\delta\xi_\infty$ are the extrapolation results. In Fig. 9, $\delta\xi_\infty$ are the intersections the linear fits in Eq. (27) make with the vertical axis.

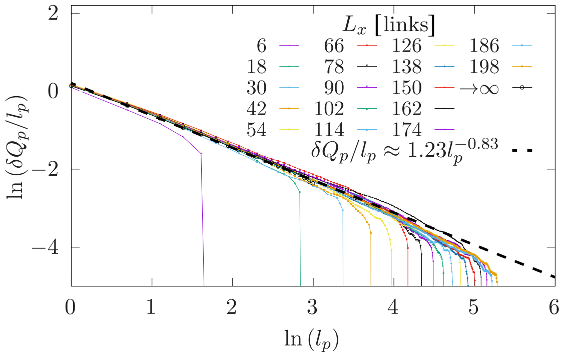

Fig. 8. Standard deviation of the volumetric flow rate per unit system width $\delta Q_p/l_p$ in systems with widths l_p residing in models with widths L_x and length 60 links.

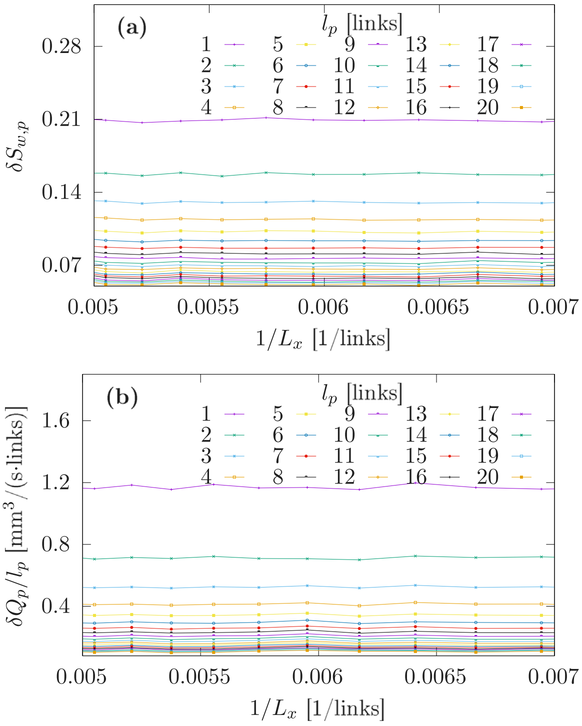

Fig. 9. Standard deviation of (a) the wetting fluid saturation $S_{w,p}$ and (b) the volumetric flow rate per unit system width Q_p/l_p in systems with widths l_p residing in models having widths L_x and length 60 links.

After obtaining estimates for $\delta\xi_\infty$ for each l_p, we do a power law fit

$$\delta\xi_\infty = c_2\, l_p^{-\beta} \tag{28}$$

to model the relationship between $\delta\xi_\infty$ and l_p where c_2 is a constant and β is an exponent. The result is

$$\lim_{L_x\to\infty} \delta S_{w,p} \approx 0.22 l_p^{-0.48} \tag{29}$$

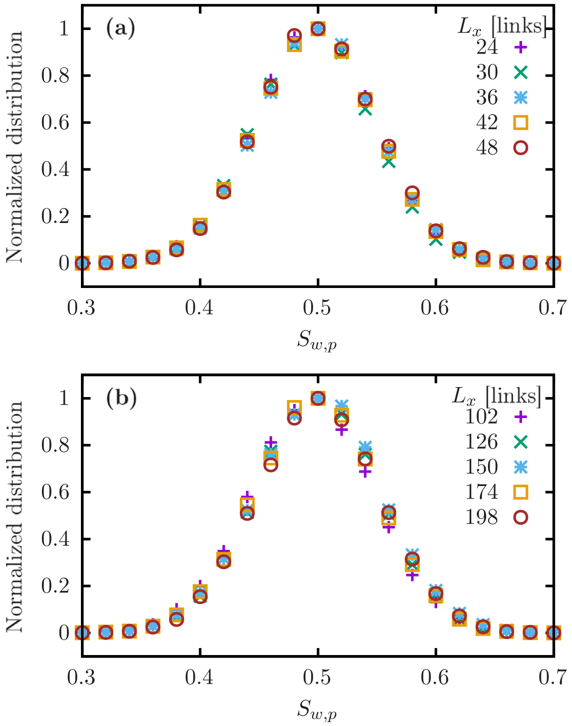

Fig. 10. Normalized histogram for the wetting fluid saturation $S_{w,p}$ in systems with width $l_p = 20$ links. The model has length 60 links and widths L_x that are close to l_p in (a) and are much larger than l_p in (b).

for Fig. 7 and

$$\lim_{L_x \to \infty} \left(\frac{\delta Q_p}{l_p} \right) \approx 1.23 l_p^{-0.83} \tag{30}$$

for Fig. 8.

Based on the central limit theorem, the standard deviation of the average of l_p equally distributed independent variables is proportional to ${l_p}^{-1/2}$. The quantities $S_{w,p}$ and Q_p/l_p are both intensive quantities representing averages in l_p. We note from Eq. (29) that this is the case with $S_{w,p}$, which could indicate that samples are uncorrelated. However, that the fluctuations $\delta Q_p/l_p$ in Eq. (30) scales as one over l_p to the power 0.83 is a surprise presumably indicative of the samples being non-zero correlated in such a way that they fall off faster than when there are no correlations. This further means that the reservoir should be larger than the spatial correlation length for the systems to be not affected by finite-size effects.

4.3. Reservoir independence

We have now reached the central aim of this paper: Testing the validity of Eq. (4) for our dynamic pore network model. This is done by keeping l_p fixed and varying L_x while monitoring histograms of $S_{w,p}$ and Q_p/l_p. If Eq. (4) is valid for this model, the histograms should be independent of the model size L_x for large enough L_x.

The normalized histograms of $S_{w,p}$ and Q_p/l_p, measured for systems of width $l_p = 20$ links, are shown in Figs. 10 and 11 respectively. We have split the two figures into two sub figures each in order to increase readability. Figs. 10(a) and 11(a) show the normalized histograms for L_x being close to l_p, whereas Figs. 10(b) and 11(b) show the normalized histograms for L_x much larger than l_p.

The normalized histograms for $S_{w,p}$ in Fig. 10 seem to overlap for essentially all values of L_x. This effect can also be seen in the standard deviations in Fig. 7 where $\delta S_{w,p}$ approximately follows Eq. (29) regardless of the model size L_x or the system size l_p. This means, in the case of $S_{w,p}$, the reservoir independence seems to be satisfied regardless of the difference between l_p and L_x.

On the other hand, the histograms of Q_p/l_p differ more from each other when L_x is close to l_p, see Fig. 11(a), compared to L_x being much larger than l_p where they overlap significantly larger, see Fig. 11(b). This behavior is reflected in the

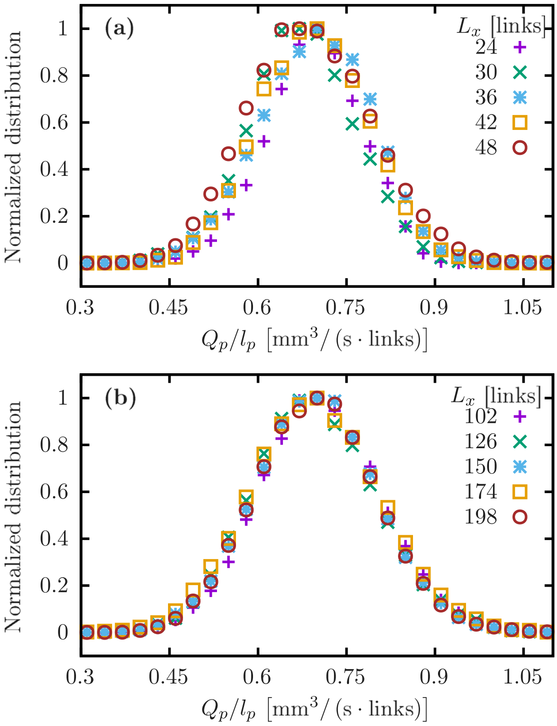

Fig. 11. Normalized histogram for the volumetric flow rate per link Q_p/l_p in systems width $l_p = 20$ links. The model has length 60 links and widths L_x that are close to l_p in (a) and are much larger than l_p in (b).

standard deviation results in Fig. 8 as well where $\delta Q_p/l_p$ following Eq. (30) only when l_p is less than L_x. From these findings, we conclude that Q_p/l_p is independent of the reservoir size when L_x is sufficiently larger than l_p. This difference in behavior is presumably related to the flow rate Q/L_x being constant in all layers whereas the wetting saturation S_w fluctuates.

The results combined indicate that reservoir independence is valid for our model when the reservoir is adequately larger than the system.

5. Conclusion

The aim of this paper has been to address the plausibility of a necessary condition for the Jaynes statistical mechanics formulation [27] to be applicable to immiscible and incompressible two-phase flow in porous media. The condition demands that a such porous medium can be split into a system, functioning as a Representative Elementary Area (REA), and a reservoir as in ordinary thermodynamics. This requires the statistics of the system to be independent of the size of the reservoir. Using dynamic pore network model simulations, we studied this by measuring distributions of key parameters using systems and reservoirs with different sizes.

First, the results show that there exist systems that can qualify as REAs within which the studied distributions have small spread and have well defined averages independent of the size of the REAs.

Second, REAs exhibit reservoir independence as demonstrated in Figs. 10 and 11. Hence, the central Eq. (4)

$$P(X) = p_r(X_r)p(X_p) \ ,$$

works for the dynamic pore network model.

As was alluded to at the end of the Introduction, the importance of the validity of Eq. (4) goes beyond verifying the Jaynes statistical mechanics framework [31]. If Eq. (4) would have failed, any attempt at constructing a local theory for immiscible two-phase flow at the Darcy scale would be in jeopardy. By local we mean that we can define variables that depend on a given point in the porous medium and the theory then provides relations between these variables depending only on that point. Relative permeability theory is an example of such a local theory. A failure of Eq. (4) would presumably necessitate the relations between variables containing integration over space.

When the reservoir size approaches to infinity, as the extrapolation results show, the fluctuations in the wetting fluid saturation depend on the system size through an exponent of −0.48. The same exponent in the case of volumetric flow rate per unit system width is −0.83. The fact that at least one of the fluctuations corresponds to an exponent significantly different from $-1/2$ indicates a non-zero spatial correlation between the links in the network, according to the central limit theorem. We speculate that this may be a consequence of total volumetric flow rate in the planes orthogonal to the average flow direction being a conserved quantity, whereas saturation in the same planes is not.

The measured distributions of saturation and volumetric flow rate inside systems are more similar when reservoir is much larger than system than when system and reservoir are closer in size. The cases with similar distributions indicate that reservoirs in these cases are adequately larger than the spatial correlation length for the systems to be unaffected by finite-size effects. Reservoir independence can be said to be achieved in these cases.

Our dynamic pore network model is capable of modeling porous media with a large number of pores (links). This comes at the cost of a simplified description of the structure of the pores and the motion of the fluids. Other models such as the Lattice Boltzmann Model [42] are capable of modeling the structure of the pores and the motion of the fluids inside them quite accurately. However, the price for this is the number of pores that may be modeled is limited. Nevertheless, attempts should be made to test reservoir independence of the systems also within the limits of this model. Another formidable task would be to analytically derive reservoir independence using hydrodynamics at the pore level.

CRediT authorship contribution statement

Hursanay Fyhn: Numerical simulations, Data analysis, Wrote the code for the model, Developing the theory, Methodology, Writing the manuscript. **Santanu Sinha:** Wrote the code for the model, Developing the theory, Methodology, Writing the manuscript. **Alex Hansen:** Developing the theory, Methodology, Writing the manuscript.

Declaration of competing interest

The authors declare that they have no known competing financial interests or personal relationships that could have appeared to influence the work reported in this paper.

Data availability

Data will be made available on request.

Acknowledgments

The authors thank Carl Fredrik Berg, Eirik G. Flekkøy, Daan Frenkel, Federico Lanza, Håkon Pedersen and Per Arne Slotte for interesting discussions.

Funding

This work was supported by the Research Council of Norway through its Center of Excellence funding scheme, project number 262644.

References

[1] J. Bear, Dynamics of Fluids in Porous Media, Dover, Mineola, 1988.
[2] M. Sahimi, Flow and Transport in Porous Media and Fractured Rock: From Classical Methods to Modern Approaches, Wiley, New York, 2011.
[3] M.J. Blunt, Multiphase Flow in Permeable Media, Cambridge Univ. Press, Cambridge, 2017.
[4] J. Feder, E.G. Flekkøy, A. Hansen, Physics of Flow in Porous Media, Cambridge University Press, Cambridge, 2022.
[5] R.D. Wyckoff, H.G. Botset, The flow of gas-liquid mixtures through unconsolidated sands, Physics 7 (1936) 325, http://dx.doi.org/10.1063/1.1745402.
[6] M.C. Leverett, Capillary behavior in porous sands, Trans. AIMME 12 (1940) 152, http://dx.doi.org/10.2118/941152-G.
[7] S. Whitaker, Flow in porous media II: The governing equations for immiscible, two-phase flow, Transp. Porous Media 1 (1986) 105, http://dx.doi.org/10.1007/BF00714688.
[8] J.-L. Auriault, E. Sanchez-Palencia, Remarques sur la loi de Darcy pour les éecoulements biphasiques en milieu poreux, J. Theor. Appl. Mech. Numér. Spéc. 141 (1986).
[9] J.-L. Auriault, Nonsaturated deformable porous media: quasistatics, Transp. Porous Media 2 (1987) 45, http://dx.doi.org/10.1007/BF00208536.
[10] J.-L. Auriault, O. Lebaigue, G. Bonnet, Dynamics of two immiscible fluids flowing through deformable porous media, Transp. Porous Media 4 (1989) 105, http://dx.doi.org/10.1007/BF00134993.
[11] D. Picchi, I. Battiato, The impact of pore-scale flow regimes on upscaling of immiscible two-phase flow in porous media, Water Resour. Res. 54 (2018) 6683, http://dx.doi.org/10.1029/2018WR023172.
[12] D. Lasseux, F.J. Valdés-Parada, A macroscopic model for immiscible two-phase flow in porous media, J. Fluid Mech. 944 (2022) A43, http://dx.doi.org/10.1017/jfm.2022.487.
[13] M. Hassanizadeh, W.G. Gray, General conservation equations for multi-phase systems: 1. Averaging procedure, Adv. Water Resour. 2 (1979) 131, http://dx.doi.org/10.1016/0309-1708(79)90025-3.
[14] S.M. Hassanizadeh, W.G. Gray, Mechanics and thermodynamics of multiphase flow in porous media including interphase boundaries, Adv. Water Resour. 13 (1990) 169, http://dx.doi.org/10.1016/0309-1708(90)90040-B.
[15] S.M. Hassanizadeh, W.G. Gray, Towards an improved description of the physics of two-phase flow, Adv. Water Resour. 16 (1993) 53, http://dx.doi.org/10.1016/0309-1708(93)90029-F.

[16] S.M. Hassanizadeh, W.G. Gray, Thermodynamic basis of capillary pressure in porous media, Water Resour. Res. 29 (1993) 3389, http://dx.doi.org/10.1029/93WR01495.

[17] J. Niessner, S. Berg, S.M. Hassanizadeh, Comparison of two-phase Darcy's law with a thermodynamically consistent approach, Transp. Porous Media 88 (2011) 133, http://dx.doi.org/10.1007/s11242-011-9730-0.

[18] W.G. Gray, C.T. Miller, Introduction to the Thermodynamically Constrained Averaging Theory for Porous Medium Systems, Springer Verlag, Berlin, 2014, http://dx.doi.org/10.1007/978-3-319-04010-3.

[19] S. Kjelstrup, D. Bedeaux, A. Hansen, B. Hafskjold, O. Galteland, Non-isothermal transport of multi-phase fluids in porous media. the entropy production, Front. Phys. 6 (2018) 126, http://dx.doi.org/10.3389/fphy.2018.00126.

[20] S. Kjelstrup, D. Bedeaux, A. Hansen, B. Hafskjold, O. Galteland, Non-isothermal transport of multi-phase fluids in porous media. Constitutive equations, Front. Phys. 6 (2019) 150, http://dx.doi.org/10.3389/fphy.2018.00150.

[21] D. Bedeaux, S. Kjelstrup, Fluctuation-dissipiation theorems for multiphase flow in porous media, Entropy 24 (2022) 46, http://dx.doi.org/10.3390/e24010046.

[22] J.E. McClure, R.T. Armstrong, M.A. Berrill, S. Schlüter, S. Berg, W.G. Gray, C.T. Miller, Geometric state function for two-fluid flow in porous media, Phys. Rev. Fluids 3 (2018) 084306, http://dx.doi.org/10.1103/PhysRevFluids.3.08430.

[23] R.T. Armstrong, J.E. McClure, V. Robins, Z. Liu, C.H. Arns, S. Schlüter, S. Berg, Porous media characterization using Minkowski functionals: theories, applications and future directions, Transp. Porous Media 130 (2019) 305, http://dx.doi.org/10.1007/s11242-018-1201-4.

[24] J.E. McClure, R.T. Armstrong, S. and Berg, Geometric evolution as a source of discontinuous behavior in soft condensed matter, arXiv:1906.04073, http://dx.doi.org/10.48550/arXiv.1906.04073.

[25] J.E. McClure, M. Fan, S. Berg, R.T. Armstrong, C.F. Berg, Z. Li, T. Ramstad, Relative permeability as a stationary process: Energy fluctuations in immiscible displacement, Phys. Fluids 34 (2022) 092011, http://dx.doi.org/10.1063/5.0107149.

[26] F. Ravndal, Scaling and Renormalization Groups, No. INIS-MF–3303, Nordisk Inst. for Teoretisk Atomfysik, 1976.

[27] E.T. Jaynes, Information theory of statistical mechanics, Phys. Rev. 106 (1957) 620, http://dx.doi.org/10.1103/PhysRev.106.620.

[28] C.E. Shannon, A mathematical theory of communication, Bell Syst. Tech. J. 27 (1948) 379, http://dx.doi.org/10.1002/j.1538-7305.1948.tb01338.x.

[29] P.S. de Laplace, A Philosophical Essay on Probabilities, Dover, New York, 1951, p. 3.

[30] L.F. Calazans, R. Dickman, Steady-state entropy: A proposal based on thermodynamic integration, Phys. Rev. E 99 (2019) 032137, http://dx.doi.org/10.1103/PhysRevE.99.032137.

[31] A. Hansen, E.G. Flekkøy, S. Sinha, P.A. Slotte, A statistical mechanics for immiscible and incompressible two-phase flow in porous media, Adv. Water Resour. 171 (2023) 104336, http://dx.doi.org/10.1016/j.advwatres.2022.104336, (Elsevier).

[32] J. Xu, M.Y. Louge, Statistical mechanics of unsaturated porous media, Phys. Rev. E 92 (2015) 062405, http://dx.doi.org/10.1103/PhysRevE.92.062405.

[33] J. Bear, Y. Bachmat, Introduction to Modeling of Transport Phenomena in Porous Media, Springer, Berlin, 2012, http://dx.doi.org/10.1007/978-94-009-1926-6.

[34] O. Rozenbaum, S.R. du Roscoat, Representative elementary volume assessment of three-dimensional x-ray microtomography images of heterogeneous materials: Application to limestones, Phys. Rev. E 89 (2014) 053304, http://dx.doi.org/10.1103/PhysRevE.89.053304.

[35] A. Hansen, S. Sinha, D. Bedeaux, S. Kjelstrup, M.A. Gjennestad, M. Vassvik, Relations between seepage velocities in immiscible, incompressible two-phase flow in porous media, Transp. Porous Media 125 (2018) 565, http://dx.doi.org/10.1007/s11242-018-1139-6.

[36] S. Roy, S. Sinha, A. Hansen, Flow-area relations in immiscible two-phase flow in porous media, Front. Phys. 8 (2020) 4, http://dx.doi.org/10.3389/fphy.2020.00004.

[37] S. Roy, H. Pedersen, S. Sinha, A. Hansen, The co-moving velocity in immiscible two-phase flow in porous media, Transp. Porous Media 143 (2022) 69, http://dx.doi.org/10.1007/s11242-022-01783-7.

[38] H. Pedersen, A. Hansen, Parametrizations of two-phase flow in porous media, 2022, http://dx.doi.org/10.48550/arXiv.2212.07285, arXiv:2212.07285.

[39] E. Aker, K.J. Måløy, A. Hansen, G.G. Batrouni, A two-dimensional network simulator for two-phase flow in porous media, Transp. Porous Media 32 (1998) 163, http://dx.doi.org/10.1023/A:1006510106194.

[40] S. Sinha, M. Aa Gjennestad, M. Vassvik, A. Hansen, Fluid meniscus algorithms for dynamic pore network modeling of immiscible two-phase flow in porous media, Front. Phys. 8 (2019) 567, http://dx.doi.org/10.3389/fphy.2020.548497.

[41] N.R. Morrow, Physics and thermodynamics of capillary action in porous media, Ind. Eng. Chem. 62 (1970) 32, http://dx.doi.org/10.1021/ie50726a006.

[42] T. Ramstad, C.F. Berg, K. Thompson, Pore-scale simulations of single- and two-phase flow in porous media: Approaches and applications, Transp. Porous Media 130 (2019) 77, http://dx.doi.org/10.1007/s11242-019-01289-9.

[43] M. Souzy, H. Lhuissier, Y. Méheust, T. Le Borgne, B. Metzger, Velocity distributions, dispersion and stretching in three-dimensional porous media, J. Fluid Mech. 891 (2020) A16, http://dx.doi.org/10.1017/jfm.2020.113.

[44] H.B. Callen, Thermodynamics as a science of symmetry, Found. Phys. 4 (1974) 423, http://dx.doi.org/10.1007/BF00708519.

[45] H.B. Callen, Thermodynamics and an Introduction to Thermostatistics, second ed., Wiley, New York, ISBN: 978-0-471-86256-7, 1991.

[46] V. Joekar-Niasar, S.M. Hassanizadeh, Analysis of fundamentals of two-phase flow in porous media using dynamic pore-network models: A review, Crit. Rev. Environ. Sci. Technol. 42 (2012) 1895, http://dx.doi.org/10.1080/10643389.2011.574101.

[47] H.A. Knudsen, E. Aker, A. Hansen, Bulk flow regimes and fractional flow in 2D porous media by numerical simulations, Transp. Porous Media 47 (2002) 99, http://dx.doi.org/10.1023/A:1015039503551.

[48] T. Ramstad, A. Hansen, Cluster evolution in steady-state two-phase flow in porous media, Phys. Rev. E 73 (2006) 026306, http://dx.doi.org/10.1103/PhysRevE.73.026306.

[49] G. Tørå, P.E. Øren, A. Hansen, A dynamic network model for two-phase flow in porous media, Transp. Porous Media 92 (2012) 145, http://dx.doi.org/10.1007/s11242-011-9895-6.

[50] M.Aa. Gjennestad, M. Vassvik, S. Kjelstrup, A. Hansen, Stable and efficient time integration of a dynamic pore network model for two-phase flow in porous media, Front. Phys. 6 (2018) 56, http://dx.doi.org/10.3389/fphy.2018.00056.

[51] M.Aa. Gjennestad, M. Winkler, A. Hansen, Pore network modeling of the effects of viscosity ratio and pressure gradient on steady-state incompressible two-phase flow in porous media, Transp. Porous Media 132 (2020) 355, http://dx.doi.org/10.1007/s11242-020-01395-z.

[52] M. Winkler, M.aa. Gjennestad, D. Bedeaux, S. Kjelstrup, R. Cabriolu, A. Hansen, Onsager-symmetry obeyed in athermal mesoscopic systems: Two-phase flow in porous media, Front. Phys. 8 (2020) 60, http://dx.doi.org/10.3389/fphy.2020.00060.

[53] H. Fyhn, S. Sinha, S. Roy, A. Hansen, Rheology of immiscible two-phase flow in mixed wet porous media: dynamic pore network model and capillary fiber bundle model results, Transp. Porous Media 139 (2021) 491, http://dx.doi.org/10.1007/s11242-021-01674-3.

[54] S. Sinha, A.T. Bender, M. Danczyk, K. Keepseagle, C.A. Prather, J.M. Bray, L.W. Thrane, J.D. Seymour, S.L. Codd, A. Hansen, Effective rheology of two-phase flow in three-dimensional porous media: Experiment and simulation, Transp. Porous Media 119 (2017) 77–94, http://dx.doi.org/10.1007/s11242-017-0874-4.

[55] B. Zhao, C.W. MacMinn, B.K. Primkulov, Y. Chen, A.J. Valocchi, J. Zhao, Q. Kang, K. Bruning, J.E. McClure, C.T. Miller, A. Fakhari, D. Bolster, T. Hiller, M. Brinkmann, L. Cueto-Felgueroso, D.A. Cogswell, R. Verma, M. Prodanovic, J. Maes, S. Geiger, M. Vassvik, A. Hansen, E. Segre, R. Holtzman, Z. Yang, C. Yuan, B. Chareyre, R. Juanes, Comprehensive comparison of pore-scale models for multiphase flow in porous media, Proc. Natl. Acad. Sci. 116 (2019) 13799, http://dx.doi.org/10.1073/pnas.1901619116.

[56] E.W. Washburn, The dynamics of capillary flow, Phys. Rev. 17 (1921) 273, http://dx.doi.org/10.1103/PhysRev.17.273.

[57] G.G. Batrouni, A. Hansen, Fourier acceleration of iterative processes in disordered systems, J. Stat. Phys. 52 (1988) 747, http://dx.doi.org/10.1007/BF01019728.

[58] M. Stroeven, H. Askes, L.J. Sluys, Numerical determination of representative volumes for granular materials, :Comput. Methods Appl. Mech. Engrg. 193 (2004) 3221, http://dx.doi.org/10.1016/j.cma.2003.09.023.

PAPER IV

Reference

Hyejeong L. Cheon, Hursanay Fyhn, Alex Hansen, Øivind Wilhelmsen and Santanu Sinha,
Steady-State Two-Phase Flow of Compressible and Incompressible Fluids in a Capillary Tube of Varying Radius.
Transport in Porous Media **147**, 15–33 (2023)
DOI: 10.1007/s11242-022-01893-2

CONTRIBUTIONS

HF's specific contribution to this article is in chapter 3.3 where she performed the data analysis regarding calculations of P_t and β and the related uncertainty analysis. In addition, HF participated in the discussions of the physics and the revision of the final manuscript. HC and SS wrote the code and the first draft, with support from AH and ØW.

Transport in Porous Media (2023) 147:15–33
https://doi.org/10.1007/s11242-022-01893-2

Steady-State Two-Phase Flow of Compressible and Incompressible Fluids in a Capillary Tube of Varying Radius

Hyejeong L. Cheon[1,2] · **Hursanay Fyhn**[2] · **Alex Hansen**[2] · **Øivind Wilhelmsen**[1] · **Santanu Sinha**[3]

Received: 21 July 2022 / Accepted: 14 December 2022 / Published online: 3 January 2023

Abstract

We study immiscible two-phase flow of a compressible and an incompressible fluid inside a capillary tube of varying radius under steady-state conditions. The incompressible fluid is Newtonian and the compressible fluid is an inviscid ideal gas. The surface tension associated with the interfaces between the two fluids introduces capillary forces that vary along the tube due to the variation in the tube radius. The interplay between effects due to the capillary forces and the compressibility results in a set of properties that are different from incompressible two-phase flow. As the fluids move towards the outlet, the bubbles of the compressible fluid grows in volume due to the decrease in pressure. The volumetric growth of the compressible bubbles makes the volumetric flow rate at the outlet higher than at the inlet. The growth is not only a function of the pressure drop across the tube, but also of the ambient pressure. Furthermore, the capillary forces create an effective threshold below which there is no flow. Above the threshold, the system shows a weak nonlinearity between the flow rates and the effective pressure drop, where the nonlinearity also depends on the absolute pressures across the tube.

Keywords Two-phase flow · Compressibility · Bubble-growth · Rheology

1 Introduction

Hydrodynamic properties of the flow of multiple immiscible and incompressible fluids, otherwise known as two-phase flow (Bear 1988; Dullien 1992; Blunt 2017; Feder et al. 2022), are controlled by a number of different factors: fluid properties such as the

---

Santanu Sinha
santanu.sinha@ntnu.no

[1] PoreLab, Department of Chemistry, Norwegian University of Science and Technology (NTNU), Trondheim N-7491, Norway

[2] PoreLab, Department of Physics, Norwegian University of Science and Technology (NTNU), Trondheim N-7491, Norway

[3] PoreLab, Department of Physics, University of Oslo (UiO), Oslo N-0371, Norway

viscosity contrast and surface tension between the fluids, driving parameters such as the applied pressure drop or the flow rate, and geometrical properties such as the size and shape of the space in which the fluids are flowing. The combined effects of these factors make two-phase flow different and more complex than single phase flow. The dimensionless parameters that play a key role to define the flow properties are the ratio between the viscous and capillary forces, referred to as the capillary number, and the ratio between the viscosities of the two fluids. Depending on the values of these parameters, the flow generates different types of fingering patterns (Chen and Wilkinson 1985; Lenormand and Zarcone 1985; Måløy et al. 1985; Løvoll et al. 2004; Zhao et al. 2019) or stable displacement fronts (Lenormand and Touboul 1988) during invasion processes where one fluid displaces another in a porous medium.

Displacement processes are transient. If one continues to inject after breakthrough, the flow enters a steady state characterized by a situation where the macroscopic flow properties fluctuate or remain constant around well-defined averages. A more general form of steady-state flow can be achieved by continuously injecting both fluids simultaneously. In this case, the dynamics at the pore scale might have fluid clusters breaking up and forming, while the macroscopic flow parameters still have well-defined averages.

Over the last decade, it has become clear that steady-state flow deviates from the linear Darcy relationship (Darcy 1856) between the total flow rate and pressure drop over a range of parameters. Rather, one finds a power law relationship between pressure drop and the volumetric flow rate (Tallakstad et al. 2009; Rassi et al. 2011) in that range. In terms of the capillary number, this range is intermediary, with linearity appearing both for lower and higher values (Sinha et al. 2017; Gao et al. 2020; Zhang et al. 2021). Theoretical work to understand the physics behind the nonlinearity has appeared in, e.g., Tallakstad et al. (2009); Sinha and Hansen (2012); Zhang et al. (2021), and computational studies have been performed using Lattice Boltzmann simulations (Yiotis et al. 2013) and dynamic pore network modeling (Sinha et al. 2021, 2017). It is now believed that a fundamental mechanism behind this nonlinearity is the capillary barriers at the pore throats, which create an effective yield threshold. When the viscous forces increase, they overcome the capillary barriers creating new flow paths. This increases the effective mobility and thus the nonlinear behavior appears (Roux and Herrmann 1987). The disorder in the pore-space properties, such as the pore-size distribution (Roy et al., 2021) and the wetting angle distribution (Fyhn et al., 2021), therefore play key roles in determining the value of the exponent relating the volumetric flow rate and the pressure drop in the nonlinear regime.

The majority of the analytical and numerical approaches mentioned above consider the two fluids to be incompressible, whereas many of the experiments and applications use air as one of the fluids. Air is strongly compressible, which can enhance the complex pore-scale mechanisms such as trapping and coalescence (Leverett 1941; Li and Yortsos 1994). Compressibility is relevant to a wide range of applications with liquid and gas transport in porous media, for example, CO_2 transport and storage (Reynolds and Krevor 2015; Abidoye et al. 2015; Iglauer et al. 2019) and the transport in fuel cells (Niblett et al. 2020). Another class of applications where the compressibility plays a key role are those involving phase transitions of the fluids such as boiling and condensation. There are industrial applications where such processes are of high importance, for example aerospace vehicle thermal protection (Huang et al. 2017), high power electronics cooling systems (Gedupudi et al. 2011; Li et al. 2012, 2020) and chemical reactors (Bremer and Sundmacher 2019). These applications utilize the high specific surface area of a porous medium with fluid flowing inside, which enhances the heat and mass transfer rates (Sapin et al. 2016; Sun et al. 2011). There are also natural processes such as drying of soil (Rossi and Nimmo 1994) where a liquid to gas transition takes place.

In this article, we present a study of two-phase flow of a mixture of compressible and incompressible fluids in a capillary tube with varying radius. We consider two fluids, one is an incompressible Newtonian fluid obeying Poiseuille flow in the steady state whereas the other is a compressible ideal gas, where the viscosity is assumed to be negligible. The fluids flow as a series of bubbles and droplets under a constant pressure drop along the tube.

In case of two-phase flow of two incompressible fluids in a corresponding capillary tube, it has been found that the volumetric flow rate (Q) depends on the square root of the pressure drop (ΔP) along the tube minus a threshold pressure (P_t), that is, $Q \sim \sqrt{\Delta P - P_t}$ (Sinha et al. 2013). One primary goal of the present work is to determine how this constitutive equation changes when one of the two fluids is compressible.

A secondary goal of this work is to provide a basis for dynamic pore network modeling (Blunt 2001; Meakin and Tartakovsky 2009; Joekar-Niasar and Hassanizadeh 2012; Sinha et al. 2021) of compressible-incompressible fluid mixtures. This opens the possibility for incorporating thermodynamic effects in such models such as boiling. However, in order to explore the effect of compressibility on the rheological properties in general, we considered a higher range of pressure drops here, whereas some specific applications mentioned earlier in this section may need a different range. We also note that the other dominating computational model in this context, the Lattice Boltzmann model (Gunstensen et al. 1991; Ramstad et al. 2012), can only incorporate fluids that are weakly compressible (Qiu et al. 2017; Guo et al. 2020).

We describe in Sect. 2.1 the equations that govern the flow through the capillary tube. In Sect. 2.2, we introduce the boundary conditions used, i.e., how we inject alternate compressible and incompressible fluid into the tube. Sect. 2.3 describes how the governing equations are integrated in time.

Section 3 presents the results of our investigation. Section 3.1 defines what we mean by steady-state flow in the context of expanding bubbles. In Sect. 3.2, we investigate how the compressible bubbles grow as they advance along the tube, thus increasing the overall flow rate of the fluids. Section 3.3 presents the relation between volumetric flow rate and pressure drop at both the inlet and outlet.

We summarize our results in Sect. 4. Section 5 contains the description of the videos provided in the electronic supplementary material.

2 Methodology

The capillary tube considered in this work is filled with an incompressible and a compressible fluid, immiscible to each other, which flow through it. The fluids are separated by menisci associated with a surface tension. In order to introduce a variation in the capillary forces along the tube, we consider a periodic variation in the radius of the capillary tube along the flow direction x. The incompressible fluid is a viscous Newtonian liquid obeying Hagen-Poiseuille flow whereas the compressible fluid is an inviscid ideal gas. The flow occurs as a plug flow with a series of alternate bubbles and droplets of the two fluids as illustrated in Fig. 1. There is no fluid film along the tube walls and therefore no coalescence or snap off taking place inside the tube during the flow. We will refer the compressible and the incompressible fluid segments as *bubbles* and *droplets*, respectively.

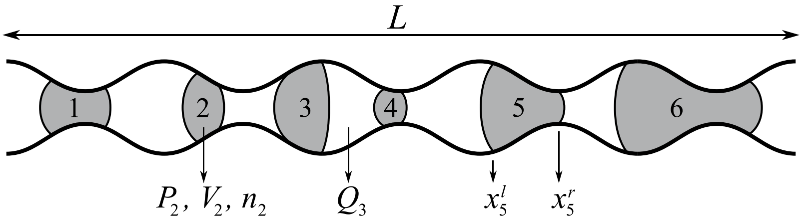

Fig. 1 Illustration of the tube geometry and the indexed variables. The shaded fluid represents the non-wetting compressible gas and the white fluid represents the wetting incompressible liquid. There are $N = 6$ bubbles here indicated by the numbers $i = 1, \dots, 6$. The indexed variables P_i, V_i and n_i, respectively, correspond to the pressure, volume and moles of the ith bubble whereas Q_i corresponds to the flow rate of the droplet between ith and $(i + 1)$th bubbles.

2.1 Governing Equations

We assume that at a given time the system contains N compressible bubbles denoted by $i = 1, 2, \dots, N$ from left to right as shown in Fig. 1. The volume V_i and the pressure P_i of the ith bubble are connected through the ideal gas law,

$$P_i V_i = n_i RT \ , \tag{1}$$

where n_i is the number of moles of gas present inside the bubble, R is the ideal gas constant and T is the temperature. The volume of an incompressible droplet on the other hand will remain constant throughout the flow and the flow rate will depend on the pressures of the two compressible bubbles bordering it. The volumetric flow rate of the incompressible droplet between i and $i + 1$ is denoted by Q_i, and follows the constitutive equation (Dullien 1992; Washburn 1921),

$$Q_i = \frac{A^2}{8\pi\mu(x_{i+1}^l - x_i^r)} \left[P_i - P_c(x_i^r) - P_{i+1} + P_c(x_{i+1}^l)\right] \ , \tag{2}$$

where μ is the viscosity of the incompressible fluid and $P_c(x)$ is the capillary pressure at x. Here we assumed that the variation in the tube radius only affects the capillary pressure P_c along the tube and therefore the area A in the above equation is considered to be the average cross-sectional area of the tube. This is an approximation that is commonly used in dynamic pore network models (Sinha et al. 2021). Furthermore, the bubbles are assumed to be smaller in size compared to the period of the tube so that the flow of the incompressible bubbles in the slowly-changing area can be considered locally as a Poiseuille flow (Panton 2013). The volume of a compressible bubble is therefore given by, $V_i = A(x_i^r - x_i^l)$ where x_i^l and x_i^r are the positions of the left and right menisci of the ith bubble, respectively.

Here we consider the incompressible fluid to be more wetting with respect to the pore walls than the compressible fluid, thus determining the sign of P_c in Equation 2. We model P_c by using the Young-Laplace equation (Dullien 1992),

$$P_c(x) = \frac{2\gamma}{r(x)} \ , \tag{3}$$

where $r(x)$ is the radius of the tube at x. Here $\gamma = \sigma \cos(\theta)$ where σ is the surface tension between the fluids and θ is the wetting angle of the fluid with respect to the tube wall. The variation in the radius of the tube shown in Fig. 1 is modeled by

$$r(x) = \frac{1}{2}\left[w + 2a\cos\left(\frac{2h\pi x}{L}\right)\right] \tag{4}$$

where L is the tube length, w is the average radius, a is the amplitude of oscillation and h is the number of periods.

2.2 Boundary Conditions

The system is driven by a constant pressure drop $\Delta P = P_0 - P_L$ where P_0 and P_L are the pressures at the inlet ($x = 0$) and outlet ($x = L$), respectively. The two fluids are injected alternatively at the inlet. Depending on the fluid that is being injected and the fluid that is leaving the tube, there will be different configurations as illustrated in Fig. 2. When a bubble is entering at the inlet [Figure 2(a)] or leaving at the outlet [Figure 2(c)], the pressure in that bubble is given by P_0 or P_L, respectively. This is because the compressible fluid has no viscosity and thus the pressure inside a bubble is uniform. The pressures inside all other bubbles are calculated using Equation 1. When a droplet is entering at the inlet [Figure 2(b) and (c)] or leaving at the outlet [Figure 2(a) and (b)], the respective flow rates Q_0 and Q_N are given by,

$$\begin{aligned} Q_0 &= \frac{A^2}{8\pi\mu x_1^l}\left[P_0 - P_1 + P_\mathrm{c}(x_1^l)\right] \text{ and} \\ Q_N &= \frac{A^2}{8\pi\mu(L - x_N^r)}\left[P_N - P_\mathrm{c}(x_N^r) - P_L\right] , \end{aligned} \tag{5}$$

whereas the flow rates of the remaining droplets are calculated using Equation 2.

The simulation is started with the tube completely filled with the incompressible fluid. The two fluids are then injected alternately at the inlet using small time steps. Whenever the injection is switched to a different fluid, a new menisci is created and the injection is continued for that fluid until the bubble or the droplet being injected has reached a given length, b_C or b_I, respectively. For each new bubble or droplet, a new value for b_C or b_I is determined using the following scheme:

$$b_\mathrm{C} = b_\mathrm{min} + kF_\mathrm{C}b_\mathrm{max} \quad \text{and} \quad b_\mathrm{I} = b_\mathrm{min} + kF_\mathrm{I}b_\mathrm{max} , \tag{6}$$

where k is chosen from a uniform distribution of random numbers between 0 and 1. F_C and F_I are the tentative values of the fractional flows for the bubbles and droplets, respectively.

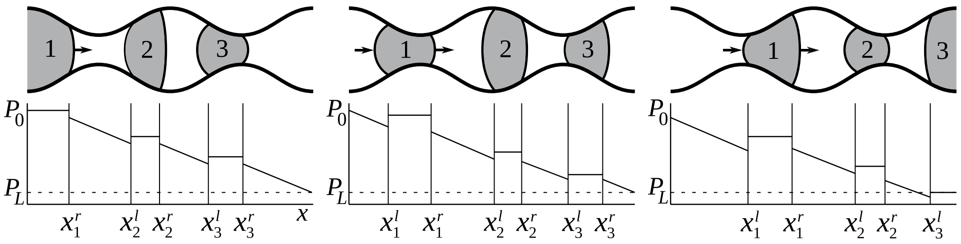

(a) (b) (c)

Fig. 2 Illustration of different configurations where bubbles and droplets are colored as gray and white, respectively. In **a**, a bubble is entering at the inlet and therefore $P_1 = P_0$ there. In **c**, a bubble is leaving at the outlet, therefore $P_N = P_L$ there. A droplet is entering at the inlet in (b) and (c), and leaving at the outlet in **a** and **b**. The flow rates of such droplets are calculated using Equation 5.

The two parameters $b_{\max}$ and $b_{\min}$ set the smallest and largest allowed sizes of any bubble or droplet. We consider here $b_{\min} = L/10^4$ and $b_{\max} = L/50$. The parameters b_{C} and b_{I} decide the initial sizes of the bubbles and droplets just after they detach from the inlet. For the compressible fluid, this determines the number of moles n_i inside a bubble,

$$n_i = \frac{Ab_{\mathrm{C}}P_0}{RT} \,, \tag{7}$$

which remains constant for that bubble throughout the flow after it gets detached from the inlet.

2.3 Updating the Menisci Positions

At any time, the two menisci bordering a droplet inside the tube move with the same velocities. The velocities of the menisci are calculated from the velocities v_i of the droplets using Equations 2 and 5,

$$\frac{\mathrm{d}x_i^r}{\mathrm{d}t} = \frac{\mathrm{d}x_{i+1}^l}{\mathrm{d}t} = v_i = \frac{Q_i}{A} \,. \tag{8}$$

We solve these ordinary differential equations using an explicit Euler scheme, thus updating positions of all menisci by choosing a small time step Δt.

Depending on the positions of the menisci and the corresponding capillary pressures, the bubbles may compress or expand. If a bubble compresses at any time step, it means the left and right interfaces of that bubble approach each other. This necessitates the choice of time step Δt to be sufficiently small, as otherwise, the two menisci around that bubble will collapse after the time step. We deal with this situation in the following way. First we calculate a time Δt_1 that is needed to pass one pore-volume of incompressible fluid through the tube,

$$\Delta t_1 = \frac{8\pi\mu L^2}{A(P_0 - P_L)} \,. \tag{9}$$

Next, we check for every bubble i if $(v_{i-1} - v_i) > 0$, that is, whether the two menisci bordering the bubble are approaching each other in that time step. If this criterion is found to be true for any of the bubbles j, we measure the time it will take for the two menisci to collapse,

$$\Delta t_2^j = \frac{x_j^r - x_j^l}{v_{j-1} - v_j} \,. \tag{10}$$

After calculating Δt_1 and Δt_2^j, we determine a time Δt for that step from,

$$\Delta t = \min(a^* \Delta t_1, b^* \Delta t_2^j) \,, \tag{11}$$

which means that if there is a possibility for a bubble to collapse during the time step, we chose Δt from the minimum of $a^* \Delta t_1$ and all of $b^* \Delta t_2^j$. If there is no possibility of collapse, we use Δt equal to $a^* \Delta t_1$. For the simulations presented in this paper, we set $a^* = 10^{-8}$ and $b^* = 10^{-6}$.

3 Results and Discussions

We perform steady-state simulations considering a tube of length $L = 100\,\mathrm{cm}$ with $w = 1\,\mathrm{cm}$, $a = 0.25\,\mathrm{cm}$ and $h = 30$ (Equation 4). The viscosity of the incompressible fluid is $\mu = 0.001$ Pa.s, the ideal gas constant is $R = 8.31\,\mathrm{J/(mol.K)}$ and the temperature is kept fixed throughout the simulation at $T = 293\,\mathrm{K}$. We fix $F_c = 0.4$ (Equation 6) which sets the volumetric fractional flow of the compressible fluid at the inlet around that value. We perform simulations varying the pressure drops ($\Delta P = P_0 - P_L$) as well as the absolute outlet pressure with different values of the surface tension, γ.

3.1 Steady-State Flow

The steady state is defined by the volumetric flow rates of the fluids fluctuating around a stable average. Due to the expansion of the compressible fluid, which we will discuss in a moment, the volumetric flow rate of the fluids changes as the fluids flow towards the outlet. We define the quantities $Q^{\mathrm{i}}_{\mathrm{T}}$, $Q^{\mathrm{i}}_{\mathrm{C}}$, $Q^{\mathrm{i}}_{\mathrm{I}}$ as the average steady-state flow rates for the total, compressible and incompressible fluids at the inlet and $Q^{\mathrm{o}}_{\mathrm{T}}$, $Q^{\mathrm{o}}_{\mathrm{C}}$, $Q^{\mathrm{o}}_{\mathrm{I}}$ as those at the outlet. The inlet and outlet flow rates are measured by tracking the displacements of the first meniscus nearest to the inlet and the last meniscus near the outlet, which are either the left or the right meniscus of the first ($i = 1$) and the last ($i = N$) bubbles. The instantaneous flow rates of the bubbles and droplets are measured as $q^{\mathrm{i}}_{\mathrm{C}} = A \sum \Delta x^{r}_{1} / \sum \Delta t$ for $x^{l}_{1} = 0$, $q^{\mathrm{i}}_{\mathrm{I}} = A \sum \Delta x^{l}_{1} / \sum \Delta t$ for $x^{l}_{1} > 0$ and $q^{\mathrm{o}}_{\mathrm{C}} = A \sum \Delta x^{l}_{N} / \sum \Delta t$ for $x^{l}_{N} = L$, $q^{\mathrm{o}}_{\mathrm{I}} = A \sum \Delta x^{r}_{N} / \sum \Delta t$ for $x^{R}_{N} < L$. This measurement is performed after every 0.05 pore-volumes of fluid are injected and the sum is therefore over the time steps in between. The total flow rates are therefore given by, $q^{\mathrm{i,o}}_{\mathrm{T}} = q^{\mathrm{i,o}}_{\mathrm{C}} + q^{\mathrm{i,o}}_{\mathrm{I}}$. This provides the measurement of the injected and outlet flow rates as a function of the injected pore volumes or of the time. In Fig. 3, we plot $q^{\mathrm{i}}_{\mathrm{T}}$ as a function of the pore-volumes (V_p) injected for (a) $P_L = 1\,\mathrm{kPa}$ and (b) $P_L = 100\,\mathrm{kPa}$. The pore-volume V_p is defined as the ratio between the total volume of the inject fluids and

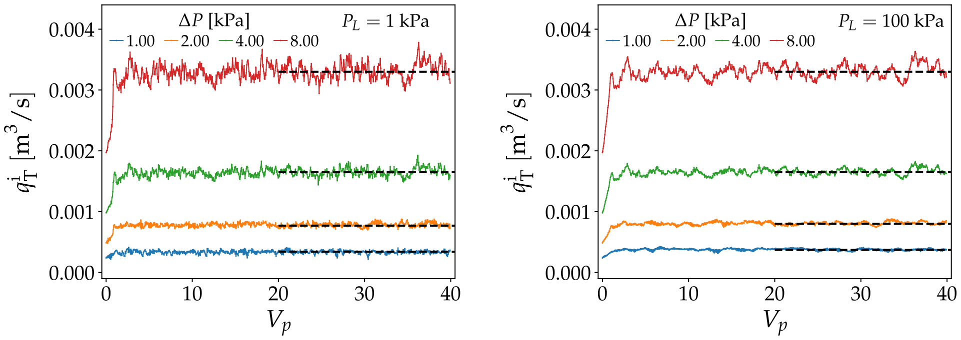

(a) (b)

Fig. 3 Total volumetric flow rate $q^{\mathrm{i}}_{\mathrm{T}}$ at the inlet as a function of the injected pore volume V_p for the outlet pressures (a) $P_L = 1\,\mathrm{kPa}$ and (b) $P_L = 100\,\mathrm{kPa}$. Here the surface tension $\gamma = 0.09\,\mathrm{N/m}$. The steady-state values of the flow rates are measured by taking averages in the range of 20 to 40 pore volumes as indicated by the dashed lines. Here we only show the data sets corresponding to the pressure drops $\Delta P = 1, 2, 4$ and 8 kPa in order to keep the clarity, however all the data sets show the similar trend of reaching the steady state.

the volume of the total pore space of the tube, which provides an estimate of how many times the pore space was flushed with the fluids. All the plots show that the total flow rate $q_{\mathrm{T}}^{\mathrm{i}}$ increases with time at the beginning of the flow. This increase in $q_{\mathrm{T}}^{\mathrm{i}}$ is due to the decrease in the effective viscosity of the system caused by the injection of inviscid compressible gas into the tube filled with viscous incompressible fluid. After the injection of a few pore volumes, $q_{\mathrm{T}}^{\mathrm{i}}$ fluctuates around a constant average ($Q_{\mathrm{T}}^{\mathrm{i}}$) shown by the horizontal dashed lines which defines the steady state. Notice that, the averages are the same for the same values of ΔP for the two different outlet pressures P_L, however the fluctuations are different. This we will see more in the following, that the outlet pressure P_L plays a significant role in the flow properties in addition to the pressure drop ΔP. We run our simulations for 40 pore volumes of fluid where the steady-state averages are taken after 20 pore volumes injected to ensure that a steady state has been reached.

3.2 Bubble Growth

As a compressible bubble moves along the tube, the volume of the bubble increases due to the decrease in the pressure towards the outlet (Vazquez et al. 2010). The bubble can also grow due to other mechanisms, such as the increase in temperature or a phase transition between liquid and gas phases (Welch 1998; Kenning et al. 2006), but these phenomena are not studied here. A simulation with a single bubble inside a short tube is shown in the supplementary material which illustrates that the bubble increases in size as it flows towards the outlet. To understand how this growth depends on different flow parameters in the steady state, we define the growth function $G_{\mathrm{C}}(x)$ by,

$$G_{\mathrm{C}}(x) = \frac{V(x) - V_0}{V_0}\ , \tag{12}$$

where V_0 and $V(x)$ are the volume of a given bubble initially after detaching from the inlet and when its center is at x. We measure G_{C} by including all the bubbles that are not attached to the inlet or outlet and calculate the time average value of $(V(x) - V_0)/V_0$ in the investigated time interval, where x is the center of the bubble.

Figure 4 shows the variation of $G_{\mathrm{C}}(x)$ along the tube for two different outlet pressures, $P_L = 1\,\mathrm{kPa}$ and $100\,\mathrm{kPa}$ where we plot the results for the same set of pressure drops ΔP. These results are with zero surface tension, $\gamma = 0$. There are a few details to note here. First, the plots show that $G_{\mathrm{C}}(x)$ increases with an increase in ΔP. In addition, $G_{\mathrm{C}}(x)$ also depends on the absolute pressures at the inlet and outlet, since we can see that the curves are nonlinear functions of x for $P_L = 1\,\mathrm{kPa}$, whereas for $P_L = 100\,\mathrm{kPa}$, they show linear behavior. Furthermore, $G_{\mathrm{C}}(x)$ approaches $\Delta P/P_L$ at $x = L$ for all the data sets.

To explain the dependency of $G_{\mathrm{C}}(x)$ on ΔP and P_L, we recall Equation 1 and rewrite Equation 12 as,

$$G_{\mathrm{C}}(x) = \frac{P_0 - P(x)}{P(x)}\ , \tag{13}$$

where $P(x)$ is the pressure inside a bubble at x. For $x = L$, $P(x) = P_L$ and therefore $G_{\mathrm{C}}(L) = \Delta P/P_L$ as observed. In Fig. 5, we plot $P(x)$, averaged over different time steps in the steady state, for the two outlet pressures, $P_L = 1\,\mathrm{kPa}$ and $100\,\mathrm{kPa}$. Both of the plots show linear variation along x with the slope $-\Delta P$. We therefore have $P(x) = -x\Delta P/L + P_L + \Delta P$ and thus,

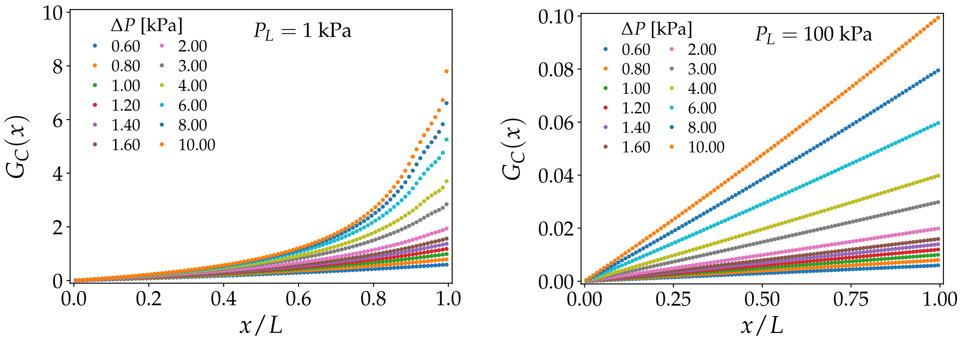

(a) (b)

Fig. 4 Plot of the bubble growth $G_C(x)$ in the steady state as a function of the scaled position x/L inside the tube for zero surface tension, $\gamma = 0$. The two plots show the results for the same set of pressure drops ΔP with different outlet pressures P_L.

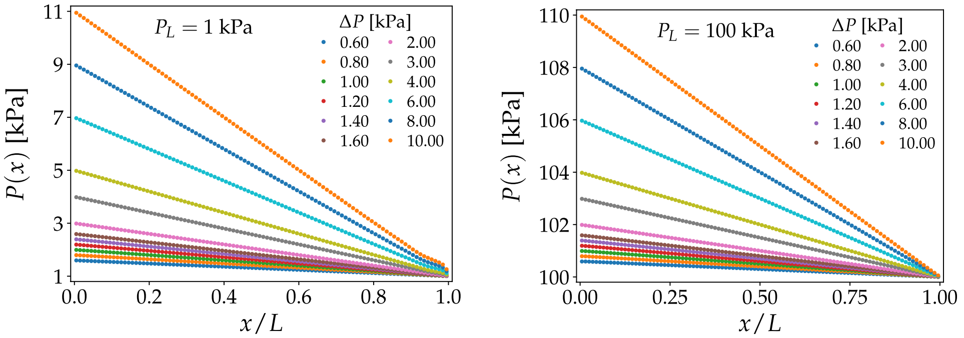

(a) (b)

Fig. 5 Variation of the pressure $P(x)$ [kPa] inside a compressible bubble along the tube during steady state flow. $P(x)$ shows a linear behavior for different values of ΔP and P_L.

$$\frac{G_C(x)}{n_P} = \frac{x/L}{1 + n_P(1 - x/L)} , \tag{14}$$

where $n_P = \Delta P/P_L$. This leads to

$$\frac{G_C(x)}{n_P} \sim \begin{cases} \dfrac{1}{n_P}\left(\dfrac{1}{1 - x/L} - 1\right) & \text{for} \quad n_P \gg 1 , \\ x/L & \text{for} \quad n_P \ll 1 , \end{cases} \tag{15}$$

which explains the concave and linear variation of G_C as function of x/L observed in Fig. 4 **a** and **b**, respectively. The growth of the bubbles along the tube is therefore a function of $n_P = \Delta P/P_L$.

In Figure 6, we plot G_C/n_P for the two outlet pressures P_L with the same sets of values of n_P for (a) $\gamma = 0$ and (b) $\gamma = 0.3\,\mathrm{N/m}$. The plots show that the results for the same values of n_P follow the same curves, irrespective of the outlet pressures P_L. Furthermore, for the non-zero surface tension case in Fig. 6 (b), G_C also shows a periodic oscillation along x

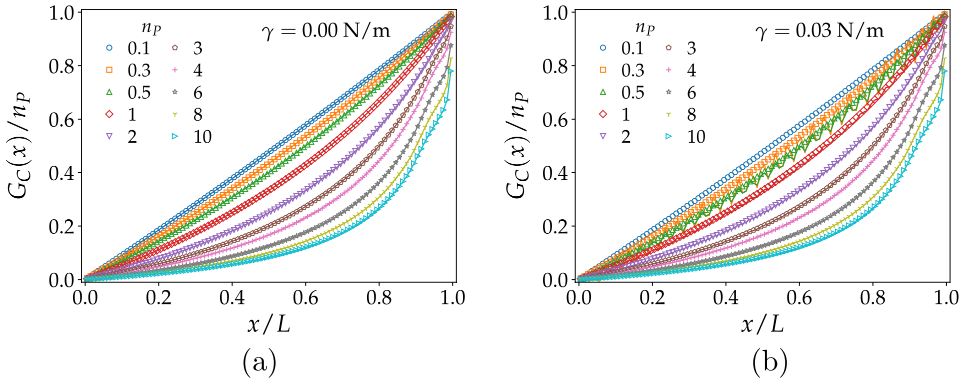

(a) (b)

Fig. 6 Variation of the bubble growth G_C, scaled with $n_P = \Delta P/P_L$, with x/L. Results are plotted for the same sets of n_P for two different values of P_L. The left and right figures correspond to $\gamma = 0$ and $0.03\,\mathrm{N/m}$, respectively. In each plot, the line corresponds to $P_L = 1\,\mathrm{kPa}$ and the symbols correspond to $P_L = 100\,\mathrm{kPa}$.

when both the n_P and P_L are small, that is, for $P_L = 1\,\mathrm{kPa}$ and $n_P \leq 1$. In addition, there is no data point for $n_P \leq 0.3$ with $P_L = 1\,\mathrm{kPa}$, as the movement of the bubbles stopped due to high capillary barriers. This suggests the existence of an effective threshold pressure, below which there will be no flow through the tube. This threshold depends on both γ and P_L, which we will explore more in the following section. We show the different characteristics of flow in the videos provided in electronic supplementary material.

3.3 Effective Rheology

Equations 1 and 2 resist analytical solutions even in the case when there is only a single compressible bubble in the tube. This is due to the pressure in the compressible bubble being inversely proportional to the difference in position of the two menisci surrounding it, whereas the motion of the two surrounding incompressible fluids is determined by the cosine of the positions of the same menisci. These equations, even in this simplest case, are therefore highly nonlinear with an essential singularity lurking in the very neighborhood where we seek solutions. We therefore stick to numerical analysis in the following.

Due to the volumetric growth of the compressible bubbles during their flow towards the outlet, the volumetric flow rate varies along the tube. In addition, this volumetric growth is a function of the pressures, making the average saturation and the effective viscosity of the two fluids inside the tube pressure dependent. These two mechanisms together control the effective rheological behavior of the steady-state flow. In Fig. 7, we show the variation of the volumetric flow rates ($Q_\mathrm{T}^{\mathrm{i,o}}$, $Q_\mathrm{C}^{\mathrm{i,o}}$, $Q_\mathrm{I}^{\mathrm{i,o}}$) as functions of the pressure drop ΔP for the outlet pressure $P_L = 1\,\mathrm{kPa}$ and for different values of the surface tension (γ). Note the differences between the inlet and outlet flow rates for the total and for the each component of flow. For the incompressible fluid, there is no increase in the outlet flow rate compared to its inlet flow rate (third row in Fig. 7) whereas there is a noticeable increase in the outlet flow rate of the compressible fluid (second row in Fig. 7). This increase in $Q_\mathrm{C}^{\mathrm{o}}$ effectively increases the total flow rate at the outlet (first row in Fig. 7). The dashed line in Fig. 7 has a slope equal to 1. The total flow rates show deviations from this dashed line. For the inlet, Q_T^{i} shows small deviations from the dashed line for $\gamma > 0$ at small ΔP. Whereas at the outlet, the deviations are significantly higher due to the increase in the volumetric growth of the compressible fluid.

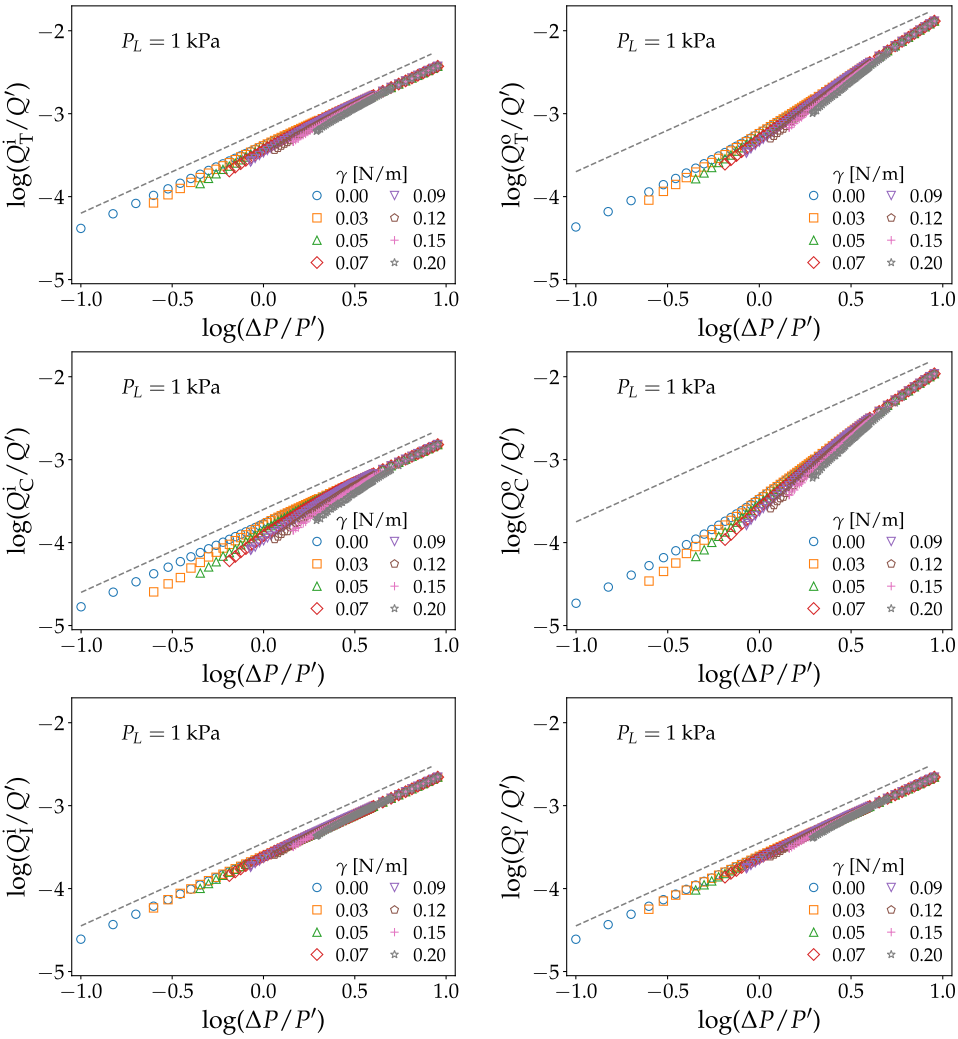

Fig. 7 Plot of the flow rates for the total ($Q_T^{i,o}$), compressible ($Q_C^{i,o}$) and incompressible ($Q_I^{i,o}$) fluids at the inlet (left column) and at the outlet (right column) for $P_L = 1$ kPa as a function of ΔP. The different sets in each plot correspond to different values of the surface tension indicated in the legends. The quantities are divided with $Q' = 1\,\mathrm{m}^3/\mathrm{s}$ and $P' = 1$ kPa, respectively, to make them dimensionless. The dashed line in each plot has a slope 1.

Another point to note in Fig. 7 is that there is a minimum value of ΔP, below which there is no data point available. This is due to the existence of a threshold pressure below which the flow stops. In the supplementary material we show a simulation video in this regime where one can observe that the flow of the bubbles stops at a certain time step. The threshold is due to the capillary forces at the menisci between the two fluids that create capillary barriers at the narrowest points along the tube. Such threshold was also observed in the case of two-phase flow of two incompressible fluids in a tube with variable radius (Sinha et al. 2013). There, it was shown analytically that the average flow rate Q in the steady state varies with the applied pressure drop ΔP as, $Q \sim \sqrt{\Delta P^2 - P_t^2}$ where P_t is the effective threshold pressure. When $|\Delta P| - P_t \ll P_t$, this relationship translates to $Q \sim \sqrt{|\Delta P| - P_t}$, that is, the flow rate varies with the excess pressure drop to the power of 0.5. The threshold pressure depends on the surface tension and on the configuration of the menisci positions inside the tube. If the total capillary barrier is higher than the applied pressure drop, the flow stops. This is similar here for the two-phase flow with one of the fluids being compressible.

We assume a general relation between the average volumetric flow rates $Q_\mathrm{T}^{\mathrm{i,o}}$ and the pressure drop ΔP as,

$$Q_\mathrm{T}^{\mathrm{i,o}} \sim (\Delta P - P_\mathrm{t})^{\beta_{\mathrm{i,o}}} \tag{16}$$

where $\beta_{\mathrm{i,o}}$ is the corresponding exponent. In order to find both the effective threshold pressure P_T and the exponent $\beta_{\mathrm{i,o}}$ from the measurements of $Q_\mathrm{T}^{\mathrm{i,o}}$, we adopt an error minimization technique that was used in earlier studies (Sinha and Hansen 2012; Fyhn et al. 2021). There we choose a series of trial values for P_t and calculate the mean square error ϵ for the linear least square fit by fitting the data points with $\log(Q) \sim \log(\Delta P - P_\mathrm{t})$. Then we select the value of P_t that corresponds to the minimum value of ϵ, implying the best fit of the data points with Equation 16. This is illustrated in the insets of Fig. 8 (a) and (b). The slope for the selected threshold P_t provides the exponent $\beta_{\mathrm{i,o}}$. The variation of the total inlet and outlet flow rates $Q_\mathrm{T}^{\mathrm{i,o}}$ with the excess pressure drop $(\Delta P - P_\mathrm{t})$ are plotted in Fig. 8 for the two outlet pressures $P_L = 1$ and 100 kPa. The data sets show agreement with Equation 16 with the selected values of P_t and β. There is a noticeable difference between the slopes for the inlet and outlet flow rates for $P_L = 1$ kPa whereas for $P_L = 100$ kPa they are similar. For $P_L = 100$ kPa the data points for both Q_T^i and Q_T^o follow a slope of ≈ 1.0 whereas for $P_L = 1$ kPa, the data points for Q_T^i and Q_T^o follow the slopes of ≈ 1.0 and 1.3, respectively. These are indicated by the dashed lines in the figures.

The variations of P_t and $\beta_{\mathrm{i,o}}$ with the surface tension γ are plotted in Fig. 9. The data points were calculated by considering different ranges of ΔP and taking averages over the ranges, and the corresponding standard deviations are plotted as error bars. The threshold pressure P_t is zero at $\gamma = 0$ and then increases gradually with γ which shows that the threshold appears due to capillary forces. The increase in P_t with γ appears to be linear here which is similar to the case of two incompressible fluids, where the linear dependence of P_t on the surface tension was shown analytically (Sinha et al. 2013). Additionally for the compressible flow here, the thresholds also depend on the outlet pressure P_L. For

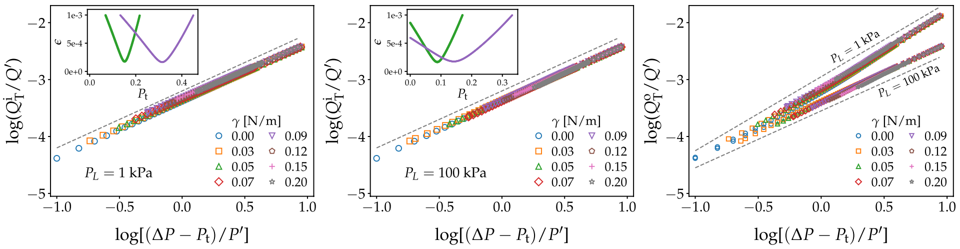

(a) (b) (c)

Fig. 8 Plot of the volumetric inlet flow rate Q_T^i as a function of the excess pressure drop $(\Delta P - P_\mathrm{t})$ for $P_L = 1$ kPa and 100 kPa, where the values of P_t are obtained from a minimization of the least square fit error ϵ. Here $Q' = 1\,\mathrm{m}^3/\mathrm{s}$ and $P' = 1$ kPa. The minimization is illustrated in the insets of **a** and **b** for $\gamma = 0.05$ N/m (green) and 0.09 N/m (purple). The dashed lines in **a** and **b** have a slope 1 whereas in **c**, the lower and upper dashed lines have slopes 1 and 1.3, respectively.

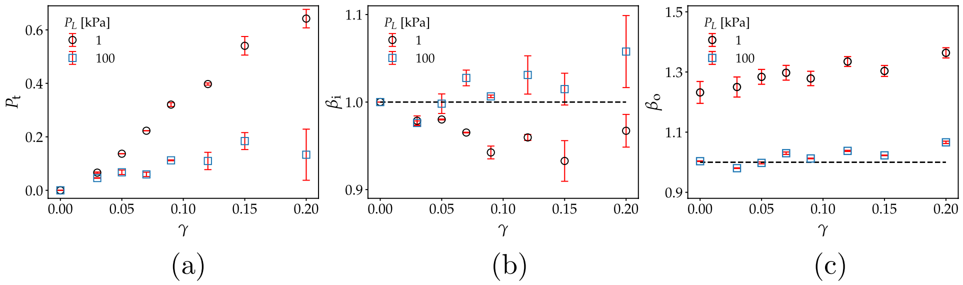

Fig. 9 Variation of the threshold pressure P_t and the exponents $\beta_{i,o}$ as functions of the effective surface tension γ for $P_L = 1$ and 100 kPa. P_t increases with the increase of γ and the values are much higher for $P_L = 1$ kPa compared to $P_L = 100$ kPa. The exponent β_i for the inlet flow rate are close to 1 for both the values of P_L whereas for the outlet flow rate $\beta_o \approx 1.3$ for $P_L = 1$ kPa. For $P_L = 100$ kPa, β_o remains close to β_i. The dashed horizontal lines indicate the value 1.0 of the y axis.

the lower outlet pressure $P_L = 1$ kPa, the thresholds are systematically higher compared to those for $P_L = 100$ kPa for the whole range of γ. Furthermore, the exponents $\beta_{i,o}$ also depend on the outlet pressure as seen from Figs. 9 (b) and (c). The difference is more visible for the exponents related to the outlet flow rates than the inlet. For the inlet flow rate, β_i has values around ≈ 0.95 and 1.02 for $P_L = 1$ kPa and 100 kPa, respectively, showing almost linear dependence for both the cases. For the outlet flow rates, β_o remains close to β_i for $P_L = 100$ kPa whereas for $P_L = 1$ kPa, β_o increases to ≈ 1.3. This increase in β_o compared to β_i reflects the dependence of the volumetric growth $G_C(x)$ of the bubbles on P_L, indicating an underlying dependence of the rheological behavior on the absolute inlet or outlet pressures. However, at this point we are unable to describe how the two parameters P_t and β scale with P_L, which needs further study. In addition, we have only considered an intermediate volumetric fractional flow $F_C = 0.4$ here, which also controls β and P_t (Roy et al. 2021). If the fractional flow or the saturation is made near to either 0 or 1, the system will approach single-phase flow and the linearity in the rheology of the Newtonian fluids should be retrieved.

Compared to the study of a single capillary tube here, a porous medium is composed of many interconnected pores of different sizes. Existing studies of two-phase flow in porous media have shown the existence of different power-law regimes for the relation between volumetric flow rate and pressure drop. These regimes are characterized by different exponents. The studies involve experiments (Tallakstad et al. 2009, 2009; Rassi et al. 2011; Sinha et al. 2017; Gao et al. 2020; Zhang et al. 2021), Lattice Boltzmann simulations (Yiotis et al. 2013), pore-network modeling (Sinha and Hansen 2012; Sinha et al. 2017) and analytical calculations (Tallakstad et al. 2009; Sinha and Hansen 2012; Roy et al. 2019; Zhang et al. 2021). There are three regimes, an intermediate nonlinear regime where the flow rate Q increases at a rate much faster than the applied pressure drop ΔP with a power law exponent larger than one and up to around 2.5. There are in addition two linear regimes for either smaller (Yiotis et al. 2013; Gao et al. 2020; Zhang et al. 2021) or larger (Yiotis et al. 2013; Sinha and Hansen 2012; Sinha et al. 2017) volumetric flow rates than the nonlinear regime. This allows the definition of a lower and upper crossover pressure drop. The origin of the power law in a porous network and the crossovers to different regimes, can be explained by two dominant factors, the rheology of individual pores and the distribution of the threshold pressures in the network (Roy et al. 2019). A simple explanation can be drawn from a disordered network of threshold resistors (Roux and Herrmann 1987) where each resistor has a threshold voltage to start conducting the current. In a network with links with a distribution of thresholds, there will be a regime when new conducting paths will appear while increasing the global pressure drop. The increase in the flow rate through each path together with the increase in the number of paths leads to an effective increase in Q faster than ΔP. This results in the nonlinear exponent being higher than 1, the value of which depends on the distribution of the thresholds in each link (Roy et al. 2019). The linear regime above this nonlinear regime appears from all the available paths being conducting whereas the linear regime below appears from the flow being in single percolating channels, which are governed by the rheology of individual pores. According to this explanation, the experimental (Gao et al. 2020; Zhang et al. 2021) and numerical (Yiotis et al. 2013) observations of two-phase flow in porous media showing linear variation of flow rate in the low pressure regime therefore indicate that the flow in the single channels consisting of many pores are linear, which is similar to what we have found for the lower outlet pressure in the present compressible/incompressible flow case.

4 Conclusions

We have studied the flow of alternating compressible bubbles and incompressible droplets through a capillary tube with variable radius. The motion of the bubbles was given by the model Equations 1 and 2, thus assuming the compressible fluid to be an ideal gas with zero viscosity, whereas the incompressible fluid is Newtonian. The incompressible fluid is more wetting than the compressible gas, but not to a degree that films form. We switch between injecting the compressible and incompressible fluid at intervals so that the fractional flow rate is essentially constant at the inlet. We fix the pressure drop along the tube in addition to an ambient pressure. This creates steady-state flow conditions in the tube.

The compressible bubbles expand as they move from the higher pressure region at the inlet towards the lower pressure at the outlet. This expansion accelerates the incompressible fluid, thus making the volumetric flow rate larger at the outlet than at the inlet. The lower the ambient pressure is, the stronger this effect is.

We measure volumetric flow rate at the inlet, finding essentially a linear relationship between the volumetric flow rate and the pressure drop. However, there is a threshold pressure that needs to be overcome in order to have flow through the tube. At the outlet, we find that the volumetric flow rate is still linear in the excess pressure drop when the ambient pressure is low. However, when the ambient pressure is high, the volumetric flow rate at the outlet becomes proportional to the excess pressure to a power of around 1.3.

This behavior is very different from that of two incompressible fluids moving through a corresponding tube: Here the volumetric flow rate, being the same at the inlet and the outlet, is proportional to the square root of the excess pressure.

We expected the flow rate-pressure drop constitutive relations to be different in this compressible/incompressible case than that of two incompressible fluids. However, that we should find *linearity* was a big surprise. A precise explanation as to why this is so, is still lacking.

Besides these surprising results, this work makes a first step in modeling of compressible/incompressible fluid mixtures in dynamic network models. We may then envision using more sophisticated equations of state for the compressible fluid beyond the ideal gas law. This allows the consideration of, e.g., phase transitions such as boiling and condensation in porous media.

Finally, we like to point out that we have not considered film-flow or contact line pinning in this study. Pinning of the contact lines will change the relation between the capillary force at the interfaces and the shape of the tube, which is determined by two more fixed parameters: the surface tension and the wetting angle. If the pinning is due to surface roughness at scales much finer than the variations in the tube radius, this will result in an effective wetting angle different from the one expected for smooth surfaces (see Blunt 2017, pp 11-14). Hence, we do not expect our results to be qualitatively different in this case. If, on the other hand, the roughness is on the same scale as the radius variations, we are dealing with a tube that essentially has a different shape than the one we are considering. Even in this case, we do not expect qualitative changes from the results we report. However, there will most probability be quantitative changes. Different tube shapes were studied by Lanza et al. for an immiscible mixture of a yield stress fluid and a Newtonian fluid, finding a quantitative difference between different tube shapes (Lanza et al. 2022; Talon et al. 2014). However, both the fluids were incompressible in that study, therefore a possible future extension of both of these studies would be to include a compressible fluid together with a non-Newtonian fluid in a capillary.

The film flow on the other hand will introduce parallel components of the two fluids in the system whereas in our present problem the two fluid components are always in series combination. Depending on the thickness of the films, this may change the effective relationship between the flow rate and the pressure drop. Film flow can be observed when the pores contain rough grain surfaces and corners (Chen et al. 2018; Cejas et al. 2018) or when a fluid phase is completely wetting (Aursjø et al. 2014), whereas in case of drainage dominated flow the film flow may be neglected. Experiments have also shown that gravity plays a role in controlling the active zone of film flow in a porous media (Moura et al. 2019). Experiments with the same porous media with different types of fluids have shown that the nonlinear exponent β was smaller for the fluids that show strong film flow (Aursjø et al. 2014) compared to those without film flow (Tallakstad et al. 2009). Fluid wettabilities in this context strongly affects the appearance of films as well as the rheological nonlinearity in general (Zhang et al. 2022; Fyhn et al. 2021). How the introduction of films or changing the wettability of the fluids will affect the results of the present study is therefore a question for the future.

5 Supplementary Material

The electronic supplementary material contains videos showing different flow characteristics. In these videos we considered a tube with $L = 10\,\mathrm{cm}$, $w = 1\,\mathrm{cm}$, $a = 0.25\,\mathrm{cm}$ and $h = 5$ (Equation 4). The simulations were performed for $P_L = 1\,\mathrm{kPa}$ and $\gamma = 0.2\,\mathrm{N/m}$. The compressible bubbles are colored with magenta whereas the incompressible droplets are colored with black. The videos are not in real time. We show four different simulations with different values of ΔP:

(a) Flow of a single bubble of compressible gas in incompressible fluid. Here $\Delta P = 5\,\mathrm{kPa}$. The video shows the increase in the volume of the bubble as it approaches the outlet.
(b) Injection of multiple compressible bubbles and incompressible droplets at a *very low* pressure drop, $\Delta P = 0.3\,\mathrm{kPa}$. The flow stops after a certain time when several inter-

faces appeared in the tube. This shows the existence of a total capillary barrier, which is higher than the applied pressure drop here.

(c) Two-phase flow of multiple compressible bubbles and incompressible droplets at a *low* pressure drop, $\Delta P = 0.4\,\text{kPa}$. Here the bubbles speed up and slow down as they flow, showing the combined effect of the surface tension and the shape of the tube. The bubbles also grow in volume towards the outlet.

(d) Two-phase flow of multiple compressible bubbles and incompressible droplets at a *higher* pressure drop, $\Delta P = 3\,\text{kPa}$. The bubbles do not show any significant slowing down in this case, indicating the capillary forces being negligible compared to the viscous pressure drop. The volumetric expansion of the compressible bubbles can also be observed here.

Supplementary Information The online version contains supplementary material available at https://doi.org/10.1007/s11242-022-01893-2.

Acknowledgements We thank Federico Lanza, Marcel Moura and Håkon Pedersen for helpful discussions.

Funding This work is supported by the Research Council of Norway through its Centers of Excellence funding scheme, project number 262644. Funding was also provided by the PredictCUI project coordinated by SINTEF Energy Research, and the authors acknowledge the contributions of Equinor, Gassco, Shell, and the PETROMAKS 2 programme of the Research Council of Norway (308770). Open access funding provided by NTNU Norwegian University of Science and Technology (incl St. Olavs Hospital - Trondheim University Hospital).

Conflict of interest The authors have not disclosed any competing interests.

References

Abidoye, L.K., Khudaida, K.J., Das, D.B.: Geological carbon sequestration in the context of two-phase flow in porous media: A review. Crit. Rev. Env. Sc. Tech. **45**, 1105 (2015). https://doi.org/10.1080/10643389.2014.924184

Aursjø, O., Erpelding, M., Tallakstad, K.T., Flekkøy, E.G., Hansen, A., Måløy, K.J.: Film flow dominated simultaneous flow of two viscous incompressible fluids through a porous medium. Front. Phys. **2**, 63 (2014). https://doi.org/10.3389/fphy.2014.00063

Bear, J.: Dynamics of Fluids in Porous Media. Dover, Mineola, New York (1988)

Blunt, M.J.: Flow in porous media pore-network models and multiphase flow. Curr. Opin. Colloid Interface Sci. **6**, 197 (2001). https://doi.org/10.1016/S1359-0294(01)00084-X

Blunt, M.J.: Multiphase Flow in Permeable Media. Cambridge University Press, Cambridge (2017)

Bremer, J., Sundmacher, K.: Operation range extension via hot-spot control for catalytic co2 methanation reactors. React. Chem. Eng. **4**, 1019 (2019). https://doi.org/10.1039/C9RE00147F

Cejas, C.M., Hough, L.A., Frétigny, C., Dreyfus, R.: Effect of geometry on the dewetting of granular chains by evaporation. Soft Matter **14**, 6994 (2018). https://doi.org/10.1039/c8sm01179f

Chen, C., Joseph, P., Geoffroy, S., Prat, M., Duru, P.: Evaporation with the formation of chains of liquid bridges. J. Fluid Mech. **837**, 703 (2018). https://doi.org/10.1017/jfm.2017.827

Chen, J.D., Wilkinson, D.: Pore-scale viscous fingering in porous media. Phys. Rev. Lett. **55**, 1892 (1985). https://doi.org/10.1103/PhysRevLett.55.1892

Darcy, H.: Les Fontaines publiques de la ville de Dijon 647, (1856)

Dullien, F.A.L.: Porous Media: Fluid. Transport and Pore Structure. Academic Press, San Diego (1992)

Feder, J., Flekkøy, E.G., Hansen, A.: Physics of Flow in Porous Media. Cambridge University Press, Cambridge (2022)

Fyhn, H., Sinha, S., Roy, S., Hansen, A.: Rheology of immiscible two-phase flow in mixed wet porous media: dynamic pore network model and capillary fiber bundle model results. Transp. Porous Med. **139**, 491 (2021). https://doi.org/10.1007/s11242-021-01674-3

Gao, Y., Lin, Q., Bijeljic, B., Blunt, M.J.: Pore-scale dynamics and the multiphase darcy law. Phys. Rev. Fluids. **5**, 013801 (2020). https://doi.org/10.1103/PhysRevFluids.5.013801

Gedupudi, S., Zu, Y.Q., Karayiannis, T.G., Kenning, D.B.R., Yan, Y.Y.: Confined bubble growth during flow boiling in a mini/micro-channel of rectangular cross-section part i: experiments and 1-d modelling. Inr. J. Therm. Sci. **50**, 250 (2011). https://doi.org/10.1016/j.ijthermalsci.2010.09.001

Gunstensen, A.K., Rothman, D.H., Zaleski, S., Zanetti, G.: Lattice boltzmann model of immiscible fluids. Phys. Rev. A **43**, 4320 (1991). https://doi.org/10.1103/PhysRevA.43.4320

Guo, S., Feng, Y., Jacob, J., Renard, F., Sagaut, P.: An efficient lattice boltzmann method for compressible aerodynamics on d3q19 lattice. J. Comput. Phys. **418**, 109570 (2020). https://doi.org/10.1016/j.jcp.2020.109570

Huang, G., Zhu, Y., Liao, Z., Ouyang, X.L., Jiang, P.X.: Experimental investigation of transpiration cooling with phase change for sintered porous plates. Int. J. Heat Mass Trans. **114**, 1201 (2017). https://doi.org/10.1016/j.ijheatmasstransfer.2017.05.114

Iglauer, S., Paluszny, A., Rahman, T., Zhang, Y., Wülling, W., Lebedev, M.: Residual trapping of co2 in an oil-filled, oil-wet sandstone core: results of three-phase pore-scale imaging. Geophys. Res. Lett. **46**, 11146 (2019). https://doi.org/10.1029/2019GL083401

Joekar-Niasar, V., Hassanizadeh, S.M.: Analysis of fundamentals of two-phase flow in porous media using dynamic pore-network models: a review. Crit. Rev. Environ. Sci. Technol. **42**, 1895 (2012). https://doi.org/10.1080/10643389.2011.574101

Kenning, D.B.R., Wen, D.S., Das, K.S., Wilson, S.K.: Confined growth of a vapour bubble in a capillary tube at initially uniform superheat: experiments and modelling. Int. J. Heat Mass Trans. **49**, 4653 (2006). https://doi.org/10.1016/j.ijheatmasstransfer.2006.04.010

Lanza, F., Rosso, A., Talon, L., Hansen, A.: Non-newtonian rheology in a capillary tube with varying radius. Transp. Porous Med. **145**, 245 (2022). https://doi.org/10.1007/s11242-022-01848-7

Lenormand, R., Touboul, E.: Zarcone: numerical models and experiments on immiscible displacements in porous media. J. Fluid Mech. **189**, 165 (1988). https://doi.org/10.1017/S0022112088000953

Lenormand, R., Zarcone, C.: Invasion percolation in an etched network: measurement of a fractal dimension. Phys. Rev. Lett. **54**, 2226 (1985). https://doi.org/10.1103/PhysRevLett.54.2226

Leverett, M.C.: Capillary behavior in porous solids. Trans. AIME **142**, 152 (1941). https://doi.org/10.2118/941152-G

Li, W., Wang, Z., Yang, F., Alam, T., Jiang, M., Qu, X., Kong, F., Khan, A.S., Liu, M., Alwazzan, M., Tong, Y., Li, C.: Supercapillary architecture-activated two-phase boundary layer structures for highly stable and efficient flow boiling heat transfer. Adv. Matter **32**, 1905117 (2020). https://doi.org/10.1002/adma.201905117

Li, D., Wu, G.S., Wang, W., Wang, Y.D., Liu, D., Zhang, D.C., Chen, Y.F., Peterson, G.P., Yang, R.: Enhancing flow boiling heat transfer in microchannels for thermal management with monolithically-integrated silicon nanowires. Nano Lett. **12**, 3385 (2012). https://doi.org/10.1021/nl300049f

Li, X., Yortsos, Y.C.: Bubble growth and stability in an effective porous medium. Phys. Fluids **6**, 1663 (1994). https://doi.org/10.1063/1.868229

Løvoll, G., Méheust, Y., Toussaint, R., Schmittbuhl, J., Måløy, K.J.: Growth activity during fingering in a porous hele-shaw cell. Phys. Rev. E **70**, 026301 (2004). https://doi.org/10.1103/PhysRevE.70.026301

Meakin, P., Tartakovsky, A.M.: Modeling and simulation of pore-scale multiphase fluid flow and reactive transport in fractured and porous media. Rev. Geophys. **47**, 3002 (2009). https://doi.org/10.1029/2008RG000263

Moura, M., Flekkøy, E.G., Måløy, K.J.: Connectivity enhancement due to film flow in porous media. Phys. Rev. Fluids **4**, 094102 (2019). https://doi.org/10.1103/PhysRevFluids.4.094102

Måløy, K.J., Feder, J., Jøssang, T.: Viscous fingering fractals in porous media. Phys. Rev. Lett. **55**, 2688 (1985). https://doi.org/10.1103/PhysRevLett.55.2688

Niblett, D., Mularczyk, A., Niasar, V., Eller, J., Holmes, S.: Two-phase flow dynamics in a gas diffusion layer - gas channel - microporous layer system. J. Power Sour. **471**, 228427 (2020). https://doi.org/10.1016/j.jpowsour.2020.228427

Panton, R.L.: Incompressible Flow, 4th edn. Wiley, New Jersey (2013)

Qiu, R.F., You, Y.C., Zhu, C.X., Chen, R.Q.: Lattice boltzmann simulation for high-speed compressible viscous flows with a boundary layer. Appl. Math. Model. **48**, 567 (2017). https://doi.org/10.1016/j.apm.2017.03.016

Ramstad, T., Idowu, N., Nardi, C., Øren, P.E.: Relative permeability calculations from two-phase flow simulations directly on digital images of porous rocks. Transp. Porous Media **94**, 487 (2012). https://doi.org/10.1007/s11242-011-9877-8

Rassi, E.M., Codd, S.L., Seymour, J.D.: Nuclear magnetic resonance characterization of the stationary dynamics of partially saturated media during steady-state infiltration flow. New J. Phys. **13**, 015007 (2011). https://doi.org/10.1088/1367-2630/13/1/015007

Reynolds, C.A., Krevor, S.: Characterizing flow behavior for gas injection: Relative permeability of co2-brine and n2-water in heterogeneous rocks. Water Resources Res. **51**, 9464 (2015). https://doi.org/10.1002/2015WR018046

Rossi, C., Nimmo, J.R.: Modeling of soil water retention from saturation to oven dryness. Water Resour. Res. **30**, 701 (1994). https://doi.org/10.1029/93WR03238

Roux, S., Herrmann, H.J.: Disorder-induced nonlinear conductivity. Europhys. Lett. **1227**, 4 (1987). https://doi.org/10.1209/0295-5075/4/11/003

Roy, S., Hansen, A., Sinha, S.: Effective rheology of two-phase flow in a capillary fiber bundle model. Front. Phys. **7**, 92 (2019). https://doi.org/10.3389/fphy.2019.00092

Roy, S., Sinha, S., Hansen, A.: Role of pore-size distribution on effective rheology of two-phase flow in porous media. Front. Water **3**, 709833 (2021). https://doi.org/10.3389/frwa.2021.709833

Sapin, P., Gourbil, A., Duru, P., Fichot, F., Prat, M., Quintard, M.: Reflooding with internal boiling of a heating model porous medium with mm-scale pores. Int. J. Heat Mass Trans. **99**, 512 (2016). https://doi.org/10.1016/j.ijheatmasstransfer.2016.04.013

Sinha, S., Bender, A.T., Danczyk, M., Keepseagle, K., Prather, C.A., Bray, J.M., Thrane, L.W., Seymour, J.D., Codd, S.L., Hansen, A.: Effective rheology of two-phase flow in three-dimensional porous media: experiment and simulation. Transp. Porous Med. **119**, 77 (2017). https://doi.org/10.1007/s11242-017-0874-4

Sinha, S., Gjennestad, M.A., Vassvik, M., Hansen, A.: Fluid meniscus algorithms for dynamic pore-network modeling of immiscible two-phase flow in porous media. Front. Phys. **9**, 548497 (2021). https://doi.org/10.3389/fphy.2020.548497

Sinha, S., Hansen, A.: Effective rheology of immiscible two-phase flow in porous media. Europhys. Lett. **99**, 44004 (2012). https://doi.org/10.1209/0295-5075/99/44004

Sinha, S., Hansen, A., Bedeaux, D., Kjelstrup, S.: Effective rheology of bubbles moving in a capillary tube. Phys. Rev. E **87**, 025001 (2013). https://doi.org/10.1103/PhysRevE.87.025001

Sun, Y., Zhang, L., Xu, H., Zhong, X.: Subcooled flow boiling heat transfer from microporous surfaces in a small channel. Int. J. Therm. Sci. **50**, 881 (2011). https://doi.org/10.1016/j.ijthermalsci.2011.01.019

Tallakstad, K.T., Knudsen, H.A., Ramstad, T., Løvoll, G., Måløy, K.J., Toussaint, R., Flekkøy, E.G.: Steady-state two-phase flow in porous media: statistics and transport properties. Phys. Rev. Lett. **102**, 074502 (2009). https://doi.org/10.1103/PhysRevLett.102.074502

Tallakstad, K.T., Løvoll, G., Knudsen, H.A., Ramstad, T., Flekkøy, E.G., Måløy, K.J.: Steady-state, simultaneous two-phase flow in porous media: an experimental study. Phys. Rev. E **80**, 036308 (2009). https://doi.org/10.1103/PhysRevE.80.036308

Talon, L., Auradou, H., Hansen, A.: Effective rheology of bingham fluids in a rough channel. Front. Phys. **2**, 24 (2014). https://doi.org/10.3389/fphy.2014.00024

Vazquez, A., Leifer, I., Sánchez, R.M.: Consideration of the dynamic forces during bubble growth in a capillary tube. Chem. Eng. Sc. **65**, 4046 (2010). https://doi.org/10.1016/j.ces.2010.03.041

Washburn, E.W.: The dynamics of capillary flow. Phys. Rev. **17**, 273 (1921). https://doi.org/10.1103/PhysRev.17.273

Welch, S.W.J.: Direct simulation of vapor bubble growth. Int. J. Heat Mass Trans. **41**, 1655 (1998). https://doi.org/10.1016/S0017-9310(97)00285-8

Yiotis, A.G., Talon, L., Salin, D.: Blob population dynamics during immiscible two-phase flows in reconstructed porous media. Phys. Rev. E **87**, 033001 (2013). https://doi.org/10.1103/PhysRevE.87.033001

Zhang, Y., Bijeljic, B., Blunt, M.J.: Nonlinear multiphase flow in hydrophobic porous media. J. Fluid Mech. **934**, 3 (2022). https://doi.org/10.1017/jfm.2021.1148

Zhang, Y., Bijeljic, B., Gao, Y., Lin, Q., Blunt, M.J.: Quantification of non-linear multiphase flow in porous media. Geophys. Res. Lett. **48**, 2020–090477 (2021). https://doi.org/10.1029/2020GL090477

Zhao, B., MacMinn, C.W., Primkulov, B.K., Chen, Y., Valocchi, A.J., Zhao, J., et al.: Comprehensive comparison of pore-scale models for multiphase flow in porous media. Proc. Natl. Acad. Sci. **116**, 13799 (2019). https://doi.org/10.1073/pnas.1901619116

ISBN 978-82-326-7364-3 (printed ver.)
ISBN 978-82-326-7363-6 (electronic ver.)
ISSN 1503-8181 (printed ver.)
ISSN 2703-8084 (online ver.)

NTNU
Norwegian University of
Science and Technology